ADVANCES IN BIOCHEMICAL ENGINEERING/BIOTECHNOLOGY 119

Series Editor T. Scheper
Volume Editors I. Endo · T. Nagamune

Nano/Micro Biotechnology

Springer

119

Advances in Biochemical Engineering/Biotechnology

Series Editor: T. Scheper

Editorial Board:
S. Belkin • I. Endo • S.-O. Enfors • W.-S. Hu •
B. Mattiasson • J. Nielsen • G. Stephanopoulos • G.T. Tsao
R. Ulber • A.-P. Zeng • J.-J. Zhong • W. Zhou

Advances in Biochemical Engineering/Biotechnology

Series Editor: T. Scheper

Recently Published and Forthcoming Volumes

Biotechnology in China II
Chemicals, Energy and Environment
Volume Editors: Tsao, G.T., Ouyang, P., Chen, J.
Vol. 122, 2010

Biosystems Engineering II
Linking Cellular Networks and Bioprocesses
Volume Editors: Wittmann, C., Krull, R.
Vol. 121, 2010

Biosystems Engineering I
Creating Superior Biocatalysts
Volume Editors: Wittmann, C., Krull, R.
Vol. 120, 2010

Nano/Micro Biotechnology
Volume Editors: Endo, I., Nagamune, T.
Vol. 119, 2010

Whole Cell Sensing Systems II
Volume Editors: Belkin, S., Gu, M.B.
Vol. 118, 2010

Whole Cell Sensing Systems I
Volume Editors: Belkin, S., Gu, M.B.
Vol. 117, 2010

Optical Sensor Systems in Biotechnology
Volume Editor: Rao, G.
Vol. 116, 2009

Disposable Bioreactors
Volume Editor: Eibl, R., Eibl, D.
Vol. 115, 2009

Engineering of Stem Cells
Volume Editor: Martin, U.
Vol. 114, 2009

Biotechnology in China I
From Bioreaction to Bioseparation and Bioremediation
Volume Editors: Zhong, J.J., Bai, F.-W., Zhang, W.
Vol. 113, 2009

Bioreactor Systems for Tissue Engineering
Volume Editors: Kasper, C., van Griensven, M., Poertner, R.
Vol. 112, 2008

Food Biotechnology
Volume Editors: Stahl, U., Donalies, U. E. B., Nevoigt, E.
Vol. 111, 2008

Protein – Protein Interaction
Volume Editors: Seitz, H., Werther, M.
Vol. 110, 2008

Biosensing for the 21st Century
Volume Editors: Renneberg, R., Lisdat, F.
Vol. 109, 2007

Biofuels
Volume Editor: Olsson, L.
Vol. 108, 2007

Green Gene Technology
Research in an Area of Social Conflict
Volume Editors: Fiechter, A., Sautter, C.
Vol. 107, 2007

White Biotechnology
Volume Editors: Ulber, R., Sell, D.
Vol. 105, 2007

Analytics of Protein-DNA Interactions
Volume Editor: Seitz, H.
Vol. 104, 2007

Tissue Engineering II
Basics of Tissue Engineering and Tissue Applications
Volume Editors: Lee, K., Kaplan, D.
Vol. 103, 2007

Tissue Engineering I
Scaffold Systems for Tissue Engineering
Volume Editors: Lee, K., Kaplan, D.
Vol. 102, 2006

Cell Culture Engineering
Volume Editor: Hu, W.-S.
Vol. 101, 2006

Nano/Micro Biotechnology

Volume Editors:
Isao Endo · Teruyuki Nagamune

With contributions by

H. Akita · T. Fujii · H. Harashima · H. Hatakeyama · Ha M. Hiep · A. Ikai · S. Kaneda · K. Kikuchi · T. Kitamori · K. Kogure · V.N. Morozov · N. Nagatani · Q. Ni · T. Nishizaka · K. Onodera · M. Saito · K. Sato · E. Tamiya · T. Torii · Y. Yamagata · J. Zhang

Springer

Editors
Prof. Dr. Isao Endo
Riken Institute
Hirosawa 2-1
Wako-shi Saitama 351-0198
Japan
za47583@pb3.so-net.ne.jp

Prof. Dr. Teruyuki Nagamune
University of Tokyo
School of Engineering
Dept. Bioengineering
Hongo 7-3-1
Bunkyo-ku
113-8656 Tokyo
Japan
nagamune@bioeng.t.u-tokyo.ac.jp

ISSN 0724-6145 e-ISSN 1616-8542
ISBN 978-3-642-14946-7 e-ISBN 978-3-642-14947-4
DOI 10.1007/978-3-642-14947-4
Springer Heidelberg Dordrecht London New York

Library of Congress Control Number: 2010934930

© Springer-Verlag Berlin Heidelberg 2010
This work is subject to copyright. All rights are reserved, whether the whole or part of the material is concerned, specifically the rights of translation, reprinting, reuse of illustrations, recitation, broadcasting, reproduction on microfilm or in any other way, and storage in data banks. Duplication of this publication or parts thereof is permitted only under the provisions of the German Copyright Law of September 9, 1965, in its current version, and permission for use must always be obtained from Springer. Violations are liable to prosecution under the German Copyright Law.
The use of general descriptive names, registered names, trademarks, etc. in this publication does not imply, even in the absence of a specific statement, that such names are exempt from the relevant protective laws and regulations and therefore free for general use.

Cover design: WMXDesign GmbH, Heidelberg, Germany

Printed on acid-free paper

Springer is part of Springer Science+Business Media (www.springer.com)

Series Editor

Prof. Dr. T. Scheper

Institute of Technical Chemistry
University of Hannover
Callinstraße 3
30167 Hannover, Germany
scheper@iftc.uni-hannover.de

Volume Editors

Prof. Dr. Isao Endo

Riken Institute
Hirosawa 2-1
Wako-shi Saitama 351-0198
Japan
za47583@pb3.so-net.ne.jp

Prof. Dr. Teruyuki Nagamune

University of Tokyo
School of Engineering
Dept. Bioengineering
Hongo 7-3-1
Bunkyo-ku
113-8656 Tokyo
Japan
nagamune@bioeng.t.u-tokyo.ac.jp

Editorial Board

Prof. Dr. S. Belkin

Interfaculty Biotechnology Program
Institute of Life Sciences
The Hebrew University of Jerusalem
Jerusalem 91904, Israel
shimshon@vms.huji.ac.il

Prof. Dr. I. Endo

Saitama Industrial Technology Center
3-12-18, Kamiaoki Kawaguchi-shi
Saitama, 333-0844, Japan
a1102091@pref.saitama.lg.jp

Prof. Dr. S.-O. Enfors

Department of Biochemistry
and Biotechnology
Royal Institute of Technology
Teknikringen 34,
100 44 Stockholm, Sweden
enfors@biotech.kth.se

Prof. Dr. W.-S. Hu

Chemical Engineering
and Materials Science
University of Minnesota
421Washington Avenue SE
Minneapolis, MN 55455-0132, USA
wshu@cems.umn.edu

Prof. Dr. B. Mattiasson

Department of Biotechnology
Chemical Center, Lund University
P.O. Box 124, 221 00 Lund, Sweden
bo.mattiasson@biotek.lu.se

Prof. Dr. J. Nielsen

Chalmers University of Technology
Department of Chemical and Biological
Engineering
Systems Biology
Kemivägen 10
41296 Göteborg
Sweden
nielsen@chalmers.se

Prof. Dr. G. Stephanopoulos

Department of Chemical Engineering
Massachusetts Institute of Technology
Cambridge, MA 02139-4307, USA
gregstep@mit.edu

Prof. Dr. G. T. Tsao

Professor Emeritus
Purdue University
West Lafayette, IN 47907, USA
tsaogt@ecn.purdue.edu
tsaogt2@yahoo.com

Prof. Dr. Roland Ulber

FB Maschinenbau und Verfahrenstechnik
Technische Universität Kaiserslautern
Gottlieb-Daimler-Straße
67663 Kaiserslautern, Germany
ulber@mv.uni-kl.de

Prof. Dr. A.-P. Zeng

Technische Universität Hamburg-Harburg
Institut für Bioprozess- und Biosystem-technik
Denickestrasse 1
21073 Hamburg, Germany
aze@tu-harburg.de

Prof. Dr. J.-J. Zhong

Bio-Building #3-311
College of Life Science & Biotechnology
Key Laboratory of Microbial Metabolism,
Ministry of Education
Shanghai Jiao Tong University
800 Dong-Chuan Road
Minhang, Shanghai 200240, China
jjzhong@sjtu.edu.cn

Dr. W. Zhou

Sr. Director, BioProcess Engineering
Technology Development
Genzyme Corporation
45 New York Avenue
Framingham, MA 01701-9322, USA
Weichang.Zhou@genzyme.com

Honorary Editors

Prof. Dr. A. Fiechter

Institute of Biotechnology
Eidgenössische Technische Hochschule
ETH-Hönggerberg
8093 Zürich, Switzerland
ae.fiechter@bluewin.ch

Prof. Dr. K. Schügerl

Institute of Technical Chemistry
University of Hannover, Callinstraße 3
30167 Hannover, Germany
schuegerl@iftc.uni-hannover.de

Advances in Biochemical Engineering/ Biotechnology Also Available Electronically

Advances in Biochemical Engineering/Biotechnology is included in Springer's eBook package *Chemistry and Materials Science*. If a library does not opt for the whole package the book series may be bought on a subscription basis. Also, all back volumes are available electronically.

For all customers who have a standing order to the print version of *Advances in Biochemical Engineering/Biotechnology*, we offer the electronic version via SpringerLink free of charge.

If you do not have access, you can still view the table of contents of each volume and the abstract of each article by going to the SpringerLink homepage, clicking on "Chemistry and Materials Science." under Subject Collection, then "Book Series," under Content Type and finally by selecting *Advances in Biochemical Bioengineering/Biotechnology*

You will find information about the

– Editorial Board
– Aims and Scope
– Instructions for Authors
– Sample Contribution

at springer.com using the search function by typing in *Advances in Biochemical Engineering/Biotechnology*.

Color figures are published in full color in the electronic version on SpringerLink.

Aims and Scope

Advances in Biochemical Engineering/Biotechnology reviews actual trends in modern biotechnology.

Its aim is to cover all aspects of this interdisciplinary technology where knowledge, methods and expertise are required for chemistry, biochemistry, microbiology, genetics, chemical engineering and computer science.

Special volumes are dedicated to selected topics which focus on new biotechnological products and new processes for their synthesis and purification. They give the state-of-the-art of a topic in a comprehensive way thus being a valuable source for the next 3-5 years. It also discusses new discoveries and applications.

In general, special volumes are edited by well known guest editors. The series editor and publisher will however always be pleased to receive suggestions and supplementary information. Manuscripts are accepted in English.

In references *Advances in Biochemical Engineering/Biotechnology* is abbreviated as *Adv. Biochem. Engin./Biotechnol.* and is cited as a journal.

Special volumes are edited by well known guest editors who invite reputed authors for the review articles in their volumes.

Impact Factor in 2009: 4.165; Section “Biotechnology and Applied Microbiology”: Rank 23 of 150

Attention all Users of the “Springer Handbook of Enzymes”

Information on this handbook can be found on the internet at springeronline.com

A complete list of all enzyme entries either as an alphabetical Name Index or as the EC-Number Index is available at the above mentioned URL. You can download and print them free of charge.

A complete list of all synonyms (more than 57,000 entries) used for the enzymes is available in print form (ISBN 978-3-642-14015-0) and electronic form (ISBN 978-3-642-14016-7).

Save 15%

We recommend a standing order for the series to ensure you automatically receive all volumes and all supplements and save 15% on the list price.

Preface

It was almost a half century ago (in 1954) when Richard P. Feynman has foretold first the possibility of a molecular machine which assembles various kinds of molecules automatically and aims to reproduce of itself (self-duplication). K. Eric Drexler has enlarged the Feyman's concept more in broad by learning the biological systems such as virus and living cells ("Engines of Creation – The Coming Era of Nanotechnology", Anchor Books, New York, 1986). Their ideas have been realized in the field of information science and technology like computers and telecommunication networks. Namely, miniaturization or downsizing of computer elements realized the integration of circuit and propelled the speed of the calculation as well as the memory of information enormously. This developed significantly the information industry.

Originally, a living cell of itself has a nature of self-duplication (growth or proliferation), self-regulation (metabolism), and evolution. These natures are caused by DNA, RNA, proteins, lipids, and oligosaccharides in a cell, represented by the central dogma of living systems. We can summarize the comparison of characteristics between living systems and artificial ones as shown in Table 1.

Nanotechnology is the creation and utilization of materials, devices, and systems through the control of matter on the nanometer-length scale. Nanobiotechnology, a part of nanotechnology and an integration of biology, chemistry, applied physics, material engineering, and biotechnology, holds considerable promise of advances in emerging area of scientific and technological opportunity and applies the tools and processes of nano/microfabrication to build devices for studying and operating biosystems. Researchers also learn from biology how to create better nano/microscale devices.

Recent developments of various kinds of nanomaterials such as fraren, carbon nanotube, nanomicelle, and biomaterials, as well as single molecule manipulation technologies and fabrication technologies such as NEMS, MEMS, and μ-TAS are remarkable. Due to these developments in nanomaterials and technologies, Feynman's and Drexler's dreams have been realized in some extent today. In this sense, we may call this innovative technology as nano/microbiotechnology. This concept is summarized in Fig. 1.

Table 1 The comparison of characteristics between living systems and artificial ones

Characteristics	Living systems	Artificial systems
Architecture of structure	Self-assembled molecular-based design written in chromosomal DNA	Planning and design written in blueprint
Organization of structure	Self-organized structure	Fabricated structure
Duplication	Self-duplication	Fabrication
Longevity	Infinite longevity under good environment (microorganisms), limited longevity controlled by genes and environment (higher organisms)	Limited longevity by the life cycle of elements
Homeostasis	Self-assembled molecular-based controlling systems for metabolism, gene expression and signal transduction	Mechanically and electronically designed controlling systems

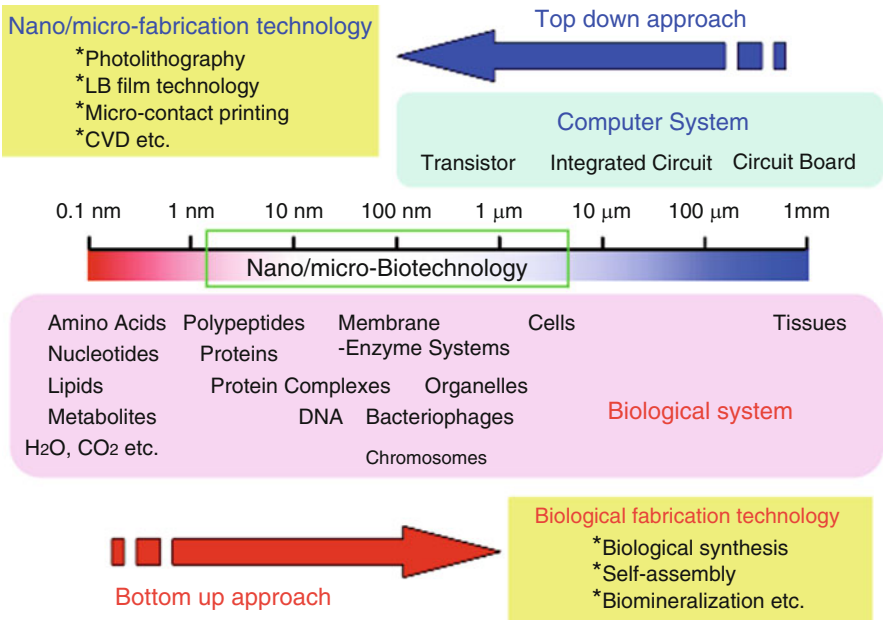

Fig. 1 Concept of nano/microbiotechnology

The aims of this book are: first, to scope over the present state of this innovative technology in the world; second, to explain in detail various technologies and materials those are relevant to this technology; and third, to survey this field in the near future so that this book will stimulate researchers of the next generation in the world.

The contents of this book are as follows.

First, we will start with an introduction to nano/microscale biological systems in nature such as self-assembly system of bacteriophage and molecular bio-motors in

living cells. In this chapter, the structures and functions of motor proteins such as myosin, kinesin, and F1-ATPase at the single molecular level will be elucidated. Biotechnology of bacteriophage is explained in the next section.

Second, the nanomaterials and technologies to detect and to characterize the materials will be explained. In this chapter, AFM-based technology to elucidate the mechanical basis of the cellular structure and its interaction with the extracellular matrix including cell-to-cell interaction will be reviewed. The recent advances in the development of fluorescence resonance energy transfer (FRET)-based molecular sensors for Zn^{2+}, second messenger dynamics, and enzyme activation/activity in living cells, tissue, and organisms will also be reviewed.

Third, fabrication and process technologies in this discipline including several technologies for the surface acoustic wave atomizer, electrospray deposition of biomolecules, and handling of droplets using pneumatic, electrokinetic, ultrasonic, and centrifugal forces will be introduced. An overview will also be given about integrated microfluidic devices incorporating functional components such as heaters for reaction temperature control, micropumps for liquid transportation, air vent structures for pneumatic manipulation of small volume droplets, optical fibers with aspherical lense structures for fluorescence detection, and electrochemical sensors.

Finally, we will summarize the application of this new technology to medicals, sensors, and biochemical reaction systems. These are non-viral gene delivery systems based on a complex of nucleotides and cationic high-molecular weight compounds or cationic liposomes, label-free monitoring systems for biorecognition events using nanomaterials, such as metal nanoparticles and carbon nanotubes, and microchip-based bioreactor systems utilizing living mammalian cells and pressure driven flow.

We would like to mention lastly that the contributors of each chapter are the front-runners of their special field in the nano/microbiotechnology in the world. We also express our sincere thanks to the readers of this book if you would kindly give us your advices and comments on this book.

Summer 2010

Isao Endo
Teruyuki Nagamune

Contents

Part I
The Nano-Scale Biological Systems in Nature

Adv Biochem Engin/Biotechnol (2010) 119: 3–15
DOI: 10.1007/10_2010_69
© Springer-Verlag Berlin Heidelberg 2010
Published online: 16 March 2010

Molecular Bio-Motors in Living Cells

Takayuki Nishizaka

Abstract The final goal of our group is to establish the missing link between chemical reaction and mechanical event in molecular motors. To achieve this, we have developed advanced versions of conventional optical microscopes and applied them into single-molecule techniques. In this chapter we present two studies: one is about the kinesin-microtubule system and the other F_1-ATPase. These techniques are applicable to other molecular machines, hopefully in more sophisticated ways, and we hope to investigate this in future studies.

Keywords 3-D tracking, F_1-ATPase, Kinesin, Motor proteins, TIRFM

Contents

T. Nishizaka (✉)
Department of Physics, Gakushuin University, Mejiro, Toshima-ku, Tokyo, 171-8588, Japan
e-mail: takayuki.nishizaka@gakushuin.ac.jp

1 Introduction

In cells in living organisms, secretory vesicles and membrane-enclosed organelles need to be carried to their appropriate locations to maintain cell function. Fascinating proteins called "motor proteins" are responsible for this transportation task; they bind to their substrate filaments and generate forces to cause mutual displacements between tail portions in motors and filaments. Notably, most motor proteins employ the chemical energy derived from hydrolysis of adenosine triphosphate, ATP, the common energy currency in living cells.

To date, much evidence shows that the directed force in a motor protein is accomplished by conformational changes in the protein. One good example is myosin in skeletal muscle; the domain called the catalytic core, a portion highlighted in green in Fig. 1a, hydrolyzes ATP and the subsequent release of hydrolysis product induces the tilting of the lever arm, a portion highlighted in red. This tilting is really tiny at just ∼5 nm, but a large displacement is realized by connecting elements in series.

Note that there are still dozens of questions to be solved as to how motor proteins work. The motor proteins can be defined as a "molecular machine" that converts chemical energy into mechanical work. However, this machine is too difficult to figure out properties because with the size is of the order of 10 nm. From the early 1990s, researchers have studied various motor proteins at the single molecular level, but the complete sequence between chemical reactions and mechanical event is not clarified. The final goal in this field is to establish the molecular basis of their mechanism.

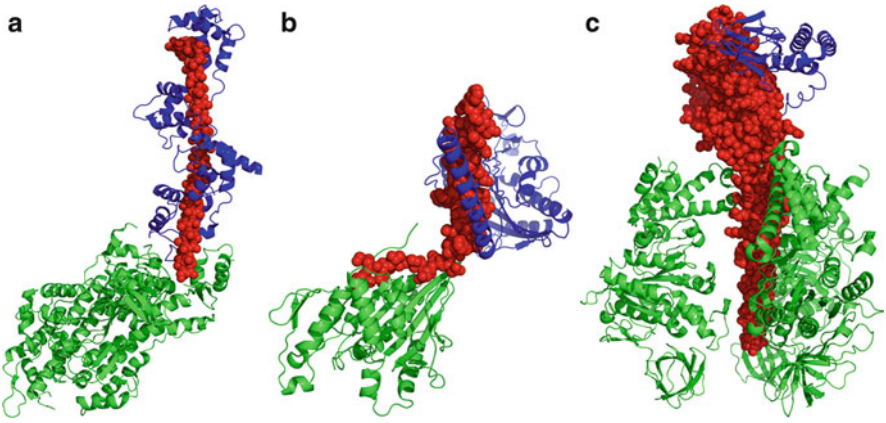

Fig. 1 Atomic structures of motor proteins. (**a**) Skeletal myosin. Myosin comprises of a dimer in a cell, but only monomer is represented for simplicity. A catalytic core, lever arm and accessory proteins are shown in *green*, *red*, and *blue*, respectively. (**b**) Double-headed conventional kinesin-1. Catalytic core is shown in *green*, while a neck linker and adjacent coiled-coil structure to make a dimer are shown in *red*. Another monomer is shown in *blue*. (**c**) F_1-ATPase. β-Subunit, γ-subunit, and accessory proteins are shown in *green*, *red*, and *blue*, respectively. For emphasis of the structure of the β-subunit, three α-subunits which alternately locate between three β-subunits are not shown

In this chapter, I will outline the recent contribution of our research group. Our aim is to visualize the chemical reaction, mechanical event, and additionally, conformational change within a single motor proteins. In order to do this, we have developed novel optical microscopes such as an advanced total internal reflection fluorescent microscope (TIRFM) and three-dimensional prismatic optical tracking (tPOT), and have studied various molecular motors such as myosin [1–3], kinesin [4] and F_1-ATPase [5–7] for the past 15 years. Here we focus on the structures and functions of motor proteins, especially at the single molecular level.

2 3-D Tracking Reveals Molecular-Motor Corkscrewing

2.1 Background

When starting research on motor proteins, "*in vitro* motility assay" is the most useful and well established method. You can use this in two ways: either the substrate filament can be attached to a glass surface and a plastic bead coated with motors runs on the track or motors can be adsorbed onto the surface and the filament runs on dense motors (Fig. 2a). Both movements can be directly visualized under optical microscopes by using illumination techniques to detect beads or fluorescent probes used for labeling filaments.

With modification of this assay, it was proven that a "torque component" exists in the interaction between actin and myosin [1]. We took advantage of the asymmetric property of actin polymerization to design artificial copolymers, in which only the front part is fixed onto the glass while the rear part continuously slides on the myosin track. Notably, the middle part transforms into a super-coil, indicating that myosin interacts with the filament in a cork-screw manner Fig. 2 b–c. This was the first report showing the torque in the actin–myosin system. But here is a problem: although the handedness of the torque can be judged through the shape of the helix, it was impossible to evaluate the pitch value, which is the sliding distance per one revolution. To quantify the pitch, we needed to design a totally new experimental setup for detecting molecular-scale rotation.

2.2 Tracking Technique

Our group used a tracking technique in order to reveal corkscrewing directly, and therefore I briefly outline the concept of this technique. The first row in Fig. 3 is the image of a single fluorescent bead only 100 nm in diameter, which is captured using high-sensitive CCD camera. So the actual size of this bead is nearly equal to the size of one pixel. The intensity profile of the bead image looks almost symmetric when you see intensities from all directions as shown in Fig. 3b. However, if you look more closely at the intensity, pixel by pixel, you notice that values are a bit asymmetric at the boundary of pixels. By fitting intensities with an appropriate

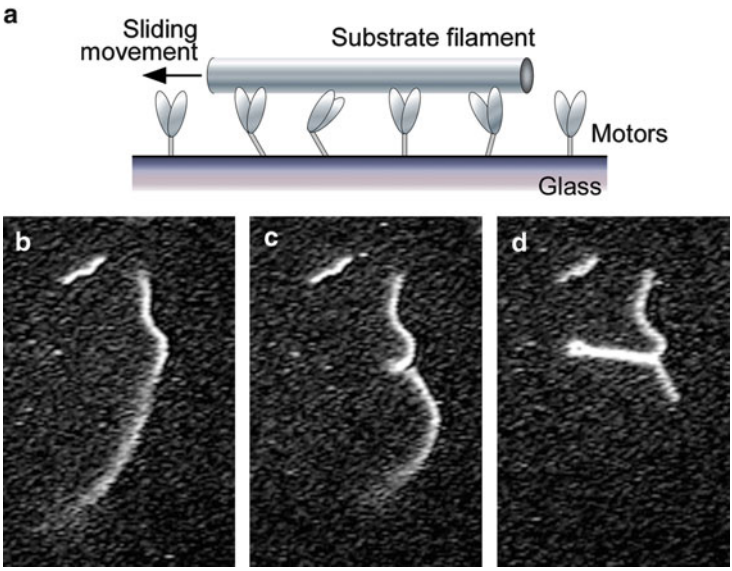

Fig. 2 (**a**) Schematic of *in vitro* gliding motility assay. Motors are adsorbed to and randomly oriented on the glass surface. In the presence of ATP, the substrate filament runs on the lawns of motors to the direction determined by both the polarity of the filament and characterirsity of motors. (**b**–**d**) Sequential micrographs to show torque component of actin-myosin interaction. An fluorescently-labeled actin filament appears as a white rope in figures, and its front part is fixed to the surface while the rear part continuously slides on the motor track, which is invisible because motors are ~10 nm in size and unlabeled. The middle part transforms into super helix (c), and subsequently into super coil (d)

function such as Gaussian, you can determine the precise position of the bead as a peak of the fitting curve. In the example in Fig. 3c, the bead displaces only 17 nm towards the left from the pixel boundary, which makes the left two pixels slightly brighter than the right two pixels. The sequence micrographs in Fig. 3a were obtained by displacing the sample stage, on which the fluorescent bead is fixed. The distance of displacement was only 20 nm in every frame, which is the size of relatively large protein. Notably, the stepwise movements are clearly recognized in each sequence, which means if a good objective lens is utilized, "an excellent vision" to distinguish protein-scale localization can be obtained without any analysis software. In our research group we extended this technique and go much further to get information of z-direction in addition to x and y.

2.3 3-D Tracking Method: tPOT

Our group developed a new method to track particles in three dimensions, using only one optical device, a wedge prism. Figure 4 represents an optical path from a

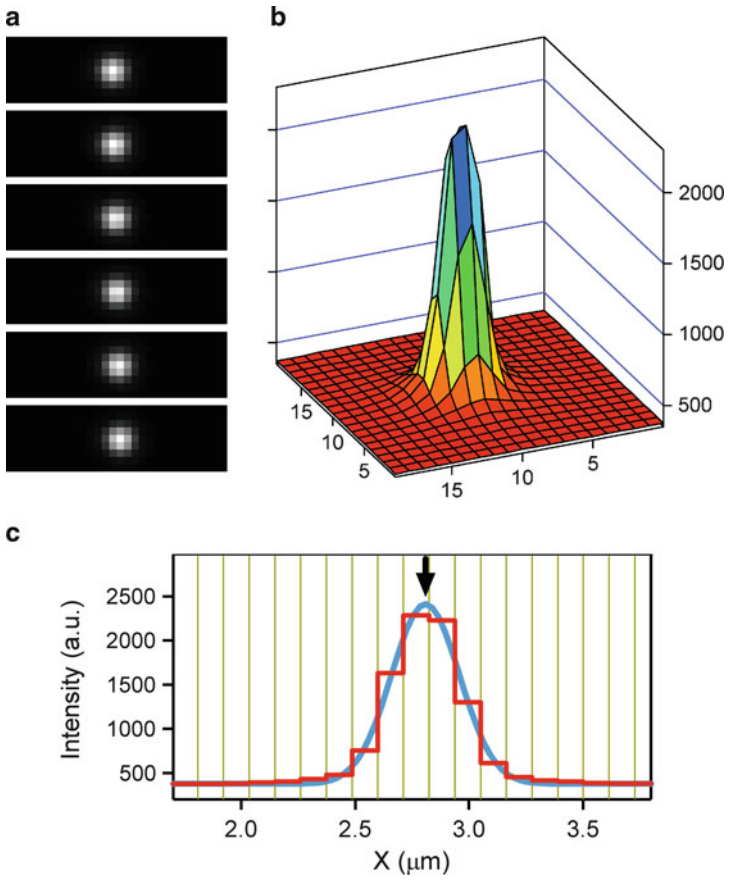

Fig. 3 (**a**) Sequential micrographs of the fluorescent microbead 100 nm in diameter, which was adsorbed onto the glass surface. The size of the pixel was also 100 nm. The sample stage was displaced 20 nm every frame, and therefore, after five frames, the center of the image appears the peak value as the real center of the bead. An objective with high numerical-aperture (Nikon, Plan Apo TIRF ×100, NA 1.49) and EM-CCD camera (Andor, iXon DU-897) were used to capture these images. (**b**) Intensity profile of the bead image. Distribution of intensity looks almost symmetrical. (**c**) one-dimensional fluorescent intensity profile of microbead. *Cyan curve* and an *arrow* represent the Gaussian fitting and the position of the peak that represent the real center of the bead, respectively

single fluorescent particle; the beam flux is divided into two components by the prism. When the particle moves upward, like from left, middle to right, the two components of light move in opposite directions on the camera plate, simply because each light comes from a different direction. Therefore, z-directed movement is converted into x-directed movement by this prism. Consequently, its x and y displacement of the particle can be determined as the average position between two images. With this idea, we established the very easy to use method to track x, y,

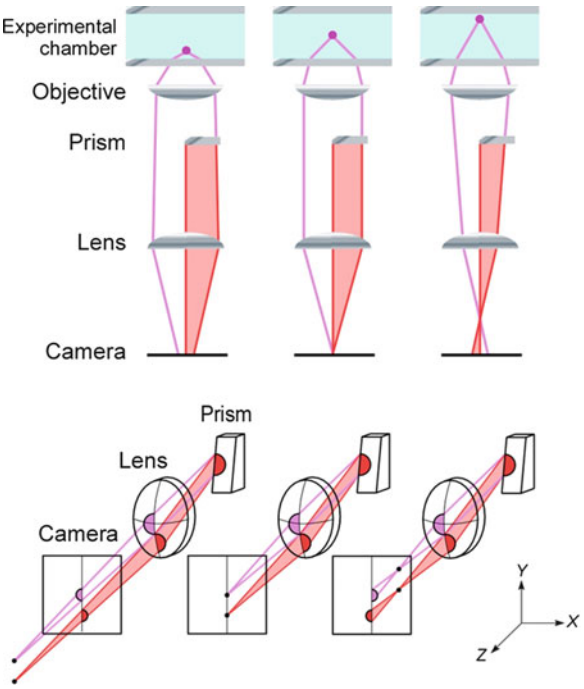

Fig. 4 Schema representing the rationale of the advanced method for 3-D tracking. For details, see the text and [4]

and z simultaneously, with the nanometer-scale precision. We named this method tPOT, the abbreviation of three-dimensional prismatic optical tracking.

2.4 tPOT Reveals Microtubule Corkscrewing

Dr. Junichiro Yajima designed an *in vitro* microtubule sliding assay, which enables us to track 3-D motions of motor proteins [4]. We focus on a motor of the kinesin group (cf. Fig. 1b). While double-headed conventional kinesin follows the microtubule structure as discussed later in detail, single-headed kinesin was reported to have a genuine property to produce torque [8], although quantitative analysis was not sufficient because of large markers which may hinder inherent rotation.

In our new experimental setup, the motor known as kinesin-5, abbreviated as Eg5, was truncated into single-headed and genetically fused with a protein called gelsolin. The recombinant motor protein was anchored to the glass surface through anti-gelsolin-antibody that makes a protein-scale spacing between a motor protein and a surface. In the presence of ATP, a microtubule slid on the kinesin-coated surface (cf. Fig. 2a). The motion of the sliding microtubule was precisely

determined through quantum dots specifically attached to the surface of the microtubule using avidin–biotin interaction. With this setup, we can directly judge whether torque components exists or not in the motion driven by single-headed kinesins.

Strikingly, the quantum dot showed corkscrewing motion (Fig. 5). Because we tracked the particle motion not only in the xy-plane but also along the z-axis, the handedness and pitch were revealed. The 3-D plot directly determined the handedness, and pitch was estimated from the sinusoidal fit to the x–z plot. The handedness was always left-handed, and the pitch was 300 nm on average. A similar value was also confirmed in the case of single-headed kinesin-1.

Please note that the size of the grids in the z-axis in Fig. 5 is only 20 nm, so what you are watching here is the corkscrewing motion with just 20 nm radius. Perhaps this is the world's smallest corkscrewing motion ever directly measured.

Interestingly enough, 300 nm pitch is different from the supertwist structure, so-called protofilament, in microtubules. The pitch of protofilament parallel to the axis, which depends on the number of oligomers to construct the hollow ring, is about 3–6 μm. Double-headed kinesin-1 is known to follow the microtubule protofilament [9], and 300 nm pitch of single-headed kinesins is ten or 20 times shorter than that of double-headed kinesin-1. In conclusion, the origin of rotation driven by single-headed kinesins is not explicable from the helical structure of substrate filament itself.

For modeling how this corkscrewing motion is produced, Yajima and Cross proposed several possibilities [8]. The following is one of them: after "the on-axis stroke of kinesin" slides the microtubule parallel to its longitudinal axis, any slight conformational change that may trigger the distortion of stalk region somehow induces the off-axis stroke as a result of the conformational change; this lateral push acts as a perpendicular vector of the force and causes the rotational motion of the microtubule. Further studies will be needed to test this simple model by applying tPOT to various motor proteins under different conditions that alter chemical states in the catalytic core.

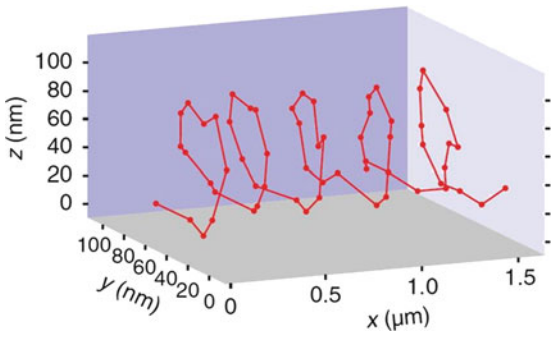

Fig. 5 Three-dimensional tracking of a quantum dot, which was labeled to the surface of a microtubule and made to slide by surface-immobilized single-headed kinesin-5. For details, see the text and [4]

3 Direct Visualization of Chemical Reaction

3.1 Concept of Watching Chemical Event

A single turnover of ATP can be detected by using fluorescent ATP, such as Cy3-ATP, under total internal reflection fluorescent microscope, abbreviated as TIRFM. This straightforward method was originally developed by Yanagida's group [10]: when Cy3-ATP binds to an immobilized protein, Cy3 appears as a stable fluorescent spot. In contrast, unbound Cy3-ATPs are virtually invisible because of their rapid Brownian motion. Figure 6 shows binding and unbinding of 2′-EDA-Cy3-ATP to single F_1-ATPase molecule immobilized onto the glass surface.

This method can address many questions, all of which are essential to understand the molecular mechanism of motor proteins – how tight is the coupling between ATP binding and mechanical step, what is the number of ATPs that can simultaneously bind to three catalytic sites, which chemical state governs which mechanical step, and so on.

3.2 The World's Smallest Rotary Motor

F_1-ATPase is the world's smallest rotary motor ever found. This enzyme is a part of ATP synthase, and mainly exists in mitochondria membrane in eucaryotic cells. As shown in the atomic structure in Fig. 1c, the γ-shaft (red portion) is surrounded by three catalytic cores called β-subunits, and the rotation of the shaft was directly visualized by Professor Yoshida and Kinosita's group in 1997 [11]. Please note that the diameter of the shaft is only 20 Å, so huge markers have to be used to visualize rotation directly.

The fluorescently labeled ATP method have been applied to F_1-ATPase, and mechanical rotation of the shaft was simultaneously detected through a plastic bead by using different wavelength of light to illuminate the bead [5].

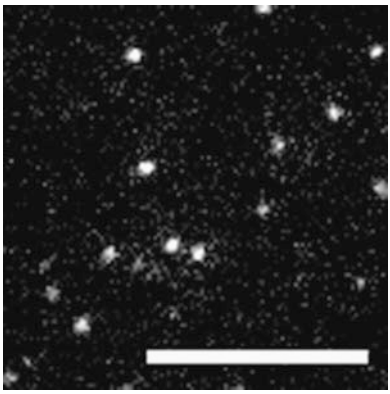

Fig. 6 Fluorescent image of Cy3-ATP binding to the surface-immobilized F_1-ATPase. It was visualized under TIRFM. Each *bright spot* corresponds to single Cy3-ATP. *Scale bar* is 5 μm

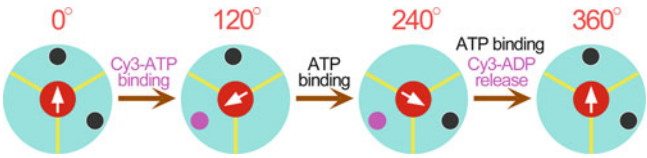

Fig. 7 Rotation mechanism of F_1-ATPase. This model, involving the so-called tri-site mode, was directly proven by visualization of chemo-mechanical coupling [5]

3.3 Rotation Mode from the Chemical Reaction Viewpoint

Figure 7 shows the model of how nucleotide states proceed in three catalytic sites, established from the direct visualization of the chemo-mechanical coupling in F_1-ATPase. When Cy3-ATP (purple circle in the direction of the white arrow at 120° in Fig. 7) binds to an empty site, it drives a step, and subsequently, another ATP (black circle in the direction of the white arrow at 240°) binds to a remaining site. This binding triggers ADP (black circle at 120°) release from the top catalytic site (black circle at 120°), but not from the left site. Finally, the third ATP (black circle in the direction of white arrow at 360°) binds, which triggers the release of Cy3-ADP (purple circle at 240°) from the left site. Therefore, one nucleotide can stay while the γ-shaft is directed to two different angles: that is, the angle 120° and the angle 240°. If it can be assumed that Cy3-ATP faithfully mimics authentic ATP, the implication is that, in three catalytic sites on F_1-ATPase, two sites are always filled with nucleotide during revolution. This mechanism is called the tri-site mode, and was directly proven in 2004.

Additionally, other essential questions were answered as follows. First, binding of ATP and release of ADP are tightly coupled to the step at the observed time resolution. Second, at least two nucleotides are always binding during rotation, and the binding of third nucleotide, new ATP, initiates the step. Third, by using the F_1-ATPase mutant, in which substeps are observed only under Cy3-ATP, it was concluded that binding of ATP governs 80° angle-substep, and hydrolysis reaction that occurs at the catalytic sites, to which ATP bounds one step earlier, governs 40° angle-substep.

All these issues are really important for complete understanding of the rotation mechanism, and can be answered only by the single-molecule technique.

4 Domain Motions in the Subunit in a Single Rotary Motor

4.1 Background

The atomic structure of F_1-ATPase shows that the γ-shaft is surrounded by the cylinder comprised of three α-subunits and three β-subunits, which are alternately arranged. This $\alpha_3\beta_3$ complex makes the hollow structure, and the sleeve made of

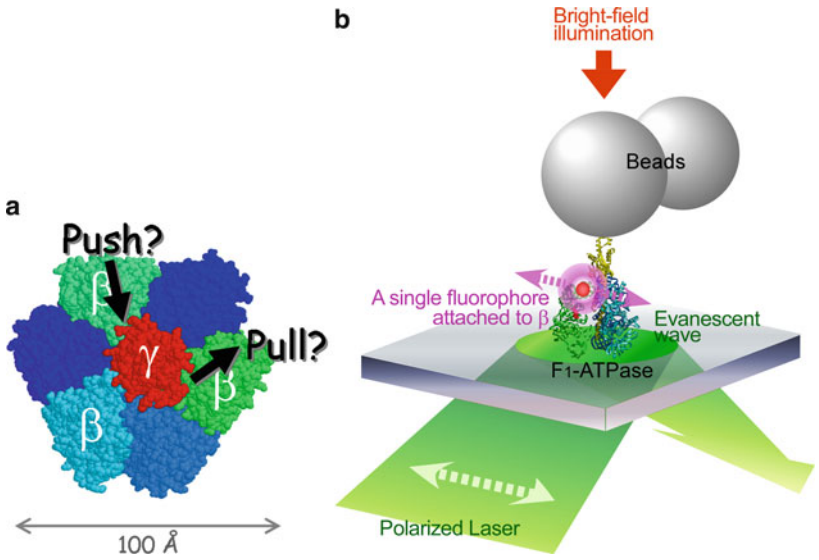

Fig. 8 (**a**) Possible idea explaining how multiple β-subunits induce one-directed rotation of the γ-subunit. (**b**) Schema of the experimental setup for simultaneous detection of γ-subunit rotation and angular conformational change of the β-subunit in a single F_1-ATPase molecule. The idea proposed in (**a**) could be directly tested with this setup

these is hydrophobic as proposed by Walker and colleagues [12]. So the idea is that the inside of the sleeve without electrostatic interaction is very slippery. As a result, internal friction between the shaft and cylinder may be minimized with this kind of architecture.

With this concept, what is the molecular mechanism of rotation in F_1-ATPase? One may think that the shaft is closely packed within the cylinder in an asymmetric manner, and some push and pull motions of three catalytic cores (cf. Fig. 8a) may produce directed rotation. If this is the case, these conformational changes could be detected as an angular change of these domains.

4.2 Technique

In order to examine the above-mentioned idea, Dr. Tomoko Masaike in our group carefully chose the helix in the C-terminal domain of the catalytic subunit, which was assumed to be very mobile in line with the chemical state in the γ-subunit, and labeled the specific region with a single fluorophore (red in Fig. 8b) by using the technique reported in Nature Structure Molecular Biology [7]. Note that we used a fluorescent probe that has two functional groups. By reacting these two functional groups with two cysteines in the helix, the absorption transition moment of the fluorophore is perfectly aligned to the orientation of the single helix.

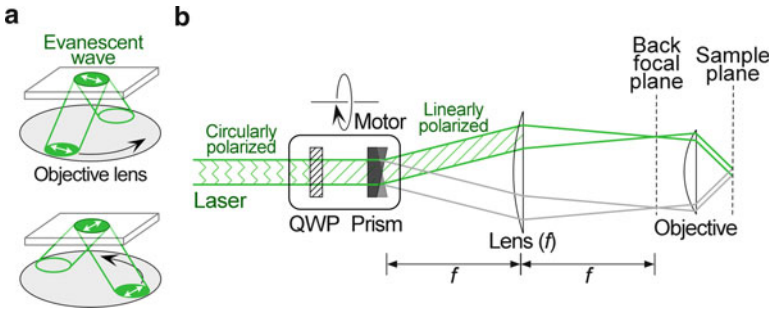

Fig. 9 (**a**) Schema of optical path and polarization of the laser for TIRFM. The polarization of the evanescent field is modulated with time only in the xy-plane. (**b**) The rationale of the polarization modulation to accomplish TIRFM. Quarter-wave plate (QWP) rotates with the prism in sync by using a hollow motor

To determine the orientation of the single fluorophore directly, we exploited an advanced type of TIRFlM, in which the polarization of evanescent fields is modulated with time (Fig. 9a, b). Suppose the single fluorophore is fixed in one orientation; its intensity is expected to show maximal and minimal when the excitation polarization becomes parallel and orthogonal, respectively, to absorption transition moment of the fluorophore. Therefore the intensity should oscillate as a sinusoidal wave. In the case that the angle of the fluorophore is changed, the phase of the signal should also be changed, indicating the fluorophore orientation. From this phase shifting, the angular change of the specific helix in the single protein molecule could be determined directly [5].

The rotation of the γ-shaft was also observed simultaneously, with the different wavelength of the light to illuminate the beads as the light source of a dark-field microscope (Fig. 9).

4.3 Rotation Mechanism of F_1-ATPase

Our research group succeeded in disclosing "the complete sequence of domain motions" as it undergoes transitions between all chemical states [7]. We used the hybrid F_1-ATPase, in which only one β-subunit is mutant and has an extremely slow rate for hydrolysis [13]. By using the intermediate angle as a signature, it can be defined as "what chemical state the fluorophore-labeled β-subunit is" in each γ-shaft angle. The implication is that large domain motion occurs only when chemical reactions (biding of ATP, cleavage of ATP, and release of ADP) proceed in the fluorophore-labeled β-subunit. Angle changes of the domain motion in β-subunit are +40° in a counter-clockwise manner looked at from the protruded side of the γ-shaft, −20°, and return to the original angle with −20°.

Therefore, it is concluded that a β-subunit in F_1-ATPase undergoes a three-step large motion of the C-terminal domain in relation to the N-terminal domain over

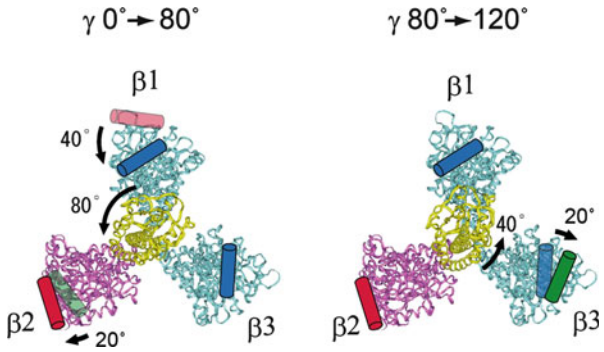

Fig. 10 Our recent model of how F_1-ATPase rotates. In this mechanism, all β-subunits show conformational changes in C-terminal domains within a unitary step (120°) and correlate with two substeps, 80° and 40°. Substeps have been proposed in various mutants and now established as the common mechanism for rotation [5, 13, 14]

one revolution of γ-shaft. This is the first report to show the correlation between the chemical state and structural change of a protein, revealed directly at the single molecular level.

Please note that what we are observing is the structure of only one fluorophore-labeled β-subunit. However, we know another two structures, because the labeled β-subunit changes into their structures after 120° and 240° rotations of the γ-shaft. In other words, by combining three β-subunit conformations that have 120° rotational phase differences in each other, whole structures of the cylinder could be re-constructed.

Figure 10 shows our latest model of "how three catalytic subunits rotate the shaft." First, ATP is bound to this β1-subunit, and 40° motion occurs at the C-terminal domain in β1-subunit. A −20° angle change also occurs in the β2-subunit, which correlates with the release of ADP. Both movements drive the rotation of the γ-shaft only 80° in a counter-clockwise manner. Subsequently, in the remaining β3-subunit, 20° clockwise angle change occurs, and drives the γ-shaft 40° more. With these motions, the γ-shaft rotates by one third. Note that during this unitary step, all three β-subunits are correlated with rotational motion of the γ-shaft. These sets of motions subsequently occur after 120° phase shifting of the γ-shaft, and so the γ-shaft continuously rotates in one direction.

References

1. Nishizaka T, Yagi T, Tanaka Y, Ishiwata S (1993) Nature 361:269
2. Nishizaka T, Miyata H, Yoshikawa H, Ishiwata S, Kinosita K Jr (1995) Biophys J 68:75s
3. Nishizaka T, Seo R, Tadakuma H, Kinosita K Jr, Ishiwata S (2000) Biophys J 79:962
4. Yajima J, Mizutani K, Nishizaka T (2008) Nat Struct Mol Biol 15:1119

5. Nishizaka T, Oiwa K, Noji H, Kimura S, Muneyuki E, Yoshida M, Kinosita K Jr (2004) Nat Struct Mol Biol 11:142
6. Adachi K, Oiwa K, Nishizaka T, Furuike S, Noji H, Itoh H, Yoshida M, Kinosita K Jr (2007) Cell 130:309
7. Masaike T, Koyama-Horibe F, Oiwa K, Yoshida M, Nishizaka T (2008) Nat Struct Mol Biol 15:1326
8. Yajima J, Cross RA (2005) Nat Chem Biol 1:338
9. Ray S, Mayhofer E, Milligan RA, Howard J (1993) J Cell Biol 121:1083
10. Funatsu T, Harada Y, Tokunaga M, Saito K, Yanagida T (1995) Nature 374:555
11. Noji H, Yasuda R, Yoshida M, Kinosita K Jr (1997) Nature 386:299
12. Abrahams JP, Leslie AG, Lutter R, Walker JE (1994) Nature 370:621
13. Shimabukuro K, Yasuda R, Muneyuki E, Hara KY, Kinosita K Jr, Yoshida M (2003) Proc Natl Acad Sci USA 100:14731
14. Yasuda R, Noji H, Yoshida M, Kinosita K Jr, Itoh H (2001) Nature 410:898

Adv Biochem Engin/Biotechnol (2010) 119: 17–43
DOI: 10.1007/10_2008_46
© Springer-Verlag Berlin Heidelberg 2009
Published online: 28 August 2009

Molecular Biology and Biotechnology of Bacteriophage

Kazukiyo Onodera

Abstract The development of the molecular biology of bacteriophage such as T4, lambda and filamentous phages was described and the process that the fundamental knowledge obtained in this field has subsequently led us to the technology of phage display was introduced.

Keywords Phage T4, Phage lambda, Filamentous phage, Phage display, Application of Phage Display.

Contents

K. Onodera
Kogakuin University, Nishishinjuku 1-24-2, Shinjuku-ku, Tokyo, Japan
e-mail: chem-kazu@giga.ocn.ne.jp

1 A Brief History

At the begining I want to clarify why I have chosen the bacteriophages as the representative of various viruses for the people who is not familiar with virus research. By the late 1930s it had been shown that specific filterable viruses were the causative agents of some diseases in plants, some cancerous growth in animals, and of the lysis of some bacterial species. One of these viruses, causing the tobacco plant mosaic (TMV) disease, had been isolated in crystalline form by W.M. Stanley in 1935 [1]. That a self-replicating object like a virus can be crystallized as if it were inorganic material gave momentum to the notion of viruses as "living molecules." Moreover it was shown that TMV was dissociated in acetic acid into protein and RNA and it was reconstructed in vitro as an infectious virus particle by adjusting to pH 7.0. The concept of "self assembly" emerged from this experiment but it was found later that the morphogenesis of viruses was different from self-assembly.

All cells contain double-stranded DNA as their genetic material. By contrast, viruses are known that have single-stranded RNA, double-stranded RNA, single-stranded DNA, or double-stranded DNA as their genetic material. This makes for interesting schemes of replication and gene expression. Many viruses are known that infect Bacteria and increasing numbers are known that infect Archaea.

I want to focus on three bacteriophages – T4 phage (virulent virus), lambda phage (template virus) and filamentous phage (not harmful to host). The study of genetic materials of virus has led to tremendous progress so that we can transfer the foreign genetic information to the cells that we want to manipulate and open the field of genetic engineering for the results to be used in bioindustry.

Therefore I will not talk about the genome of bacteriophages but rather discuss the structural features of these bacteriophages in this article.

It was thought that Felix d'Herelle recognized the particulate nature of phages [2]. However the real breakthrough was made by Max Delbrück who came to biology from physics. He organized the Phage group with Salvador Luria and Alfred D. Hershey in the late 1930s. Their meeting in 1940 marked the origin of the Phage Group. [3]

The members of this group were united by a common goal, namely the desire to understand how, during the brief half-hour latent period, the simple bacteriophage particle achieves its 100-fold self reproduction within the bacterial host cells.

To see the structure of virus particles, we need an electron microscope. From the beginning, Thomas F. Anderson, one of the first American electron microscopists, was a member of this group. Therefore the structure of the bacteriophage was explored extensively [4].

He brought a few stereoscopic pictures of adsorbed T2 phage to the Virus: 1950 meeting at Caltech to show it to Delbrück. Delbruck finally agreed that the phages are adsorbed by the tips of their tails and that none of the particles seem to enter the bacteria or their ghosts Other critical evidence was shown by the so-called Hershey, Chase experiment [5]. He described the experiment as follows.

Anderson had found that stirring the cell suspension in a blender prevented attachment of phage particles to bacteria, and perhaps Case and I (Hershey) should

have thought of using that machine first. Instead, we tried various grinding arrangements, with results that were not very encouraging. But when Margaret McDonald loaned us her blender, the experiments quickly succeeded.

A chilled suspension of bacterial cells recently infected with phage T2 is spun for a few minutes in a blender and afterwards centrifuged briefly at a speed sufficient to throw the bacterial cells to the bottom of the tube. One thus obtains two fractions: a pellet containing the infected bacteria and a supernatant fluid containing any particles smaller than bacteria.

Each of these fractions is analyzed for the radiophosphorus in DNA or radiosulfur in protein with which the original phage particles have been labeled. The results are:

1. Most of the phage DNA remains with the bacterial cells
2. Most of the phage protein is found in the supernatant fluid
3. Most of the initially infected bacteria remain competent to produce phage
4. If the mechanical stirring is omitted, both protein and DNA a sediment with the bacteria
5. The phage protein removed from the cells by stirring consists of more-or-less intact, empty phage coats, which may therefore be thought of as passive vehicles for the transport of DNA from cell to cell which, having performed that task, play no further role in phage growth

At present it is fair to say that bacteriophage injected their DNA into the host cell and bacteria produced virus particles through the subtle interaction between bacteria and phage genome.

However, the mechanism of entry of animal virus into the host cell is quite different from that of bacteriophage. The entry of influenza virus is described as follows.

The influenza virus nucleocapsid is of helical symmetry, about 6–9 nm in diameter and about 60 nm long. This nucleocapsid is embedded in an envelope that has a number of virus-specific proteins as well as lipid derived from the host. Because of the way influenza virus buds as it leaves the cell, the virus has no defined shape and is said to be polymorphic. There are proteins on the outside of the envelope that interact with the host cell surface. One of these is called hemagglutinin, so named because it causes agglutination of red blood cells. The red blood cell is not the type of host cell the virus normally infects, but contains on its surface the same type of membrane component, sialic acid, that the mucous membrane cells of the respiratory tract contain. Thus, the red blood cell is merely a convenient cell type for assaying agglutination activity. An important feature of the influenza virus hemagglutinin is that antibodies directed against this hemagglutinin prevent the virus from infecting a cell. A second type of protein on the influenza virus surface is an enzyme called neuraminidase. This enzyme breaks down the sialic acid component of the cytoplasmic membrane, which is a derivative of neuraminic acid. Neuraminidase appears to function primarily in the virus assembly process, destroying host membrane sialic acid that would otherwise block assembly or become incorporated into the mature virus particle.

It is helpful to choose simple paradigms to represent more complex systems.

The relative simplicity of the bacteriophage and of its bacterial host played an important role in the development of molecular biology. Therefore I want to choose three bacteriophages – T4 phage, lambda (λ) phage and filamentous phage.

I also want to discuss the molecular biology of these phages from the viewpoint of their structure and application of the results obtained from study of the structure to the biotechnology.

2 One Step Growth of Phage T4

2.1 Sequence of Events in T4-Infected Bacteria

In the 1950s chemical analysis of highly purified T-even phage by means of modern techniques fully substantiated that DNA and protein, in roughly equal proportions, constitute more than 90% of the dry weight of the particles. The total DNA complement of a single T-even phage was found to amount to 175 kb pairs, or about 6% that of the chromosome of the *E. coli* host cell.

Chemical analyses of the total T-even phage protein did not bring to light any facts; its amino acid composition resembles more or less that of the total *E. coli* protein. The phage protein is composed of at least five different types of polypeptides, of which the head protein makes up by far the major part. Each of the tail components – sheath, tube, base plate, tail pins, and tail fibers – contains one or more specific polypeptides. Chemical analysis of the phage DNA did show the difference.

The T-even phage DNA, unlike all other types of DNA, was found to have no cytosine. Instead of cytosine, it contains the cytosine analog 5-hydroxymethylcytosine (HMC). Thus T-even phage DNA obeys the [A]=[T] and [G]=[C] equivalence relation demonstrated by the Watson–Crick structure, provided that HMC, which can form the same three hydrogen bonds with G as can C, replaces C in the double helix (Fig. 1).

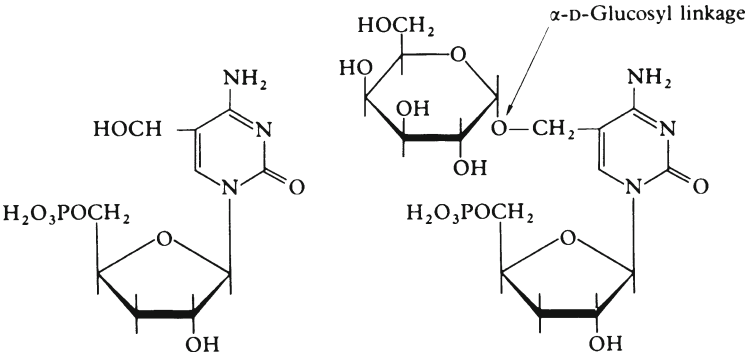

Fig. 1 The unusual deoxynucleotide containing 5-hydorxymethylcytosine (HMC) found in the DNA of T-even phages (*left*) and the manner in which glucose is attached to some of the HMC bases (*right*) (Stent GS, Calendar R (1978) Molecular genetics: an introductory narrative, 2nd edn. W.H. Freeman, San Francisco, p 300)

The low [G]+[HMC] content of 35% places the T-even phage DNA in a compositional range quite remote from that of the DNA of its *E. coli* host, which has a [G]+[C] content of 52%. The T-even phage DNA was found to contain glucose attached to some of the hydroxymethyl groups of HMC. The one-step growth experiment demonstrated that the progeny of the infecting phage particle appear after a period of constant phage titer. The one-step growth experiment is a basic procedure for studying phage multiplication.

A dense suspension of growing bacteria is infected with phages, incubated for a few minutes to allow most of the phage particles to attach themselves to the bacteria, and then diluted with nutrient medium to a concentration that may range from one ten-thousandth to one millionth that of the suspension. The diluted culture is incubated further and samples plated on sensitive bacteria from time to time for plaque assay of the instantaneous number of infective units in the culture. The protocol and the results of a typical one-step growth experiment are shown in Fig. 2. The number of plaque-forming units in the culture remains constant for the first 24 min after infection. This initial period is the latent period. After some 24 min have elapsed, the number of plaque-forming units in the culture

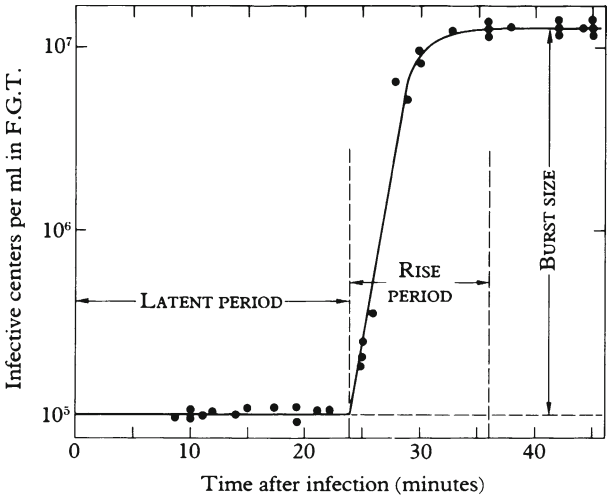

Fig. 2 The one-step growth experiment of phage T4 Procedure: *E. coli* growing exponentially are concentrated by centrifugation to a density of 109 cell/mL and infected with an average of one T4 phage/cell. The mixture is incubated in an aerated medium for 2 min, during which time at least 80% of the phage input becomes fixed to the bacterial cells. The infected bacteria are then diluted 10,000-fold into fresh growth medium. The tube containing this dilution (first-growth tube or FGT) and another tube containing a 20-fold further dilution of the first-growth tube (second-growth tube) are incubated, and samples from both tubes are plated periodically for plaque assay on sensitive indicator bacteria. During the latent period and early in the rise period, the titer of infective centers shown on the ordinate of the graph is estimated from plaque counts obtained by assay of the first-growth tube; thereafter, the titer is reckoned from plaque counts obtained by assay of the second-growth tube (Stent GS, Calendar R (1978) Molecular genetics: an introductory narrative, 2nd edn. W.H. Freeman, San Francisco, p 304)

begins to rise rapidly, until a final plaque is attained 10 min later. The period of time during which the number of plaque-forming units increases is the rise period, and the ratio of the final titer of the plateau to the initial titer of phage-infected bacteria is the burst size. The latent period represents the time that elapses between the moment at which the bacterial culture is infected with a phage stock and the moment at which the first infected cells in the culture lyse, thereby liberating into a medium a litter of progeny phage particles. The rise period represents the time span during which more and more of the infected bacteria lyse, and the final plateau of infectivity is attained when all the infected bacteria that are going to lyse have done so; no further phage multiplication occurs after this stage, since progeny and residual uninfected bacteria on the culture have been separated from each other by the high dilution of the culture just after the initial infection.

The burst size corresponds to the average number of progeny phage particles produced per infected bacterium, which in the experiments presented here amounts to about 100 phages per infected cell. After the conclusion of the latent period, when the intracellular phages have escaped from the host cell into medium, each progeny phage can form its own focus of infection on the agar surface (Fig. 3).

The phage enters accompanied by several minor peptides and protein. At least one protein, the product of phage 2 (gp2), probably enters attached to the lead part of the DNA. Examination of T4-infected bacteria at various times after infection by electron microscopy and by a combination of analytical methods reveals the pattern illustrated in the Fig. 2. Phage DNA increases after a brief delay; virion-specific

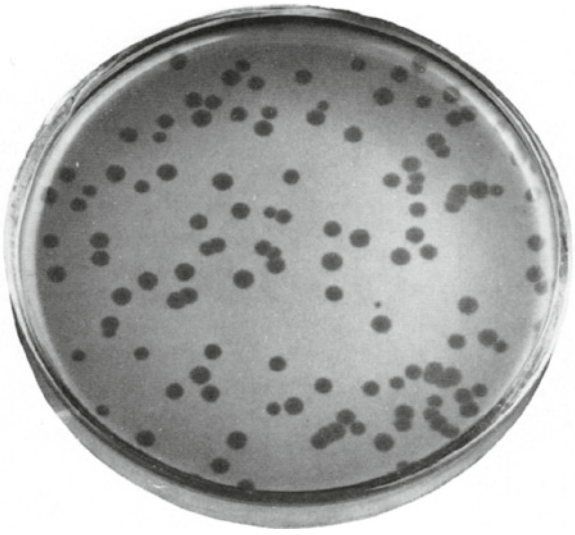

Fig. 3 A petri plate showing growth of a lawn of *E. coli* bacteria on which T2 phages have formed plaques (Stent GS, Calendar R (1978) Molecular genetics: an introductory narrative, 2nd edn. W.H. Freeman, San Francisco, p 297)

proteins begin to appear somewhat later and their appearance is soon followed by appearance of organized capsid precursors and then by the formation of mature infectious capsid. Some mRNA of viral specification is made promptly after glucosylated derivatives in phage DNA also provide infection and throughout the latent period. Bacterial mRNA and bacterial proteins stop being synthesized within a few minutes after the entry of phage DNA. Bacterial DNA is rapidly degraded to acid-soluble fragments and the "nuclear bodies" or DNA-containing areas of the bacterium become dispersed.

2.2 DNA synthesis

T-even phages have hydroxymethylcytosine (HMC) instead of cytosine in their DNA. In mature DNA, HMC has a pattern of glucosylation specific for each T-even phage: phage-coded glucosylating enzymes glucosylate HMC groups in DNA. HMC is a good chemical marker for T-even DNA. Its glucosylated derivatives in phage DNA also provide antigenic specificities recognizable by specific antibodies. By tracing DNA from the infecting phage it has been established that replication of T-even phage DNA takes place. The DNA molecules that enter from T-even virions into the bacterium are linear, circularly permuted, and have a terminal redundancy of 2–4% corresponding to 2–4 × 10^6 Da of DNA.

2.3 Phage-Coded Enzyme

The early transcription of newly entered phage DNA is done by the bacterial RNA polymerase. A number of phage proteins are made from such transcripts. Then the RNA becomes modified by the action of early phage products, its specificity changes, transcription of host genes stops even before the host DNA is broken up and other phage genes are transcribed.

Among the phage-coded proteins are enzymes belonging to several classes: (1) enzymes that produce unique phage DNA constituents such as HMC deoxynucleotides, or glucosylate these nucleotides, or destroy precursors of cytosine deoxynucleotides; (2) enzymes that play specific roles in DNA replication and recombination (Fig. 4); (3) enzymes that destroy host-cell DNA and make its nucleotides available for phage DNA synthesis; (4) enzymes that take part in the processing of virion proteins.

A critically important protein is gp32, the product of gene 32. This is a DNA unwinding protein that associates with single-stranded DNA stretches in stoichiometric amounts, one molecule per ten nucleotides. This protein can actually promote some unwinding of double-stranded DNA to allow initiation of replication to occur at sites where single-strand nicks are present. A peculiarity of gp32 is its ability to regulate its own rate of synthesis by a feedback mechanism: when more single-stranded regions are present in DNA, more gp32 is synthesized.

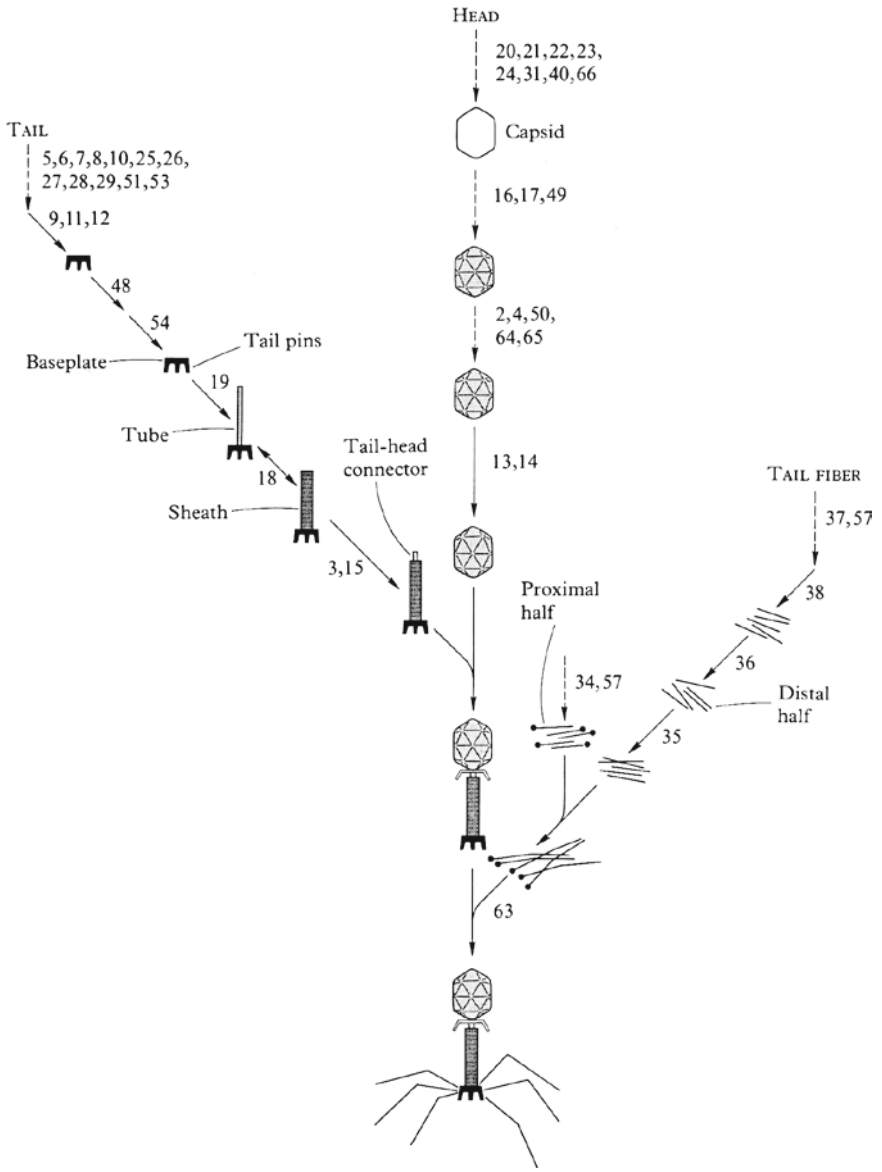

Fig. 4 The morphogenetic pathway of phage maturation has three principal branches leading independently to formation of heads, tails, and tail fibers, which then combine to form complete phage particles. The numbers refer to the T-even phage genes whose products are involved at each step. The *solid arrows* indicate the steps that have been shown to occur in extracts. Infection of *E. coli* with a phage carrying a mutation in any one of these genes leads to accumulation of the electron-microscopically visible structure shown immediately before the step in which that gene is involved, as well as of the last structure(s) of the other converging pathway branches (Stent GS, Calendar R (1978) Molecular genetics: an introductory narrative, 2nd edn. W.H. Freeman, San Francisco, p 319)

The six proteins needed for DNA synthesis may form a multienzyme complex. Thus T-even phage produce in their host bacterium a complex of enzymes and subsidiary proteins that make their replication independent of the DNA synthesizing systems of the bacterium.

2.4 Program of Phage Gene Expression

Based on the time of appearance of their messengers or gene products one can distinguish immediate early, delayed early, quasi-late, and late genes. The immediate early, whose mRNA is made even in the presence of an inhibitor of protein synthesis such as chloramphenicol, are transcribed from phage DNA by *E. coli* RNA polymerase either in vivo or in vitro. Another early class is that of delayed early genes, whose mRNA is initiated early but whose products are made only after a delay because they are coded by genes located distally from their promoters on the phage operons. The quasi-late genes are transcribed by RNA polymerase that has been altered by the action of certain products of immediate early phage genes. Particularly important are the loss or modifications of polypeptide σ and alterations in other subunits of polymerase, which thereby acquire new promoter-recognition specificities. Especially interesting is the alteration of the α-polypeptides of the enzymes, which acquire an adenosine diphosphoribose residue donated by nicotinamide adenosine dinucleotide. Host promoters are no longer recognized, and no more host specific RNA is transcribed. A second shift in RNA polymerase specificity occurs later (about 6–8 min in bacteria infected at 30 °C) and is due to the association of *E. coli* polymerase with three polypeptides including gp33 and gp55. At this point in the program two events occur: a more or less complete shut-off of the synthesis of the phage enzymes under control of phage gene 62 and the start of synthesis of all the late gene products, including the virion constituent proteins and phage lysozyme.

The switch from bacterial to phage program caused by changes in RNA polymerase has one important consequence. Since no more ribosomal RNA or proteins are made after T-even infection and since the phage does not code for new ribosomes, all phage protein synthesis must take place on bacterial ribosomes made before the first shift on program. This circumstance made possible one of the classical experiments that demonstrated the existence of mRNA as distinct from ribosomal RNA, confirming an earlier surmise also based on experiments with T-even phage. It is believed that this result is clear evidence to demonstrate the existence of messenger RNA. Not all the synthesizing apparatus for phage proteins is purely bacterial; several tRNAs different from the bacterial ones are coded by phage T4.

2.5 Assembly of Virions

In contrast to the early phases of phage development, the assembly of capsids and complete virions is not programmed in time by successive expression of phage genes.

All virion proteins and other late proteins such as phage lysozyme appear to be synthesized more or less simultaneously and accumulate in "precursor pools." From the pool they are then withdrawn by direct specific interactions with other protein molecules to construct subassemblies that are then assembled into complete virions.

Essentially, virion assembly consists of five major processes interacting with each other only at some critical points (Fig. 4):

1. The baseplate of the phage tail consists of 15 gene products and its synthesis involves also several other genes. The baseplate appears to contain some molecules of two phage-coded enzymes; dihydrofolate reductase and thymidylate synthetase.
2. The complete baseplate, specifically after the addition of gp54, provides a primer for the assembly of the tail tube. Around the tube the sheath assembles as a polymer 114 copies of gp18. The products of two other genes stabilize this assembly.
3. The shell of the phage head is the product of many genes and consists of more than ten proteins, one of them, gp23, representing the bulk of it. In complete heads gp23 is present in a partially cleaved form due to removal of a 10,000 molecular weight piece from the original polypeptide. Protein gp22 is an internal protein that digests itself to small peptides.
4. Once the tail and head of the phage are assembled separately they combine spontaneously in vitro as well as in vivo.
5. The tail fibers are made up of four gene products. Their assembly is independent of the rest of the virion, but they attach to the baseplate only after head and tail have been joined. The gp63 plays a role in this reaction, which also involves an interaction with whiskers attached to the collar between head and tail.

The specific shape of the phage head is determined by gp23 and by other proteins. The normal T4 head consists of a distorted icosadeltahedron with an inserted extra band of subunits in the long axis with about 840 copies of gp23; the gp20 is located at vertices. This shape must reflect precise constraints resulting from protein–protein interaction.

2.6 Packaging the DNA

In the T-even virions the phage DNA is tightly packed. The topography of packing is unknown; there may be a central hollow. It is believed that the DNA collapses into a compact within the capsid when the gp22 protein inside the capsid is cleaved. How DNA is "sucked" into the capsid head is not clear; it may simply be brought in by a displacement reaction caused by exit of internal proteins. The gp49 is needed to fill the head normally with DNA.

2.7 Lysis

One of the late gene products of T-even phage is a lysozyme (gpe) that cleaves bacterial peptidoglycans. Lysozyme is made within infected cells well before the onset of lysis. Lysis takes place, however, only if the lysozyme gains access to the peptidoglycan layer.

One other gene, sp, is involved in the lysis control program. This gene may normally act to maintain the integrity of the cytoplasmic membrane, making continuing aerobic metabolism possible and preventing the rigid layer from being attacked prematurely by bacterial enzymes.

T-even phages have been a major model system in the development of modern genetics and molecular biology since 1940 and bacteriophages T2 and T4 were instrumental in the first formulation of many fundamental biological concepts. The advantages of T4 as a model system came from the fact that virus infection inhibited host gene expression, which allows investigators to differentiate between host and phage macromolecular synthesis.

Quite recently the sequence of its total genome was completed [6].

Therefore I will confine my story to T4 phage. First of all let us look at the structure of T4 phage (Fig. 5). Everyone will be impressed with the complexity and the beauty of its morphology.

Historically, Edward Kellenberger wrote an article in the same book as mentioned before entitled "Electron Microscopy of Developing Bacteriophage" and introduced the concept of morphopoiesis [7].

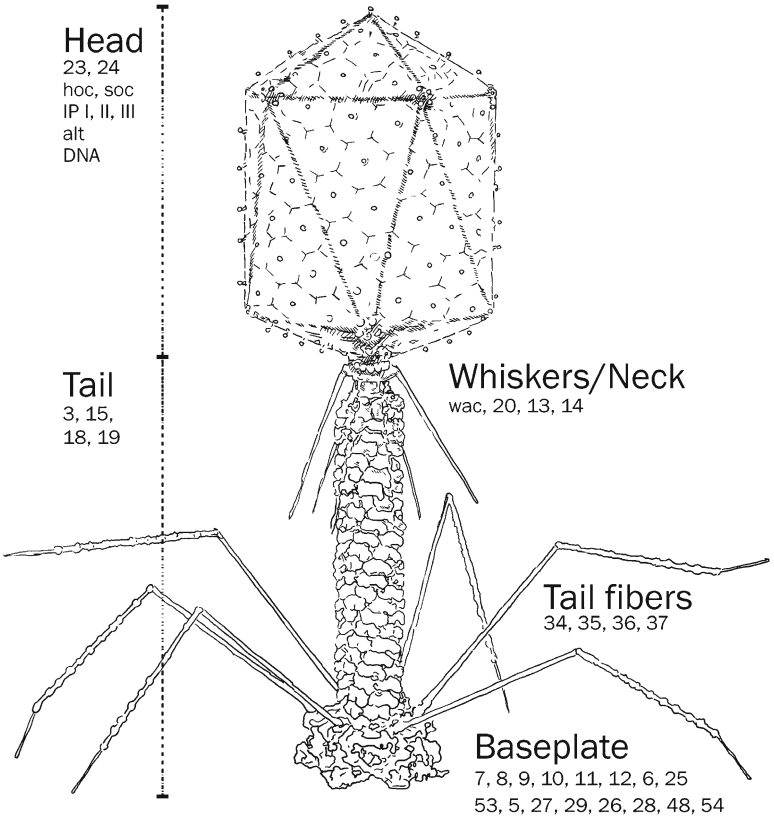

Fig. 5 Structure components of the T4 particle. Features of the particle have been resolved to about 3 nm. The positions of several head, tail, baseplate, and tail fiber proteins are indicated [6]

He has defined morphopoiesis as the process leading from a pool of subunits to a morphologically characterized biological entity (like an organelle or a virus). Within one system, only a determined number of different types of subunits participate. Substances contributing specifically to the specific morphology are called "morphopoietic factors or principle." They can – but need not – be a part of the final product.

A morphopoiesis is of the first order if only one type of subunit is used to build a structure by self-assembly

In morphopoiesis of higher order, supplementary bits of morphopoietic information are contributed through morphological factors. Morphopoietic regulation appears to act at the level of the gene products through the phenomenon of sequential triggering.

About 40 years later, since the Phage group started, the genome of the host cell, *E. coli* was also determined [8] and the morphopoiesis of phage can be explained through the interaction of viral genes and host genes.

T4 phage has about 300 genes packed into 168,903 bp genome and a total of 289 probable protein-encoding genes, 8 tRNA genes, and at least 2 other genes that encode small, stable RNAs of unknown function [6]. T4 phage builds the most complex virus particles. It devotes more than 40% of its genetic information to the synthesis and assembly of the prolate icosahedral heads, tail with contracted sheaths, and six tail fibers that contribute to its high efficiency of infection.

Extensive genetic and biochemical analysis revealed the complex assembly pathway of the T4 particle [9–11]. Twenty-four proteins are involved in head morphogenesis, and there are 22 for tail morphogenesis, and seven for tail fibers, including 1 for tail fiber attachment. Five of the 54 proteins are catalysts for assembly rather than components of the final virion. In the assembly pathway, the head, tail and tail fibers are assembled independently. A head and tail are associated, and then the six tail fibers attach to the baseplate [12].

Of the 24 proteins assigned to head morphogenesis, 16 are involved in prohead formation and maturation, 5 are responsible for DNA packaging, and 3 complete and stabilize the head. Only 10 of the 16 genes for prohead formation are essential; these include GroEL, the one host-coded protein involved in head assembly. This contrasts with phage lambda, where GroES, DnaK, DnaJ, GrpE, and GroEL are all essential [13–15]. It was shown that T4 gp31 can substitute for the function of GroES [16]. T4 gp31 has an extra loop that makes the inner cavity of the GroEL–gp31 complex larger so that it can accommodate for the folding intermediate of gp23, the major capsid protein [17].

The head is assembled on the initiator complex, which is a 12-mer of gp20 arranged in a ring. The scaffold, made of gp22–gp21 and the capsid protein, gp23, are assembled onto the initiator, which eventually becomes the portal vertex.

Pentamers of gp24, which is 28% identical in amino acids residues to gp23, are placed at the other 11 vertices. After the scaffold is completely surrounded by gp23 and gp24, the T4 prohead protease, gp21, degrades the scaffold and cleaves most of the other head proteins, including gp23 and gp24.

This creates space in the cavity of prohead. The prohead thus formed is then detached from the membrane. It was demonstrated by pulse-chase experiment that ESP (empty small particle) then initiates DNA packing and forms the ISP (initiated

small particle), which contains about 10 kb of DNA. The resulting mature head is much more resistant to any kind of perturbation [18, 19].

The tail and tail fibers are responsible for the high efficiency of T4 infection. The tail is made of a baseplate and two cocylinders. The inner cylinder consists of 144 subunits of gp19 arranged in 24 stacked hexameric rings. The inner space of the tail tube allows for the passage of phage DNA. The same number of gp18 molecules form the outer tail sheath, with the subunits arranged in the same manner as gp19.

Each stacked sheath ring is offset 17° to the right of the one below it, which gives an apparent right-handed helix [20]. While the noncontracted tail sheath is 98.4 nm long, the contracted tail sheath is only 36 nm long and the twist angle of sheath proteins is increased to 32°.

The baseplate consists of a hub surrounded by six wedges, which are assembled independently. Hub assembly is very complex. The six products of genes 5, 27, 29, 26, 28 and 51 have been reported to be involved in the assembly.

gp51 is a catalytic protein, and gp26 and gp28 have not been proven to be components of the hub or baseplate. gp5 and gp27 associate first. The hub is completely by binding of gp29 to the gp5–gp27 complex. It appears that some structural modification of gp29 is necessary before associating with the gp5–gp27 complex. Wedge assembly is initiated by the association of gp10 and gp11, followed by addition of gp7, gp8, gp6, gp53 and gp25, in that order. In the absence of any of the other components, the assembly stops at that point and the remaining components are left free in "assembly-naïve states" [21].

Baseplate morphogenesis appears to occur in association with the cell membrane. The baseplates remain attached to the membrane by 300-Å fibers from the six corners of the baseplate during the remainder of phage assembly until the time of cell lysis, as shown by electron microscopy [22]. The finding that gp7 has a predicted membrane-spanning domain near its C-terminus suggests a possible mechanism for this attachment. The gp5–gp27 heterohexameric complex is attached at the tip of the tube. When the tail sheath contracts and the tail tube protrudes from the bottom of the baseplate, the triple-stranded β-helix is considered to play a role like that of a needle to puncture the cell. The short tail fiber is a trimer of gp12. It consists of three domains called the pin (N terminus), shaft, and head (C terminus).

The shaft is mainly β-helix and β-spiral. gp11 is located at the tip of the tail pin and bound to the middle part of the P12 trimer, at a site where the P12 shaft is bent about 94°. gp9 forms the socket of a long tail fiber [23] consisting of four gene products, gp34, gp35, gp36, and gp37, where gp34 and gp37 are the proximal and distal long tail fibers, respectively. gp35 and gp36 attach to the distal fiber, forming the junction between the half-fibers.

Structural analysis of the C-terminal portion of the whisker [24] revealed a three-stranded coiled-coil structure with a beta structure "propeller" at the C terminus. This beta structure is thought to bind the bend or "knee" in long tail fibers to facilitate tail attachment to the baseplate. The assembly of the tail fibers requires two molecular chaperone-like proteins, gp57A and gp38.

About 100–150 phage particles have accumulated in the cell by the lysis that occurs. Two proteins are involved in the lysis process: gpe and gpt. gpe is the so-called T4

lysozyme [25]. The gp5 lysozyme can substitute for gpe [26]. gpt is the T4 polin, which creates a hole in the inner membrane so that lysozyme can reach the peptidoglycan layer form the cytosol: the timing of polin assembly determines the time of lysis [27, 28]. In the absence of either lysozyme or the polin, lysis does not occur.

The T-even phages display a unique phenomenon, lysis inhibition, which allows them to sense when there are numerous phages around and respond appropriately to delay lysis, maximize the use of their host, and potentially await the accumulation of additional host [29], Lysis is delayed if more phages attack the infected cell at any time after 5 min into infection. This signal is somehow mediated by the rI protein, which regulates assembly of the t holing [30].

After we have got the whole DNA sequence of T4, we can list the proteins whose functions are not clear at this moment. It is conceivable that the proteins which are related to the membrane seem to be involved somehow in the process of T4 morphogenesis. We are still far from completely understanding T4 morphogenesis.

3 Molecular Biology of Morphogenesis of Bacteriophage Lambda

Bacteriophage lambda was an important tool in the study of *E. coli*. And lambda is the major prototype for a template phage, which has two types of life cycle, lytic cycle and lysogenic cycle, and has played a central role in studies defining current concepts of gene regulation and genetic regulatory circuitry. The lysogenic life cycle, in which its DNA is inserted at a specific site in the host chromosome such that phage DNA passably replicates with the host DNA. A bacteriophage that can follow either a lytic or a lysogenic life style is known as a temperate phage, whereas those that have only a lytic mode are said to be virulent.

More recently, lambda strains were used to refine concepts of how cloning and expression vectors should work, and lambda vectors are still commonly used in the construction of genomic libraries. The genome size is 48,502 base pairs and the complete genome sequence is available online (accession number JO2459).

It has a linear genetic and physical map, sometimes presented in circular representation since the molecule circularizes at the cohesive ends during some stages of virus activity. In general, dsDNA phages are assembled by putting together separately tails and empty head shells, packing DNA in the head shells, and attaching tails to the filled heads. The structure of the lambda phage is shown in Fig. 6.

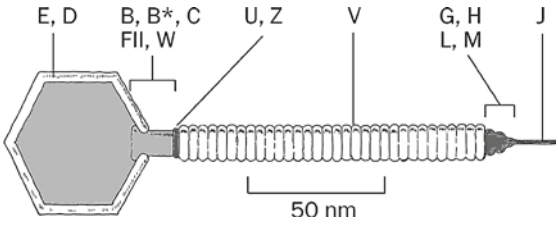

Fig. 6 A sketch of bacteriophage λ indicating the locations of its components. The letters refer to specific proteins. The *bar* represents 50 nm [31]

The form is simpler compared with that of T4 phage. The size of DNA is about one third of T4 phage DNA. It has a 55-nm-diameter icosahedral head and a flexible 15- to 135-nm long tail that bears a single thin fiber at its end. Bacteriophage lambda (λ) adsorbs to *E. coli* through a specific interaction between the viral tail fiber and maltoporin which is coded by *E. coli* gene. This is a component of bacterium's outer membrane.

The mature λ phage head contains two major proteins: gp*E*, which forms its polyhedral shell, and gp*D*, which "decorates" its surface. The λ head contains four major proteins, gp*B*, gp*C*, gp*FII*, and gp*W*, which form a cylindrical structure that attaches the tail to the head. The tail is a tubular entity that consists of 32 stacked hexagonal rings of gp*V* for a total 192 subunits. Phage assembly is studied through a procedure developed by Robert Edgar and William Wood that combines genetics, biochemistry, and electron microscopy. Conditionally lethal mutations are generated that, under non-permissive conditions, block phage assembly at various stages.

The assembly of bacteriophage λ occurs through a branched pathway in which the phage heads and tails are formed separately and then joined to yield mature virions.

Phage head assembly occurs in four stages [31]:

1. gp*B* and gp*Nu3*, with two host-supplied chaperonin proteins, GroEL and GroES, interact to form an "initiator" that consists of 12 copies of gp*B* arranged in a ring with a central orifice. This precursor of the mature phage head-tail connector apparently organizes the phage head's subsequent formation. GroEL and GroES, provide a protected environment that facilitates the proper folding and assembly of proteins and protein complexes such as the connector precursor. gp*Nu3* functions as a molecular chaperone in that it has but a transient role in phage head assembly.
2. gp*E* and gp*Nu3* associate to form a structure called an immature prohead. If gpB, GroEL, or GroES is defective or absent, some gp*E* assembles into spiral or tubular structures, which indicates that the missing proteins guide the formation of a proper shell.
3. In the formation of mature prohead, the N-terminal 22-residue segment of ~75% of the gp*B* is excised to form gp*B**; the gp*Nu3* is degraded and lost from the structure; and ten copies of gp*C* participate in a fusion-cleavage reaction with ten additional copies of gp*E* to yield the hybrid proteins p*X1* and p*X2*, which form the collar that apparently holds the connector in place. The enzymes that catalyzes this process has not been identified.
4. In the final stage of phage head assembly, gp*W* and gp*FII* add in that order to stabilize the head and form the tail-binding site.

Tail assembly occurs independently of head assembly from the 200-Å-long tail fiber toward the head-binding end. This strictly ordered series of reactions can be considered to have three stages:

1. The formation of the "initiator," which ultimately becomes the adsorption organelle, requires the sequential actions on gp*J* (the tail fiber protein) of the products of

phage genes *I*, *L*, *K*, *H*, and *M*. Of these, only gp*I* and gp*K* are not components of the mature tail.
2. The initiator forms the nucleus for the polymerization of gp*V*, the major tail protein, to form a stack of 32 hexameric ring. The length of this stack is thought to be regulated by gp*H*, which, becomes extended along the length of the growing tail and somehow limits its growth.
3. In the termination and maturation stage of tail assembly, gp*U* attaches to the growing tail, thereby preventing its further elongation. The resultant immature tail has the same shape as the mature tail and can attach to the head. In order to form an infectious phage particle, the immature tail must be activated by the action of gp*Z* before joining the head.

The completed tail spontaneously attaches to a mature phage head to form an infectious λ phage particle.

4 Morphogenesis of Filamentous Phage

The filamentous bacteriophage are a group of viruses that contain a circular single-stranded DNA genome encased in a long capsid cylinder. Many use some type of bacterial pilus to facilitate the infection process. Ff class of the filamentous phages (f1, fd, and M13) have been the most extensively studied. These bacteriophages use the tips of the F conjugative pilus as a receptor and thus are specific for *E. coli* containing the F plasmid. The DNA sequences of these three phages shows them to be 98% homologous; consequently, the protein sequences of the gene products are practically the same. Phage M13 is the model filamentous bacteriophage [32]. The phage has been of extensive use as a cloning vector and DNA-sequencing vehicle in genetic engineering. The virion of phage M13 is only 6 nm in diameter but is 860 nm long and is semi-flexible (worm-like). These filamentous DNA phage have the additional interesting property of being released from the cell without lysing the host cell. Thus, a cell infected with phage M13 can continue to grow, all the while releasing virions. Virus infection causes a slowing of cell growth, but otherwise a cell is able to coexist with its virus. Typical plaques are not observed; only areas of reduced turbidity occur within a bacterial lawn. Many aspects of DNA replication in filamentous phages are similar. The property of release without cell killing occurs by budding. With phage M13 there is no accumulation of intracellular virions as with typical bacteriophages. Instead, the assembly of mature M13 virions occur on the inner surface of the cytoplasmic membrane and virus assembly is coupled with the budding process.

Several features of phage M13 make it useful as a cloning and DNA sequencing vehicle. First, it has single-stranded DNA, which means that sequencing can easily be carried out by the Sanger dideoxynucleotide method. Second, a double stranded form of genomic DNA essential for cloning purposes is produced naturally when the phage produces the replicative form. Third, as long as infected cells are kept in the growing state, they can be maintained indefinitely with cloned DNA, so a continuous

source of the cloned DNA is available. And there is an intergenic space in the genome of phage M13 that does not encode proteins and can be replaced by variable amounts of foreign DNA. So phage M13 is an important part of the biotechnologist's toolbox.

The mass of the particle is approximately 16.3 MD, of which 87% is contributed by protein. The genome is a single-stranded, covalently close DNA molecule of about 6,400 nucleotides encased in a somewhat flexible protein cylinder. The length of cylinder consists of approximately 2,700 molecules of the 50-amino-acid major coat protein, also called gene VIII protein (pVIII). At one end of the particle, there are about 5 molecules each of the 33-residue gene VII (pVII) and the 32-residue gene IX protein (pIX). The other end contains approximately 5 molecules each of the 406-residue gene III and 112-residue gene VI proteins (pIII and pVI). The DNA is oriented within the virion such that a 78-nucleotide hairpin region called the packaging signal (PS) is always located at the end of the particle containing the pVII and pIX proteins.

Filamentous phage assembly is a non-lytic, membrane-associated process. This is quite different from that of T4 or lambda phage. Phage particles are extruded from the infected host, which continues to grow and divide, albeit at a reduced rate. Prior to assembly, newly synthesized coat proteins are anchored in the inner membrane (IM) by single transmembrane domains. Filamentous phage proteins pI and pIV are morphogenic proteins required for phage assembly not part of virion. Neither pI nor pIV from phage f1 can substitute for its equivalent in other related phages. When the two proteins are supplied as pairs, partial restoration of heterologous phage assembly occurs. This observation suggests that the two proteins interact. A selection for revertants of a temperature sensitive mutants of f1 gene IV resulted in the isolation of a suppressor mutation in gene I. Another similar evidences suggest that it is pI that interacts with both pIV and pVIII. Thus the process by which filamentous phage are concomitantly assembled and secreted across the cell membranes is likely to involve a series of protein–protein interactions that are accessible to genetic analysis [33].

It has been proposed that f1 is secreted through the outer membrane (OM) via a phage-encoded channel protein, pIV. A functional pIV mutant was isolated that allowed *E. coli* to grow on large maltodextrins and rendered *E. coli* sensitive to large hydrophilic antibiotics that normally do not penetrate the OM. In planar lipid bilayers, both mutant and wild-type pV formed highly conductive channels with similar permeability characteristics but different gating properties: the probability of the wt channel being open much less than that of the mutant channel. The high conductivity of the pIV channel suggests a large-diameter pore, thus implicating pIV as the OM phage-conducting channel [34].

Thus it is concluded that the phage genome is encoded for proteins that are not found in the phage particle but are necessary for phage assembly and export. Multimers of protein IV in the outer membrane (OM) interact with multimers of protein-I and protein-II in the IM to form an assembly site that may function as a gate pore through which assembling phage are extruded.

The M13 filamentous bacteriophage coat protein is a symmetric assembly of several thousand α-helical major coat proteins (pVIII) that surround the DNA core.

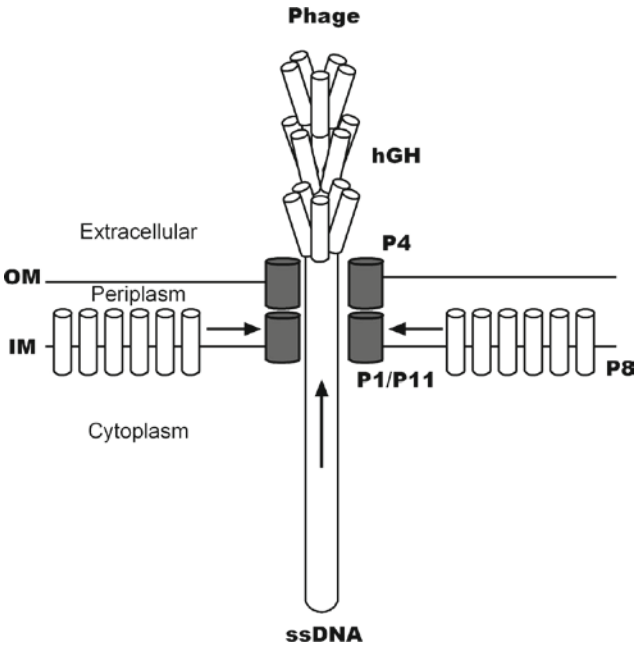

Fig. 7 Filamentous bacteriophage assembly and phage display. Newly synthesized major coat protein molecules (P8) are imbedded in the IM with their N termini on the periplasm and their C termini in the cytoplasm. Single-stranded viral DNA (ssDNA) is extruded from the host at assembly sites composed of phage-encoded proteins (P1/P11) and P4 that together span the IM and the OM. Coat proteins interact with the assembly site, where they surround the ssDNA and are transferred from the bacterial membrane into the assembling phage particle, which is extruded without lysis of the host. Phage display of hGH was achieved using an hGH-P8 fusion gene carried on a phagemid

pVIII molecules initially reside in the host membrane and subsequently transit into their role as coat proteins during the phage assembly process. A comprehensive mutational analysis of the 50-residue pVIII sequence revealed that only a small subset of the side-chains were necessary for efficient incorporation into a wild-type (wt) coat. In the three-dimensional structure of pVIII, these side-chains cluster into three functional epitopes: a hydrophobic epitope located near the N terminus and two epitopes (one hydrophobic and the other basic) located near the C terminus on the opposite faces of the helix. These interactions could facilitate the transition of pVIII from the membrane into the assembling phages, and the incorporation of a single pVIII would be completed by the docking of additional pVIII molecules with the second hydrophobic epitope at the C terminus. In this chapter the authors have constructed a minimized pVIII that contained only nine non-Ala side-chains yet retained all three functional epitopes. The minimized pVIII assembled into the wt coat almost as efficiently as wt pVIII, thus defining the minimum requirements for protein incorporation into the filamentous phage coat. The complex mechanism is shown in Fig. 8 [35].

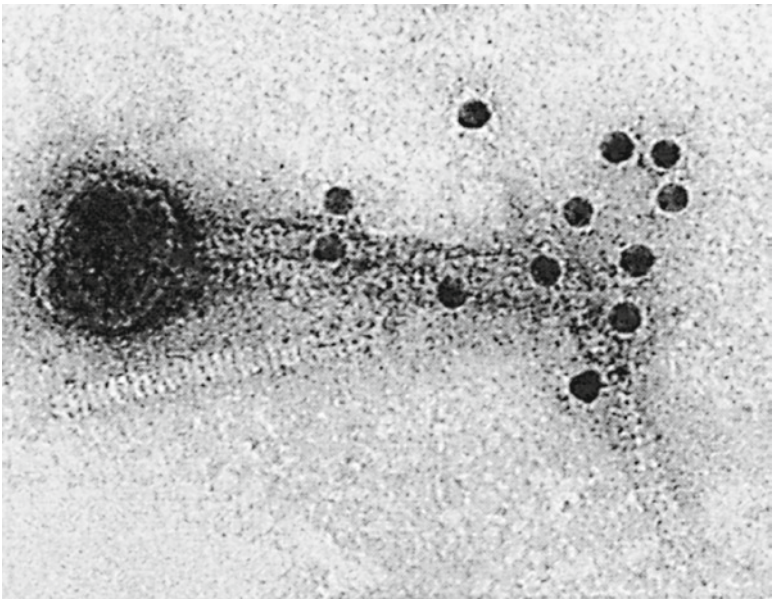

Fig. 8 Electron microscopy of λcI857S7 grown in the presence of gpV-β-galactosidase fusion proteins. The sample was treated with monoclonal anti-βgalactosidase and recombinant protein immunogold reagent

The Ff genome encodes only ten proteins, a simplicity which is achieved by encoding a variety of functions within individual proteins. For example, during the phage life cycle, the major coat protein (gene VIII) must be stably inserted into *E. coli* host inner membrane prior to interacting with phage DNA in the lipid-free virion.

A key characteristic of this 50-residue coat protein is that "small" residues on one face of the effective transmembrane (TM) [36], helical segment (gly34, Ala35 and Gly38), have been shown to participate in in vitro helix-helix dimerization and oligomerization of micelle-solubilized protein; this process may facilitate the interaction of protein chains in preparation for extrusion from the membrane during phage assembly. Once the coat protein leaves the host membrane, it encapsulates the Ff circular single-stranded DNA genome to produce an elongated virion about 100 times longer than it is wide [32]. The coat protein N-terminal segment consists of an amphipathic helix with an Ala-rich face (Ala7, Ala10, Ala18, Ala25) upstream from the residues which comprise the TM helix-helix interface [37–40]. It is possible that these "small" residues enable close helix-helix packing between successive layers of coat protein in the virion. To approach this question experimentally, it was reported that they used randomized mutagenesis techniques established for preparation and analysis of M13 viable mutants [41]. About 100 viable M13 mutants of the entire gene VIII may be used to assess the susceptibility of each position to mutation. In the resulting library, "small" residues (Ala, Gly, Ser), which constitute the non-polar

face of the N-terminal amphipathic helical segment, and a face of the hydrophobic helical segment, were found to be highly conserved. They propose a model in which coat protein packing is stabilized by the presence within each protein subunit of the two "oligomerization segments," i.e. specific helical regions with faces rich in small residues which function to promote the close approach of helices.

5 The Genes of Host Cell *(E. coli)* Govering Phage Morphogenesis

Virus particles are aggregates of protein and nucleic acid, synthesized with the aid of small molecules, enzymes and ribosomes of the host cell. Many viruses depend on host proteins for the synthesis of viral nucleic acid and for the transcription of viral genes. Therefore it is surprising that all structural proteins of virus particles seem to be specified by viral genes as described above. It is reasonable to ask whether host proteins or other host structures might be required for particle assembly but not incorporated into the finished structure.

An attempt to isolate bacterial mutants which fail to support phage growth was taken in the 1970s. It was shown with certain bacterial mutants, called groE, that T4 phage head assembly was blocked specifically, implying that the host plays a direct role in head assembly. The block occurred early in the assembly process at the level of action of T4 gene 31 [42]. And it was also shown that bacterial strains of *E. coli* which have groE mutants were defective for λ head formation [43]. Mutants of λ, designated λEP, which were able to grow in the three groE strains, had been isolated. An analysis of these mutants indicated that at least some carried a mutation in λ head gene E and these made reduced levels of active gene E protein in groE hosts. The results indicated that it was the interaction between the gene E protein and the proteins specified by genes B and C that was adversely affected by the groE mutation. It is conceivable that the relative level of gene E protein is too high in groE strains for proper head formation. The λEP mutation compensates for this effect by reducing the level of this protein, and so restoring a balance.

It was demonstrated that during normal head assembly the protein encoded by phage head gene B or C appeared to be converted to a lower molecular weight form, h3, which was found in phage. The appearance of h3 protein in fast sedimenting head related structures required the host groE function. It was then suggested that the proteins encoded by phage gene E, B and C, and the bacterial component defined by groE mutations, acted together at an early stage in head assembly [44].

Many groE mutations exerted pleiotropic effects, such as the inability to propagate phage T4 and T5 and inability to form colonies at 43 °C. The groE bacterial gene product as a protein of 65,000 molecular weight was identified [45]. Lately one groE gene, groEL, has been shown to encode the synthesis of a 65,000 molecular weight polypeptide, whereas the second, groES, codes for the synthesis of a 15,000 M polypeptide [46].

6 Phage Display

Phage display began with the paper by George Smith in 1985 and it became a core biotechnology [47]. This technology is based on two concepts. The first is that phage can be used to link protein recognition and DNA replication. The protein is displayed on the surface of the phage particle and the genes encoding it are contained within the particle. The second is that large libraries of the DNA sequences encoding these molecules can be cloned into phage.

6.1 The Phage Genome

The genomes of the Ff phage (M13, f1 and fd) have been completely sequenced [48–50]. Each genome encodes 11 genes, whose products are listed in Table1.

Two of the gene products, pX and pXI, are the result of a translational start at the internal methionine codon in genes II and I, respectively. These internal methionine codons are in-frame, so the smaller proteins have the same sequence as the carboxy-terminal portions of their larger counterparts. The genes are grouped in the genome according to their function in the life cycle of phage. One group (gene II, V, X) encodes the proteins required for the replication of the phage genome. Other encodes capsid proteins (pI, pX, and PIV) are involved in the membrane-associated assembly of the bacteriophage. There is a short sequence called the intergenic region that does not code for protein. It contains the sites of origin for synthesis of viral (+) and complementary (−) DNA. The PS is in the intergenic region near the end of gene IV.

There are very few regions in the phage genome that do not code for protein. Cassettes encoding antibiotic resistance are generally inserted in the intergenic region or in the space between the end of gene VIII and the beginning of gene III. In the latter case, some alterations of the positions of the terminator and promoter in this region must be made, and care must be taken not to interfere with the origins of replication or other control areas. There appears to be a delicate balance in the

Table 1 Genes and gene products of the f1 bacteriophage

Gene	Function	Protein MW
II	DNA replication	46,137
X	DNA replication	12,672
V	Binding ss DNA	9,682
VIII	Major capsid protein	5,235
III	Minor capsid protein	42,522
VI	Minor capsid protein	12,342
VII	Minor capsid protein	3,599
IX	Minor capsid protein	3,650
I	Assembly	39,502
IV	Assembly	43,476
XI	Assembly	12,424

synthesis of the phage proteins that allows phage production without seriously affecting bacterial cell growth.

Needless to say, the technology which is developed using filamentous phage can be applicable to other phage such as T4 or lambda phage as mentioned earlier. However, I want to discuss here only filamentous phage.

6.2 Display of Peptides and Proteins on Phage Particles

Large libraries of peptides and proteins have been made using pIII as the display vehicle [51, 52], leading to the development of a number of techniques for selecting the molecules desired from such libraries [53, 54]. Peptides and proteins have been fused to the amino-terminal portion of the major capsid protein pVIII [55]. There has been a report of phage particles displaying proteins that are fused to the carboxy-terminal portion of pVI, although the efficiency of display appears to be lower in this case [56]. Recently, antibody heavy- and light-chain variable regions have been fused to the amino terminus of pVII and pIX and displayed on phage, showing that these two minor coat proteins can also be used for display [57].

Proteins can be displayed on smaller filamentous particles called phagemids [58, 59]. The phagemid genome contains the filamentous phage intergenic region with its origin of replication for viral and complementary strand synthesis as well as the hairpin packing signal. The genome contains a plasmid origin of replication and a gene coding resistance to a specific antibiotic. Chimeric genes encoding peptide–phage protein fusion can be placed under control of a specific promoter in these phagemid genomes. The phagemid can maintain itself as a plasmid, directing the expression of the protein in bacteria. Infection of bacteria with a filamentous helper phage activates the phage origin of replication, resulting in single-stranded phagemid DNA being encapsulated into filamentous phage-like particles using helper phage proteins. A helper phage containing a defective packaging signal can be used so that the majority of particles produced contain the phagemid single-stranded DNA [60]. Bacteria can be infected with phagemid-phage mixture and colonies selected that are resistant to the antibiotic. The resistant colonies will contain only the phagemid DNA, which can be propagated again by infection with helper phage. Because the phagemid particles can transmit antibiotic resistance, they are referred to as “transducing particles.”

To access technical details readers should consult Phage Display [61].

6.3 Application of Phage Display in Biotechnology

Phage display, largely developed in the 1990s, has begun to make critical contribution to major endeavors of biological scientists. In 1985, George Smith first showed that the linkage between phenotype and genotype could be established in filamentous bacteriophage and gave birth to the new technology of phage display.

First of all I want to show you G. Smith's work and subsequent works using other phage.

6.4 Filamentous Phage

Gene III of filamentous phage encodes a minor coat protein, pIII, located at one end of the virion. The amino terminal half of pIII binds to the F pilus during infection, while the carboxy-terminal half is buried in the virion and participates in morphogenesis. It was reported that foreign DNA fragments could be inserted into filamentous phage gene III to create a fusion protein with the foreign sequence in the middle. The fusion protein was incorporated into the virion, which retained infectivity and displayed the foreign amino acid in immunological accessible form. These "fusion phages" can be enriched more than 1000-fold over ordinary phages by affinity for antibody directed against the foreign sequence. Fusion phages may provide a simple way of cloning a gene when an antibody against the product of that gene is available [47].

6.5 Phage Lambda

The tolerance of bacteriophage lambda morphogenesis for C-terminal additions to the tail tube major protein subunits (the V gene product; gpV) was shown to be useful for the application of phage display for the biotechnology (Fig. 8). A second modified copy of the lambda V gene, either within a novel phage vector itself or plasmid-borne, was expressed during phage growth. High-level substitution of wild-type gpV by modified gpV bearing a basic C-terminal peptide sequence (RRASV; a target site for cAMP-dependent protein kinase) was possible using multiple repeats of a serine-glycine (SGGG) linker sequence. Highly purified phage bearing copies of gpV-RRASV could be efficiently phosphorylated by the appropriate protein kinase, and the incorporated label was shown to migrate exclusively at the expected size in protein gels. A large tetrameric protein (β-galactosidase) could be incorporated into active virions in at least one copy, again using a Ser-Gly linker. This result suggested that with a suitable spacing linker and controlled levels of expression, it is likely that a wide range of protein or peptide substitute can be fused with gpV at its terminus and assembled as component subunits of the tail tube [62].

6.6 Phage T7

The ideology of "rational drug design" embraces the notion that (1) drugs should be targeted against specific proteins known to malfunctioning within cells, (2) the candidacy of these proteins as attractive targets for therapeutic intervention should

be further determined by their predicted drug ability, and (3) the detailed molecular structures of such target proteins should inform the design of the chemical structures of the drugs that are to be developed.

In the case of tyrosine kinase inhibitors, attempts at identifying all of the kinases that might be affected by a drug have involved assays of only a small proportion of the large cohort of protein kinases known to be present in human cells. Consequently, certain off-target effects are likely to have eluded drug developers. This has begun to change with the advent of more systematic screening of a far large portion of the kinases that might be affected by these inhibitors. Discovery of off-target activities of a drug is actually useful in two ways; (1) it may explain toxicities of a drug and (2) it may reveal new clinical application for the drug.

A promising example of application of phage display using T7 phage for this purpose was reported [63]. Kinase inhibitors are important cancer drugs, demonstrating powerful clinical activity in tumors in which the target kinase is activated by mutation. The success of imatinib (Gleevec, Novartis Pharma AG), an inhibitor of the mutant kinase, Bcr-Abl, in treating chronic myelogenous leukemia, has stimulated many scientists' interest in finding new kinase inhibitors. The new in vitro assay for determining kinase inhibitor specificity and using it to create interaction map of 20 different kinase inhibitors against 119 different protein kinases was reported. The majority of kinase inhibitors target the kinase ATP site, and because all of the more than 500 protein kinases identified in human genome have an ATP site, there is great potential for cross-reactivity. Compounds must be tested experimentally against many kinases to assess molecular specificity and to identify off-target interactions. Binding specificity and affinity are not readily predicted based on available sequence or structural information, and conventional profiling methods based on in vitro activity are limited by the difficulty of building and running large numbers of kinase activity assays. A quantitative assay is shown in Fig. 9.

Kinase domains are expressed as fusions to T7 bacteriophage, and test drugs in solution compete with tethered "bait" compounds for binding to the ATP-binding site of each kinase. The amount of phage bound to the tethered ligand is then quantified to determine the affinity of the drug. In addition to simply expanding the kinase profile of some of the 20 drugs tested, the authors reported a potpourri of unanticipated interactions. These include inhibition of an imatinib-resistant mutant of ABL by the p38 inhibitor BIRB-766 and inhibition of SRC family kinase LKC by imatinib. The key assay compounds are human kinases expressed as fusions to T7 bacteriophage and a small set of immobilized probe ligands that bind to the ATP site of one or more kinases. The results are read out by quantifying the amount of fusion protein bound to the solid support, which is accomplished with extraordinary sensitivity by either traditional phage plaque assay or by quantitative PCR using the phage DNA as a template.

T7 phage replication leads to lysis of the bacterial host, and lysates containing properly folded, tagged kinase are used directly in the assay with no need for conventional protein purification.

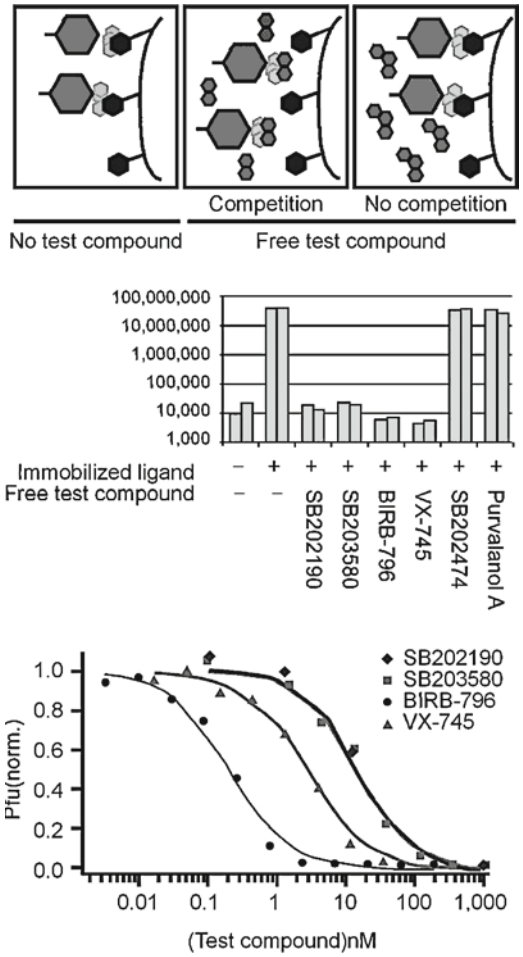

Fig. 9a–c Competition binding assay for measuring the interaction between unlinked, unmodified (free) small molecules and kinases. **a** Schematic overview of the assay. The phage-tagged kinase is shown in blue, "free" test compound in green and immobilized "bait" ligand in red. **b** Binding assay for p38MAP kinase. The immobilized ligand was biotinated SB202190. The final concentration of the test compounds during the binding reaction was 10 μM. **c** Determination of quantitative binding constants. Binding of tagged p# (to immobilized SB202190 was measured as a function of unlinked test compound concentration. Tagged p38 kinase was quantified by real-time quantitative PCR and results normalized.

References

1. Stanley WM (1935) Science 81:644
2. Stent G (1992) In: Cairns J, Stent GS, Watson JD (eds) Phage and the origins of molecular biology, expanded edn. Cold Spring Harbor Laboratory, New York, p 3

3. Delbrück M (1992) In: Cairns J, Stent GS, Watson JD (eds) Phage and the origins of molecular biology, expanded edn. Cold Spring Harbor Laboratory, New York, p 9
4. Anderson TF (1992) In: Cairns J, Stent GS, Watson JD (eds) Phage and the origins of molecular biology, expanded edn. Cold Spring Harbor Laboratory, New York, p 63
5. Harshey AD (1992) In: Cairns J, Stent GS, Watson JD (eds) Phage and the origins of molecular biology, expanded edn. Cold Spring Harbor Laboratory, New York, p 100
6. Miller SE, Kutter E, Mosig G, Arisaka F, Kunisawa T, Rüger W (2003) Microbiol Mol Biol Rev 67:86
7. Kellenberger (1992) In: Cairns J, Stent GS, Watson JD (eds) Phage and the origins of molecular biology, expanded edn. Cold Spring Harbor Laboratory, New York, p 116
8. Blattner FR, Plunkett G III, Bloch CA, Perna NT, Burland V, Riley M, Collado-Vides J, Glasner JD, Rode CK, Mayhew GF, Gregor J, Davis NW, Kirkpatrick HA, Goeden MA, Rose DJ, Mau B, Shao Y (1997) Science 277:1453
9. Black IW, Shove MK, Steven AC (1994) In: Karam J, Drake JW, Kreuzer KN, Mosig Hall DH, Eiseling FA, Black LW, Spicer E, Kutter E, Carlson K, Miller ES (eds) Molecular biology of bacteriophage T4. American Society for Microbiology, Washington, DC, p 218
10. Coombs DH, Arisaka F (1994) In: Karam J, Drake JW, Kreuzer KN, Mosig Hall DH, Eiseling FA, Black LW, Spicer E, Kutter E, Carlson K, Miller ES (eds) Molecular biology of bacteriophage T4. American Society for Microbiology, Washington, DC, p 259
11. Ferguson PL, Coombs DH (2000) J Mol Biol 297:99
12. Edgar RS, Wood WB (1966) Proc Natl Acad Sci USA 55:498
13. Coppo A, Manzi A, Pultzer JF, Takahashi H (1973) J Mol Biol 76:61
14. Georgopoulos CP, Hendrix RW, Casjen SR, Kaizer AD (1973) J Mol Biol 76:45
15. Tilly K, Murialdo H, Georgopoulos C (1981) Proc Natl Acad Sci USA 78:1629
16. van der Vries SM, Gatenby AA, Georgopoulos C (1994) Nature 368:654
17. Hunt JF, van der Vries SM, Henry L, Deisenhofer J (1997) Cell 90:361
18. Jardiner PJ, Coombs DH (1998) J Mol Biol 284:661
19. Jardiner PJ, McCormick MC, Lutze-Wallace C, Coombs DH (1998) J Mol Biol 284:647
20. Moody MF (1971) Philos Trans R Soc Lond Ser B 261:181
21. Kikuchi Y, King J (1975) J Mol Biol 99:695
22. Simon LD (1969) Virology 38:285
23. Urig MS, Brown SM, Tedesco P, Wood WB (1983) J Mol Biol 169:427
24. Strelkov SV, Tao Y, Rossmann MG, Kurochkina LP, Shneider MM, Mesyanzhino VV (1996) Virology 219:190
25. Streisinger G, Mukai F, Dreyer WJ, Miller B, Horiuchi S (1964) Cold Spring Harbor Symp Quant Biol 26:25
26. Kao SH, McClain WH (1980) J Virol 34:104
27. Grundling A, Manson MD, Young R (2001) Proc Natl Acad Sci USA 98:9348
28. Ramanculov E, Young R (2001) Mol Genet Genomics 265:345
29. Behenek AL, Smith A, Drake JW (1999) J Bacteriol 181:3123
30. Paddison P, Abedons T, Dressman HK, Gailbreath K, Tracy J, Mosser E, Neitzel J, Guttman B, Kutter E (1998) Genetics 148:1539
31. Voet D, Voet JG (2004) Biochemistry, 3rd edn. Wiley, Hobcken, pp 1038–1041
32. Russel M, Model P (1988) In: Calendar R (ed) The bacteriophage, vol 2. Plenum Press, New York, p 375
33. Russel M (1993) J Mol Biol 231:689
34. Marciano DK, Russel M, Simon SM (1999) Science 284:16
35. Roth TA, Weiss GA, Eigenbrot C, Sidhu SS (2003) J Mol Biol 322:357
36. NakashimaY, Frangione B, Wiseman RL, Konigsberg WH (1981) J Biol Chem 256:5797
37. Henry GD, Sykes BD (1990) Biochem Cell Biol 68:318
38. Peelen SJCJ, Sanders JC, Hemminga MA, Marsh D (1992) Biochemistry 31:2670
39. Li Z,Glibowicka M, Joensson C, Deber CM (1993) J Biol Chem 268:4584
40. Deber CM, Khan AR, Li Z, Joensson C, Glibowicka M, Wang J (1993) Proc Natl Acad Sci USA 90:11648

41. Williams KA, Glibowicka M, Li Z, Li H, Khan AR, Chen YMY, Wang J, Marvin DA, Deber CM (1995) J Mol Biol 252:6
42. Georgopoulos CP, Hendrix RW, Kaiser AD, Wood WB (1972) Nat New Biol 239:38
43. Sternberg N (1973) J Mol Biol 76:25
44. Georgopoulos CP, Hendrix RW, Casjens SR, Kaiser AD (1973) J Mol Biol 76:45
45. Georgopoulos CP, Hohn B (1978) Proc Natl Acad Sci USA 75:131
46. Tilly K, Murialdo H, Georgopoulos C (1981) Proc Natl Acad Sci USA 78:1629
47. Smith GP (1985) Science 228:1315
48. van Wezenbeck PMGF, Hulsebos TJM, Schoenmakers JGG (1980) Gene 11:129
49. Beck E, Zink B (1981) Gene 16:35
50. Hill DF, Petersen GB (1982) J Viol 44:32
51. Smith GP, Scott JK (1993) Methods Enzymol 217:228
52. Winter G, Griffith AD, Hawkins RE, Hoogenboom HR (1994) Annu Rev Immunol 12:173
53. Clackson T, Wells JA (1994) Trends Biotechnol 12:173
54. Hoogenboom HR (1977) Trends Biotechnol 15:62
55. Iannolo G, Minenkova O, Petruzzelli R, Cesareni G (1995) J Mol Biol 248:835
56. Malik P, Terry TD, Bellintani F, Perham RN (1998) FEBS Lett 436:263
57. Gao C, Mao S, Lo CHI, Wirshing P, Lerner RA, Janda K (1999) Proc Natl Acad Sci USA 96:6025
58. Bass S, Green R, Wells JA (1990) Proteins 8:309
59. Breitling F, Dubel S, Seehaus T, Klewinghaus I, Little M (1991) Gene 104:147
60. Russel M, Model P (1986) J Biol Chem 261:14997
61. Brabas CF III, Burton DR, Scott JK, Silverman GJ (eds) (2001) Phage display: a laboratory manual. Cold Spring Harbor Laboratory Press, New York
62. Dunn IS (1995) J Mol Biol 248:497
63. Fabian MA, Biggs WH III, Treiber DK, Atteridge CE, Azimioara MD, Benedetti MG, Carter TA, Ciceri P, Edeen PT, Floyd M, Ford JM, Galvin M, Gerllach JL, Grotzfeld RM, Herrgard S, Insko DE, Insko MA, Lai AG, Lelias JM, Mehta SA, Milanov Z, Velasco AM, Wodicka LM, Patel HK, Zarrinka PP, Lockhart DJ (2005) Nat Biotechnol 23:329

Part II
Detection and Characterization Technology

Adv Biochem Engin/Biotechnol (2010) 119: 47–61
DOI: 10.1007/10_2008_41
© Springer-Verlag Berlin Heidelberg 2009
Published online: 27 March 2009

A Review on: Atomic Force Microscopy Applied to Nano-mechanics of the Cell

Atsushi Ikai

Abstract Since its introduction in 1986, AFM has been applied to biological studies along with its widespread use in physics, chemistry and engineering fields. Due to its dual capabilities of imaging nano-materials with an atomic level resolution and of directly manipulating samples with high precision, AFM is now considered an indispensable instrument for nano-technological researchers especially in physically oriented fields. In biology in general, however, and in biotechnology in particular, its usefulness must be critically examined and, if necessary as it certainly is, further explored from a practical point of view. In this review, a new trend of applying AFM based technology to elucidate the mechanical basis of the cellular structure and its interaction with the extracellular matrix including cell to cell interaction is reviewed. Some of the recent studies done by using other force measuring or force exerting methods are also covered in the hope that all the nano-mechanical work on the cellular level will eventually contribute to the emergence of the mechano-chemical view of the cell in a unified manner.

Keywords Atomic force microscopy, Force curves, Molecular fracture mechanics, Nano-biomechanics, Young's modulus,

A. Ikai
Graduate School of Bioscience and Biotechnology, Tokyo Institute of Technology
4259 Nagatsuta, Midori-ku, Yokohama, 226-8501, Japan
e-mail: ikai.a.aa@m.titech.ac.jp

Contents

1 Introduction

Atomic force microscope (AFM) was introduced in 1986 by Binnig et al. as a new member of the scanning probe microscope family [1] following the invention of the scanning tunneling microscope (STM) in 1982 [2]. Compared with an STM which required an electrical conducting sample, the AFM could be operated on both conducting and nonconducting samples with imaging and force detection capabilities. AFM was welcomed by biologically oriented researchers because of this quality since most of the biological materials are electrically nonconductive and difficult to be studied by an STM. Although the operating principle of the AFM has been explained in detail in the literature [3–5], a brief introduction is given here with an emphasis on the potential benefit and difficulty in its application to nano-biotechnological specimens.

The heart of the AFM is in the cantilever probe which is a thin rectangular or triangular wafer made of either silicon or silicon nitride (Si_3N_4) and with approximate dimensions of: 100, 30 and 1 μm in, respectively, length, width and thickness. The cantilever has a built-in stylus of pyramidal shape with dimensions 4–5 μm both of the width at the base and the length. The tip of the pyramidal shaped stylus has an effective radius of 5–50 nm at its apex corresponding to the approximate radius of globular protein molecules. For imaging, samples must be immobilized on a solid surface and the sample-probe distance is reduced until they make a slight mutual contact so that the stylus and therefore the cantilever is pushed upward. By keeping the slight upward deflection of the cantilever, thus constantly applying a small force called the set-point force to the sample, the stylus-cantilever system raster scan over the two-dimensional surface of the sample and the up and down movement of the cantilever is recorded on the computer to reproduce an image of the sample surface contour. This is the basic contact mode of AFM operation. The small force which is constantly applied to the sample from the cantilever has no visible effect to solid samples and therefore to the images obtained, but when a

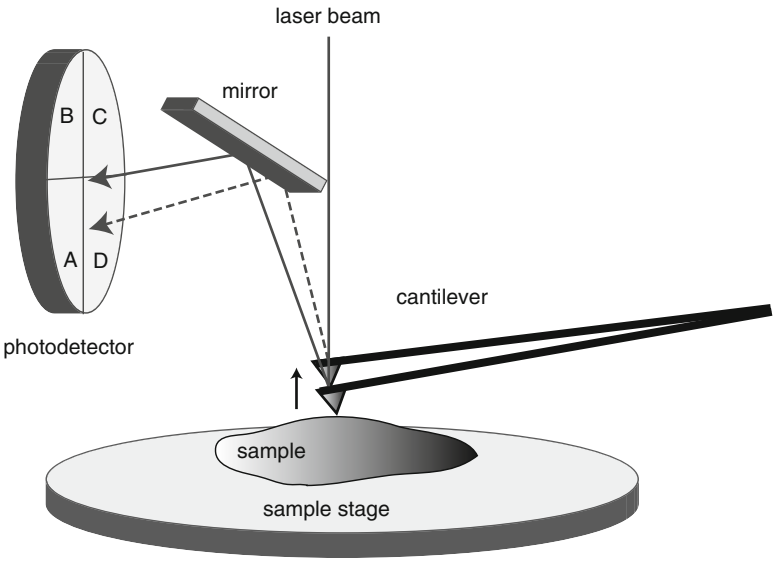

Fig. 1 Working principle of AFM. The cantilever is deflected according to the force between the probe and the sample. The deflection is monitored by the change in the direction of the laser beam reflected from the back of the cantilever. The change is proportional to the change in the tangent of the cantilever. The photodiode detector converts the change in the reflected beam into the differential output of the voltage converted from the photocurrent

soft sample is raster scanned with a similar level of the set-point force, it is likely that the sample would be damaged both vertically and laterally. An improvement has been obtained to successful imaging of biological samples by the introduction and application of Tapping Mode™ [6]. Principal features of AFM operation is given in Fig. 1.

Both imaging and force measurement studies flourished in the early years of the application of AFM based technologies to biological samples. Several review articles on the early applications of AFM to biological and other soft materials are cited [7–10]. A particular difficulty has been recognized from early days in an effort to achieve the same quality and resolution in imaging biological soft samples as those for inorganic hard materials. Biological samples such as cells and proteins are several thousand times softer than inorganic materials in terms of Young's modulus (Y). For example, live cells have Young's modulus in the range of 10^3–10^5 Pa (pascal) and native proteins from 10^8 to 10^9 Pa; while that of inorganic materials ranges between 10^9 and 10^{12} Pa. In the Tapping Mode, the cantilever is constantly vibrated near its resonance frequency and with a large amplitude of nearly 10 nm while it is raster scanned over the sample surface to keep the contact time between the probe and the sample to a minimum to reduce both vertical and lateral damage.

Besides imaging, AFM has the capability of measuring the force exerted on the cantilever from the nano-sized sample material. For example, if the probe is pushed further into the sample beyond the set-point force for imaging, the sample would

be indented but, at the same time, the cantilever would be deflected upward unless the sample is a nonviscous fluid. A comprehensive review on the force measurement application of AFM has been published by Butt et al. [11].

The relative depth of indentation and the magnitude of cantilever deflection depend on the relative stiffness of the former and the latter. After converting the cantilever deflection (d) into the force of compression by multiplying d with the spring constant of the cantilever (k), we obtain the relationship between the compressive force and the sample indentation. Such a relationship is widely used in macroscopic mechanics to obtain Young's modulus (elastic modulus) of sample materials by applying theoretical results of the Hertz model and its expansion by Sneddon [12] and Tatara [13]. The fracture mechanics of globular proteins and virus particles has been studied by applying the theoretical results of macroscopic mechanics as described [14–17].

By applying the same principle to the tensile force, the sample may be stretched from its original shape, giving rise to a force–extension (F–E curve) relationship. In this manner, AFM has been applied to measure (1) the internal rigidity of single protein molecules by the so-called "mechanical unfolding" experiments [18–22], (2) unbinding force of pair-wise interacting complexes such as biotin–avidin, antigen–antibody, ligand–receptor, etc. [23–26], (3) up-rooting force of intrinsic membrane proteins from the biomembrane [27–29], and (4) tethering force of lipid nanotubes from the surface of cells and liposomes [30–33].

2 Atomic Force Microscopy and Its Recent Advances

In addition to the mode of operation of AFM given above, a recent advance in noncontact mode of AFM operation and introduction of a high speed scanning AFM apparatus must be mentioned for future technology in the biomedical field [34–36].

While both contact and Tapping Mode AFM work in the repulsive interaction regime in the Lennard–Jones potential diagram, a noncontact AFM detects the attractive interaction between the sample and the probe [34]. Since the attractive interaction has less pronounced dependency on the sample–probe distance, a special technique is needed to detect the cantilever deflection. Instead of directly measuring the angle of cantilever deflection as routinely done in the contact mode, in the nc-AFM, the cantilever is vibrated at its resonance frequency with a small amplitude of less than 1 nm. As the probe enters the attractive force regime and it approaches the sample surface, the resonance frequency of the cantilever becomes slightly less (a few to a few tens of Hz, which effectively reduces the spring constant of the cantilever) which is detected accurately by a dedicated lock-in amplifier. In this mode of operation, a vacuum AFM now has better resolution than a contact mode AFM. Under liquid conditions, the noncontact AFM is still difficult to be operated due to a dramatic decrease in the Q-value of cantilever vibration but improvement will come in the near future.

A normal AFM takes a few minutes to a few tens of minutes to complete one round of raster scans with 256 × 256 imaging points, but recently Ando et al. reported

construction of a fast imaging of AFM which can complete a similar imaging within less than 100 ms enabling the dynamic imaging of actual movement of several motor proteins and other dynamic systems [36]. There is a big potential in fast imaging AFM to visualize the dynamics events in biological systems.

Since molecular level studies of stretching single molecules of proteins and DNA and unbinding force of ligand–receptor pairs have been extensively reviewed in recent years, it will not be treated here because of lack of the space. Interested readers are referred to references [11, 18–26].

3 Fracture Mechanics of Proteins and Viruses

3.1 Compression of Single Protein Molecules

The rigidity of a protein molecule can be evaluated by compressing it. When two spheres are compressed against each other with a force normal to the plane of contact, the spheres will be flattened in the contact region and the degree of flattening depends on the mechanical rigidities (Young's modulus and Poisson's ratio) of the materials making up the two spheres. The resulting compression curves can be analyzed according to the theoretical result of the Tatara model which is an extension of the classical Hertz model to yield Young's modulus after assuming an appropriate value for Poisson's ratio [13].

By applying the Tatara model to the compression curve of carbonic anhydrase II, Afrin and Ikai found that nearly 50% of the compression curve was fitted by using a constant value of Young's modulus (Y), whereas fitting of the Hertz model was possible only in the initial 10% of the compression curve as shown in Fig. 2.

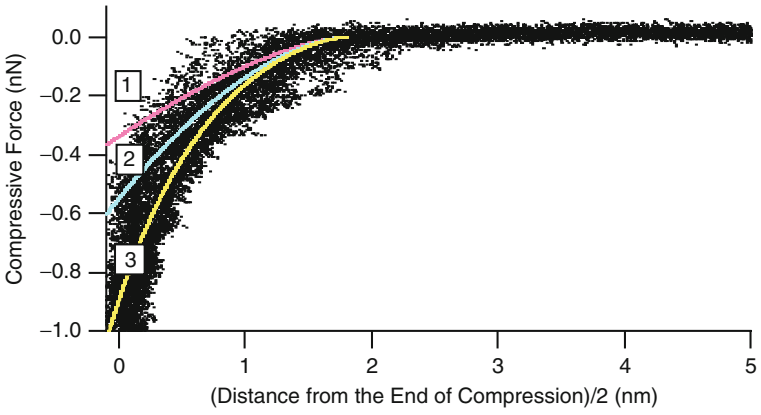

Fig. 2 Compression curve of bovine carbonic anhydrase II. *Curve 1*: Hertz model fitting; *curve 2*: Tatara model fitting; *curve 3*: exponential fitting. Reproduced from [14] with permission

Furthermore, they found that a forced fitting of the Hertz model to 50% of the curve required a 2–3 times larger value of Y [14].

3.2 *Fracture Mechanics of Virus Particles*

The fracture mechanics of virus particles has been studied by several groups using AFM. Kol et al. [15] studied the mechanical properties of murine leukemia virus particles before and after its maturation. Fig. 3. shows the result of their force measurement together with that of the finite element simulation.

The virus particle is made of self-assembly of Gag protein molecules into a spherical particle of radius 50 nm covered by an outermost lipid bilayer membrane. According to Kol et al., after budding from the cell, virus particles undergo a maturation step essential for infectivity. Maturation is induced by the cleavage of the Gag proteins by a virus-encoded protease into at least three products. Immature particles are far more stable under mild detergent treatment than are mature particles. Kol et al. therefore compared the stiffness of immature and mature virus particles. The indentation force for immature particles were nonlinear against the depth of indentation but those for mature particles were almost linear. The deformation mechanics of the two types of particles was simulated by finite element analysis with estimated Young's moduli of 0.233 and 1.027 GPa, respectively, for mature and immature particles cited paper. The change in the stiffness of the particle was explained by the detachment of processed Gag proteins from the outer membrane

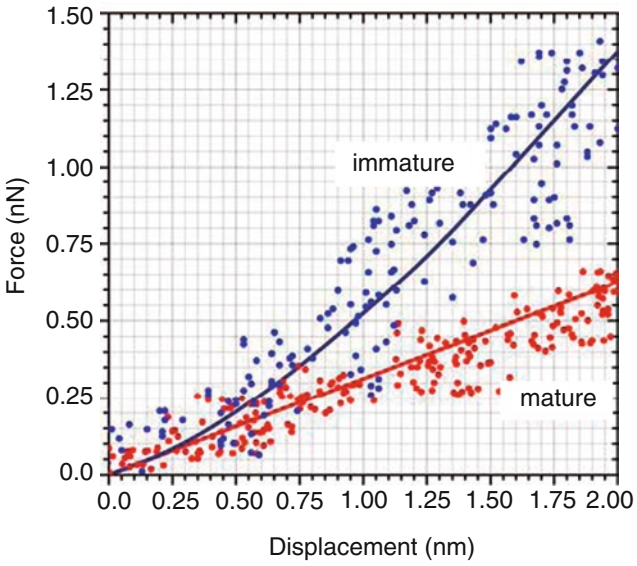

Fig. 3 Indentation curves of AFM probe into mature and immature virus particles. Reproduced from [15] with permission

forming an inner core structure. The outer protein layer of a mature particle was therefore much thinner than that of an immature particle. This maturation softening of virus particles was considered as a necessary process for infectious processes.

Michel et al. investigated the change in rigidity of cowpea chlorotic mottle virus in both empty and RNA filled state [16] and found that the latter is more rigid than the former. The indentation force curves were linear and reversible against the compressive force of about 1 nN applied from the AFM probe, but then there was a sudden decrease in force signifying a fracture event. The whole process was simulated by finite element analysis with Young's modulus of 140 and 190 MPa for the empty and RNA filled viruses.

Schmatulla et al. studied the rigidity of tobacco mosaic virus by treating it as a uniform beam with local loads [17]. The experimental results of both methods can be described when we attribute a Young modulus of 6 ± 3 GPa to the virus..

4 Cellular Level Work

4.1 Local Stiffness of the Cell Revealed by Mapping of Young's Modulus

When AFM is applied to the cellular level work, one of the most prominent advantages is in its capability to image and manipulate live cells in a culture medium with molecular level precision. Imaging of cells with AFM gives their three-dimensional contours with the possibility of repeatedly imaging them with intervals of a few minutes, enabling the researchers to create a movie of the detailed movement of the cell. Combined use of AFM with optical microscopes, such as a phase contrast, fluorescence, and confocal microscopes has become very popular and many commercially available AFMs are now equipped with specially fitted optical microscopes.

Imaging of a live cell with an AFM reveals the detailed architecture of intracellular structures such as cytoskeletons or stress-fibers as in a typical example image given in Fig. 4 [37].

Much effort has been put into the visualization of membrane proteins with molecular resolution but, regrettably, it is still not feasible to image molecular details of the cell membrane. Due to an extreme flexibility of the phospholipid bilayer which comes from a low value of its bending modulus, the membrane deforms so easily under the AFM probe that the latter visualizes any submembrane structures with higher rigidity than the lipid membrane itself. The phospholipid bilayer membrane has, however, a very large bulk two-dimensional modulus (i.e., a very low lateral compressibility) and, as a result, it sustains the compressive force of the AFM probe without yielding to form a hole.

The rigidity of a live cell under physiological conditions was probed by several groups in the early stage of AFM application in the biological field. Kawabata and

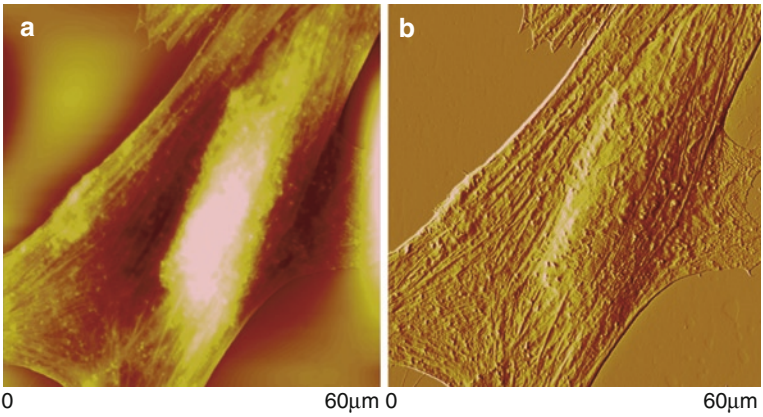

Fig. 4a,b AFM image of a live fibroblast cell in culture medium. (**a**) Height image and (**b**) error signal image which roughly corresponds to the derivative of the height image. Courtesy of Umme Salma Zohora

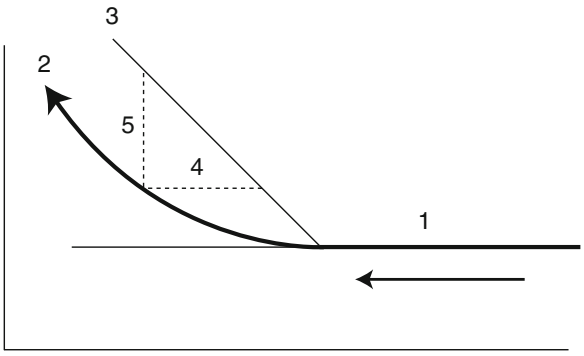

Fig. 5 Schematic view of indentation force curve of AFM. *Curve 1*: approach from distance; *curve 2*: indentation into a soft sample; *curve 3*: approach curve on a solid surface; *curves 4 and 5*: depth of indentation

his colleagues studied the distribution of stiffness over a cultured cell and a group of cells [38–39]. In principle, an AFM probe is lowered onto a targeted cell in a culture medium and, after the contact with the cell surface, it is further pushed on to form an indentation to the cell. The resulting force curve, which looked like the one given in Fig. 5, was analyzed by applying equations used in macroscopic mechanics of materials to obtain a numerical value of the elastic modulus.

In particular, equations derived by Sneddon for three different types of axi-symmetric probes are widely used [12]. In the following formulae, F, Y, I and ν are, respectively, force, Young's modulus, depth of indentation, and Poisson's ratio:

$$F = \frac{2Ya}{(1-v^2)}1 \tag{1}$$

for a flat probe of radius of a, and

$$F\frac{2Y\tan\theta}{\pi(1-v^2)}\ I^2 \tag{2}$$

for a conical probe with an opening angle of θ. Finally

$$F\frac{4}{3}\frac{Y\sqrt{R}}{(1-v^2)}I^{3/2} \tag{3}$$

for a spherical probe with a radius of R.

Sneddon's equations were derived on the assumption that, compared to the size of indenting probes, the sample is semiinfinitely large, meaning it occupies a half space, has a perfectly flat surface, and is homogeneous and isotropic. Such conditions are never met when a live cell is the specimen but, due to the lack of more appropriate equations, (1)–(3) are widely used to obtain at least an estimate of the stiffness of live cells in terms of Young's modulus, Y.

It is especially meaningful to have a numerical estimate of Young's modulus when its distribution over the cell surface or the difference in stiffness among a population of cells is to be studied. Kawabata and his colleagues reported a distribution of Y over a single live cell and its time-dependent change over a period of several hours. According to their results, the stiffness was high where stress fibers were visualized and it was low over the nucleus.

4.2 *Force Curves Obtained by Pulling Membrane Proteins*

Instead of indenting the live cell surface, Afrin et al. tried to pull out intrinsic membrane proteins from fibroblasts [27, 28]. They first applied an AFM probe which was coated with covalent cross-linkers so that, when it touched the live cell surface, covalent bonds between the cross-linkers and the amino groups on the membrane proteins were formed. When they pulled up the probe from the cell surface, they observed a prolonged extension of force curves up to a few μm which was ruptured with a force of approximately 450 pN. Since a larger force was expected to break a covalent bond, the observed rupture force was assigned to the extraction force of intrinsic membrane proteins.

In another study on red blood cells, they used both AFM probes coated with lectins, wheat germ agglutinin and concanavalin A, and with covalent cross-linkers [40]. They found different characteristics for the force curves obtained by differently coated probes and attributed the difference to the different linkage status of membrane proteins to the cytoplasmic structure, such as the cytoskeleton.

Desmeules et al. pulled out the myristoyl acid anchored protein recoverin from the lipid bilayer yielding a force of 48 ± 5 pN as an average uprooting force [29].

4.3 Biomembrane Force Probe

AFM is not the only instrument capable of manipulating live cells. Evans et al. introduced the biomembrane force probe (BFP) and reported a large body of work on the effect of pulling out a part of the cell membrane after forming a contact with a latex bead which is attached to the force transducer of the apparatus [41]. In a typical experimental setup using BFP, the force transducer of BFP is a red blood cell which is immobilized at the end of a glass pipette by the suction pressure from the pipette and, as a result, spherically deformed. The sample cell is also immobilized at the end of another glass pipette which faces the first pipette on the opposite side. By approaching the sample cell and forcing it to make contact with the latex bead having specific ligand molecules against a certain type of membrane receptors on the sample cell, the sample cell is pulled away from the bead. Since the entire operation is recorded on video, the distance between the sample cell and the bead is readily available, and the force applied to the sample cell can be calculated from analyzing a small deformation of the spherical red blood cell (force transducer). The advantage of this apparatus over a conventional AFM is that, since the pipettes are arranged horizontally over an inverted optical microscope, processes accompanying the pullout operation can be visualized.

By using BFP, Evans and his colleagues made a number of new findings and measurements of physical parameters associated with membrane deformations.

Evans et al. have recently reported the dynamics of P-selectin detachment from the leukocyte interface [42]. They used BFP system to record both the video image of the entire process of pulling mechanics of P-selectin pulling and the level of tensile force as reproduced in Fig. 6.

4.4 Cell Traction Force Measurement

Locomotion of attached cells is a focus of interest for many research groups. At the molecular level, formation and destruction of adhesion points between the ventral side of the cell and the substrate is considered to be responsible for the movement of the cell. Wang et al. measured the traction force by placing the cell on microfabricated culture substrate made of soft acrylamide gel [43].

The deformation of the flexible substrate was converted to the traction force by the method of Butler et al. [44]. They tried to establish the relationship between the traction force in terms of force/extension area and the extension area and obtained a roughly linear relationship between the two parameters because there was an indication that the force over the extending parts of the cell was more relevant to its locomotion. The average force of traction was reported as approximately 1 nN/μm^2.

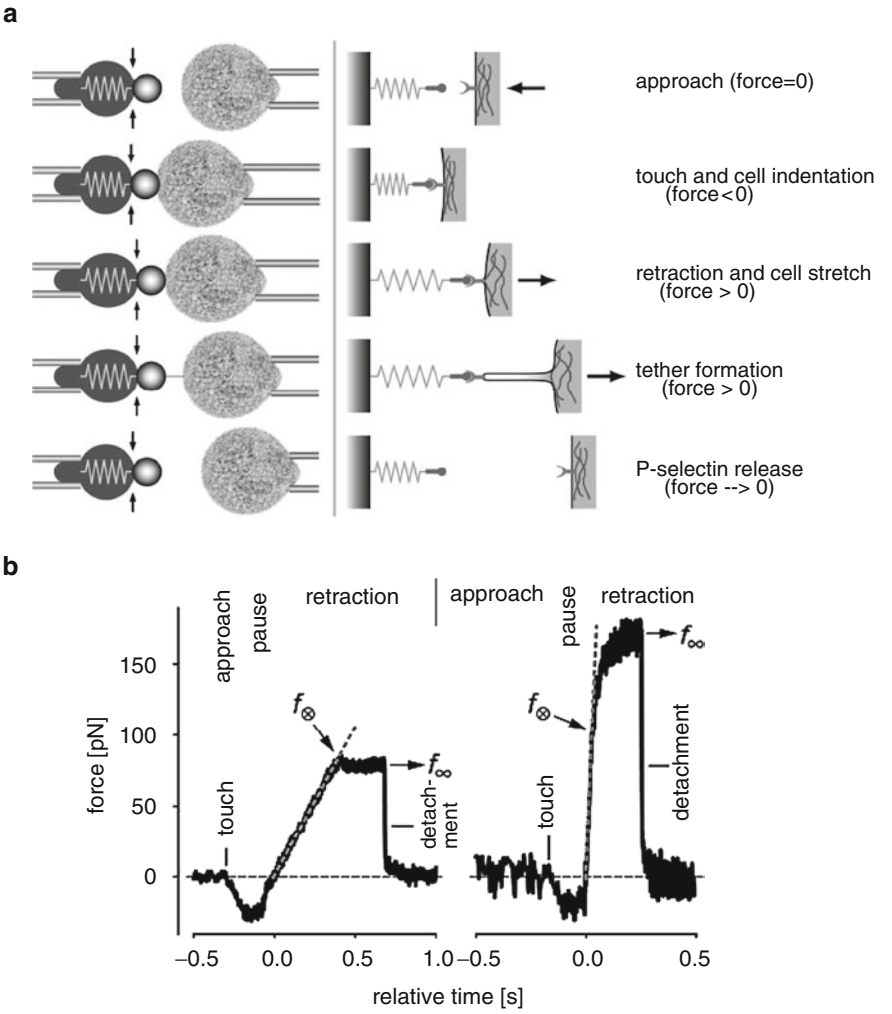

Fig. 6a,b Extraction of lipid tether and L-selection from the immobilized neutrophile using BFP. **a** Schematic representation of the pulling process of a lipid tether from the immobilized cell on the left by using BFP. **b** Force curves obtained from the process given in **a**. An initial linear increase of force against time (corresponding to the length of the tether) was followed by a nearly constant plateau force of tether elongation. Reproduced from [42] with permission

The mathematical procedure of solving the inverse problem of the Boussinesq solution to the effect of distributed traction force to the displacement of the traction field of the flexible substrate has been treated by Butler et al. [44] and Schwartz et al. [45]. The displacement field vector at position $\boldsymbol{r}$ of the two-dimensional surface

is given by the convolution of the traction force vector at position $\boldsymbol{r}'$ and the Green's function associated to the point traction on the surface which is

$$G_{ij} = \frac{3}{4\pi Er}\delta_{ij} + \left(\frac{x_i x_j}{r^2}\right) \tag{4}$$

where E and r are Young's modulus and the distance from the center of force application to the position of effect evaluation. x_i and x_j are two-dimensional coordinates in two-dimensional substrate ($1 \le i, j \le 2$). δ_{ij} is Kronecker's delta. By using the Green's function given above, the displacement field $u_i(r)$ is calculated by Eq. (5) where $F(r)$ is the stress field, i.e., the distribution of the intensity of the applied force over the two-dimensional substrate:

$$u_i(r) = \int \mathrm{d}r' G_{ij}(r - r')F_j(r') \tag{5}$$

In the Fourier transformed k space, it is a simple product of the Fourier transforms of the two functions. The inverse problem is treated within the realm of elastic mechanics as given by Landau and Lifshitz [46].

In order to apply tensile force to cells in culture, synthetic polymer film was also used. By using such films, Sawada et al. reported involvement of the protein, p130Cas (Crk-associated substrate) as a mechanosensor [47]. They prepared extensible substrate to grow cells on and applied tensile force to the cells on it and found that

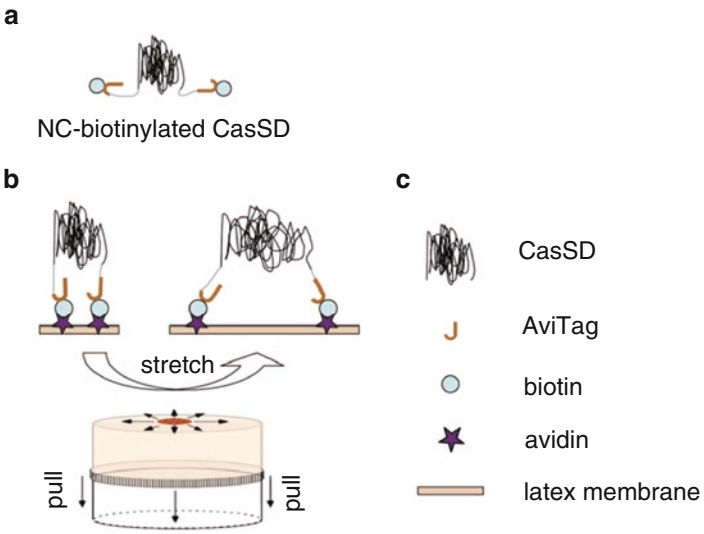

Fig. 7a–c Mechanical extension of CasSD on the stretchable substrate. **a** A construct of CasSD with biotin molecules at its two ends. **b** An extension of CasSD due to the stretching of the substrate. **c** Identities of the items in the figure. Reproduced from [47] with permission

the phosphorylation of Cas protein is enhanced in stretched cells. To explain this result, they postulated that Cas protein has an elastic structure which could be reversibly stretched out to accommodate binding of phosphorylation related proteins as indicated in Fig. 7.

In their previous report, Sawada and Sheetz showed that the Triton cytoskeleton itself binds the following proteins more strongly under stretched condition than in an unstretched state – paxillin, focal adhesion kinase, and p130Cas – whereas binding of vinculin is not affected and actin binding reduced [48]. Force measurement of Cas stretching has not been reported but their proposal of Cas with force sensitive structure and function as an important force sensor in mechanochemical information transduction is very interesting.

5 Result of Fast Scanning AFM on Biological Samples

Yokokawa et al. reported imaging of the fast process of binding of unbinding of GroES to GroEL in an ATP dependent manner by using the fast scanning AFM developed by Ando et al. [49]. Using this system, they visualized the GroES binding to and dissociation from individual GroEL with a lifetime of 6 s ($k = 0.17\ s^{-1}$). They also found that the ATP/ADP bound GroEL can change its conformation "from closed to open" without additional ATP hydrolysis.

6 Result of Nc-AFM Used on Biological Samples

Yamada reported the progress of high Q imaging by nc-AFM in liquid [50] of a two-dimensional array of polydiacetylene molecules. High resolution images of two-dimensional arrays of protein molecules are within the reach of nc-AFM operated in liquid media.

7 Perspectives

Imaging and force measurements using AFM and other nano-technological instruments are at a promising stage now. Many of the cellular information transfer pathways and the biochemical reactions associated with them have been elucidated and are waiting for a more integrated way of research on the cellular activities. Such study is necessary from both a fundamental biological point of view and that of biomedical applications. Improvement of AFM itself into fast scanning and noninvasive directions is sure to appeal to the many biologists wanting to visualize the dynamics of the biochemical processes of their special interest with superb temporal and spatial resolutions.

Mechanical measurement of biological structures is an important first step to a successful modeling of live cells and other higher level of life processes. AFM and other force devices will make vital contributions from various different angles.

Acknowledgment Financial assistance in the form of Grant-inAid to A.I. from JSPS (Creative Scientific Research: 19GS0418) is deeply appreciated.

References

1. Binnig G, Quate CF, Gerber CH (1986) Phys Rev Lett 56:930
2. Binnig G, Rohrer H, Gerber Ch, Weibel E (1982) Phys Rev Lett 49:57
3. Morris VJ, Kirby AR, Gunning AP (1999) Atomic force microscopy for biologists. Imperial College Press, London
4. Sarid D (1994) Scanning force microscopy. Oxford University Press, Oxford
5. Bonnel DA (2001) Scanning force microscopy and spectroscopy. Wiley-VCH, New York
6. Hansma HG, Sinsheimer RL, Groppe J, Bruice TC, Elings V, Gurley G, Bezanilla M, Mastrangelo IA, Hough PV (1993) Scanning15:296
7. Ikai A (1996) Surf Sci Rep 26:261
8. Hansma PK, Elings VB, Marti O, Bracker CE (1988) Science 242:209
9. Hansma HG, Kim KJ, Laney DE, Garcia RA, Argaman M, Allen MJ, Parsons SM (1997) J Struct Biol 119:99
10. Colton RJ, Baselt DR, Dufrene YF, Green JB, Lee GU (1997) Curr Opin Chem Biol 1:370
11. Butt HJ, Cappella B, Kappl M (2005) Surf Sci Rep 59:1
12. Sneddon IN (1965) Int J Eng Sci 3:47
13. Tatara Y (1989) J Eng Mater Tech 111:163
14. Afrin R, Alam MT, Ikai (2005) Protein Sci 14:1447
15. Kol N, Gladnikoff M, Barlam D, Shneck RZ, Rein A, Rousso I (2006) Biophys J 91:767
16. Ivanovska IL, de Pablo PJ, Ibarra B, Sgalari G, MacKintosh FC, Carrascosa JL, Schmidt CF, Wuite GJ (2004) Proc Natl Acad Sci USA 101:7600
17. Schmatulla A, Maghelli N, Marti O (2007) J Microsc 225:264
18. Mitsui K, Hara M, Ikai A (1996) FEBS Lett 385:29
19. Rief M, Gautel M, Oesterhelt F, Fernandez JM, Gaub HE (1997) Science 276:1109
20. Carrion-Vazquez M, Oberhauser AF, Fisher TE, Marszalek Pe, Li H, Fernadez JM (2000) Prog Biophys Mol Biol 74:63
21. Muller DJ, Heymann JB, Oesterhelt F, Moller C, Gaub H, Buldt G, Engel A (2000) 1460:27
22. Alam MT, Yamada T, Carlsson U, Ikai A (2002) FEBS Lett 519:35
23. Florin EL, Moy VT, Gaub HE (1994) Science 264:415
24. Merkel R, Nassoy P, Leung A, Ritchie K, Evans E (1999) Nature 397:50
25. Sekiguchi H, Arakawa H, Taguchi H, Ito T, Kokawa R, Ikai A (2003) Biophys J 85:484
26. Lee CK, Wang YM, Huang LS, Lin S (2007) Micron 38:446
27. Afrin R, Arakawa H, Osada T, Ikai A (2003) Cell Biochem Biophys 39:101
29. Desmeules P, Grandbois M, Bondarenko VA, Yamazaki A, Salesse C (2002) Biophys J 82:3343
30. Song J, Waugh RE (1990) J Biomech Eng 112:235
31. Brochard-Wyart F, Borghi N, Cuvelier D, Nassoy P (2006) Proc Natl Acad Sci USA 103:7660
32. Marcus WD, McEver RP, Zhu C (2004) Mech Chem Biosyst 1:245
33. Hosu BG, Sun M, Marga F, Grandbois M, Forgacs G (2007) Phys Biol 4:67
34. Morita S, Wiesendanger R, Meyer E (2002) Noncontact atomic force microscopy. Springer, Berlin Heidelberg New York
35. Seo Y, Park H, Moon JB, Jhe W (2000) Appl Phys Lett 77:4274

36. Ando T, Kodera N, Naito Y, Kinoshita T, Furuta K, Toyoshima YY (2003) ChemPhysChem 4:1196
38. Haga H, Sasaki S, Kawabata K, Ito E, Ushiki T, Sambongi T (2000) Ultramicroscopy 82:253
39. Mizutani T, Haga H, Kawabata K (2007) Acta Biomater 3:485
40. Afrin R, Ikai A (2006) Biochem Biophys Res Commun 348:238
41. Evans E, Heinrich V, Ludwig F, Rawicz W (2003) Biophys J 85:2342
42. Evans E, Heinrich V, Leung A, Kinoshita K (2005) Biophys J 88:2288
43. Wang N, Ostuni E, Whitesides GM, Ingber DE (2002) Cytoskeleton 52:97
44. Butler JP, Tolic-Norrelykke IM, Fabry B, Fredberg JJ (2002) Am J Physiol Cell Physiol 282:C595
45. Schwarz US, Balaban NQ, Riveline D, Bershadsky A, Geiger B, Safran SA (2002) Biophys J 83:1380
46. Landau LD, Lifshitz EM (1986) Theory of elasticity, 3rd English edn. Butterworth-Heinemann, Cambridge
47. Sawada Y, Tamada M, Dubin-Thaler BJ, Cherniavskaya O, Sakai R, Tanaka S, Sheetz MP (2006) Cell 127:1015
48. Sawada Y, Sheetz MP (2002) J Cell Biol 156:609
49. Yokokawa M, Wada C, Ando T, Sakai N, Yagi A, Yoshimura SH, Takeyasu K (2006) EMBO J 25:4567
50. Yamada H (2007) In: Morita S (ed) Roadmap of scanning probe microscope, chap 13. Springer, Berlin Heidelberg New York, p 101

Adv Biochem Engin/Biotechnol (2010) 119: 63–78
DOI: 10.1007/10_2008_42
© Springer-Verlag Berlin Heidelberg 2009
Published online: 1 August 2009

Design, Synthesis, and Biological Application of Fluorescent Sensor Molecules for Cellular Imaging

Kazuya Kikuchi

Abstract Cellular imaging has achieved many new biological findings, among them GFP and other fluorescent proteins and small molecule based fluorescent sensors have been widely used, especially in the last decade. The design concept and application of chemical sensors are described, these being FRET based sensors and Zn^{2+} sensors.

Fluorescence resonance energy transfer (FRET) has been used extensively as the designing principle for fluorescent sensor molecules. One of the most significant advantages of designing sensor molecules with FRET modulation is that it can enable ratiometric measurement in living cells, which reduces the artifact from microscopic imaging systems. The design strategy for the development of small molecular FRET sensors is described in terms of avoiding close contact of donor fluorophore and acceptor fluorophore in aqueous solution. Furthermore, a strategy to design FRET sensors with modulating overlap integrals of donor and acceptor is introduced.

Numerous tools for Zn^{2+} sensing in living cells have become available in the last 8 years. Among them, fluorescence imaging using fluorescent sensor molecules has been the most popular approach. Some of these sensor molecules can be used to visualize Zn^{2+} in living cells. Some of the biological functions of Zn^{2+} were clarified using these sensor molecules, especially in neuronal cells, which contain a high concentration of free Zn^{2+}.

Keywords Imaging, Fluorescence, Microscope, Zinc, FRET

K. Kikuchi
Department of Materials and Life Sciences, Graduate School of Engineering,
Osaka University, 2-1 Yamada-oka, Suita City, 565-0871 Osaka, Japan
e-mail: kkikuchi@mls.eng.osaka-u.ac.jp

Contents

1 Introduction

One of the great challenges in the postgenome era is to clarify the biological significance of intracellular molecules directly in living cells. If we can visualize or manipulate a molecule in action, it is possible to acquire biological information, which is unavailable if we deal with cell homogenates. One possible approach is to design and synthesize chemical sensors that can convert biological information into chemical reactions that are easily monitored. For this purpose, fluorescence sensor molecules for intracellular messengers have been developed and successfully applied to living cells.

2 Why Ratiometric Imaging for Cellular Application is Important

Fluorescent sensor molecules for imaging cellular molecules have become a hot topic in chemical biology research during the last two decades [1–3]. During this time a lot of sensor molecules were reported for biological applications and were also commercialized [4–7]. A fluorescent sensor is advantageous due to its high sensitivity; however, the fluorescence measurement by an increase of the fluorescence intensity without much shift of either excitation or emission wavelength can be influenced by many factors, such as the localization of the sensor, changes of environment around the sensor (pH, polarity, temperature, and so forth), emission collection efficiency, effective cell thickness in the optical beam, and changes in the excitation intensity. To reduce the influence of such factors, ratiometric measurement is utilized, namely, simultaneous recording of the fluorescence intensities at two wavelengths and calculation of their ratio [8]. This technique provides greater precision than measurement at a single wavelength, and is suitable for cellular imaging studies. To carry out ratiometric measurement, the sensor must exhibit a large shift in its emission or excitation spectrum after it reacts (or binds) with the target molecule.

There are two types of fluorescent sensor molecules for this wavelength shift; these are intramolecular charge transfer (ICT) mechanism based sensors [4, 9–11] and fluorescence resonance energy transfer (FRET) mechanism based sensors.

ICT was employed for designing a benzofuran based Ca^{2+} fluorescent sensor molecule, Fura-2, which was the first example for ratiometric imaging of cellular function. The ICT mechanism is described briefly as follows. When a fluorophore contains an electron-donating group (often an amino group) conjugated to an electron-withdrawing group, it undergoes ICT from the donor to the acceptor upon excitation by light. If the electron-rich terminal of the fluorophore (e.g., an amino group) interacts with a cation, a partial positive charge is photogenerated adjacent to the cation and that affects the absorption or excitation spectral wavelength of the fluorophore with an ICT excited state. So, a cation-induced blue shift is expected in the absorption or excitation spectra. The ratiometric imaging can be operated using this wavelength shift. Fluorescence emission spectra are less affected due to cation ejection during the excited state. However, there are several sensor molecules whose emission spectra were also shifted by the reaction with analytes. This approach is widely used because of the success of low-molecular-weight sensors in physiological monitoring of H^+, Ca^{2+}, Na^+, Mg^{2+}, and Zn^{2+}. The development of ICT based sensor molecules opened up the opportunities for a system of ratiometric imaging by microscope.

In this review, small molecular fluorescent senor molecules for ratiometric imaging based on FRET will be described in detail.

3 FRET Principle for Designing Sensor Molecules

FRET is one mechanism used as a basis to obtain a large shift in the spectral peak [12]. FRET is an interaction between the electronic excited states of two fluorophores, in which excitation energy is transferred from a donor to an acceptor without emission of a photon. When a fluorophore is excited, the energy level will reach S_1 after internal conversion, then it will return to ground state S_0 via an emission process, a non-radiative process, or via an energy transfer process. When the rate constants of donor emission and energy transfer processes were defined as k_f and k_T, the Förster equation has been accepted as in Eq. (1), where n is the refractive index of the medium, and N_A is Avogadro's number:

$$k_r = \{9{,}000(\ln 10)\kappa^2 J/128\pi^5 n^4 N_A r^6\} k_f, \tag{1}$$

Of these factors in Eq. (1), there are three which can be modulated by designing a small molecule based sensor molecule. These three factors are κ^2: orientation factor, J: overlap integral, and r: distance between donor and acceptor.

κ^2 is a factor describing the relative orientation in space of the transition dipoles of the donor and acceptor. κ^2 can lie between 0 and 4. When the donor and the acceptor are in perpendicular orientation, κ^2 is 0. When the donor and the acceptor

are in parallel orientation with parallel dipoles, κ^2 is 1. When the donor and the acceptor are in parallel orientation with parallel transition dipoles, κ^2 is 4. If both donor and acceptor are based on small molecule, which are randomly moving, κ^2 can be assumed to be 2/3. This value is used, in general, for synthetic small molecule based FRET sensors. To date, there has not been experimental confirmation of the dependence of the transfer rate on κ^2 [12].

J is a factor of spectral overlap of the donor emission and the acceptor absorption. As shown in Eq. (1), energy transfer rate, k_f, depends linearly on J. If the wavelength is expressed in nanometers, then J is in units of M^{-1} cm^{-1} $(nm)^4$. It is noteworthy that J is dependent on the absorption spectrum of acceptor, not on the excitation spectrum of the acceptor. This means that energy transfer occurs whenever the acceptor is in the range of RET, regardless of acceptor emission quantum yield. r is the distance between the donor and the acceptor. k_f depends on $1/r^6$, confirmed experimentally using different lengths of proline based polypeptides. This factor is the most used factor to control RET efficiency by designed small molecule sensors or GFP based RET sensors.

4 FRET Sensor Design Based on Donor and Acceptor Distance Changes

The distance at which the energy transfer is 50% efficient is defined as the Förster distance, R_0. R_0 depends on the combination of donor and acceptor, and it can be 2–10 nm for commonly used fluorophores. The energy transfer efficiency E_T can be expressed using r and R_0 according to Eq. (2):

$$E_r = R_0^6/(r^6 + R_0^6). \tag{2}$$

When the donor and acceptor are closer than R_0, the FRET efficiency is very high. When the distance becomes larger than R_0, the efficiency drastically decreases and become 0. The first FRET sensor based on changes of the donor-acceptor distance is reported in 1991 [13], using tetramer of cAMP dependent protein kinase scaffold. After the advent of an explosive numbers of GFP papers starting from 1994, Miyawaki et al. produced FRET sensors based on GFPs of two different colors [5, 14]. Among them, intracellular Ca^{2+} and protein phosphorylation status were successfully developed to lead to some new biological findings of their physiological functions. Recently, several ratiometric fluorescent sensors using FRET have been developed using these distance changes, such as the β-lactamase sensor CCF2 [15], membrane potential sensor [16], and the phosphodiesterase sensor CPFs [17–19]. They have all been based on the same principle, i.e., that FRET efficiency is dependent upon the donor-acceptor distance.

To design such sensors, it is necessary that the donor and acceptor should be located on opposite sides of an enzyme-cleavable structure. Before the enzyme cleavage, when the donor–acceptor distance is smaller than R_0, FRET efficiency is high; however, after the cleavage the distance will be infinite, resulting in no energy

transfer. Thus, by the enzyme cleavage, the measured fluorescence wavelength shifts to blue from acceptor emission to donor emission.

The developmental process of a ratiometric fluorescent sensor molecule for phosphodiesterase activity will now be introduced.

First, we intended to visualize caspase-3 activity during the induction of apoptosis [20]. Microscopic visualization of caspase-3-like activities in cells would provide valuable information about the apoptotic mechanism. However, DEVD-MCA and its derivatives [21], which are generally used to detect caspase-3-like activities, can only be used in cell-free systems, because DEVD-MCA is excited at 380 nm and autofluorescence of cells excited at around 380 nm interferes with measurements. In order to provide a fluorescent sensor with longer wavelength measurement, we designed and synthesized novel fluorescent sensors to allow direct visualization of caspase-3-like activity in cells. It is known that poly-ADP-ribose polymerase (PARP) is cleaved by caspase-3-like proteases (group II caspases) during apoptosis and the cleavage site sequence is –GDEVDGV– [22]. Using an oligopeptide containing –GDEVDGV–, we designed novel fluorescent sensors to detect the activities of caspase-3. Two different fluorophores were conjugated to the two terminals of the oligopeptide: donor fluorophore was conjugated to the N-terminal of the oligopeptide, and acceptor to the C-terminal. Lucifer yellow (LY) and carboxydichlorofluorescein (CDCF) were chosen as donors, and carboxytetramethylrhodamine (CTMR) and carboxy-X-rhodamine (CXR) as acceptors, based on their spectral characteristics. However, when we measured the fluorescence spectra of these compounds, the emissions of the donors were highly quenched. Presumably the acceptor absorbs the donor's energy, because the conformation of the peptide in aqueous solution would allow the donor and acceptor to be in close proximity. Therefore, we found that donor fluorophore and acceptor fluorophore should not be in close contact in aqueous solution if we want to make a fluorescence sensor molecule for ratiometric measurement.

This quenching mechanism can be explained in terms of ground-state complex formation [23]. It has been reported that the fluorescence quenching of the ground-state dye-to-dye complex formation is observed in various fluorophore pairs [20, 24, 25]. In general, if the fluorophores have the hydrophobic characteristics, they would form dye-to-dye close contact in aqueous environment and the fluorescence should be quenched [26, 27]. For practical use of peptide-based FRET sensors, it is necessary to employ conformationally constrained oligopeptides such as proline-containing oligopeptides as linkers of the donor and acceptor dyes [28]. In other words, there were no successful examples of FRET peptide sensors with conformationally flexible oligopeptides as linkers. If such FRET systems could be developed, they would be useful for assay of a wide range of proteolytic activities. So, in the second phase, the development of a conformationally flexible FRET system usable in an aqueous environment without quenching of the two dyes were intended [19].

Taking into consideration the above results, we set out to develop a phosphodiesterase fluorescent sensor molecule using a rigid linker by restricting the flexibility. Phosphodiesterases catalyze the hydrolysis of phosphodiester bonds and their substrates are nucleic acids and cyclic nucleotides [29]. Although phosphodiesterases have many important cellular roles, there is no effective method to monitor

their activity in real time with high sensitivity. For example, nucleotide pyrophosphatase/phosphodiesterases (NPPs) [30, 31], one group of phosphodiesterases, have been reported to be implicated in the regulation of various intra- and extracellular processes, including cell differentiation and motility, bone and cartilage mineralization, and signaling by nucleotides and insulin. Some important proteins categorized in NPPs such as PC-1 [32] and Autotaxin [33] have been the focus of much interest in recent years. Since NPPs consist of phosphodiesterase I (EC 3.1.4.1), the sensor for phosphodiesterase I activity will be a useful tool for investigating the role of NPPs. Berkessel and Riedl have developed fluorescence reporters for phosphodiesterase I activity, in which a naphthalene moiety acts as the fluorophore and an azobenzene moiety as the quencher [34]. These reporters fluoresce upon addition of phosphodiesterases, but have limitations for biological application because of their short excitation wavelength and weak fluorescence. Also, the change of fluorescence intensity is observed at one wavelength.

To obtain a ratiometric fluorescent sensor molecule for phosphodiesterase activity, the intramolecular FRET compounds (CPFs: Coumarin, Phosphate linked Fluoresceins) were designed and synthesized which have coumarin as a donor, fluorescein as an acceptor, and phosphodiester as a linker (Fig. 1) [17]. The R_0 of this RET pair was calculated as 4.8 nm, which is larger than the estimated distance of two fluorophores with used linkers, 3.0 nm. Ethylene was used as flexible linker and cyclohexane or phenyl group were used as rigid linker, which can prevent free movement of the fluorophores in aqueous solution, resulting in the hindrance of close contact of the two fluorophores. CPF1 with two ethylene linkers and CPF3 with one ethylene and one cyclohexane linker exhibited fluorescence quenching due to the dye-to-dye close contact. If the fluorophores are introduced intramolecularly with a flexible linker, they should form the ground state dye-to-dye close contact in an aqueous environment and the fluorescence should be quenched [20]. However, when CPF1 and CPF3 were dissolved in methanol, strong emission from fluorescein was observed. Thus, the close contact can only be observed in aqueous solution, in which hydrophobic interaction is not negligible. CPF2 with two cyclohexane linkers exhibited acceptor fluorescence due to FRET by hindering the close contact of the two fluorophores by the rigid linker (Fig. 2). So it is necessary that the structure of the sensor molecule is such as to prevent dye-to-dye close contact in an aqueous environment. This is noteworthy because, when we want to design sensor molecules

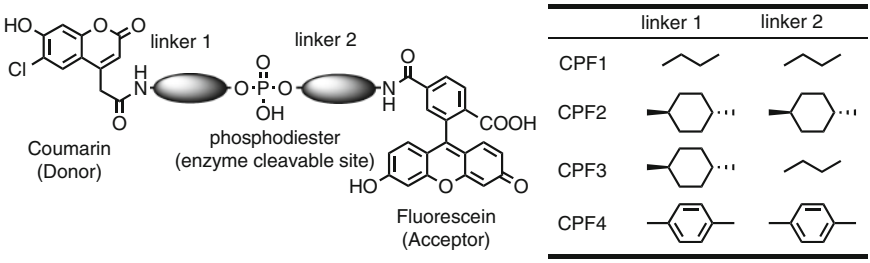

Fig. 1 Structures of CPFs, with different linkers

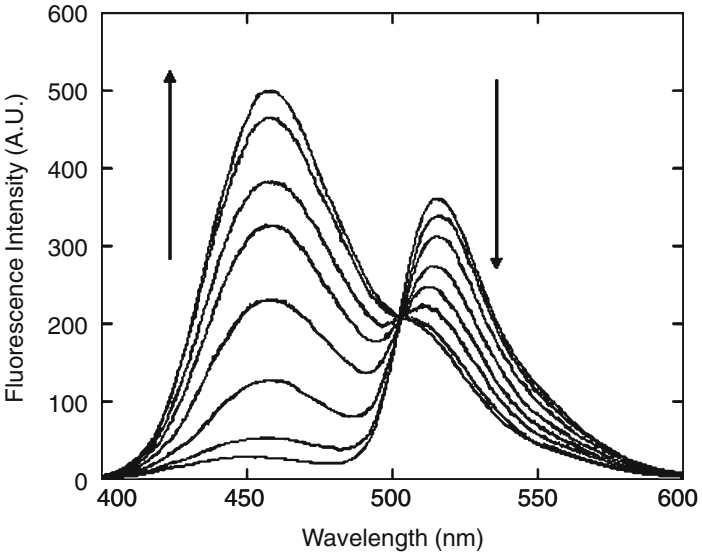

Fig. 2 The emission spectra of a 1.0 μM solution of CPF4. 0; 1, 5, 10, 15, 20, 30, and 45 min after addition of 0.05 u phosphodiesteraseI

for cellular application, we have to take into consideration the aqueous environment like cytosol. However, CPF2 was not hydrolyzed by phosphodiesterases due to the structural features of the molecule. Thus, it was also necessary that the molecule should be recognized as a substrate by phosphodiesterases. Then CPF4 was designed, which has two phenyl linkers and can be hydrolyzed by phosphodiesterases. The phenyl ring was employed because it has less steric hindrance than the cyclohexane. CPF4 satisfied both requirements (no close contact of fluorophores in aqueous environments and recognition as a substrate by the enzyme) and worked as a ratiometric fluorescent sensor molecule for phosphodiesterase activity.

5 FRET Sensor Design Based on Modulation of Spectral Overlap

As was discussed in the previous section, it is important to prevent quenching by hindrance of dye-to-dye close contact for the development of small molecule based FRET sensors. To expand the range of application of FRET-based fluorescent sensors we have utilized a novel approach to design sensors whose absorption characteristics are altered by enzymatic reaction. When this absorbance change was applied to the FRET acceptor, the overlap integral *J*, which acts as off/on switch of FRET, can be drastically changed by enzymatic reaction. As was discussed before, energy transfer rate is linearly related to *J*. So the modulation of *J* can enable FRET efficiency tuning [35].

FRET efficiency is dependent on the spectral overlap integral between the donor emission and acceptor absorption. We thought that if the acceptor absorption was dramatically changed by hydrolytic enzymes, FRET switching by spectral overlap integral would be possible. It was anticipated that fluorescein would be appropriate as such an acceptor, because it has two conformations (lactone form and quinoid form) with distinctly different absorption properties. Fluorescein in quinoid form has strong absorption at around 490 nm, whereas the lactone form has absorption only in the UV region. This lactone and quinoid transformation can be observed by both pH changes and esterification of phenolic hydroxyl group of xanthene ring; fluorescein can be lactone form in acidic pH and ester protection; on the other hand, it can be quinoid form at neutral pH and free phenolic acid. This lactone and quinoid transformation can be used as an on/off switch for FRET. If a coumarin derivative is chosen as the donor, there is a significant difference in the spectral overlap between the two forms of fluorescein (Fig. 3). So we proposed a novel ratiometric detection method for hydrolytic enzyme activity based on resonance energy transfer switching by spectral overlap integral.

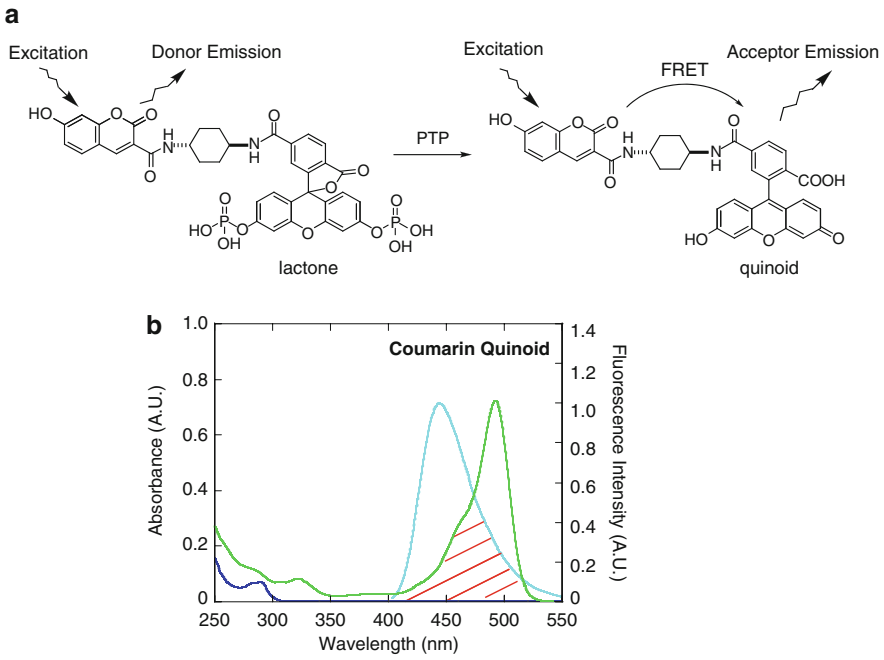

Fig. 3 **a** FRET-based detection mechanism by spectral overlap modulation. **b** Spectral overlap of the coumarin emission with the fluorescein absorption. *Light blue line*: normalized emission spectrum of 7-hydroxycoumarin-3-carboxylic acid, λ_{ex} = 400 nm; *dark blue line*: absorption spectrum of 10 μM 6-carboxy-fluorescein diacetate (lactone form); *green line*: absorption spectrum of 10 μM 6-carboxyfluorescein (quinoid form); *red shadow*: the overlap integral

Our method employs fluorescent sensors with 3′-*O*,6′-*O*-protected fluorescein linked to coumarin through an appropriate linker. As fluorescein is locked in the lactone form, it has no absorption band in the wavelength region of the coumarin emission, so there will be no overlap integral between the coumarin emission and fluorescein absorption. Thus, the fluorescein moiety cannot accept the excitation energy of the donor moiety, and the donor fluorescence can be observed. After cleavage of the protective groups by hydrolytic enzymes, the fluorescein structure changes to the quinoid form, which has a strong absorption in the coumarin emission region. Then acceptor fluorescence due to FRET will occur and so the sensors will exhibit a large red shift in their emission spectrum after the reaction with the target enzymes. So there is no difference in donor and acceptor distance, the overlap integral being the only factor which changes the energy transfer efficiency. To validate the proposed strategy, we designed and synthesized novel fluorescent compounds bearing phosphate groups in the fluorescein moiety.

As shown in Fig. 4, two compounds which have a coumarin moiety as the donor and a phosphorylated fluorescein moiety as the acceptor were designed and synthesized as candidate sensors for protein tyrosine phosphatase (PTP). There was little effective real-time method to monitor PTP activity in living cells. In compound **1**, two phosphate residues are introduced into the fluorescein moiety as enzyme-cleavable groups, and this moiety is linked to the coumarin donor through a cyclohexane moiety as a rigid linker. To investigate the effect of the linker structure on the fluorescence properties and the affinity for PTPs, an ethylene moiety was introduced as a flexible linker in compound **2**.

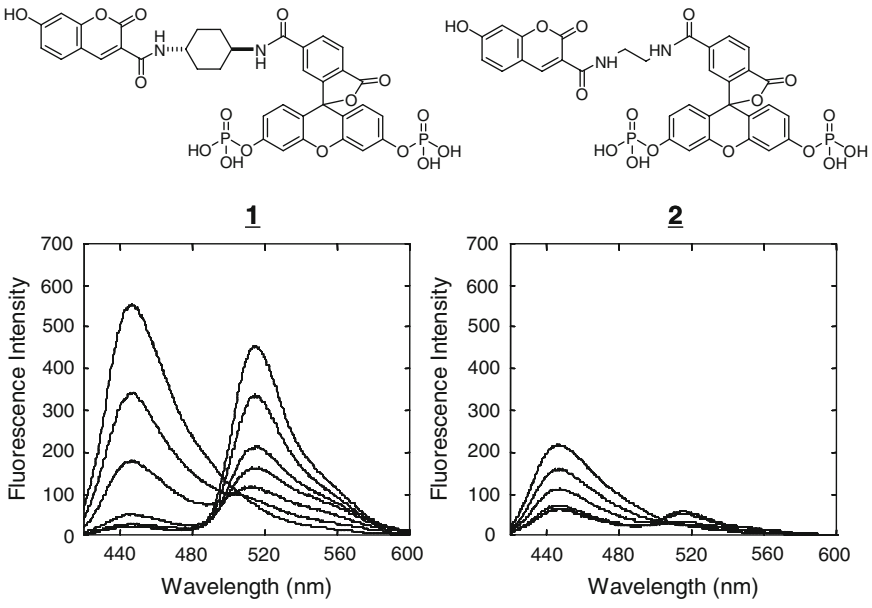

Fig. 4 The structures of **1** and **2**. The emission spectra of **1** and **2** after addition of PPT

The emission spectra of **1** in an aqueous buffer excited at the excitation wavelength of the coumarin donor exhibited the emission of the coumarin donor at around 450 nm before the enzymatic reaction. Addition of PTP1B, an intracellular PTP [36], to aqueous solutions of **1** resulted in a decrease in the donor fluorescence at around 450 nm and an increase in the acceptor fluorescence at around 515 nm, as shown in Fig. 4. The same spectral changes were also observed upon the addition of CD45, a receptor-like PTP [37]. These observations demonstrate that the proposed FRET switching by spectral overlap integral worked as expected. As the time-courses of the changes in the emission spectra show, the enhancement of the acceptor fluorescence was slower than the decrease of the donor fluorescence in **1** and **2**.

The absorption spectra of **1** and **2** measured in an aqueous buffer exhibited the donor absorption peak at around 400 nm. After the addition of PTP1B or CD45, the absorption peaks of the fluorescein moiety appeared and increased with time. In **1** and **2**, the absorption at around 450 nm was initially enhanced, then the absorption at around 500 nm was enhanced with a slight decrease of the absorption at around 450 nm. These observations in the fluorescence and absorption spectra indicate that the two phosphate groups of **1** and **2** are hydrolyzed in two steps through the monophosphate intermediates. Compound **2** with the flexible ethylene linker exhibited weaker fluorescence and longer wavelength of the absorption maxima compared to **1** with the rigid cyclohexane linker. These observations indicate that fluorescence quenching due to dye-to-dye close contact occurred in **2**. In other words, the cyclohexane linker is sufficiently rigid to prevent dye-to-dye close contact. After hydrolysis by PTPs, efficient FRET could be observed in **1**.

The compounds **1** and **3** showed that they are cleavable by cellular PTPs like PTP1B and CD45. This indicates that the rigid and bulky structure of the cyclohexane linker does not affect substrate binding.

Since compounds **1** have low membrane permeability due to their negative charges, we derivatized compound **1** to the membrane-permeable **1-AM**, which bears acetoxymethyl residues on the phosphate and hydroxyl groups. This is a commonly used strategy to induce drug administration efficiency. There is no negative or positive charge on compound **1-AM**, that it is more lipophilic, and so should permeate better into the cells, where it should be hydrolyzed to compound **1** by esterase in the cytosol. After cleavage of these ester groups, the dye will have negative charges so that it cannot cross the membrane again and thus stays in the cytosol. In order to determine whether compound **1-AM** can detect intracellular PTPs activity, it was used for ratiometric imaging in human umbilical vein endothelial cells (HUVEC). The fluorescence ratio of the acceptor and donor within the cells was monitored, in the presence and absence of sodium orthovanadate, a membrane-permeable PTP inhibitor. We observed a significant difference in the increase of the fluorescence ratio between inhibitor-treated and untreated cells. Thus, compound **1-AM** should be practically useful for the ratiometric measurement of intracellular PTP activity.

6 Zn^{2+} Sensing

Numerous tools for Zn^{2+} sensing in living cells have become available in the last 3 years. Among them, fluorescence imaging using fluorescent sensor molecules has been the most popular approach. Some of these sensor molecules can be used to visualize Zn^{2+} in living cells. Some of the biological functions of Zn^{2+} were clarified using these sensor molecules, especially in neuronal cells, which contain a high concentration of free Zn^{2+}. Biological imaging of specific molecules can provide direct information of molecular functions in living systems. The most important breakthrough for this purpose is to create selective and sensitive sensing tools. For the last 3 years, rapid improvements have been made in the development of Zn^{2+} specific sensor molecules. Among several approaches, a lot of fluorescent sensor molecules for the detection of chelatable Zn^{2+} were reported. Some of these sensor molecules like Zinquin [38], ZnAF-2 [39], FluoZin-3, FuraZin, and RhodZin-3 [40] were used to lead new biological findings of Zn^{2+} in living systems. Fluorescent sensor molecules, which allow visualization of cations or enzyme activity in living cells by fluorescence microscopy, are useful tools for studying biological systems.

Zinc (Zn^{2+}) is the second most abundant transition metal cation, and several grams of Zn^{2+} are present in the adult human body [41]. The biological function of Zn^{2+} has been reported for the protein bound form. However, free or loosely bound (labile, chelatable) Zn^{2+} exists at high concentration, especially in the brain, pancreas, and spermatozoa, and can be visualized by a fluorescent dye [42]. In the brain, labile Zn^{2+} is reported to exist at a concentration of several mM in the vesicles of presynaptic neurons, and is released by synaptic activity or depolarization, modulating the functions of certain ion channels and receptors [43]. Although the significance of Zn^{2+} in biological systems has been reported, its mechanisms of action are poorly understood.

Thus, fluorescent sensor molecules for detecting labile Zn^{2+} are needed to clarify the function of Zn^{2+}. A lot of fluorescent sensor molecules, which can selectively detect Zn^{2+}, have been reported in the last 3 years. Here, we will describe recent progress in the development of fluorescent sensor molecules for Zn^{2+}, especially in the light of biological application.

7 Fluorescent Sensor Molecules Based on Fluorescein Structure

The fluorescent sensor molecules with visible light excitation are advantageous over sensors with shorter excitation, because the excitation wavelength in the ultraviolet range may cause cell damage, and cellular autofluorescence may interfere with the measurement. Fluorescein is one of the most widely used fluorophores in

biological experiments and is advantageous in that it has a high quantum yield of fluorescence in aqueous solution, and its excitation wavelength is in the visible range. Thus, fluorescein can be a favorable fluorophore for Zn^{2+} fluorescent sensor molecules and several Zn^{2+} sensor molecules have been reported in the last couple of years, which can be used in biological applications. The intensity of the fluorescence can be controlled by photo-induced electron transfer (PeT) between the xanthene ring, which act as an electron acceptor and fluorophore, and the substituted benzoic acid moiety, which serves as electron donor [44].

As a receptor for Zn^{2+}, we chose TPEN (*N,N,N′,N′*-tetrakis (2-pyridylmethyl) ethylenediamine) derivatives (Fig. 5). We synthesized several compounds and ZnAFs, whose acceptor for Zn^{2+} *N,N*-bis(2-pyridylmethyl)ethylenediamine is directly attached to the benzoic acid moiety via the aliphatic amine nitrogen. The dyes exhibited good properties as Zn^{2+} sensor molecules, and are specific for Zn^{2+} against other heavy metal ions and several cations, that exist at high concentration in living cells such as Ca^{2+}, Mg^{2+}, Na^{+}, and K^{+}, which did not enhance the fluorescence intensity even at high concentration [45, 46]. We applied ZnAF-2 to monitor extracellularly released Zn^{2+} to clarify its function. Labile Zn^{2+} plays many physiologically important roles, especially in the central nerve system (CNS), where it is mainly stored in the synaptic vesicles of excitatory synapses, particularly the synaptic terminals of hippocampal mossy fibers (MFs), and is coreleased with neurotransmitters in response to synaptic activity. When high-frequency stimulation was

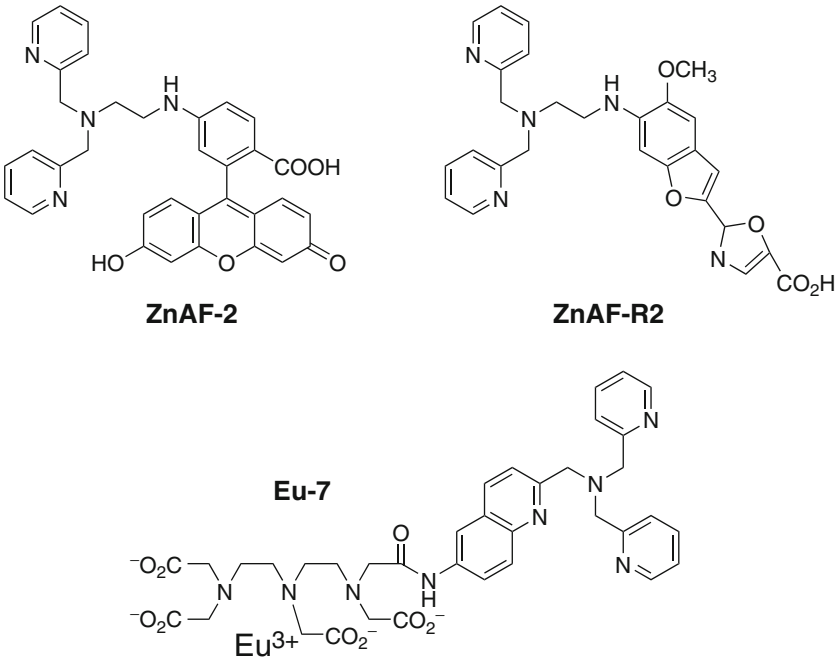

Fig. 5 The structures of fluorescent Zn^{2+} sensor molecules

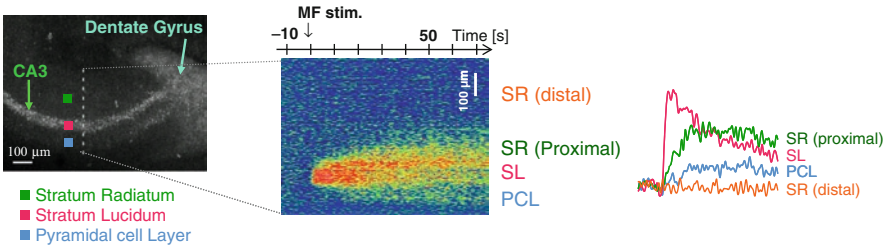

Fig. 6 Hippocampal release of Zn^{2+} in rat brain slice after electric stimulation of mossy fiber

delivered to the MFs, the concentration of extracellular Zn^{2+} was immediately elevated in the stratum lucidum (SL), and this was followed by a slight increase in the stratum radiatum adjacent to the stratum lucidum (SR proximal). Electrophysiological analyses revealed that NMDA-receptor-mediated synaptic responses ($fEPSP_{NMDA}$) in CA3 proximal stratum radiatum were inhibited in the immediate aftermath of MF activation and that this inhibition was no longer observed in the presence of a Zn^{2+}-chelating agent, which indicates that Zn^{2+} serves as a heterosynaptic mediator [39]. From these results, Zn^{2+} can be the only messenger substance that is released presynaptically and moves into postsynaptic neurons after release of other neurotransmitter like glutamate [47]. The combination experiments using ZnAF-2 also showed the following results of Zn^{2+} in the rat hippocampus (Fig. 6). The modulation of the Zn^{2+} affinity revealed that the released Zn^{2+} varies in the location of rat hippocampal slice [48]. Extracellular chelator of Zn^{2+} revealed that Zn^{2+} is released extracellular milieu by ischemia stimulation [49].

8 Other Types of Fluorescent Sensor Molecules

Recently other types of fluorescent probes have also been reported. One particularly interesting type is probes which enable ratiometric imaging. Ratiometric imaging is a technique that involves observing the changes in the ratio of fluorescence intensities at two wavelengths. Compared with the measurement of the fluorescence intensity at one wavelength, this method reduces artifacts by minimizing the influence of extraneous factors, such as the changes of the probe concentration and excitation light intensity. Based on the structure of Fura-2, novel fluorescent probes have been developed for ratiometric measurement of Zn^{2+}: FuraZin, whose chelator structure is that of FluoZin-1, and ZnAF-R2 (Fig. 5), whose chelator structure is that of ZnAF-2 [50]. Their selectivity for Zn^{2+}over other cations and their dissociation constants are similar to fluorescent sensor molecules with the same type of chelators. Reynolds et al. reported the significance of intracellular sensor concentration for monitoring Zn^{2+} concentration by the comparison of ratiometric measurement using FuraZin (K_d ~ 3 μM) and Magfura-2 (K_d ~ 0.02 μM) [51]. Eide et al. used FuraZin to monitor Zn^{2+} level in yeast *Saccharomyces cerevisiae* for

clarifying the function of *ZRC1*, which works in storage and detoxification of excess Zn^{2+} [52]. It was shown that Zrc1 was required for restoration of Zn^{2+} into the vacuole during Zn^{2+} shock. An interesting concept for ratiometric measurements was reported by Fahrni et al. and is based on Zn^{2+} induced inhibition of excited-state intramolecular proton transfer (ESIPT) [53, 54]. In these sensors the intramolecular hydrogen bond that is responsible for the ESIPT process is replaced by Zn^{2+} coordination, resulting in a significant shift of the emission wavelength. They further derivatized these lead compounds to provide ratiometric Zn^{2+} sensors with various affinities for Zn^{2+} [55]. A similar approach was reported by O'Halloran et al. to design Zinbo-5 for ratiometric measurements [56].

Another new type is long-lifetime luminescent sensor molecule with lanthanide complex structures. Luminescent lanthanide complexes, in particular Tb^{3+} and Eu^{3+} complexes, have long luminescence lifetimes of the order of milliseconds. Zn^{2+} sensor molecules were reported, based on the conjugation of (DTPA)-bisamide lanthanide complex with two picolylamide Zn^{2+} chelators [57]. The emission intensity was increased by the addition of Zn^{2+} for Tb^{3+} complexes, and its lifetimes were in the millisecond range. This increase is supposed to be ascribed to the efficiency of intramolecular energy transfer from the pyridyl group to the lanthanide ion induced by the proximity effect from Zn^{2+} chelation. Lanthanide complex based Zn^{2+} sensors were developed **[Eu-7]** (Fig. 5). This europium (Eu^{3+}) complex employs a quinolyl ligand as both a chromophore and an acceptor for Zn^{2+}. Upon addition of Zn^{2+} to a solution of **[Eu-7]**, the luminescence of Eu^{3+} is strongly enhanced, with high selectivity for Zn^{2+} over other biologically relevant metal cations. One of the important advantages of **[Eu-7]** is that this complex can be excited with longer excitation wavelengths (around 340 nm) as compared with previously reported Zn^{2+} -sensitive luminescent lanthanide sensors, whose excitation wavelength is at too high an energy level for biological applications. The usefulness of **[Eu-7]** for monitoring Zn^{2+} changes in living HeLa cells was confirmed. This novel Zn^{2+}-selective luminescent lanthanide chemosensor **[Eu-7]** should be an excellent lead compound for the development of a range of novel luminescent lanthanide chemosensors for biological applications [58, 59].

9 Conclusion

The sensor molecules introduced above indicate that FRET switching by either donor–acceptor distance or by spectral overlap integral is feasible for practical use. It should be possible to develop novel ratiometric fluorescent sensors for various hydrolytic enzymes by introducing other appropriate enzyme-cleavable groups into these switches. The fluorescence quenching problem that usually arises in developing FRET sensors can be overcome by using the FRET cassette moiety with two fluorophores linked by a rigid linker. In addition to fluorescein, it should be possible to use rhodamine as the acceptor, because rhodamine also exhibits a large

shift in its absorption spectrum. Consequently, those study has provided important information about the design and synthesis of FRET-based fluorescent sensors.

Reported Zn^{2+} fluorescent sensor can be used for monitoring intracellular Zn^{2+} concentration changes. However, all the reported fluorescent sensor molecules are not necessarily appropriate in all the studies for clarifying the physiological function of Zn^{2+}. So careful consideration in both the chemical and biological properties of the sensor molecules is necessary. The effective concentration range and the kinetic parameters, such as association and dissociation rates constants, are important. In addition to these chemical parameters, biological parameters, for example, cell-membrane permeability, intracellular localization, and the toxicity of the excitation light and the sensor molecules themselves to the cells, should also be considered. The purpose of the measurement is also important. For example, to study the distribution of Zn^{2+} in biological samples with high resolution and no requirement for temporal resolution, a staining method, such as Timm's staining, measured by electron microscopy, would be the most suitable. The future direction of Zn^{2+} sensor molecules can be headed toward longer fluorescence wavelength towards infrared region, specific cellular localization and mostly ratiometric sensors. These purposes should be accomplished with set up for variety of sensor molecules in the near future.

References

1. Tsien RY (1994) Chem Eng News 72:34
2. Czarnik AW (1995) Chem Biol 2:423
3. Rurack K, Resch-Genger U (2002) Chem Soc Rev 31:116
4. Grynkiewicz G, Poenie M, Tsien RY (1985) J Biol Chem 260:3440
5. Miyawaki A, Llopis J, Heim R, McCaffery JM, Adams JA, Ikura M, Tsien RY (1997) Nature 388:882
6. Kojima H, Nakatsubo N, Kikuchi K, Kawahara S, Kirino Y, Nagoshi H, Hirata Y, Nagano T (1998) Anal Chem 70:2446
7. Hirano T, Kikuchi K, Urano Y, Higuchi T, Nagano T (2000) J Am Chem Soc 122:12399
8. Tsien RY, Harootunian AT (1990) Cell Calcium 11:93
9. Minta A, Tsien RY (1989) J Biol Chem 264:19449
10. Mizukami S, Nagano T, Urano Y, Odani A, Kikuchi K (2002) J Am Chem Soc 124:3920
11. Maruyama S, Kikuchi K, Hirano T, Urano Y, Nagano T (2002) J Am Chem Soc 124:10650
12. Lakowicz JR (1999) Principles of fluorescence spectroscopy. Kluwer, New York
13. Adams SR, Harootunian AT, Buechler YJ, Taylor SS, Tsien RY (1991) Nature 349:694
14. Mochizuki N, Yamashita S, Kurokawa K, Ohba Y, Nagai T, Miyawaki A, Matsuda M (2001) Nature 411:1065
15. Zlokarnik G, Negulescu PA, Knapp TE, Mere L, Burres N, Feng L, Whitney M, Roemer K, Tsien RY (1998) Science 279:84
16. Gonzalez JE, Tsien RY (1995) Biophys J 69:1272
17. Kawanishi Y, Kikuchi K, Takakusa H, Mizukami S, Urano Y, Higuchi T, Nagano T (2000) Angew Chem Int Ed 39:3438
18. Takakusa H, Kikuchi K, Urano Y, Sakamoto S, Yamaguchi K, Nagano T (2002) J Am Chem Soc 124:1653

19. Takakusa H, Kikuchi K, Urano Y, Higuchi T, Nagano T (2001) Anal Chem 73:939
20. Mizukami S, Kikuchi K, Higuchi T, Urano Y, Mashima T, Tsuruo T, Nagano T (1999) FEBS Lett 453:356
21. Gurtu V, Kain SR, Zhang G (1997) Anal Biochem 25:198
22. Tewari M, Quan LT, O'Rourke K, Desnoyers S, Zeng Z, Beidler DR, Poirier GG, Salvesen GS, Dixit VM (1995) Cell 81:801
23. Packard BZ, Toptygin DD, Komoriya A, Brand L (1997) Biophys Chem 67:167
24. Daugherty DL, Gellman SH (1999) J Am Chem Soc 121:4325
25. Geoghegan KL, Rosner PJ, Hoth LR (2000) Bioconjug Chem 11:71
26. Valdes-Aguilera O, Neckers DC (1989) Acc Chem Res 22:171
27. West WS, Pearce J (1965) Phys Chem 69:1894
28. Li Y, Glazer AN (1999) Bioconjug Chem 10:241
29. Sträter N, Lipscomb WN, Klabunde T, Krebs B (1996) Angew Chem Int Ed 35:2024
30. Bollen M, Gijsbers R, Ceulemans H, Stalmans W, Stefan C (2000) Crit Rev Biochem Mol 35:393
31. Zimmermann H (1999) Trends Pharmacol Sci 20:231
32. Goding JW, Terkeltaub R, Maurice M, Deterre P, Sali A, Belli SI (1998) Immunol Rev 161:11
33. Clair T, Lee HY, Liotta LA, Stracke ML (1997) J Biol Chem 272:996
34. Berkessel A, Riedl R (1997) Angew Chem Int Ed 36:1481
35. Takakusa H, Kikuchi K, Urano Y, Kojima H, Nagano T (2003) Chem Eur J 9:1479
36. Majeti R, Weiss A (2001) Chem Rev 101:2441
37. Wang QP, Scheigetz J, Gilbert M, Snider J, Ramachandran C (1999) Biochim Biophys Acta 1431:14
38. Zalewski PD, Forbes IJ, Betts WH (1993) Biochem J 296:403–408
39. Ueno S, Tsukamoto M, Hirano T, Kikuchi K, Yamada MK, Nishiyama M, Nagano T, Matsuki N, Ikegaya Y (2002) J Cell Biol 158:215–220
40. Sensi SL, Ton-That D, Sullivan PG, Jonas EA, Gee KR, Kaczmarek LK, Weiss JH (2003) Proc Natl Acad Sci U S A 100:6157–6162
41. da Silva JJRF, Williams RJP (2001) The biological chemistry of elements: the inorganic chemistry of life, 2nd edn. Oxford University Press, New York pp 315–339
42. Zalewski PD, Jian X, Soon LLL, Breed WG, Seamark RF, Lincoln SF, Ward AD, Sun FZ (1996) Reprod Fertil Dev 8:1097–1105
43. Weiss JH, Sensi SL, Koh JY (2000) Trends Pharm Sci 21:395–401
44. Hirano T, Kikuchi K, Urano Y, Higuchi T, Nagano T (2000) Angew Chem Int Ed 39:1052–1054
45. Hirano T, Kikuchi K, Urano Y, Higuchi T, Nagano T (2000) J Am Chem Soc 122:12399–12400
46. Hirano T, Kikuchi K, Urano Y, Nagano T (2002) J Am Chem Soc 124:6555–6562
47. Lee YV, Hough CJ, Sarvey JM (2003) Sci STKE:pe19
48. Komatsu K, Kikuchi K, Urano Y, Kojima H, Nagano T (2005) J Am Chem Soc 127:10197
49. Kawabata E, Kikuchi K, Urano Y, Kojima H, Odani A, Nagano T (2005) J Am Chem Soc 127:818
50. Maruyama S, Kikuchi K, Hirano T, Urano Y, Nagano T (2002) J Am Chem Soc 124:10650
51. Dineley KE, Malaiyandi LM, Reynolds IJ (2002) Mol Pharmacol 62:618
52. MacDiarmid CW, Milanick MA, Eide DJ (2003) J Biol Chem 278:15065
53. Henary MM, Fahrni CJ (2002) J Phys Chem A 106:5210
54. Fahrni CJ, Henary MM, VanDerveer DG (2002) J Phys Chem A 106:7655
55. Henary MM, Wu Y, Fahrni CJ (2004) Chem Eur J 10:3015
56. Taki M, Wolford JL, O'Halloran TV (2004) J Am Chem Soc 126:712
57. Hanaoka K, Kikuchi K, Kojima H, Urano Y, Nagano T (2003) Angew Chem Int Ed 42:2996
58. Hanaoka K, Kikuchi K, Kojima H, Urano Y, Nagano T (2004) J Am Chem Soc 126:12470
59. Hanaoka K, Kikuchi K, Kobayashi S, Nagano T (2007) J Am Chem Soc 128:13502

Adv Biochem Engin/Biotechnol (2010) 119: 79–97
DOI:10.1007/10_2008_48
© Springer-Verlag Berlin Heidelberg 2009
Published online: 5 June 2009

Dynamic Visualization of Cellular Signaling

Qiang Ni and Jin Zhang

Abstract Our understanding of cellular signaling is critically dependent on our ability to visualize and quantify specific signaling events with high spatial and temporal resolution in the cellular context. Over the past decade or so, biosensors based on fluorescent proteins and fluorescence resonance energy transfer (FRET) have emerged as one major class of fluorescent probes that are capable of tracking a variety of cellular signaling events, such as second messenger dynamics and enzyme activation/activity, in time and space. Here we review recent advances in the development of such biosensors and some biological insights revealed by these biosensors in living cells, tissue, and organisms.

Keywords Biosensor • FRET • Live-cell Imaging • Signal Transduction

Contents

Q. Ni
Department of Pharmacology and Molecular Sciences, The Johns Hopkins University School of Medicine, Baltimore, MD 21205, USA

J. Zhang (✉)
Department of Pharmacology and Molecular Sciences, The Solomon H. Snyder Departments of Neuroscience and Oncology, The Johns Hopkins University School of Medicine, Baltimore, MD 21205, USA
e-mail: jzhang32@jhmi.edu

1 Introduction

A live cell can maintain appropriate responses in an ever changing environment. This is quite remarkable for a single cell given that numerous cellular processes at different locations have to be tightly regulated all at the same time throughout its life cycle. This continuous decision-making process is orchestrated by an intricate cell signaling network which is an integral part of a live cell. Recent years have seen tremendous progress in identification of signaling components constituting this signaling network, especially with the help of emerging genomic, proteomic and bioinformatic approaches [1, 2]. Less well developed is our understanding of how these components are tightly regulated to achieve highly specific signaling within a living cell, which may be responding to multiple physiological cues simultaneously.

The key is believed to lie in the spatiotemporal information encoded in a particular cellular context. For instance, a small signaling molecule like Ca^{2+} is known for its ability to activate selectively and specifically distinct cellular functions in response to a variety of stimuli [3, 4]. Such diverse Ca^{2+} signals are attributed to the ability of a cell to produce complex patterns of Ca^{2+} transients, either local or global, in various forms of spikes, waves, and oscillations [5], specific to its cellular context. Therefore, tools that are capable of deciphering such information are essential for a better understanding of dynamic cellular signaling in its native environment. Over the past 20–30 years, many different Ca^{2+} sensors have been created to unravel the fine details of Ca^{2+} dynamics at all levels, from submicrodomains in single cells to different tissues in whole organisms. On the other hand, however, visualization of other signaling events, even those closely related to Ca^{2+}, remained a challenge, limiting our ability to elucidate the physiological roles of Ca^{2+} in different cellular contexts [6]. Therefore there exists a tremendous need for biosensors that are capable of tracking specific signaling events of interest in living cells.

Thanks to the rapid development of fluorescent proteins and continuing advances in imaging technology, several generalizable biosensor designs that can be applied to a variety of signaling events have become available in the past decade or so. Here we review recent advances in biosensor development that have made real-time visualization of a variety of signaling events a reality as well as some biological insights revealed by these biosensors. In particular, we focus on biosensors that are based on fluorescent proteins and fluorescence resonance energy transfer (FRET), two cornerstones of live-cell imaging.

2 A Rainbow of Fluorescent Proteins

Since the successful cloning of the jellyfish green fluorescent protein (GFP) [7] and its first demonstrations as a useful gene expression marker [8, 9], fluorescent proteins have rapidly grown to become one of the cornerstones of live-cell imaging and

an indispensable tool for researchers in many fields of life sciences [10–12]. The most remarkable feature of GFP is its spontaneous fluorescence which requires no additional cofactors other than molecular oxygen. Furthermore, a highly stable β-can structure of GFP effectively protects its chromophore from its environment, making it a robust visual tag for tracking proteins in complex cellular environments [10]. These unique features make GFP especially useful in living cells, tissue and even whole organisms.

As a result, there have been continuing efforts aimed at improving and developing new fluorescent proteins based on the gene sequence and structural information of the original GFP [10]. By using many different mutagenesis and screening methods, this has led to the generation of mutant GFPs with a series of improved and novel properties, including better mammalian expression, faster maturation, simplified excitation spectrum, improved photostability, increased fluorescence intensity, reduced environmental sensitivity to pH and halides, reduced tendency to dimerize, among many others, as well as color variants ranging from blue to yellow. Notably, however, longer wavelength emission such as red is missing from these GFP color variants. In addition to offering more distinct colors, longer wavelengths are especially useful for in vivo applications owing to their desirable properties like better separation from common cell autofluorescence and better tissue penetration. Seeking longer wavelength emitting fluorescent proteins, researchers turned to other natural sources. The first red fluorescent protein (RFP) known as DsRed was isolated from the coral of *Dicosoma* genus [13] as an obligate tetramer and subsequent engineering efforts have yielded a whole range of orange to far red monomeric fluorescent proteins with improved properties to make a complete rainbow of fluorescent proteins [14, 15].

Importantly, some pairs of fluorescent proteins in this rainbow can undergo FRET, a “spectroscopic ruler” capable of tracking distance and conformational changes at molecular level [16]. This has further expanded the applications of fluorescent proteins in live cells, especially for the dynamic visualization of signaling events. Aside from the common requirements for the successful use of fluorescent proteins in an imaging experiment [17], fluorescent proteins used as a FRET pair should have sufficient spectral overlap between the donor emission and the acceptor excitation. In addition, these fluorescent proteins should also have reasonable spectral separation of both excitation and emission to minimize crosstalk or bleedthrough. At present, cyan fluorescent protein (CFP) and yellow fluorescent protein (YFP) are still the most commonly used FRET pair, although a variety of color variants have been used in various applications. To facilitate the choice of appropriate FRET pairs, Table 1 summarizes a list of currently available fluorescent proteins that are among the best candidates from different color classes. These particular fluorescent protein variants are selected based on properties important for FRET imaging, including brightness, photostability, proper spectral overlap, and reduced tendency to dimerize.

Table 1 Properties of fluorescent proteins

Fluorescent protein	Excitation peak (nm)	Emission peak (nm)	Extinction coefficient (mM^{-1} cm^{-1})	Fluorescence quantum yield	References
EBFP2	383	448	32	0.56	[18]
Azurite	384	450	22	0.59	[18, 19]
mCerulean	433	475	44	0.62	[20, 21]
mCFP	433	475	32	0.40	[15]
mEGFP	488	507	55	0.62	[20]
mVenus	515	528	96	0.52	[20]
mCitrine	516	529	77	0.76	[15]
TagRFP	555	584	100	0.48	[22]
mCherry	587	610	72	0.22	[15]

3 FRET

As visual tags, fluorescent proteins have been extremely useful in revealing gene expression patterns and protein localization and translocation. However, to visualize many dynamic signaling events such as second messenger dynamics, enzyme activation/activity, and dynamic protein–protein interactions, simple fluorescence readout is often insufficient. As a result, more sophisticated fluorescence based methods that are capable of providing dynamic information, including FRET, have been explored for monitoring the dynamics of cellular signaling events. In simple terms, FRET can be described as radiation-less transfer of the energy from an excited donor to an acceptor in close proximity. Since FRET occurs only when the donor and acceptor are in molecular proximity (i.e., <10 nm apart) and the efficiency of this process is proportional to the inverse sixth power of the distance between the donor and acceptor, it has been commonly applied as a spectroscopic ruler for measuring distance, interaction, folding and conformational changes of biomolecules in various biological systems [16].

Quantitatively, FRET efficiency (E) can be determined by the equation

$$E = 1/[1 + (r/R_0)^6] \quad (1)$$

where r is the distance between the donor and acceptor and R_0 is the distance at which FRET efficiency is 50%, known as the Förster distance. The value of R_0 depends on the spectral overlap between the donor emission and the acceptor absorption, the quantum yield of the donor, the reflective index of the environment and the relative orientation between the donor and acceptor, represented by the orientation factor k^2 [23]. The strong distance dependence of FRET efficiency (Fig. 1) can be demonstrated with a simple calculation using (1) in which E decreases from 95.5% with a distance of $0.6R_0$ to 2.9% with a distance of $1.8R_0$. For an R_0 value of 5 nm, which is a reasonable value for the commonly used CFP

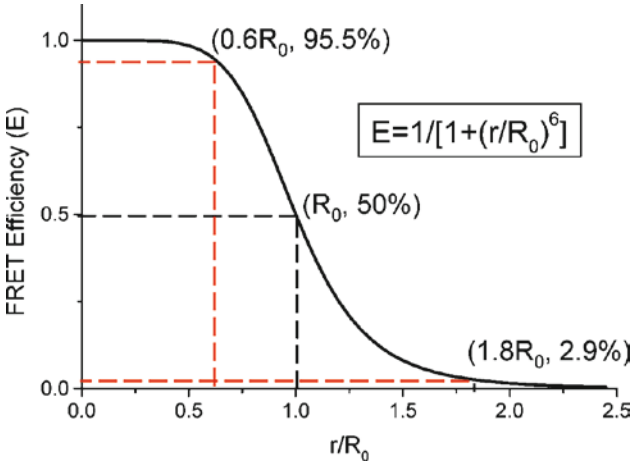

Fig. 1 Dependence of FRET efficiency (E) on distance (r). R_0 is the Förster distance. E decreases from 95.5% with a distance of $0.6R_0$ to 2.9% with a distance of $1.8R_0$

and YFP FRET pairs [20], this translates to a drop of FRET efficiency from almost quantitative to nearly negligible over a distance increase of mere 6 nm. Together with the fact that a standard FRET setup can now routinely detect a FRET efficiency change of less than 1%, a FRET-based biosensor can indeed provide very sensitive readout.

Donor–acceptor fluorophores used for FRET are of wide range from small molecules to complex nanoparticles [24]. However, specific labeling of protein molecules with FRET fluorophores in cellular environment was a major challenge until GFP color variants that are capable of FRET became available. Since then, the marriage between FRET and fluorescent proteins has yielded a variety of FRET biosensors that enable visualization of complex cellular processes such as second messenger dynamics, enzyme activation/activity and protein–protein interactions in living cells, tissue, and organisms.

4 Illuminating Cellular Signaling Using Biosensors Based on Fluorescent Proteins and FRET

Over the past decade or so, biosensors based on fluorescent proteins and FRET have emerged as one major class of fluorescent probes that are capable of tracking a variety of cellular signaling events in real time and space. The growing popularity of this class of sensors can be attributed to the following reasons that make the design of such sensors readily generalizable. First, there exists a plethora of built-in signal sensing modules for virtually any cell signal. These endogenous sensing modules offer plenty of choices for the design of protein based molecular switches

for a particular biosensor. Second, the development of fluorescent proteins has made the task of adding visual tags to the protein based molecular switches as easy as simple molecular cloning, alleviating the need for in vitro conjugation and other manipulations. Third, the high spatial sensitivity offered by FRET readout makes it straightforward to decode the signaling-dependent conformation change of the sensor. Put together, this lays out a general design for a protein based biosensor, i.e., genetically encodable, in which a FRET pair generates a readout corresponding to the distinct states of a signal sensing molecular switch. Here we discuss examples of such sensors in the context of different classes of signaling molecules, including proteases, second messengers, small GTPases and protein kinases.

4.1 Proteases

Proteases are enzymes that catalyze the hydrolysis of a peptide amide bond, i.e., proteolysis. These enzymes are involved in a multitude of highly regulated signaling pathways such as the apoptotic and metabolic pathways. The earliest genetically encoded FRET sensors used blue fluorescent protein (BFP) and GFP linked together with protease cleavable substrates in which proteolysis leads to disruption of FRET by separating the donor and acceptor [25, 26]. While not demonstrated in either case, the potential of fluorescent protein based FRET biosensors for live cell applications has been noted.

Among all proteases, probably the most famous is a family of specialized proteases called caspases. They are directly linked to apoptosis, a process by which a cell undergoes programmed cell death, which is essential in development, tissue homeostasis and malignancy. Functionally, these caspases can be divided into two distinct groups, namely initiator caspases (capases-2, 8, 9, and 10) and effector caspases (caspase-3, 6, and 7). Effector caspases cleave multiple cellular substrates during apoptosis while initiator caspases mainly function to activate effector caspases. By sandwiching various caspase specific substrates between a fluorescent protein FRET pair (e.g., BFP and GFP or CFP and YFP), a series of caspase activity sensors have been created for the study of the complex activation mechanisms of different caspases and their temporal correlation in living cells [27–34].

In *Drosophila*, the salivary gland is sculpted by caspase mediated apoptosis initiated by the steroid hormone 20-hydroxyecdysone (ecdysone). In a recent study analyzing the spatiotemporal patterns of caspase activation in the salivary glands of developing *Drosophila* in vivo, a FRET based caspase-3 sensor has been proven to be useful [35]. In this study it was shown that caspase activation is initiated locally in the anterior cells and then propagated to the posterior cells of the salivary glands using the caspase-3 sensor. Furthermore, this caspase activation is inhibited in flies with mutations in E93 gene, an ecdysone induced early gene, suggesting the E93 gene is an executor for caspase activation in *Drosophila* salivary glands.

4.2 Spatiotemporal Dynamics of Second Messengers

Second messengers are diffusible small intracellular signaling molecules. They play important roles in transmitting signals originated at different cellular locations to their destinations. Some, such as Ca^{2+} and cAMP, are hydrophilic and diffuse in the cytosol, while others, like phosphoinositides (PIs) and diacylglycerol, are hydrophobic and diffuse in the membranes. In either case, they exert their effects by binding to and altering the conformation of the effector proteins, leading to activation/deactivation of the target proteins. Second messenger signaling is truly versatile and of various spatiotemporal patterns; therefore it is necessary to dissect their roles in regulating cell signaling in the cellular context.

4.2.1 Ca^{2+}

Ca^{2+} is a central signaling molecule in cellular signaling and the most studied among all second messengers for its important roles in many physiological systems. Despite being a diffusible ion, Ca^{2+} signaling is highly regulated both spatially and temporally. The dynamic Ca^{2+} signals are deciphered and transduced further down specific signaling pathways by a variety of Ca^{2+} binding proteins.

To elucidate the mechanisms and functions of Ca^{2+} signaling, numerous sensors for cellular imaging of Ca^{2+} have been created. Among them, cameleons represent a class of FRET-based calcium sensors that are widely used. Cameleons were constructed by sandwiching between a fluorescent protein FRET pair, e.g., CFP and YFP, a tandem fusion protein of calmodulin, a Ca^{2+} binding protein, and the calmodulin-binding peptide M13 from myosin light chain kinase [36]. This rational design was based on the observation that a calmodulin-M13 fusion, separated by a flexible Gly–Gly linker, undergoes a conformational change from an extended dumb-bell form to a compact, globular form in the presence of Ca^{2+} [37]. Therefore, it was reasoned that this change in conformation may be detected as a FRET change by fusing FRET donor and acceptor at the N- and C-termini of the fusion protein respectively. Indeed, visualization of Ca^{2+} dynamics in the cytosol, nucleus and endoplasmic reticulum (ER) of single living cells as well as quantitative measurements of Ca^{2+} concentration in the ER were achieved using targeted cameleons [36].

Following the original cameleons, a variety of FRET-based Ca^{2+} biosensors [38–43] have been engineered with improved features for general application (e.g., improved dynamic range/sensitivity, better subcellular targeting, reduced environmental sensitivity and less interference with the endogenous signaling) as well as altered properties suitable for specific applications (e.g., detection range, fast kinetics and desirable spectral characteristics). So far, these FRET-based Ca^{2+} biosensors have been successfully applied in the investigation of Ca^{2+} signaling dynamics in various subcellular organelles of many different cell types as well as a number of transgenic organisms [44–47]. However, for in vivo imaging in mammals, technical

challenges still prevent quantitative measurements of subtle but physiologically significant Ca^{2+} signals such as the neuronal Ca^{2+} transient caused by a single action potential. Despite the limited applications of FRET-based Ca^{2+} biosensors in in vivo imaging, recent progresses along this research direction all point to a brighter future [48, 49]. Importantly, the same design principle of cameleons has been adapted to create biosensors for many other signaling events [50].

4.2.2 cAMP

As a ubiquitous intracellular second messenger, cAMP signaling plays a key role in the regulation of a variety of cellular processes, from gene expression, ion transport, cardiac contraction, to cell growth and apoptosis. Since cAMP exerts many biological effects via only a limited number of effectors, including cAMP dependent protein kinase (PKA), exchange proteins directly activated by cAMP (Epac) and cAMP-gated ion channels, its spatial and temporal control is believed to be crucial to differential regulation of cellular targets involved in various signaling cascades. As a result, several cAMP sensors have been created to investigate such dynamic cAMP signaling. The first FRET-based sensor for real-time imaging of cAMP was based on PKA holoenzyme, in which the catalytic and regulatory subunits were labeled with a small molecule FRET pair, fluorescein and rhodamine, respectively, so that cAMP induced dissociation of the holoenzyme disrupted FRET [51]. Replacement of the small molecule dyes with fluorescent protein FRET pairs made the PKA-based cAMP sensor genetically encodable [52]. Application of this sensor in neonatal cardiomyocytes revealed discrete microdomains of cAMP [53], providing direct evidence for the existence of subcellular compartments of cAMP in cardiomyocytes [54]. More recently, several unimolecular cAMP sensors based on Epac have been generated to achieve more reliable measurements and better subcellular targeting for live-cell imaging of cAMP dynamics [55–57].

On the other hand, the dynamic interplay between cAMP and Ca^{2+} has been suggested to play an important role in regulating physiological functions such as the cardiac contractility [58] while the molecular mechanisms underlying this remain unclear. With Ca^{2+} sensors suitable for co-imaging with the CFP-YFP pair already available, the development of cAMP sensors have made investigation into these mechanisms possible by enabling real-time imaging of two signaling events simultaneously at singe cell level. In one study using MIN6 β-cells, simultaneous measurements of Ca^{2+} and cAMP levels were conducted using Fura-2 and Epac1-camps respectively [59]. It was found that membrane depolarization led to an antiphase temporal correlation between Ca^{2+} and cAMP oscillations. It was further suggested that this Ca^{2+} dependent cAMP oscillation is due to periodic activation and inactivation of Ca^{2+} sensitive phosphodiesterase instead of changes in adenylyl cyclase activity. This antiphasic correlation between Ca^{2+} and cAMP oscillations was also observed with another cAMP sensor, ICUE-RY, in which the original CFP-YFP pair has been replaced with a YFP-RFP pair (Ni and Zhang, unpublished data) (Fig. 2). This switch of FRET pairs should address the issue of possible signal

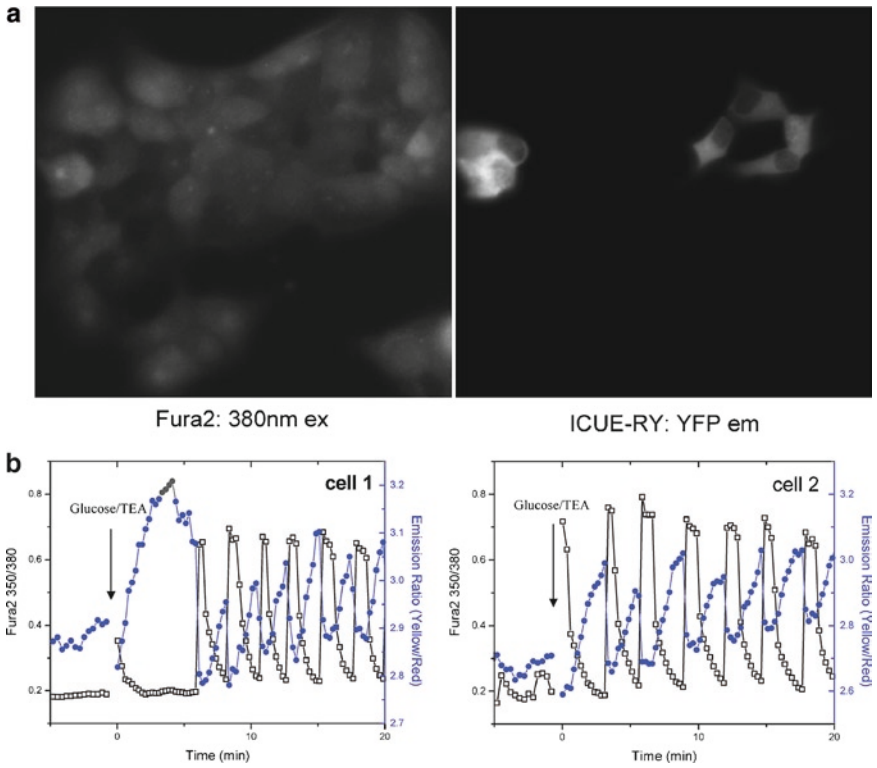

Fig. 2a,b Simultaneous imaging of Ca^{2+} and cAMP dynamics in MIN6 cells. **a** Images of cells expressing ICUE-RY and loaded with Fura2. **b** Ca^{2+} and cAMP oscillations in two individual MIN6 cells after addition of glucose and tetraethylammonium chloride (TEA) at time zero in time courses

contamination between Fura2 and the CFP-YFP FRET pair [60]. A similar approach was taken to examine the interplay between Ca^{2+} and cAMP dynamics in HEK293 cells expressing a Ca^{2+} sensitive adenylyl cyclase [61]. In this case, phasic oscillations in cAMP levels were observed with respect to the Ca^{2+} oscillations induced by physiological stimuli. It was also demonstrated that this Ca^{2+} dependent cAMP oscillation is mediated by adenylyl cyclase activity as well as phosphodiesterase activity. Interestingly, these phasic oscillations in Ca^{2+} and cAMP levels were also observed in INS-1 β-cells upon hormone stimulation using a modified PKA-based cAMP FRET sensor [62]. This marked difference in phase correlation, phasic vs antiphasic, between Ca^{2+} and cAMP oscillations in β-cells probably reflects differential crossregulation in response to different stimulation signals. Taken together, these results highlight the incredible ability of a cell in deciphering and transmitting diverse signals in a highly efficient and specific manner using a dynamic network of signaling molecules. As a result, it is crucial to understand such nonlinear nature of cellular signaling in its biological context.

More recently, in the context of studying differential signaling of β-adrenergic receptor subtypes at the level of cAMP dynamics, another cAMP sensor was created using the cAMP binding domain of the hyperpolarization-activated cyclic nucleotide gated channel 2 (HCN2) as opposed to the binding domains from PKA or Epac [63]. The resulting biosensor, HCN2-camps, maintains a high sensitivity for cAMP but does not appear to saturate at physiological cAMP concentrations in adult cardiomyocytes, a potential concern with other cAMP sensors. Using single adult cardiomyocytes isolated from the transgenic mice expressing HCN2-camps, it was shown that selective stimulation of b_1-adrenergic receptor led to robust cAMP accumulation and propagation throughout the entire cells, whereas selective stimulation of b_2-adrenergic receptor resulted in a smaller localized increase in cAMP that did not propagate even in the presence of phosphodiesterase inhibitors.

4.2.3 PIP_3

Like many other second messengers, phosphatidylinositol 3,4,5-triphosphate (PIP_3) is involved in the regulation of a variety of cellular processes, including cell survival, polarization, and proliferation among others. Many of these functions are achieved via activation of serine/threonine kinase Akt. To investigate the spatiotemporal regulation of PIP_3 dynamics in live cells, several FRET based biosensors have been developed.

One of these biosensors, named "fllip," consisted of a pleckstrin homology (PH) domain from GRP1, which selectively binds PIP_3, sandwiched between CFP and YFP through rigid linkers with a built-in Gly–Gly hinge in the linker between the PH domain and YFP [64]. Using this PIP_3 biosensor in CHO-PDGFR cells, it was found that the sensor localized to the endomembranes showed a delayed but greater response comparing to the sensor targeted to the plasma membrane. Further experiments revealed that this in situ production of PIP_3 at the endomembranes is mediated through receptor endocytosis upon growth factor stimulation, suggesting a new mode of regulation of PIP_3 signaling.

Another genetically targetable PI biosensor specific for PIP_3 and $PI(3,4)P_2$, named "InPAkt," was constructed by sandwiching the PH domain of Akt and a "pseudoligand" containing acidic amino acid residues, between CFP and YFP [65]. In living cells, elevations in PIP_3 and $PI(3,4)P_2$ by growth factor induced activation of phosphatidylinositol 3-kinase (PI3K) resulted in a change in FRET between the fluorescent proteins. Using this sensor, differential dynamics of PIs were observed at the plasma membrane of NIH3T3 cells, stimulated by various growth factors. On the other hand, the nuclear targeted InPAkt showed no response within an hour after platelet derived growth factor stimulation, suggesting that no appreciable amounts of accessible PIP_3 and $PI(3,4)P_2$ were produced in the nucleus. Furthermore, simultaneous imaging of a plasma membrane targeted InPAkt and a nuclear targeted Akt activity reporter [66] revealed a gradual and sustained accumulation of Akt activity in the nucleus after rapid and transient production of PIP_3 and $PI(3,4)P_2$ at the plasma membrane in the same cell.

4.3 Small GTPases

Small GTPases, also known as the Ras GTPase superfamily, have a molecular weight of about 20 kDa and function as molecular switches for a variety of intracellular signaling cascades by cycling between an active GTP-bound form and an inactive GDP-bound form. Their regulation is mediated by guanine nucleotide exchange factor (GEF), the activator, and GTPase activating protein (GAP), the inactivator. According to their primary amino acid sequences and biochemical properties, the Ras superfamily can be divided into five major subfamilies: Ras/Rap, Rho/Rac, Rab, Ran and Arf.

To monitor the activation/activity of these small GTPases, a family of genetically encodable FRET sensors, designated as Ras and interacting protein chimeric unit (Raichu), was developed using a molecular switch that consisted of the small GTPase of interest and a GTPase specific binding domain, sandwiched between CFP and YFP. The first member of this senor family, Raichu-Ras [67], was created using H-Ras and the Ras-binding domain of Raf. Similarly, Raichu-Rap1 [67] was created for the detection of active Rap1 by replacing H-Ras with Rap1. Results using these sensors in living cells showed spatially restricted activation of Ras and Rap1 by different growth factors. Furthermore, using the fluorescence recovery after photobleaching (FRAP) technique, it was determined that the high Ras activity observed at the extending neurites was due to high GTP/GDP exchange rate and/or low GTPase activity, but not to the retention of active Ras. To date, the Raichu family has been expanded to include Raichu-Rac [68], Cdc42 [68], RhoA [69] and RalA [70] for investigating the spatiotemporal dynamics of these small GTPases in living cells.

In another RhoA sensor [71], a different design was used by placing RhoA and its binding domain at the C- and N-termini of the protein chimera respectively, instead of CFP and YFP. This design preserves the reversible membrane association of RhoA which is dependent on its intact C-terminus. Spatiotemporal dynamics of RhoA visualized with this sensor in migrating cells showed differential RhoA activity in membrane protrusions of randomly migrating cells compared to those induced by growth factor stimulation. Therefore, membrane protrusion in migrating cells is regulated by distinct mechanisms in response to different extracellular signals.

4.4 Protein Kinases

Protein kinases are crucial components of intracellular signaling pathways that transmit signals by phosphorylation of various downstream targets. Many members in the kinome [72], which includes 518 putative protein kinases in humans, 540 in mice, and 122 in yeast, are known to have a plethora of downstream targets playing different roles. Therefore, critical for generating appropriate cellular responses, precise spatial and temporal control of kinase activity must be achieved within a biological context. Compartmentalization of kinases and their substrates is one key

strategy used by the cellular machinery in achieving such signaling specificity. For PKA, a ubiquitous protein kinase involved in many parallel signaling cascades, its signaling often requires A-kinase anchor proteins (AKAPs), which provide a molecular framework to orient PKA toward selected substrates [73]. In the case of mitogen activated protein kinases (MAPKs), scaffold proteins are required to bring together various components in the MAPK pathway signaling pathway, including MAPK and its upstream kinases (i.e., MAPKK and MAPKKK), to create functional signaling modules [74–76].

To investigate the spatiotemporal regulation of this important class of enzymes, FRET-based biosensors have been developed for various serine/threonine and tyrosine kinases [66, 77–87]. These sensors utilize, as a molecular switch, a kinase substrate domain attached to a phosphoamino acid binding domain (PAABD). Upon phosphorylation of the substrate, the PAABD binds the phosphopeptide, altering the distance and/or orientation between donor and acceptor fluorophores, resulting in a detectable change in FRET [88] (Fig. 3).

4.4.1 PKA Anchoring and Microcompartmentalization

A-kinase activity reporter 1 (AKAR1), consisting of fusions of CFP, a phosphoamino acid binding domain (14-3-3), a consensus substrate for PKA known as kemptide, and YFP, was created to study compartmentalized PKA activity in living cells [77].

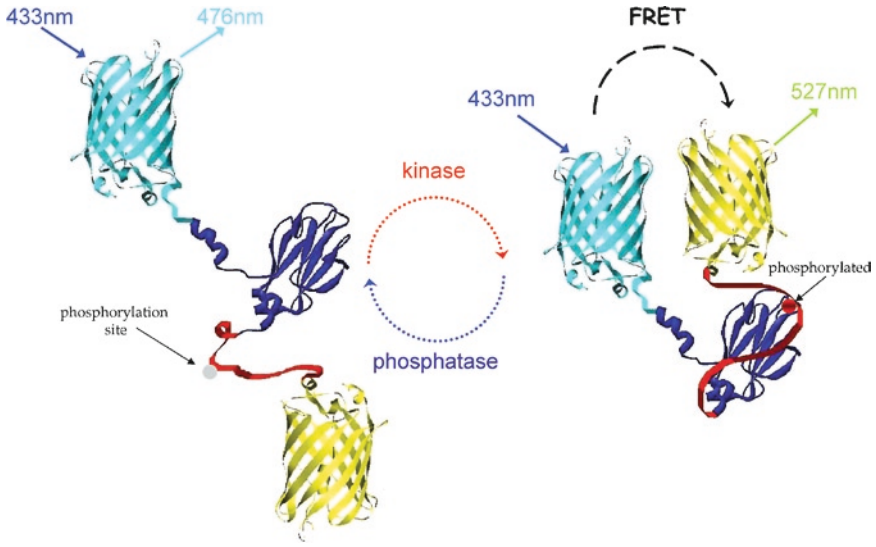

Fig. 3 Structural representation of FRET-based kinase sensors before and after phosphorylation by the target kinase, based on known structures of CFP, YFP and forkhead associated domain bound to a phosphopeptide. A *red dot* on the substrate peptide represents the phosphorylated residue whereas a *grey dot* represents the unphosphorylated state. Shown is a phosphorylation-induced increase in FRET between CFP and YFP

By targeting AKAR1 to different subcellular locations, it was found that comparing to the untargeted AKAR1, the reporter response was faster when tethered to PKA holoenzyme and slower when targeted to the nucleus. Thus deliberate redistribution of a substrate with regard to a kinase can modulate its susceptibility to phosphorylation by the kinase. In this particular case, it indicates that the catalytic subunit of PKA, upon dissociation from PKA holoenzyme, would preferentially phosphorylate a local pool of substrates. As such, substrates tethered to the regulatory subunit of PKA through AKAPs would be preferentially phosphorylated before the catalytic subunit diffuses away to phosphorylate substrates in other locations, e.g., the cytoplasm and nucleus. Therefore, this study lays the foundation for studying the functional effects of PKA-AKAPs mediated cAMP/PKA signaling. The major limitation of AKAR1, however, is its poor reversibility in living cells, probably due to the tight binding of 14-3-3 with the phosphorylated substrate (Fig. 4).

AKAR2, the second generation of AKAR, was made reversible by replacing the high-affinity pair in AKAR1, 14-3-3 and a serine-containing kemptide substrate, with a lower-affinity pair, forkhead associated domain 1 (FHA1) and a threonine-containing

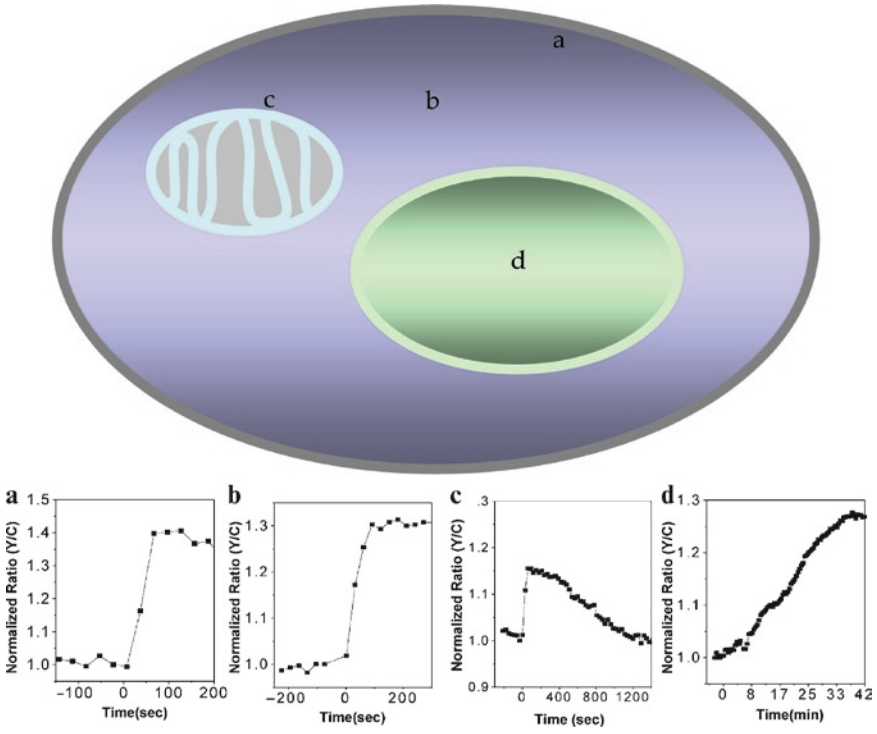

Fig. 4a–d Representative time courses of the A-kinase activity reporter (AKAR) targeted to plasma membrane (**a**), cytosol (**b**), mitochondria (**c**) and nucleus (**d**) with the corresponding subcellular sites are labeled in a cartoon showing the basic the cell structure. Agonists (isoproterenol, an agonist for beta adrenergic receptor or forskolin, an activator of adenylyl cyclase) are added at time zero in time courses

kemptide substrate, thus enabling tracking of the dynamic balance between the PKA and phosphatases activities in living cells [83]. The effects of chronic hyperinsulinemia on cAMP/PKA signaling were examined using AKAR2 in 3T3-L1 adipocytes. In adipocytes, lipolysis is enhanced through β-adrenergic receptor mediated activation of cAMP/PKA pathway, in which PKA phosphorylation leads to increased lipase activity. Interestingly, chronic hyperinsulinemic conditions (typical of type 2 diabetes) enhance β-adrenergic receptor mediated cAMP production but not lipolysis. Using AKAR2, it was shown that chronically high insulin levels delays PKA activation in response to β-adrenergic receptor stimulation, despite overproduction of cAMP under the same condition. Furthermore, disruption of PKA scaffolding mimics the effects of chronic insulin on β-adrenergic receptor signaling, suggesting that β-adrenergic receptor and PKA are compartmentalized in adipocytes and chronically elevated insulin may disrupt this close coupling.

In another study of muscle-specific AKAP (mAKAP) mediated cAMP/PKA signaling, modified AKAR2s, namely AKAR–PKA and AKAR–PKA–PDE, were generated through introduction of AKAP-derived binding sites for PKA or for both PKA and phosphodiesterase, respectively [89]. Combining live-cell imaging with biochemical experiments, it was discovered that PKA, PDE, Epac, as well as extracellular signal regulated protein kinase (ERK) are all part of a dynamic signaling complex mediated by mAKAP that functions as a bidirectional regulator of local cAMP action by integrating signals from both the cAMP and ERK pathways.

More recently, visualization of PKA activity at different subcellular regions has also been achieved in neurons of mouse brain slices using tissue imaging [90]. Using AKAR2, distinct kinetics of PKA activation were observed in response to stimulation of the G_s-coupled, 5-HT7 receptor at different locations within morphologically intact mammalian neurons: rapid at the plasma membrane, slow in the cytosol, and even slower in the nucleus.

Taken together, these studies using AKARs have provided important insights into the compartmentalized cAMP/PKA signaling and demonstrated that these biosensors can be targeted to signaling complexes or used as scaffolds of artificial signaling complexes that mimic endogenous ones for elucidating spatiotemporal regulation of protein kinases.

4.4.2 Oscillatory PKC Activity

PKC transduces cellular signaling by phosphorylating a variety of target substrates. In cells, regulation of PKC activity is achieved by a number of mechanisms, including phosphorylation, membrane targeting, and interactions with additional signaling regulators, all working in a coordinated manner. As such, our understanding of PKC signaling is critically dependent on our ability to decipher the spatiotemporal information of PKC activity in live cells. Analogously to AKAR, C-kinase activity reporter (CKAR) was constructed by flanking a tandem fusion of FHA2 domain and a PKC substrate with monomeric CFP and YFP FRET pair [80]. Like AKAR2, CKAR is reversible, thereby enabling continuous monitoring of the dynamic

balance between PKC and phosphatases. Targeting of CKAR to the plasma membrane, where PKC is most active, revealed oscillatory PKC activity in HeLa cells in response to histamine stimulation. Co-imaging with the Ca^{2+} indicator Fura red showed that the oscillations in CKAR phosphorylation are phase locked with Ca^{2+} oscillations, with a peak delay of about 10 s. A similar observation was also made in MDCK cells with ATP stimulation. However, there exists a marked difference in phospholipase C (PLC) activity with regard to Ca^{2+} oscillations in these two different cell lines, suggesting that ATP stimulated PKC responses in MDCK cells and histamine stimulated PKC responses in HeLa cells represent two distinct mechanisms for temporal regulation of PKC activity.

4.4.3 Long-Range Activation of Src in Mechanotransduction

While it is well recognized that mechanical signals are critically involved in many cell processes, little is known about how mechanical stimuli are transmitted into biochemical signals. Src, a non-receptor tyrosine kinase, plays important roles in regulating transduction of mechanic signals via regulation of integrin-cytoskeleton interaction. It is in this context that an integrated approach combining genetically encodable FRET biosensors and laser tweezers has been developed for studying the spatial and temporal dynamics of Src activity during mechanotransduction [82]. Using this approach, it was shown that when a local mechanical stimulus was applied to cells expressing a FRET-based Src activity reporter, a wave of Src activity was observed from the site of stimulation to distal parts of the cell periphery in the opposite direction of the applied force. It was further shown that this force-induced, directional and long-range activation of Src is dependent on both actin polymers and microtubules. Therefore, spatial difference in Src activity was revealed and quantified using the FRET-based biosensor in this study, providing direct evidence for the critical role of Src kinase in mechanotransduction.

5 Practical Considerations

It is important to keep in mind the intrinsic limitations and possible consequences when using these fluorescent protein based FRET biosensors in living systems. First, despite much improvement, the fluorescence properties of currently available fluorescent proteins (Table 1) are still not ideal for FRET applications, often limiting signal detection and the dynamic range of such sensors. Second, while fluorescent proteins are quite inert in cellular environment, their relatively bulky sizes could cause severe perturbation when size does matter. Third, the sensing and/or binding modules commonly used in these biosensors usually have their endogenous counterparts. As a result, overexpression of these sensors could potentially interfere with the endogenous signaling of interest. Fortunately, all these limitations can be and have been addressed to varying degrees with different engineering strategies.

And in cases where some limitations cannot be overcome, sensors based on alternative designs, which are not based on fluorescent proteins and FRET, have been developed [91, 92].

Furthermore, proper control experiments should always be done when using these biosensors in live cells [88]. This is of particular importance given the dynamic nature of cellular environment and the somewhat unpredictable photophysical behavior of a fluorescent protein, where artifacts can be easily misinterpreted as signals without proper controls.

6 Perspectives

Cellular signaling constitutes an integral part of a live cell in which dynamic signals control cell fates. It is therefore essential to understand cellular signaling in its native context with important spatiotemporal information intact. However, studying signaling events in live cells in general has been a challenge due to a lack of suitable methods. Now with the development of various biosensors suitable for live-cell imaging, coupled with significant advances in imaging instrumentation, monitoring of specific signaling events in live cells with high spatial and temporal resolutions has become more attainable. In particular, several general designs based on fluorescent proteins and FRET have been successfully applied in engineering biosensors for several major classes of cellular signaling molecules, including G-proteins, second messengers, and protein kinases. Therefore, it is reasonable to expect that soon most signaling events, if not all, will become visible.

However, achieving visualization of individual signaling events is just the first step. Dynamic cross regulation or interplay between various signaling events and pathways are fundamental to the integrity of cellular signaling. As such, it is essential to establish interactions between various signaling molecules and events in their native context to achieve a better understanding of the information flow in the complex cell signaling network. To this end, biosensors with orthogonal fluorimetric properties will offer the unique opportunity, along with other compatible techniques, such as patch clamp, for simultaneous monitoring of multiple signaling events within the same or different signaling pathways. This approach should allow establishing definitive links between different signaling molecules or events in a context-dependent manner.

Furthermore, in vivo tracking of signaling events using these fluorescent protein based FRET biosensors has been realized in several instances and the scope of their application will continue to expand. Currently, in vivo FRET imaging primarily uses multi-photon microscopy for better tissue penetration [93, 94]. Fibred fluorescence microscopy, which uses a tiny fibre-optic probe to provide real-time images, offers a promising alternative, with high resolution for deep region imaging [95]. Biosensors constructed with fluorophores emitting at near infrared wavelength or with bioluminescent moieties, as well as more advanced in vivo imaging technologies, should allow imaging of signaling events in whole organisms and tracking of

multi-tissue/systems signaling dynamics simultaneously, thereby providing a global view of signaling functions in physiological context.

In conclusion, combining the unique features of genetic encodability, targetability, high sensitivity, and specificity, FRET-based biosensors have enabled real-time tracking of signaling events in native environments ranging from single cells to whole organisms with high spatial resolution. Applications of these sensors have greatly advanced our knowledge of cellular signaling and will continue to play an important role in our quest for a comprehensive understanding of the molecular mechanisms underlying the complex cellular signaling of a cell.

References

1. Linding R, Jensen LJ, Ostheimer GJ, van Vugt MA, Jorgensen C, Miron IM, Diella F, Colwill K, Taylor L, Elder K, Metalnikov P, Nguyen V,Pasculescu A, Jin J, Park JG, Samson LD, Woodgett JR, Russell RB, Bork P, Yaffe MB, Pawson T (2007) Cell 129:1415
2. Musso GA, Zhang Z, Emili A (2007) Chem Rev 107:3585
3. Dolmetsch RE, Xu K, Lewis RS (1998) Nature 392:933
4. Li W, Llopis J, Whitney M, Zlokarnik G, Tsien RY (1998) Nature 392:936
5. Berridge MJ, Lipp P, Bootman MD (2000) Nat Rev Mol Cell Biol 1:11
6. De Koninck P, Schulman H (1998) Science 279:227
7. Prasher DC, Eckenrode VK, Ward WW, Prendergast FG, Cormier MJ (1992) Gene 111:229
8. Chalfie M, Tu Y, Euskirchen G, Ward WW, Prasher DC (1994) Science 263:802
9. Inouye S, Tsuji FI (1994) FEBS Lett 341:277
10. Tsien RY (1998) Ann Rev Biochem 67:509
11. Zhang J, Campbell RE, Ting AY, Tsien RY (2002) Nat Rev Mol Cell Biol 3:906
12. Giepmans BN, Adams SR, Ellisman MH, Tsien RY (2006) Science 312:217
13. Matz MV, Fradkov AF, Labas YA, Savitsky AP, Zaraisky AG, Markelov ML, Lukyanov SA (1999) Nat Biotechnol 17:969
14. Campbell RE, Tour O, Palmer AE, Steinbach PA, Baird GS, Zacharias DA, Tsien RY (2002) Proc Natl Acad Sci USA 99:7877
15. Shaner NC, Campbell RE, Steinbach PA, Giepmans BN, Palmer AE, Tsien RY (2004) Nat Biotechnol 22:1567
16. Stryer L (1978) Ann Rev Biochem 47:819
17. Shaner NC, Steinbach PA, Tsien RY (2005) Nat Methods 2:905
18. Ai HW, Shaner NC, Cheng Z, Tsien RY, Campbell RE (2007) Biochemistry 46:5904
19. Mena MA, Treynor TP, Mayo SL, Daugherty PS (2006) Nat Biotechnol 24:1569
20. Rizzo MA, Springer G, Segawa K, Zipfel WR, Piston DW (2006) Microsc Microanal 12:238
21. Rizzo MA, Springer GH, Granada B, Piston DW (2004) Nat Biotechnol 22:445
22. Merzlyak EM, Goedhart J, Shcherbo D, Bulina ME, Shcheglov AS, Fradkov AF, Gaintzeva A, Lukyanov KA, Lukyanov S, Gadella TW, Chudakov DM (2007) Nat Methods 4:555
23. Clegg RM (1992) Methods Enzymol 211:353
24. Sapsford KE, Berti L, Medintz IL (2006) Angew Chem Int Ed Engl 45:4562
25. Heim R, Tsien RY (1996) Curr Biol 6:178
26. Mitra RD, Silva CM, Youvan DC (1996) Gene 173:13
27. Xu X, Gerard ALV, Huang BCB, Anderson DC, Payan DG, Luo Y (1998) Nucleic Acids Res 26:2034
28. Mahajan NP, Harrison-Shostak DC, Michaux J, Herman B (1999) Chem Biol 6:401
29. Tyas L, Brophy VA, Pope A, Rivett AJ, Tavare JM (2000) EMBO Rep 1:266

30. Rehm M, Dussmann H, Janicke RU, Tavare JM, Kogel D, Prehn JH (2002) J Biol Chem 277:24506
31. Onuki R, Nagasaki A, Kawasaki H, Baba T, Uyeda TQ, Taira K (2002) Proc Natl Acad Sci USA 99:14716
32. Luo KQ, Yu VC, Pu Y, Chang DC (2003) Biochem Biophys Res Commun 304:217
33. Takemoto K, Nagai T, Miyawaki A, Miura M (2003) J Cell Biol 160:235
34. Wu X, Simone J, Hewgill D, Siegel R, Lipsky PE, He L (2006) Cytometry A 69:477
35. Takemoto K, Kuranaga E, Tonoki A, Nagai T, Miyawaki A, Miura M (2007) Proc Natl Acad Sci USA 104:13367
36. Miyawaki A, Llopis J, Heim R, McCaffery JM, Adams JA, Ikura M, Tsien RY (1997) Nature 388:882
37. Porumb T, Yau P, Harvey TS, Ikura M (1994) Protein Eng 7:109
38. Miyawaki A, Griesbeck O, Heim R, Tsien RY (1999) Proc Natl Acad Sci USA 96:2135
39. Truong K, Sawano A, Mizuno H, Hama H, Tong KI, Mal TK, Miyawaki A, Ikura M (2001) Nat Struct Biol 8:1069
40. Heim N, Griesbeck O (2004) J Biol Chem 279:14280
41. Mank M, Reiff DF, Heim N, Friedrich MW, Borst A, Griesbeck O (2006) Biophys J 90:1790
42. Palmer AE, Jin C, Reed JC, Tsien RY (2004) Proc Natl Acad Sci USA 101:17404
43. Palmer AE, Giacomello M, Kortemme T, Hires SA, Lev-Ram V, Baker D, Tsien RY (2006) Chem Biol 13:521
44. Kerr R, Lev-Ram V, Baird G, Vincent P, Tsien RY, Schafer WR (2000) Neuron 26:583
45. Reiff DF, Thiel PR, Schuster CM (2002) J Neurosci 22:9399
46. Fiala A, Spall T, Diegelmann S, Eisermann B, Sachse S, Devaud JM, Buchner E, Galizia CG (2002) Curr Biol 12:1877
47. Higashijima S, Masino MA, Mandel G, Fetcho JR (2003) J Neurophysiol 90:3986
48. Kotlikoff MI (2007) J Physiol 578:55
49. Garaschuk O, Griesbeck O, Konnerth A (2007) Cell Calcium 42:351
50. Miyawaki A (2003) Developmental Cell 4:295
51. Adams SR, Harootunian AT, Buechler YJ, Taylor SS, Tsien RY (1991) Nature 349:694
52. Zaccolo M, De Giorgi F, Cho CY, Feng L, Knapp T, Negulescu PA, Taylor SS, Tsien RY, Pozzan T (2000) Nat Cell Biol 2:25
53. Zaccolo M, Pozzan T (2002) Science 295:1711
54. Buxton IL, Brunton LL (1983) J Biol Chem 258:10233
55. DiPilato LM, Cheng X, Zhang J (2004) Proc Natl Acad Sci USA 101:16513
56. Nikolaev VO, Bunemann M, Hein L, Hannawacker A, Lohse MJ (2004) J Biol Chem 279:37215
57. Ponsioen B, Zhao J, Riedl J, Zwartkruis F, van der KG, Zaccolo M, Moolenaar WH, Bos JL, Jalink K (2004) EMBO Rep 5:1176
58. Cooper DM, Mons N, Karpen JW (1995) Nature 374:421
59. Landa LR Jr, Harbeck M, Kaihara K, Chepurny O, Kitiphongspattana K, Graf O, Nikolaev VO, Lohse MJ, Holz GG, Roe MW (2005) J Biol Chem 280:31294
60. Gerbino A, Ruder WC, Curci S, Pozzan T, Zaccolo M, Hofer AM (2005) J Cell Biol 171:303
61. Willoughby D, Cooper DM (2006) J Cell Sci 119:828
62. Dyachok O, Isakov Y, Sagetorp J, Tengholm A (2006) Nature 439:349
63. Nikolaev VO, Bunemann M, Schmitteckert E, Lohse MJ, Engelhardt S (2006) Circ Res 99:1084
64. Sato M, Ueda Y, Takagi T, Umezawa Y (2003) Nat Cell Biol 5:1016
65. Ananthanarayanan B, Ni Q, Zhang J (2005) Proc Natl Acad Sci USA 102:15081
66. Kunkel MT, Ni Q, Tsien RY, Zhang J, Newton AC (2005) J Biol Chem 280:5581
67. Mochizuki N, Yamashita S, Kurokawa K, Ohba Y, Nagai T, Miyawaki A, Matsuda M (2001) Nature 411:1065

68. Itoh RE, Kurokawa K, Ohba Y, Yoshizaki H, Mochizuki N, Matsuda M (2002) Mol Cell Biol 22:6582
69. Yoshizaki H, Ohba Y, Kurokawa K, Itoh RE, Nakamura T, Mochizuki N, Nagashima K, Matsuda M (2003) J Cell Biol 162:223
70. Yoshizaki H, Mochizuki N, Gotoh Y, Matsuda M (2007) Mol Biol Cell 18:119
71. Pertz O, Hodgson L, Klemke RL, Hahn KM (2006) Nature 440:1069
72. Manning G, Whyte DB, Martinez R, Hunter T, Sudarsanam S (2002) Science 298:1912
73. Wong W, Scott JD (2004) Nat Rev Mol Cell Biol 5:959
74. Chang L, Karin M (2001) Nature 410:37
75. Kyriakis JM, Avruch J (2001) Physiol Rev 81:807
76. Morrison DK, Davis RJ (2003) Annu Rev Cell Dev Biol 19:91
77. Zhang J, Ma Y, Taylor SS, Tsien RY (2001) Proc Natl Acad Sci USA 98:14997
78. Ting AY, Kain KH, Klemke RL, Tsien RY (2001) Proc Natl Acad Sci USA 98:15003
79. Sato M, Ozawa T, Inukai K, Asano T, Umezawa Y (2002) Nat Biotechnol 20:287
80. Violin JD, Zhang J, Tsien RY, Newton AC (2003) J Cell Biol 161:899
81. Sasaki K, Sato M, Umezawa Y (2003) J Biol Chem 278:30945
82. Wang Y, Botvinick EL, Zhao Y, Berns MW, Usami S, Tsien RY, Chien S (2005) Nature 434:1040
83. Zhang J, Hupfeld CJ, Taylor SS, Olefsky JM, Tsien RY (2005) Nature 437:569
84. Johnson SA, You Z, Hunter T (2007) DNA Repair (Amst) 6:1277–1284
85. Kunkel MT, Toker A, Tsien RY, Newton AC (2007) J Biol Chem 282:6733
86. Kurokawa K, Mochizuki N, Ohba Y, Mizuno H, Miyawaki A, Matsuda M (2001) J Biol Chem 276:31305
87. Sato M, Kawai Y, Umezawa Y (2007) Anal Chem 79:2570
88. Ni Q, Titov DV, Zhang J (2006) Methods 40:279
89. Dodge-Kafka KL, Soughayer J, Pare GC, Carlisle Michel JJ, Langeberg LK, Kapiloff MS, Scott JD (2005) Nature 437:574
90. Gervasi N, Hepp R, Tricoire L, Zhang J, Lambolez B, Paupardin-Tritsch D, Vincent P (2007) J Neurosci 27:2744
91. Hoffmann C, Gaietta G, Bunemann M, Adams SR, Oberdorff-Maass S, Behr B, Vilardaga JP, Tsien RY, Ellisman MH, Lohse MJ (2005) Nat Methods 2:171
92. Zhang L, Lee KC, Bhojani MS, Khan AP, Shilman A, Holland EC, Ross BD, Rehemtulla A (2007) Nat Med 13:1114
93. Stockholm D, Bartoli M, Sillon G, Bourg N, Davoust J, Richard I (2005) J Mol Biol 346:215
94. Heim N, Garaschuk O, Friedrich MW, Mank M, Milos RI, Kovalchuk Y, Konnerth A, Griesbeck O (2007) Nat Methods 4:127
95. Vincent P, Maskos U, Charvet I, Bourgeais L, Stoppini L, Leresche N, Changeux JP, Lambert R, Meda P, Paupardin-Tritsch D (2006) EMBO Rep 7:1154

Part III
Fabrication Technology

Adv Biochem Engin/Biotechnol (2010) 119: 101–114
DOI: 10.1007/10_2009_14
© Springer-Verlag Berlin Heidelberg 2009
Published online: 14 October 2009

Surface Acoustic Wave Atomizer and Electrostatic Deposition

Yutaka Yamagata

Abstract A new methodology for fabricating thin film or micro patters of organic/bio material using surface acoustic wave (SAW) atomizer and electrostatic deposition is proposed and characteristics of atomization techniques are discussed in terms of drop size and atomization speed. Various types of SAW atomizer are compared with electrospray and conventional ultrasonic atomizers. It has been proved that SAW atomizers generate drops as small as electrospray and have very fast atomization speed. This technique is applied to fabrication of micro patterns of proteins. According to the result of immunoassay, the specific activity of immunoglobulin was preserved after deposition process.

Keywords Electrospray deposition • Immunoassay chip • Micro pattern formation • Surface acoustic wave • Ultrasonic atomization

Contents

Y. Yamagata (✉)
VCAD System Research Program, Applied Fabrication Team,
RIKEN, 1–2 Hirosawa, Wako, Saitama zip, 351-0198, Japan
e-mail: yamagata@riken.jp

Abbreviations

BSA	Bovine serum albumin
CCD	Charge coupled device
ESD	Electrospray deposition
FE-SEM	Field emission type scanning electron microscope
IDT	Inter-digital electrode
IgG	Immunoglobulin G
ITO	Indium tin oxide
RF	Radio frequency
SAW	Surface acoustic wave
SAW-ED	Surface acoustic wave atomizer and electrostatic deposition

1 Introduction

Thin film formation and micro patterning are essential processes in the production of semiconductor devices, flat panel displays, biochips, etc. Deposition techniques of inorganic materials are well studied and sophisticated equipment is available. Those techniques include vacuum evaporation, sputtering, and chemical vapor deposition. Combined with photo resist masking by lithographic technique, fine patterns well below 100 nm are already in mass production. Concerning the deposition of organic materials, polymers, or biomacromolecules, such established techniques are difficult to adopt because those materials can be damaged by high temperature, vacuum, or chemical etchants. As for thin film formation and patterning of such organic or biomacromolecules, additive patterning method are used. These methods include screen/contact printing, spray coating, ink-jet printing, and spotting.

Screen printing is widely used in the printing and electronics industries, especially coating of solder paste to printed circuit boards. The metal stencil mask used in this process has a resolution between 10 and 50 μm. Ink-jet printing is quite common in printers for PCs and is also used for fabrication of flat panel displays and biochips [1]. Ink-jet printing is basically a serial process which requires numerous dots to be ejected from a nozzle. Spotting is a method to use a pin with a small gap to hold sample liquids just like a fountain pen. Early DNA chips were made by spotting [2] and this method is still used as a handy way for fabricating DNA/protein chips in the laboratory. The uniformity and repeatability of this method is rather limited by the durability and precision of spotting pins. Spray coating methods can be divided into two different techniques: wet deposition and dry deposition. Most pressurized spray nozzles generate droplets larger than several tens of micrometers, which will land on the substrate before drying. Electrospray deposition (ESD) as described in an earlier chapter, is a dry deposition method [3]. The droplet diameters by electrospray are as small as 1 μm and they will land on the substrate as dry particles.

ESD can be divided into two processes: one is the liquid atomization process by electrostatic force and the other is the collection process of sprayed droplets or particles.

ESD is a quite effective method to fabricate thin films of organic or biological material, but the drawbacks of this method are that it is difficult to spray highly conductive solution and that the spray speed is rather slow. To overcome these drawbacks, different atomization processes may be adopted. The authors have developed a new method using a surface acoustic wave (SAW) atomizer to generate droplets of several micrometers in diameter. This process is called SAW atomizer and electrostatic deposition (SAW-ED). By using SAW-ED, deposition of organic and biomacromolecule is possible, and is similar to ESD but with a higher speed. The atomization principles and mechanism will be described in the following chapter and application to immunoassay chip fabrication will be described.

2 Atomization Process

The most common atomization process involve pressurized spray nozzles, which utilize turbulent flow of liquid and gas [4]. This conventional process has the advantage of fast atomization speed and low device cost, but diameters of atomized droplets are usually around several tens of micrometers and cannot be used for dry deposition. Ultrasonic atomization is another common process, which utilizes a piezoelectric vibrator to generate droplets. Common ultrasonic atomizers use vibration frequencies around several tens of kilohertz, which generate droplets of 10–100 μm in diameter [5]. Lang et al. studied the relationship between ultrasonic vibration frequency and diameters of atomized droplets [6]. When ultrasonic vibration is applied to a liquid surface, a capillary wave is generated, the wavelength of which is shown by equation (1)

$$\lambda_c = \left(\frac{8\pi\sigma_L}{\rho_L f^2} \right)^{1/3} \tag{1}$$

where λ_c is wavelength, σ_L surface tension, ρ_L density of liquid, and f excitation frequency.

Lang et al. proposed an experimental formula showing that diameters of atomized droplets are approximately $0.34\lambda_c$. According to this theory, when the excitation frequency is higher, droplet diameters will decrease. The conventional piezoelectric vibrator has a limit of excitation frequency around 1 MHz due to the dielectric loss of sintered piezoelectric material and mechanical damping of Langevin type resonators. Kurosawa et al. proposed a new atomization method using SAW [7]. They used a progressive type SAW generated on a single crystal $LiNbO_3$. The excitation frequency is about 10 MHz and they obtained average droplet sizes of 20 μm. Figure 1 shows a relationship between drop size and excitation frequency reconstructed by the authors based on previous publications [7, 8]. The results of Kurosawa et al. do not match Kelvin's equation based on capillary wave theory. This may be because Kurosawa et al. observed two peaks in drop diameter distribution. The second peak may be generated by the intermittent drive

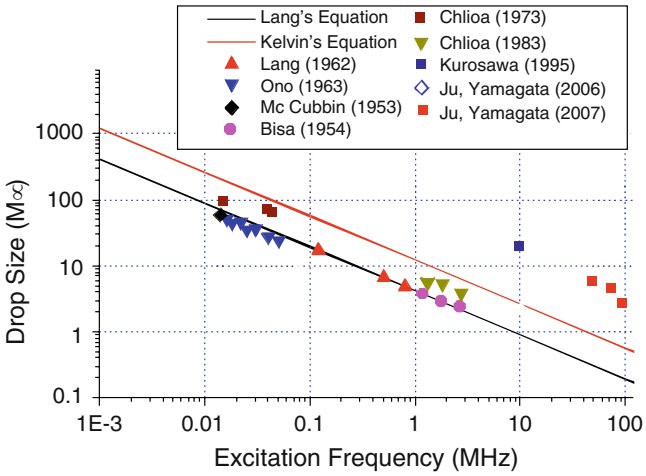

Fig. 1 Excitation frequency and drop size. (Reconstructed by author based on publications of Chiba and Kurosawa)

mode they adopted to prevent damage of the SAW device from excessive heating. The authors have developed more efficient types of SAW atomizer, results from which match Kelvin's equation [9].

3 Atomization Characteristics

3.1 Experimental Apparatus

The SAW atomizer consists of $LiNbO_3$ single crystal substrate (128°-Y cut) with an inter-digital electrode (IDT) formed on the surface. When a radiofrequency signal is applied to the IDT, a SAW is generated on the surface. SAW is also referred to as Rayleigh wave [10], the vibration energy of which is concentrated on the surface of the piezoelectric substrate. This energy concentration effect, together with low dielectric and mechanical loss in single crystal $LiNbO_3$, means that the SAW vibrator requires very little power at higher frequency compared to the conventional ultrasonic vibrator like the Langevin type resonator. This is quite advantageous in raising the excitation frequency of ultrasonic atomization. Figure 2 shows the configuration variation of SAW devices. Type 1 is a progressive wave type, which was used by Kurosawa et al. IDT generates progressive SAW to both sides of the electrode, hence the input power is not efficiently used for atomization. Reflector electrodes can be used to concentrate vibration energy by reflecting progressive wave. Types 4 and 5 are standing wave type SAW atomizers with two IDTs and two reflector electrodes. This enables vibration energy to be concentrated at the central area of the substrate,

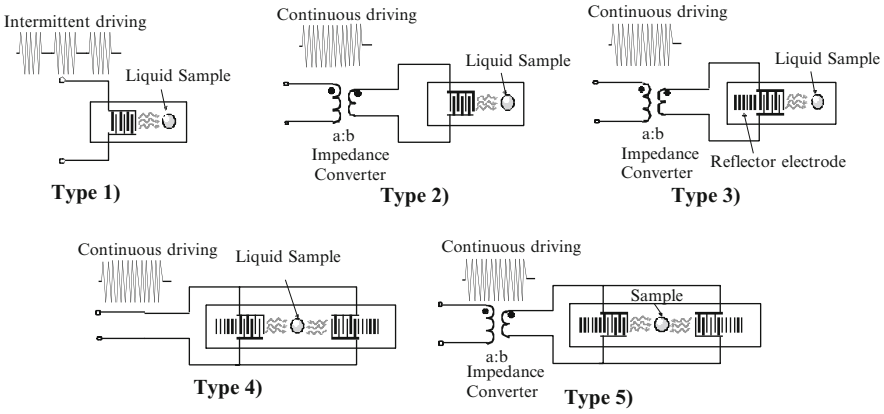

Fig. 2 Variations of SAW atomizer

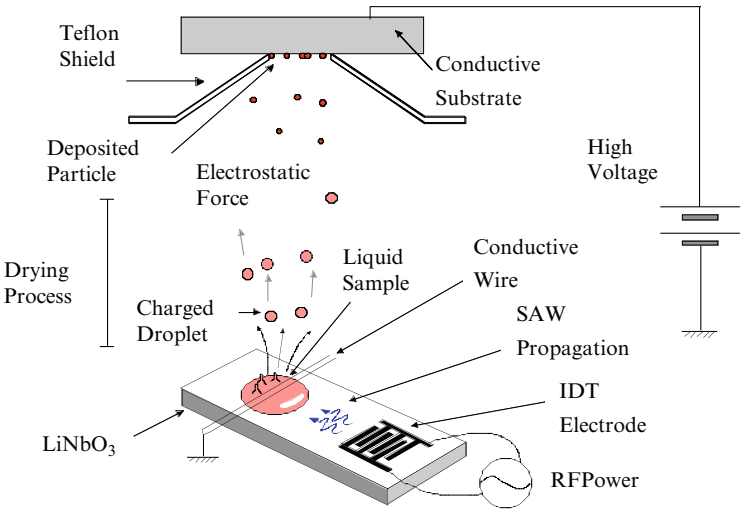

Fig. 3 SAW-ED apparatus configuration

which means lower energy is required to start atomization. Impedance converters also improve energy efficiency by preventing reflected RF power.

Figure 3 shows the configuration of SAW atomizer and electrostatic deposition apparatus. The liquid sample is placed on the SAW atomizer and in contact with thin metal wires that are grounded. The deposition substrate is set above the atomizer and several kilovolts are applied for collecting atomized drops/particles. The whole system is stored in a plastic chamber to prevent air turbulence. Teflon shield on the conductive substrate works as insulating mask to concentrate deposition to the central aperture. The distance between atomizer and substrate is about 15 cm. Sample liquid is supplied by pipette.

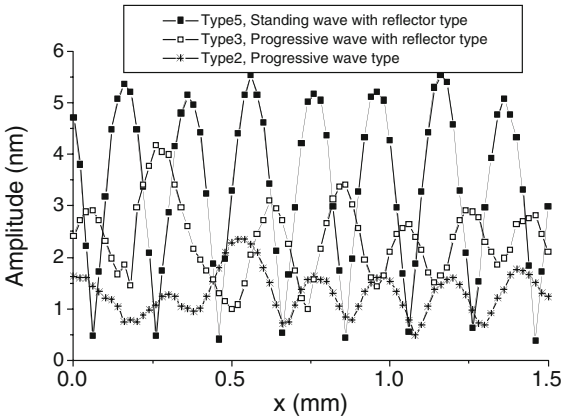

Fig. 4 Vibration amplitude distribution by different SAW devices

3.2 Atomization Characteristics

Figure 4 shows the vibration amplitude distribution at the central area of the SAW device measured by Laser Doppler Vibrometer micrometer. This result shows that the standing wave type with two electrodes has the highest vibration amplitude compared to other types of SAW devices with the same input RF power. This result indicates that thermal loss with piezoelectric material can be the lowest with a standing wave type SAW device.

The sizes of atomized drops are estimated from the diameters of deposited particles. Deposited particles are observed by field emission type scanning electron microscope (FE-SEM) and particle sizes are measured by image analysis software (Image-J, NIH; Fig. 5).

To verify the characteristics of different atomization methods, three types of atomizers – electrospray, SAW atomizer, and mesh-type nebulizer (OMRON) – are compared in the same manner [11]. As the sample liquid, bovine serum albumin solutions of different concentrations were used. Concerning the deposited particle diameter, ESD is smallest and nebulizer largest. As the concentration of BSA increases, the diameter of deposited particle increases. The original drop diameter is estimated from the deposited particle diameter by assuming that the deposit is spherical and its density is 1. This may give errors to absolute diameter values, but comparison of the three methods is possible. The drop size of ESD is estimated to be about 1.0–1.6 μm, SAW-ED 1.4–2.2 μm, and nebulizer 4.3–5.7 μm (Table 1).

Atomization speeds of the three types of atomizers are also measured by atomizing 2.5 μL of sample and measuring the required time. The atomization speed for ESD is 0.01 μL s^{-1}, SAW-ED 0.3 μL s^{-1}, and nebulizer 7 μL s^{-1}.

Collection efficiency is measured by collecting deposited particle by dissolving in water. The quantification is carried out by Coomassie reagents (Pierce Co.).

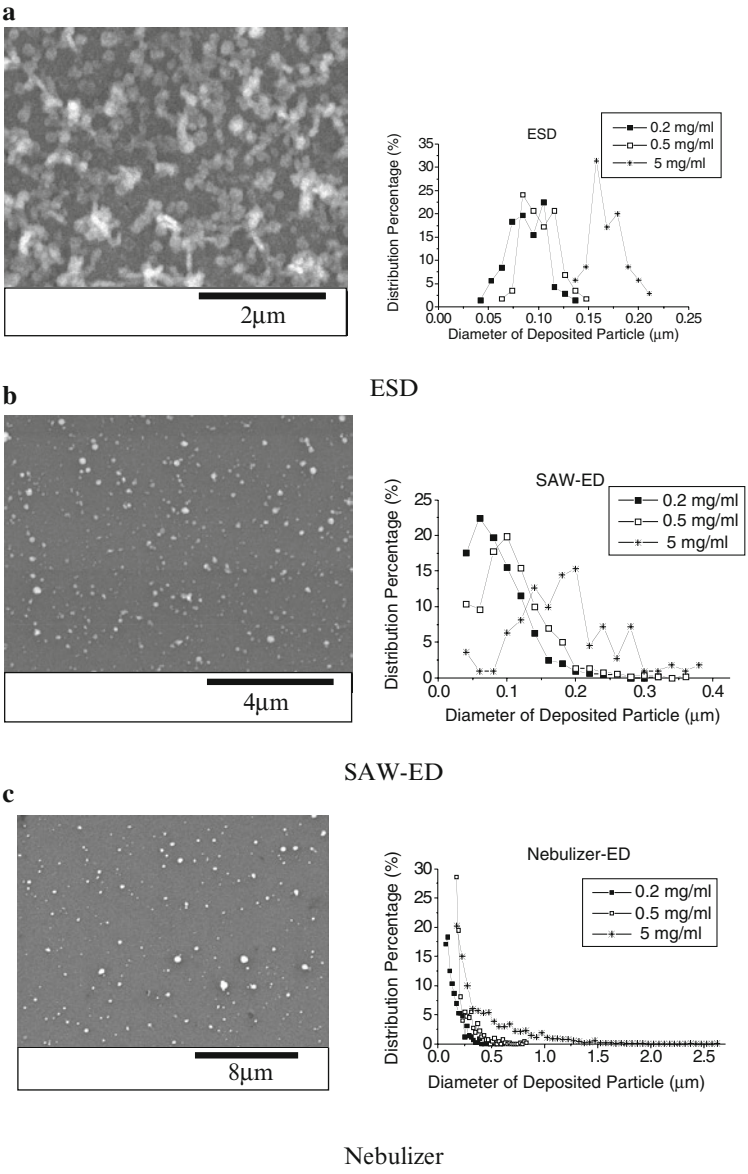

Fig. 5 FE-SEM image of deposited particle by and diameter distribution

The collection efficiency of ESD was about 15–30% depending on the concentration. That of SAW-ED was about 2% and nebulizer, less than 1%. One reason for this difference may be that ESD is a top-down process while other processes are bottom-up process (Fig. 6).

Table 1 Estimated drop diameter by different atomization methods

	Concentration (mg mL^{-1})	0.2	0.5	5
ESD	Linear mean diameter (μm)	1.5	1.3	1.0
	Sauter mean diameter (μm)	1.6	1.4	1.0
SAW-ED	Linear mean diameter (μm)	1.5	1.4	1.1
	Sauter mean diameter (μm)	2.2	1.9	1.4
Nebulizer-ED	Linear mean diameter (μm)	2.5	3.2	2.7
	Sauter mean diameter (μm)	4.3	4.7	5.7

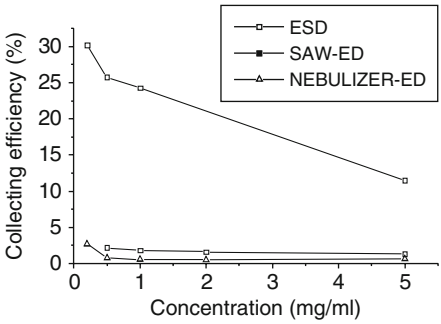

Fig. 6 Collection efficiency by different atomization method and sample concentration: **a** ESD; **b** SAW-ED; **c** nebulizer

Comparing those results of drop diameters, atomization speed and collection efficiency, ESD is a slow process but can generate excellent drop size distribution. Mesh-type nebulizer is a quite rapid atomizer, but drop size is quite large. SAW-ED has rather small droplet size and medium speed so it can be considered as a replacement for the electrospray atomizer.

3.3 High Frequency Atomization

Atomization experiments at even higher frequency have been carried out using same methodology [12].

According to the Lang's formula, diameters of atomized drops will decrease as the excitation frequency rises. SAW atomizers with resonant frequencies of 50, 75, and 95 MHz were fabricated and their characteristics tested through electrostatic deposition. Figure 7 shows FE-SEM images of particles deposited by 50, 75 and 95 MHz SAW atomizers. The diameters of deposited particle do not become smaller following Lang's equation. Figure 8 shows the diameter distribution of deposited particle based on the image analysis. Minimum required power for atomization increases at higher frequency and collection efficiency drops. This may be because of ultrasonic vibration absorbed in the liquid due to internal damping of water.

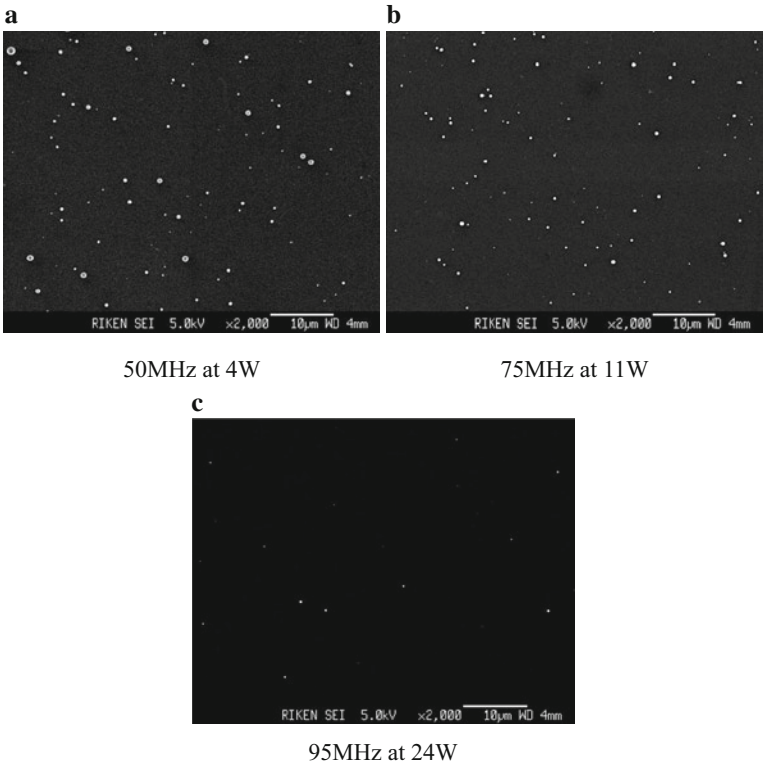

Fig. 7 SEM image of deposited BSA particles using SAW-ED method, magnification ×2000, 0.5 mg mL^{-1} BSA: **a** 50 MHz at 4 W; **b** 75 MHz at 11 W; **c** 95 MHz at 24 W

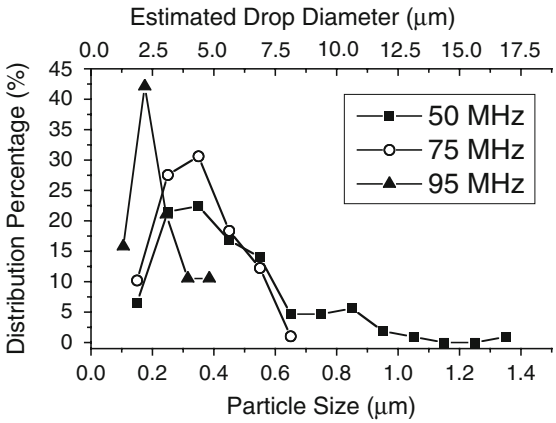

Fig. 8 Size distribution according to the excitation frequency

4 Applications of SAW-ED

4.1 Micro Pattern Formation

Micro patterns can be generated by using insulating stencil mask as in the case of ESD. A glass mask can be fabricated by abrasive jet machining method. The glass stencil mask will be charged soon after applying high voltage and starts to repel charged particles generated by the SAW atomizer. As a result, only a small amount of sample will deposit on the glass stencil mask and a thin film pattern is formed on the substrate. Figure 9 shows the patterns generated by SAW-ED with glass mask. Arbitrary pattern like (a) RIKEN logo or (b) regular pattern like microarray can be generated on the substrate.

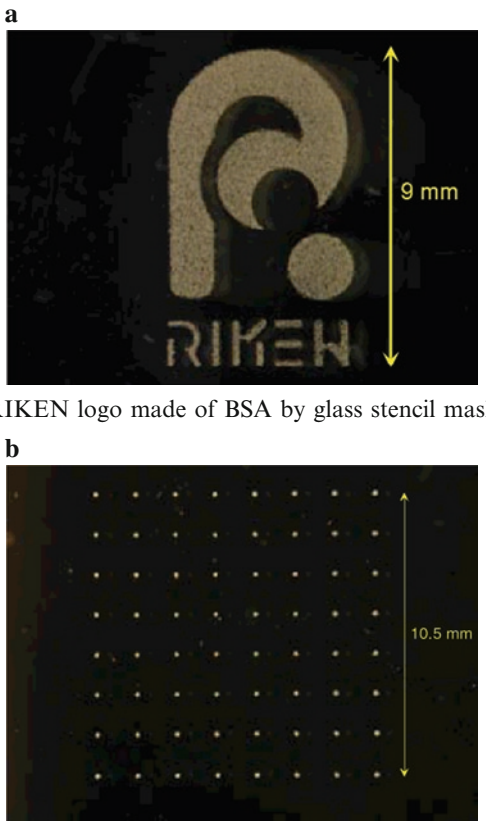

Fig. 9 Pattern generation by glass stencil mask: **a** RIKEN logo made of BSA by glass stencil mask; **b** micro array made of BSA by glass mask

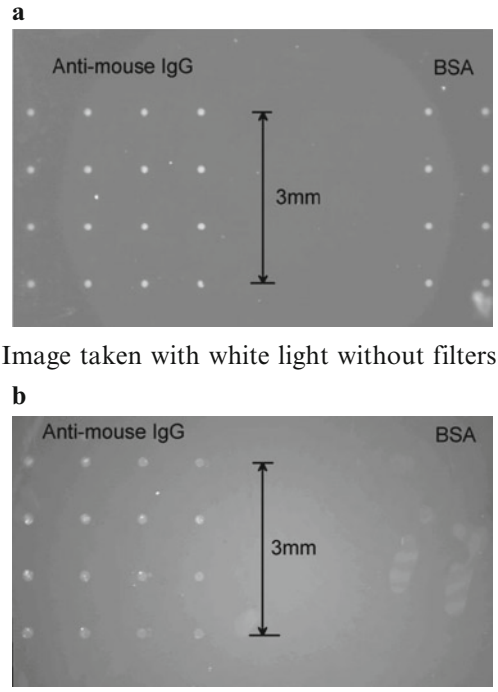

Fig. 10 Test of specific activity of SAW-ED-deposited immunoglobulin: **a** image taken with white light without filters; **b** fluorescent image of 490 nm excitation and 525 nm emission

4.2 Immunoassay Chip Fabrication

As an application to biochip fabrication, an immunoassay chip may be fabricated by SAW-ED [13]. There is concern about damage to the activity of proteins deposited by SAW-ED since it uses ultrasonic vibration and generates heat. To verify the specific activity of the deposited protein, a comparison was made with BSA and anti-mouse IgG. BSA solution (0.5 mg mL^{-1}) and anti-mouse IgG (0.5 mg mL^{-1}) was deposited on the ITO coated glass substrate. The deposited substrate was processed following a standard direct immunoassay protocol. After blocking by PBS with 2% skim milk, substrate was incubated in FITC-labeled mouse IgG in PBS (10 μg mL^{-1}) and then washed five times by PBS with 0.1% Tween20. Substrate was observed with fluorescent microscope. Figure 10a shows the white light image of the chip. Both BSA spots and anti-mouse IgG spots are observed as white spots, while Fig. 10b shows the fluorescent image and only the anti-mouse IgG spots are observed. Figure 11 shows the quantitative comparison of BSA and IgG. This indicates that the specific activity of anti-mouse IgG is well preserved after the SAW-ED process. Figure 12 shows the relationship between net intensity and concentration

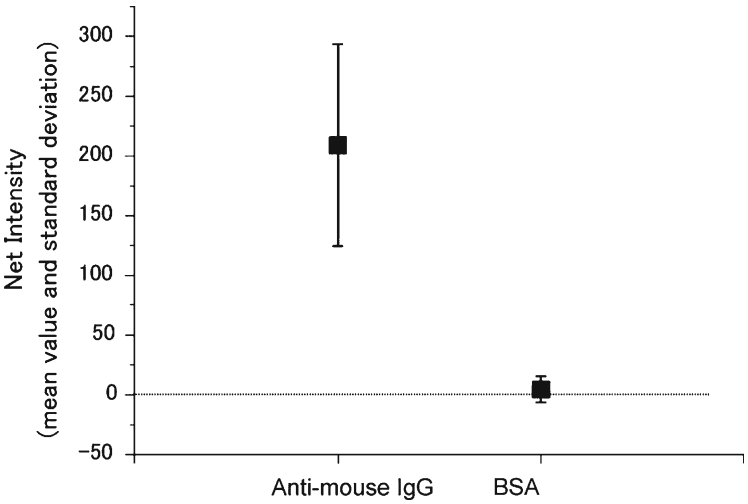

Fig. 11 Comparison of net intensity between anti-mouse IgG spots and BSA spots

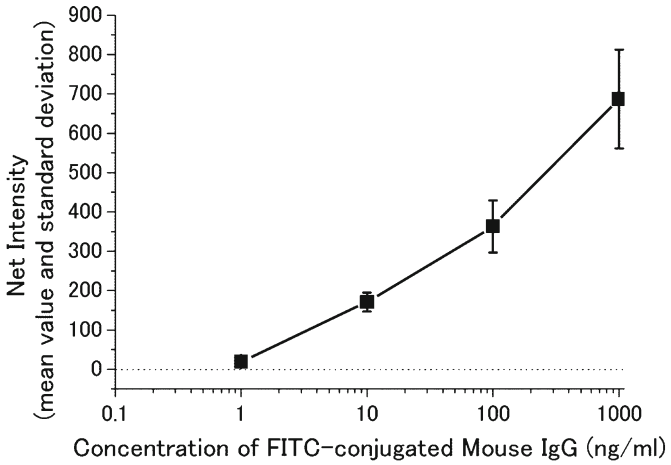

Fig. 12 Sensitivity of FIA detecting FITC-labeled mouse IgG

of FITC-labeled Mouse IgG. According to the results, sensitivity of about 1 ng mL^{-1} is obtained, which indicates that activity damage to anti-mouse IgG in this condition is small.

To test the specific activity of immunoglobulin deposited by SAW-ED, a cross activity test is carried out using four different kinds of IgGs. Anti-mouse IgG, anti-human IgG, anti-guinea pig IgG, and anti-bovine IgG are deposited as array on aldehyde-modified ITO glass substrate by SAW-ED. Four substrates are immersed in different IgGs (mouse, human, guinea pig, and bovine) labeled by horseradish

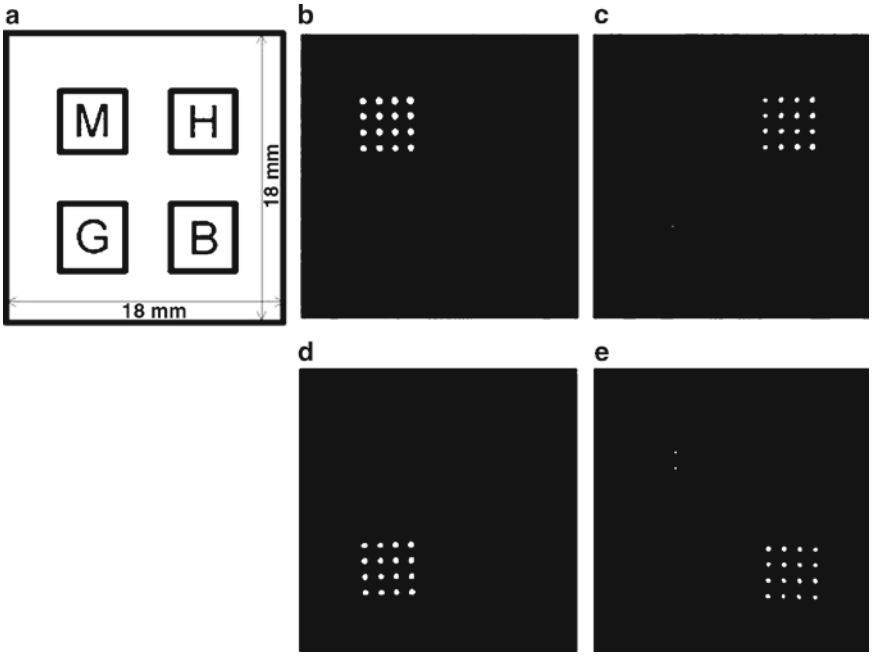

Fig. 13 Multi-component anti-IgG micro array and their specificity. The chip **a** has four area: *upper left*: anti-mouse IgG, *upper right*: anti-human IgG, *lower left*: anti-guinea pig IgG, and *lower right*: anti-bovine IgG. Each area has 4×4 spots. Images of cooled CCD camera incubated with **b** HRP-conjugated mouse IgG, **c** HRP-conjugated human IgG, **d** HRP-conjugated guinea pig IgG, and **e** HRP-conjugated bovine IgG using chemiluminescent reagent

peroxidase (HRP). Figure 13 shows the result image obtained by cooled CCD camera with chemiluminescent reagents (ECL advance, Roche). As can be seen from the image, there is no cross activity observed under these conditions, which indicates that specific activity of IgGs are well preserved during the SAW-ED process.

5 Conclusion and Future Prospects

SAW atomizer is examined as an alternative to electrospray atomization. This new technique can overcome the drawbacks of ESD although the performance is not fully compatible with electrospray atomization in terms of drop size and collection efficiency. There may be other solution of high frequency ultrasonic excitation using piezoelectric or magnetostrictive transducers. Still the SAW-ED method proved to be quite an effective means to fabricate thin films by nano-sized particle deposition of organic or biomacromolecules. The drop size of SAW-ED is estimated to be 1.4–2.2 μm which is quite acceptable for dry particle deposition.

The atomization speed is about 30 times faster than standard ESD, but collection efficiency is 10 times as small as that of ESD. Despite low collection efficiency, film deposition rate is faster than the ESD method.

Low collection efficiency of SAW-ED could be improved by adding auxiliary electrode, since SAW-ED is an upward deposition method while ESD is a downward deposition method. Temperature rise during the SAW atomization process is greatly reduced by a standing wave type atomizer with reflectors to concentrate vibration energy. At higher frequency, where smaller particle diameter is expected, there is room for lowering heat generation by vibration.

Besides application to immunoassay chip fabrication, there could be a number of applications for this technology. One is organic electronics including organic light emitting devices, organic semiconductors, and organic photovoltaic cells. Since many organic polymers have been shown to present conductive or semi-conductive properties, thin film and pattern formation using those material will be more important. Other applications including printers, particle production, and biochemical coating can also be considered.

Acknowledgments The author would like to thank Mr. Jungmyoung Ju for the experiments concerning SAW atomizer, Dr. Joon-wan Kim for the experiments concerning applications, and Dr. Kozo Inoue, who is the president of Fuence Co., Ltd. for the assistance in experimental apparatus construction.

References

1. Lemmo AV, Fisher JT, Geysen HM, Rose DJ (1997) Anal Chem 69:543–551
2. Haab BB, Dunham MJ, Brown PO (2001) Genome Biol 2(2)
3. Morozov VN, Morozova TY (1999) Anal Chem 71:1415–1420
4. Atomization Technology, Institute of Liquid Atomization and Spray Systems, Morikita-Shuppan, Tokyo, ISBN 4-627-67171-7 (in Japanese)
5. Abramov OV Original Publication year is 1998, although ISBN number says 90. (1998) High intensity ultrasonics. Moscow, Amsterdam, Gordon and Breach Science. ISBN 90-5699-041-1
6. Lang RJ (1962) Ultrasonic atomization of liquids. J Acoust Soc Am 34(1):6
7. Kurosawa M, Watanabe T, Futami A, Higuchi T (1995) Surface acoustic wave atomizer. Sens Actuators A 50(1–2):69–74
8. Chiba C (1990) Ultrasonic Spray. Sankaido, Japan, pp 207–210 in Japanese. ISBN 4-381-10036-0
9. Ju J, Yamagata Y, Ohmori H, Higuchi T (2008) Standing wave type surface acoustic wave atomizer. Sens Actuators A Phys 147(2):570–575
10. Rayleigh JWS (1945) The theory of sound, vol 2. Dover, New York, p 344. ISBN 0-486-60293-1
11. Ju J, Kim JW, Yamagata Y, Ohmori H, Inoue K, Higuchi T (2006) Comparison study on electrostatic deposition methods using electrospray, surface acoustic wave atomizer and mesh-type nebulizer, ICLASS, C4-10-211
12. Ju J, Yamagata Y, Ohmori H, Higuchi T (2008) High-frequency surface acoustic wave atomizer. Sens Actuators A Phys 145–146:437–441
13. Kim J-W, Yamagata Y, Takasaki M, Lee B-H, Ohmori H, Higuchi T (2005) A device for fabricating protein chips by using a surface acoustic wave atomizer and electrostatic deposition. Sens Actuators B Chem 107(2):535–545

Adv Biochem Engin/Biotechnol (2010) 119: 115–162
DOI: 10.1007/10_2008_44
© Springer-Verlag Berlin Heidelberg 2009
Published online: 27 March 2009

Electrospray Deposition of Biomolecules

Victor N. Morozov

Abstract This chapter describes the basic physics underlying the newly emerging technique of electrospray deposition (ESD) as applied to biological macromolecules. Fabrication of protein films and microarrays are considered as the most important applications of this technology. All the major stages in the ESD process (solution electrification, formation of a cloud of charged microdroplets, transformation of microdroplets into ions and charged clusters, deposition, and neutralization) are discussed to reveal the physical processes involved, such as space charge effects, dissipation of energy upon landing and neutralization mechanisms. Fundamentals of ESD are presented together with a discussion of potential practical problems in realizing ESD through dielectric masks. Retention of structure and functional properties of protein molecules in ESD-fabricated films and microarrays is discussed in detail.

Keywords Deposition, Electrospray, Microarrays, Proteins, Soft landing

Contents

V.N. Morozov
The National Center for Biodefense and Infectious Diseases, George Mason University, 10900 University Blvd. MS 4E3, Manassas, VA 20110, USA,
Institute of Theoretical and Experimental Biophysics, Russian Acad. Sci., Pushchino, Moscow region 142290, Russia
e-mail: vmorozov@gmu.edu

Abbreviations and Symbols

AFM	Atomic force microscopy
AP	Alkaline phosphatase
BSA	Bovine serum albumin
ES	Electrospray
ESD	Electrospray deposition
ESI	Electrospray ionization
ESI-MS	MS with electrospray ionization
Hb	Hemoglobin
HSA	Human serum albumin
MS	Mass spectrometry
PS	Polystyrene
QCMB	Quartz crystal micro-balance
STM	Scanning tunneling microscopy
A	Relative humidity
C_p	Heat capacity
D	Diameter (of capillary tip, hole)
G	Elastic (Young's) modulus
H	Distance, capillary – substrate
D	Diameter (of droplets, ions, clusters)
e	Elementary charge
F	Faraday constant
E	Electric field
E_m	Electrical breakdown strength
I	Current
I_c	Current though ES capillary
I_r	Current through collimating ring
P	Pressure (difference)

Q Charge
q_R Rayleigh limiting charge
r Radius, distance
R Characteristic size of charged cloud
S Surface area
T Temperature
t Time
U_c Potential on capillary
U_r Potential on collimating ring
V Voltage
v Linear velocity
Q Volumetric flow rate
W_e Impact energy
Z Number of charges
γ Surface tension
Δ Increment
ε Dielectric constant
ε_o Dielectric constant of vacuum
η Viscosity
θ Protein density
κ Conductivity
ρ 3D density of charges, space charge
σ 2D charge density on substrate
χ Mobility of ions
ω Air density

The purpose of this chapter is to provide a broad view of the physical processes involved in the electrospray deposition (ESD) technique. ESD includes four major stages: (1) generation of gas-phase micro- and nano-scale charged aerosols, (2) electrostatically controlled transport of the charged cloud to a substrate, (3) controlled deposition on a conducting substrate and (4) neutralization of the deposited material. While the first stage, common in ESD and in the electrospray ionization (ESI) method used in mass spectrometry (MS) has been discussed in many publications and reviews, the three other stages have never been analyzed in detail. In this discussion of the ESD process, focus will be placed in its application to fabrication of protein films and microarrays, both because of the author's personal experience and because fabrication of protein microarrays and protein microfilms are the most developed biotechnological applications of the ESD technology at present. In treating the problems we will limit ourselves to simple estimates in order to illustrate the relationship of different parameters which control ESD (conductivity, flow, rate, pressure, current, surface tension) rather than to present exact solutions, which are lacking for many critical stages in this new technology.

1 History of Electrospray Deposition

The first description of the phenomena of dispersion of electrified liquids into a cloud of charged droplets was made by the German scientist G. M. Bose in 1745 [1]. Later, Lord Rayleigh explained the basic physics underlying this electrodynamic dispersion in his analysis of the stability of charged droplets [2]. More than a century later different realizations of the electrospray phenomena were described by a number of authors [3–6]. At the same time in the early twentieth century, several patents were issued for applications of ESD in painting [7–9]. These applications of electrospraying as well as other technical applications for pesticide spraying, ion thrusters and fuel dispersion in engines are reviewed in a number of monographs [10, 11].

Production of thin sources for radioactivity measurements was among the earliest applications of ESD [12–15]. This method attracted the attention of physicists due to its safety (deposition could be performed in a closed chamber), easy scaling down to minute amounts of material, and its economy (100% transfer to a surface without loss). Large surfaces could be uniformly coated with a thin layer, or deposition could be localized by introduction of a dielectric mask, collimator, or protective ring. Later, ESD was used to prepare samples for mass spectrometry (MS) with laser and plasma desorption–ionization [16–18]. We shall concentrate further on ESD applications where biological macromolecules are deposited, leaving aside numerous ESD applications in the preparation of polymer coatings [19–21], in formation of ceramic layers [22, 23], in the deposition of ink [24] and others.

ESD of biological molecules became possible in the second half of the twentieth century when Dole et al. [25–27] and Alexandrov et al. [28, 29] independently developed the ESI method for generation of molecular ions for MS. These works heralded a renaissance in the electrospray technology by stimulating profound studies in both the physical mechanisms underlying the ESI process as well as in the related problem of retention of the structure of complex biological polymers such as protein molecules as they were converted to gas-phase ions. A number of excellent reviews summarize the results of these studies [30–36].

It was established in these studies that when sprayed under nondenaturing conditions (neutral pH, absence of denaturants like organic solvents) protein ions acquired fewer charges in comparison to the same protein ions sprayed under denaturing conditions, which supported the idea of retention of a compact protein structure under nondenaturing conditions. In addition, in many cases ions with masses corresponding to a sum of the mass of protein molecule plus the mass of its specific ligand were found in the MS spectra, indicating that weak noncovalent complexes may survive the ESI process [37].

These findings stimulated early attempts to combine the electrospray process with deposition in preparation of biological molecules for microscopy. For example, DNA and protein molecules were deposited for imaging by scanning tunneling microscopy [38, 39]. Whereas Thundat et al. [38] electrosprayed a DNA solution directly onto a conductive substrate, this author [39] interposed a protective sheet, containing an ion canal, between the electrospray source and the substrate onto

which the protein ions were deposited. The greatest concern in these first ESD works was retention of structural properties of the deposited molecules. Though structural integrity of protein molecules was retained in Morozov et al. [39], Cheng et al. revealed numerous altered DNA molecules in their electrophoretic analysis of plasmid DNA electrodeposited onto a dry stainless steel electrode [40]. Heavy destruction of both protein ions and the surface itself were reported after collisions of accelerated protein ions with mica and graphite [41–45]. However, similar deposition in vacuum without application of an excessive potential to the substrate resulted in a soft landing of protein macro-ions in vacuum after separation in MS: the structural and functional activity of proteins and other biomolecules were retained [46–53].

In the late 1990s, the first applications of ESD technology in the manufacture of protein films [54] and protein and DNA microarrays [55, 56] were described. So far, the ESD technology has been commercialized by one Japanese company (Fuence Co., Ltd., Tokyo, Japan) which manufactures an ESD-based microarrayer and a device for preparation of free protein samples for screening protein interactions with metabolites.

2 Fundamentals of the Electrospray Deposition Technique

ESD technology involves a good piece of physics and physical chemistry, both of which underlie atomization of solutions, formation of ions and charged nano-clusters, motion of charged clouds to the substrate, landing on a surface and transfer of charges to the substrate or to a layer of deposit (neutralization). Very low currents, extremely high electric fields and injection of charges make the situation rather complex and difficult to predict based on conventional properties of dielectrics. Many of these factors are not well studied but need to be addressed here because they are occasionally responsible for problems in practical applications of ESD technology.

2.1 General Description of the ESD Process

Liquid to be electrosprayed is placed into a capillary as illustrated in the schematic presented in Fig. 1. A voltage is applied to the liquid either by insertion of a metal electrode (e.g., platinum wire) or by making the capillary itself from a conducting material (stainless steel, conducting plastic). A high-voltage power supply (5–20 kV), a nano-ammeter to measure current in the range of 0–1 μA and a low-power laser to observe the torch (plume) of ejected microdroplets provide a minimum system to be used in deposition. Other elements enhancing the efficiency of deposition (collimating ring), improving the distribution uniformity (perforated cylinder), or protecting from dust (chamber) will be introduced later.

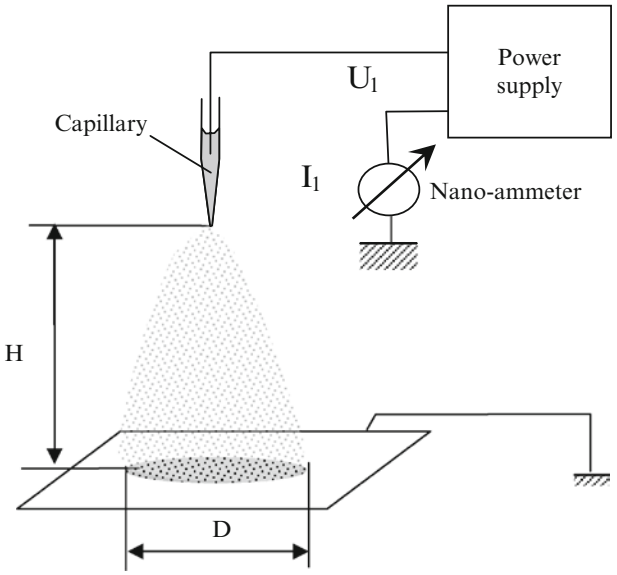

Fig. 1 Schematic of ESD process

2.2 Generation of Charged Products

2.2.1 Electrification of the Solution Surface

Electrification of the solution surface is the physical process which initiates a sequence of events resulting in deposition of a nonvolatile dissolved substance. In the majority of ESD applications this is accomplished by placing a solution in a capillary which has an electron-conductive element in its design. A number of different designs for the ES capillary have been described [54, 57–59] and an excellent review of recent developments in ESI sources has been published recently by Manisali et al. [60].

Most early designs were made from a thin stainless steel hypodermic needle with a rounded edge to increase the onset of corona discharge [57]. Quartz or glass capillaries with metal coating appeared as ES sources when MS began to be used as a detector for liquid chromatography [60]. In another design, an electrode made of a noble metal wire is inserted into a capillary made of a nonconducting material. The simplest design of this kind has been described by Aksyonov and Williams: it is composed of a disposable pipette tip with a platinum wire inserted [61]. Ultrasound-assisted electrospraying without a capillary has been also described [62] and this technique allows the flow rate of sprayed liquid to be increased ~100 times.

The author has compared the performance of three different ES capillary designs [54] in deposition of alkaline phosphatase (AP) on a Quartz Crystal MicroBalance

(QCMB) electrode. After measuring the deposition mass on QCMB, the deposit was dissolved and the specific activity of the deposited AP was determined from each capillary. It was found that deposition from a capillary with an internal electrode, schematically presented in Figs. 2 and 3, better preserved enzyme activity than capillaries with an external conducting coating or a liquid bridge. Therefore, this design was used in all our further experiments. It consists of a glass capillary 1.57 mm in OD, 25–30 mm long, with one end pulled to 20–50 μm in OD using an automatic micropipette puller. After pulling, the external surface of the capillary is made hydrophobic by exposure to a vapor of dimethyldichlorosilane in nitrogen for 10 min followed by baking at 100–120 °C for 1–2 h. Hydrophobization substantially reduces formation of droplets at the end of the capillary and reduces tip contamination with biological materials.

As shown schematically in Fig. 2, the capillary (A) is placed in a holder and is fixed with a piece of silicon tube (D) on a stainless steel tube (C) into which a platinum wire (B) is inserted. The stainless steel tube serves as a connector to the electrode and as a means by which the internal pressure in the capillary may be changed by applying pressure or pulling a vacuum via plastic tubing (H) connected to the rear end of the stainless steel tube. The tube (C) is attached to another tube (F), 4–5 mm in diameter, which is inserted into another long tube (G). The capillary is pulled inside the tube (G) to protect it upon installation into the ES chamber. Conducting tubes G and F, in contact with the hypodermic needle (C), are also used to connect the capillary to a power supply. Normally, solution is not allowed to contact the stainless steel tube in order to avoid contamination, though solution may be fed via stainless steel tube (C) and plastic tubing (G) if necessary. The platinum wire is flamed to clean its surface before insertion into the solution. The capillary is usually filled with solution by suction through the tip. This method of capillary filling ensures that no large dust particles capable of plugging the tip during ESD enter the capillary.

To avoid the risk of electric shock when using a powerful DC high-voltage power supply it is recommended to introduce a 20–50 MΩ high-voltage resistor (or 8–10 resistors, 5 MΩ, 0.25 W, connected in a series) between the power supply and the capillary to limit the current.

Because the flow rate in ESD usually does not exceed 1–2 μL min^{-1}, many attempts to increase the rate as well as to multiplicate ESI-MS analysis have

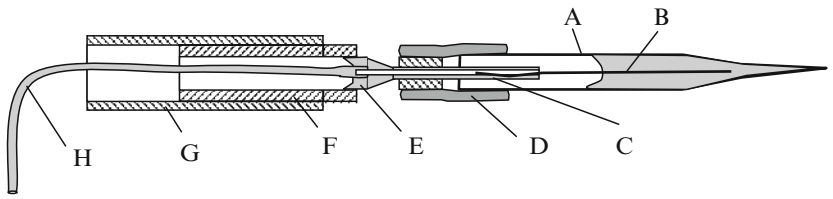

Fig. 2 Schematic of ES capillary with an internal electrode. The components are glass capillary (A), platinum wire (B), stainless steel tube (C), rubber O-ring (D), end of hypodermic needle (metal) (E), metal tube (F), metal tube (G), silicon tubing (H)

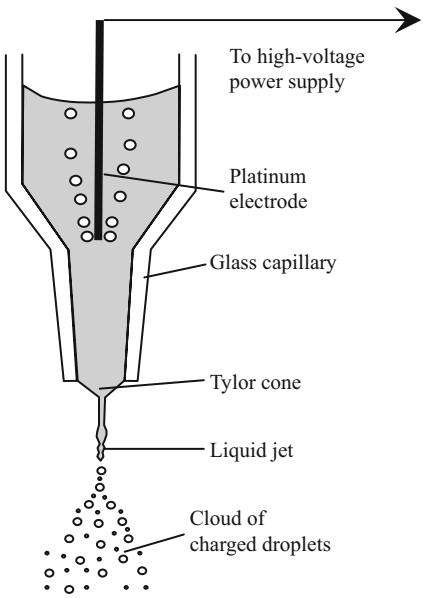

Fig. 3 Electrospray from a capillary with internal electrode

recently been performed. Some of these are based on the use of multiple tips fabricated as multiple channels in a microfluidic chip [63], others as grooves at the tip of a stainless steel needle [64], or as a multinozzle structure fabricated from a silicon wafer using planar technology [65]. Multinozzle sprayers may be supplied with additional electrode-extractors having an array of holes placed over a corresponding array of nozzles [66, 67] to increase ES efficiency. An array of 96 tips molded in plastic has been described for high throughput MS analysis [68].

2.2.2 Electrochemical Reactions at the Capillary Electrode

Because liquid electrification is produced by noncompensated free ions and because the process of electrification should be supported while these charges are constantly removed with charged microdroplets, some electrochemical mechanism which transforms a current of electrons into a current of ions continuously should operate in each ES capillary. The details of the electrochemical reactions have been described in a number of reviews and original publications, mostly devoted to ESI [69–73].

We will only consider ESI in aqueous solutions since most biological macromolecules denature in organic solvents. In contrast to the majority of organic solvents which cannot generate ions and have a limiting current for each flow rate (due to complete separation of ions which are present in the solvents as impurities [74]),

ions in water are generated both by dissociation of water molecules and by electrochemical reactions on the electrode. We will further consider only water oxidation, because ESD in aqueous solutions occurs almost exclusively at a positive potential (see other possible electrochemical reactions in [72]).

At a positive potential, the rate of proton generation during electrochemical reactions at the electrode can be estimated from Faraday's law:

$$d\mathrm{H}^+ / d\mathrm{t} = I/F, \tag{1}$$

where I is the ES current and F is the Faraday constant (9.65×10^4 C mol^{-1}). If all these protons were equally distributed within the liquid in the capillary at a volumetric flow rate, Q, through the ES capillary, the pH of the solution would change by

$$\Delta\mathrm{pH} = -\log(1+I/FQH_0^+), \tag{2}$$

where is $[H^+_o] = 10^{-\mathrm{pHo}}$ is the concentration of protons in the initial solution with pH_o. At I = 100 nA and Q = 1 μL min^{-1}, the pH of the unbuffered water solution should change from 7 to 4.2 [69]. This estimate is based on the assumption that protons will be evenly distributed inside the liquid, and the latter assumption is only valid if other ions are present in the liquid at concentrations much higher than the concentration of generated protons ($[H^+] = I/FQ$ = 62 μM in the example above). If the generated protons are the predominant unbalanced ion species in solution (no salt added) they will quickly reach the Taylor cone without accumulation throughout the liquid. Thus, desalination of solutions by dialysis is one way to avoid large changes in solution pH upon ESD.

The presence of buffering compounds in the sprayed solution will also prevent pH changes. In ES experiments with a 1 mM aqueous bromothymol blue solution, pH = 7.0, we did not see any changes in the solution color in the capillary at a current as high as 200 nA, provided a good spraying plume was observed. Small microdroplets of oxygen were observed to emerge from the platinum wire (see schematic in Fig. 3), indicating electrochemical oxidation of water. Occasionally, however, it was observed that current continued to pass without a visible ES torch. In these cases a yellow cloud quickly formed at the end of the Pt electrode and rapidly moved to the capillary end, indicating acidification of the bromothymol blue solution in the capillary. This phenomenon of current without spray was first described by Zeleny [5]. Drastic and rapid acidification of the solution may result from ignition of the corona discharge at the water meniscus in the absence of ES. A good practical test for this is to probe how the ES current responds to a slight increase in voltage. In contrast to the normal current–voltage characteristics, which are smooth (see Fig. 4), a sudden severalfold increase in the current/voltage derivative is indicative of ion emission from the capillary tip. We will discuss potential corona involvement in the ES process below.

In view of the possibility that current can flow through the capillary without ES it is important to monitor the ES visually, e.g., by shining a laser beam through the electrospray chamber (or a transparent window in the chamber) and observing the ES plume or torch by a low-power microscope.

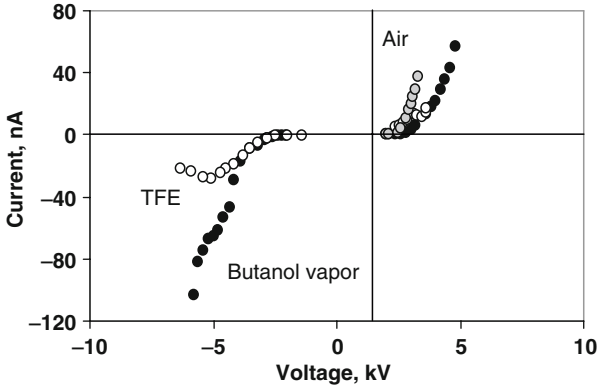

Fig. 4 Current–voltage dependence upon spraying water in air (*grey circles*), in air saturated with 2,2,2-trifuoroethanol vapor (*open circles*), and in butanol vapor (*solid circles*). No stable ES of water was achieved in air (*grey circles*) at the negative voltage

2.2.3 Formation of Microdroplets; Taylor Cone

Charges on the liquid surface at the end of the capillary repel each other and expand the solution/gas interface so that a cone is formed, as shown in Fig. 3, when the electrostatic force is counter-balanced by the surface tension of the liquid, resulting in zero hydrostatic pressure inside the liquid, as first observed by Zeleny [5]. It has been shown that in the cone jet mode monodisperse droplets of water predominate [74, 75]. We shall further consider only cone jet mode since it has been used in most of the practical ESD applications. It was demonstrated that a stable ES can only be achieved at certain combinations of the flow rate and voltage [74, 76]. These combinations form the so called "stability islands."

The cone, named after Sir Geoffrey Taylor who first described it [77], has a fixed angle of 98.6° at equilibrium at the minimum flow rate. The process of cone formation and behavior at different flow rates has been analyzed in multiple publications [78, 79]. Unfortunately, it was concluded that the spraying characteristics at low flow rate of the most practically important liquid, water, which has a high dielectric constant and low viscosity, cannot be described theoretically [79]. In addition, most analysis has kept the volumetric flow rate, Q, fixed while we found that ESD with a fixed flow rate suffers from occasional ejection of macro-droplets from the capillary tip, which ruins the deposited material. For this reason we abandoned this technique in favor of ESD from a free capillary or from a capillary to which a low positive pressure is applied. The author has not found a theoretical analysis of ES under such conditions. Still, many laws governing ES do not depend on the ES regime.

Electrospraying starts when the voltage on the capillary reaches a minimum critical value scaled as [32]:

$$V_{\min} \sim [\gamma D / \varepsilon_0]^{1/2}, \tag{3}$$

where γ is the surface tension of the liquid, D is the diameter of the capillary tip, and ε_o is the permittivity of vacuum. One can see from (3) that liquids with high surface tension, like water, will require larger voltages. The voltage, however, may be increased in a gas atmosphere to only a certain limit before corona discharge begins. To avoid this discharge, the gas phase should contain high-voltage breakdown gases, such as oxygen, carbon dioxide [74, 80] or air. Pure nitrogen, noble gases, or gases under a reduced pressure should be avoided because of the low voltage onset of corona discharge. Corona onset occurs at a lower voltage at the negative electrode than at the positive one [81]. This is the main reason why water solutions are difficult to electrospray in the negative mode. Previous attempts to perform ESI of water solutions at negative potential were performed in a carbon dioxide atmosphere [74, 80] where the onset of corona discharge is larger than in air. Equation (3) also explains why water solutions are more difficult to electrospray at positive mode as compared to solutions in alcohol or other organic solvents with lower surface tension. It was experimentally found that electrospraying of water occurs at higher voltages on the same capillary as compared to other organic solvents [82].

As follows from (3), the voltage may be reduced by using thinner tips and choosing solvents with a lower surface tension. It is a common practice in electrospinning from polymer water solutions to add a low concentration of detergent [83–85]. Some authors also added detergents to protein solutions to be electrospray deposited [56, 86, 87]. Below we present another simple way to reduce the surface tension of water solutions and to make ESD more rapid.

2.2.4 Effects of Volatile Surface-Active Compounds in ES of Water Solutions

Stoilov [88] has recently demonstrated that vapors of certain fluorocarbon compounds can dramatically reduce water surface tension. His estimates showed that adsorption of these vapors at the water interface proceeds on the microsecond time-scale. Exploitation of these effects may make the negative ES mode of aqueous solutions in air possible and also make ESD easier and quicker.

We tested different volatile organic solvents for their effects on ES of water. The solvent was applied to a piece of Whatman paper and introduced into a closed ES chamber. After solvent evaporation, water was electrosprayed from a glass capillary at negative and positive voltages. No ES torch was observed from pure water at negative voltage in pure air, only occasional large droplets at high voltage. However, evaporation of 2,2,2-trifluoroethanol resulted in a very bright torch under otherwise similar conditions. This substance is known to reduce the surface tension of water from 0.0072 to 0.003 N m^{-1} when added in 10% mole fraction [89]. A similar, though less pronounced, effect was observed when acetone or ethanol vapors were introduced into the chamber. A less bright plume was observed for 2-propanol, 2-butanol and 1-octanol vapors. No ES plume was observed in vapors of 2-aminoethanol, formamide, acetonitrile, 1,2-ethanediol and

o-xylene, as well as in saturated water vapor. Thus, introduction of a hydroxyl or amino group at the 2 position of ethanol results in a complete disappearance of the stimulating ability of vapors of ethylene glycol, and aminoethanol, respectively, presumably due to loss of surface activity.

Simple estimates of the surface tension in the presence of vapor were made by counting droplets slowly emerging from a capillary at a constant pressure difference. Using Taft's equation:

$$W_d = \pi D\gamma, \tag{4}$$

where W_d is weight of the droplet and D is the capillary diameter. We calculated that when dropping into a jar filled with vapors of 2,2,2-trifluoroethanol, the water surface tension, γ, decreases by 23% while only 8% decrease in the surface tension was observed in contact with ethanol vapor. This difference correlates well with the effects these two compounds produced in ES.

It is interesting to mention that spraying in the negative mode in the presence of 1-octanol vapor produced a pulsating torch which appeared for a fraction of a second and then disappeared for about 1 s. This phenomenon was observed only with 1-octanol vapor as vapors of other alcohols produced a stable, constant spray. We speculate that the high boiling point of octanol (195 °C) and low vapor pressure even at saturation (0.05 Torr at room temperature) makes 1-octanol adsorption onto water surface slow. Surface tension decreases and ES starts only after a certain amount of 1-octanol is adsorbed. When 1-octanol is removed together with the ejected microdroplets, the surface tension increases above the threshold level, the ES process stops, and the whole cycle is repeated again.

The voltage–current characteristics of ES in the presence and absence of 2,2,2-trifluoroethanol and butanol are presented in Fig. 4. In the positive mode the presence of solvent vapors results in a considerable decrease in current at the same voltage. Since the visible brightness of the ES plume was greater in the presence of the solvent vapors, one can conclude that milder electric conditions are required when ES occurs in the presence of vapors. Using the same capillary at the same voltage, a much larger current is observed in the presence of butanol than in the presence of 2,2,2-trifluoroethanol. This could be accounted for by a larger reduction in the surface tension produced by the fluorocarbon compound as compared to butanol. It is interesting to note the saturating character of the current dependence on voltage in the presence of trifluoroethanol vapor: an increase in the voltage above 5 kV is not accompanied by a further increase in the current. This could be explained by a certain voltage-independent rate with which trifluoroethanol vapor is adsorbed onto the water surface. However, it is difficult to explain why this saturation is not observed in butanol vapor.

The phenomena just described may be practically used to accelerate the ESD process, to perform ESD under milder conditions, and to enable use of the negative mode from water solutions. Of course, possible effects of alcohol vapor on the functional activity of ES deposited biological molecules should be evaluated before

using this method. One should also take care not to increase the vapor content over the explosive limit and avoid inhalation of the vapors.

2.2.5 Effects of Pressure on ESD

As mentioned above, using a syringe pump to feed the electrospray capillary at a fixed flow rate has the drawback of occasional spills. It is safer to let ES proceed freely and accelerate the process, if necessary, by applying pressure inside the capillary. As we demonstrate below, the interdependence of current and flow rate under these conditions is different from those established for ES regimes at fixed flow rate [78, 79, 90].

Device for Direct ESD Monitoring

A simple device has been designed to monitor the rate of ESD by measuring changes in the resonance frequency of a quartz crystal (AT-cut) connected to a Colpitts transistor generator. The grounded electrode of the quartz crystal was exposed to ES products through a hole in an aluminum foil guard which was also grounded as seen in the schematic in Fig. 5. A perforated cylinder plastic screen was placed on the aluminum foil to evenly distribute the deposit (the action of this screen will be described later). As seen from Fig. 5, only a small portion of the electrosprayed product is collected on the quartz electrode; the rest is deposited on the aluminum foil. This allows the rate of deposition to be monitored for a lengthy period of time.

The typical dynamics of frequency changes upon ESD of a solution at different currents is presented in Fig. 6. The arrows indicate timing of current changes.

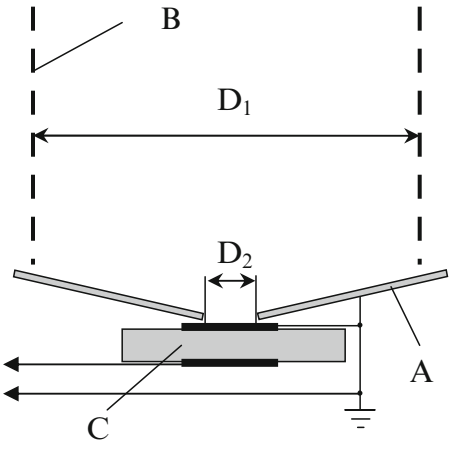

Fig. 5 Schematic of an arrangement used to monitor the ESD rate under different conditions using a quartz crystal microbalance. The cylinder perforated screen was made of a polyester mesh CMY-0500 (Small Parts, Inc., Miami Lakes, FL). The cylinder had a diameter of D_1 = 30 mm. The diameter of hole, D_2 = 5 mm

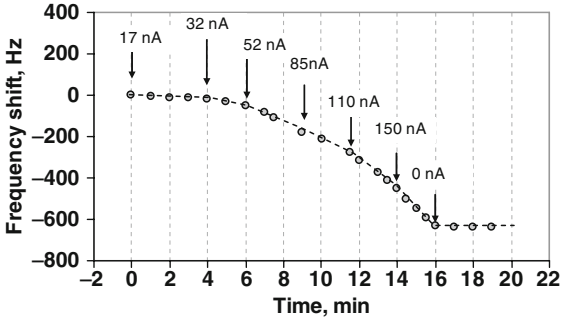

Fig. 6 Changes in the resonance frequency shift of a quartz resonator with the fundamental frequency of 12,251,740 Hz following ESD of a 0.8% sugar solution containing 2 mM KCl at different currents. According to the Sauerbrey equation [91], the quartz resonance frequency changes by 1.65 Hz as a 1 ng mass is deposited per electrode area of 0.196 cm^2

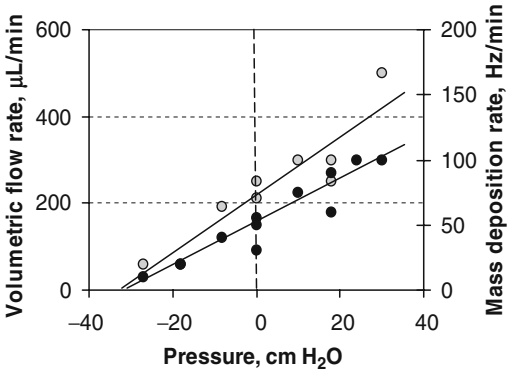

Fig. 7 Effect of pressure applied to the interior of the ES capillary on the ESD rate measured by flow rate (*grey circles*) and by mass deposition rate (*filled circles*). A 0.8% sucrose solution in water containing 0.2 mM KCl was sprayed at +4.0 kV. The current changed between 23 and 30 nA throughout the experiment

Dashed lines show the deposition rate at each current used. No external pressure was applied to the ES capillary during this experiment. It is clearly seen from Fig. 6 that an increase in the current drastically accelerates the deposition rate.

Effect of Pressure on ESD Rate

The rate of ESD as a function of pressure applied to the capillary may be studied either by measuring changes in the position of the water meniscus inside the capillary or by monitoring the rate of accumulation of solid deposits on the QCMB, as described above. As shown in Fig. 7, both techniques give a linear dependence of the ESD rate on the applied pressure. When negative pressure is applied to an aqueous

solution inside the capillary, both the deposition rate and the flow rate reach zero at the same pressure, $P_E = -32$ cm of water. This external pressure exactly counterbalances the electrostatic pressure under the Taylor cone, thus stopping ES.

Knowledge of this electrostatic pressure is of practical important since it allows calculation of the hydrodynamic flow of viscous liquids in the ES capillary and reliable design of the ES capillary. It was noted that upon application of positive pressure a brighter plume is observed, indicating that larger droplets are generated. This conclusion is in good agreement with the data obtained in experiments with fixed flow rates [90]. At a positive pressure exceeding 30–40 cm of water a jet of macroscopic droplets (with a diameter approximately corresponding to the ID of the capillary, 20–30 μm) was seen inside the plume of micron-sized droplets. It is important to note that while the flow rate increased sixfold upon a pressure change from −20 cm water to +30 cm water, the current increased by only 50%, indicating that much less charge was attached per unit volume of dispersed water at the high positive pressure inside the capillary. In practice, pressure is a convenient parameter for control of the rate of deposition.

2.2.6 Effect of Current on Deposition Rate

When the deposition and flow rates are plotted vs current at different liquid conductivities, a series of linear functions emerges, as illustrated in Figs. 8a,b. This indicates that the charge per unit volume of liquid remains constant under different currents (voltage) for the same liquid at a fixed pressure. Since the extent of droplet charging is directly connected with protein denaturation and unfolding upon ES [92], one may expect that an increase in the ES current does not change the charging state of proteins. It is, therefore, safe to increase the rate of deposition by increasing the current until this proportionality between the rate and current is fulfilled. The flow rate deviates from a linear dependence on the current only when

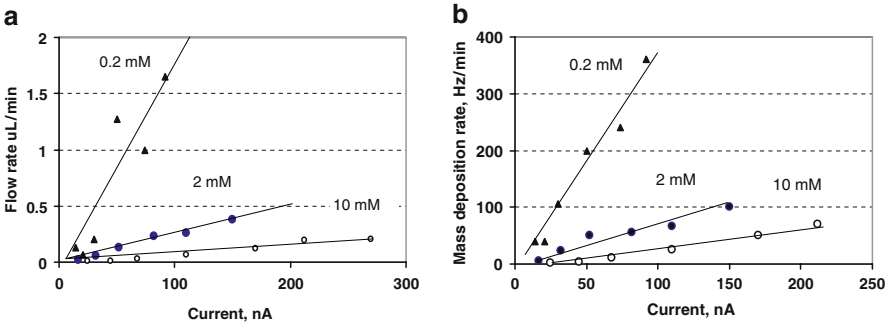

Fig. 8 Flow rate (**a**) and rate of mass deposition (**b**) as a function of current. No external pressure was applied to the capillary filled with a 0.8% sucrose solution. KCl was added to the final concentration indicated over each line in the figure

the latter exceeds 250 nA. This is due to corona discharge involved in the ES process under high voltage which results in notable damage of protein function [54]. Thus, measurement of the dependence of the flow rate on current can be practically used as a diagnostic means for keeping the ESD process in a safe zone.

It is interesting to note that the linear dependence of flow rate on current in ES from free capillaries contradicts the classic scaling law obtained for a fixed flow rate [79, 93, 94], which predicts that a stable ES is obtained when the flow rate, Q, grows as a square of the current (I):

$$Q \approx I^2 / \gamma \kappa \varepsilon, \tag{5}$$

where κ is the electrical conductivity, and ε is the electric permittivity of solution. A linear relationship between the electric current and the flow rate has been predicted for a highly polar liquid at a low flow rate by Higuera [95] as a result of polarization of the liquid surface in the electric field.

2.2.7 Effect of Solution Conductivity

The conductivity of protein solutions greatly affects the ESD rate. We note from Figs. 8 and 9 that much larger currents should be allowed in ESD of 10 mM KCl solutions in order to obtain a rate of deposition comparable with that for low-conducting solutions. Despite some deviations at high conductivities, the flow rate at a constant current may be described as inversely proportional to the solution conductivity in accordance to the scaling law presented above.

It is worth noting that, although the total charge per unit volume is preserved in ES (due to the linear dependence of flow on current), the extent of charging per unit volume is expected to increase for solutions of higher conductivity. According to theoretical predictions, the diameter of primary mother droplets, *d*, generated in ES is the following function of conductivity and flow rate [79, 93, 94]:

$$d = (Q\varepsilon / \kappa)^{1/3}. \tag{6}$$

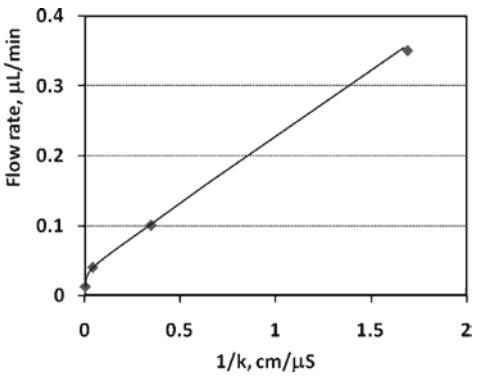

Fig. 9 Rate of electrospraying as a function of solution conductivity sprayed at a constant current, I = 23 nA

Thus, the increase in conductivity together with the decrease in the flow rate observed in ES of highly conductive solutions (see Figs 8 and 9) is expected to result in a considerable decrease in the droplet diameter. Direct observations support the expectations: it was noted that ES of a 10-mM KCl solution was invisible even upon illumination with a beam of a 5-mW He/Ne laser, though changes in the resonance frequency of QCMB as well as changes of liquid volume in the ES capillary indicated that the ESD proceeded slowly. We speculate that the 10-mM KCl solution ($\kappa = 1.41$ mS cm^{-1} at 25 °C) was dispersed into droplets with a diameter much smaller than 1 μm; such small droplets scatter laser light negligibly. Though the interval of conductivities of solutions for which ES is applicable is shown in the literature as 1 μS cm^{-1} to 10 mS cm^{-1} [79] we found that the ESD becomes very slow at conductivity of 1–2 mS cm^{-1}. It is expected that at a conductivity larger than 10 mS cm^{-1} ions will directly escape from the meniscus point [79].

2.2.8 Is Corona Discharge Involved in ESD?

The phenomenon of corona discharge from water tip was originally studied by Zeleny [4–6], though he did not made a clear distinction between emission of charged droplets (electrospraying) and emission of ions (corona discharge). Early descriptions of ES phenomena often mentioned a diffuse glowing within the plume of droplets [96].

Corona discharge from a negatively charged water droplet was studied in a number of publications [97–99] and was even used to produce ozone in discharge from aqueous Taylor cones [100]. At high ES currents (30 μA), spectroscopic analysis of glowing during ES became possible [101] and showed spectral emission lines of the elements dissolved in the water. At the much lower current (~1,000-fold less than in Jaworek et al. [101]) typically employed in ESD, glowing is not observed. Nevertheless, data concerning the effects of gas phase composition on ES lead to the conclusion that a mild corona discharge always accompanies the electrospray and that it actually stabilizes electrospraying and allows its onset at a lower voltage [74, 102, 103]. Ozonolysis of phospholipids in ESI-MS [104] and oxidation of polypeptides during ESI [105] provide another set of evidence for the presence of reactive corona products in ES. The idea behind corona involvement in ES is that a leaving droplet in a strong electric field in the vicinity of the Taylor cone is polarized (in addition to being charged) to the extent that corona discharge starts and droplets lose part of their charges not through coulomb fission but by corona discharge [97, 100].

The question of whether corona discharge is involved in ESD is especially important for deposition of fragile biological macromolecules. It was found in our experiments on fabrication of protein films by the ESD technique that addition of a radical scavenger, 2-mercaptoethanol, to a protein solution results in a better retention of functional properties of the ES deposited protein [106]. This substance is also known for its protecting function against radiolysis damage [107, 108].

2.3 *Formation of a Charged Aerosol from a Cloud of Charged Droplets*

If ES is performed at a low solvent pressure, e.g., at low humidity in case of ES of aqueous solutions, the microdroplets ejected from the Taylor cone evaporate on their way to the substrate. When the size of the droplet approaches a Rayleigh limit of electrostatic stability, a train of daughter nano-droplets is ejected in a process known as "coulombic fission" [79, 109, 110]. The maximum charge, q_R, which a droplet of liquid with the surface tension, γ, and diameter, d, may reach before fission occurs was first estimated by Lord Rayleigh as [2]

$$q_R = (eZ)_{max} = 8\pi(\varepsilon_0 \gamma d^3 / 8)^{1/2}, \quad (7)$$

where e is the elementary charge and Z is the number of such charges on the droplet. Further evaporation of the mother droplet and smaller daughter droplets interrupted with a series of fissions results in formation of a cloud of nano-droplets, 10–20 nm in diameter, and an increase in the electrostatic field on their surface to a level where evaporation of small ions becomes possible. The whole process results in a cloud containing small ions and highly charged hydrated residues [111, 112] if ESD is performed at low or moderate humidity. Some of these residues contain single charged protein molecules which are used in MS analysis.

Considering the example in Fig. 8 at 0.2 mM KCl and assuming that microdroplets with a diameter of 1 μm are formed [113] at a flow rate of 1.5 μL min^{-1}, we estimate that ~5×10^7 microdroplets are generated in 1 s. With a current of 100 nA, all transported by droplets, we have 1.2×10^4 charges on each droplet. The Rayleigh limiting charge for the water droplets of such size would have 1.5×10^4 charges, which corresponds to known data about the charge of emitted droplets (typically ~50–70% of the Rayleigh limit [79]). The generated microdroplets move one after another, forming a jet which then turns into a torch (plume) due to fission of the droplets, space charge and interaction with gas atoms. Droplets of different sizes separate quickly within the plume with smaller (satellite) droplets pushed to the periphery of the cloud while the main droplets are concentrated in the middle [114]. Satellite droplets are presumably formed upon breakage of a bridge which connects a droplet with a jet at the end of the Taylor cone.

2.3.1 How Quickly do Microdroplets Turn into a Cloud of Dry, Charged Products?

The theory of droplet evaporation was well developed in the middle of the twentieth century [115]. Based on this theory and taking into account that coulomb fission occurs when the charge reaches a certain fraction of the Rayleigh limit (~60–70% of q_r), we showed [113] that for a typical ESD arrangement (capillary tip at a distance of 40 mm from a substrate at a voltage difference of 4 kV) the maximum distance a water ES generated microdroplet, d = 1 μm in diameter, will travel before complete evaporation is 9.5 mm and 12.7 mm at a humidity A = 0% and A = 25%,

respectively. The total time required to evaporate such a droplet is 5 and 7 ms at the humidities indicated. These estimates show that micron-sized water droplets should evaporate well before they reach the substrate surface, provided the capillary tip-to-plane distance exceeds 15 mm.

2.4 Role of Space Charge in Electrospray

Whether space charge of a cloud of ES products affects the ES process is a fundamental question in ESD. The problem was first solved in analysis of I(V) curves in electronic vacuum tubes in the last century [116]. However, the solution obtained, called the Child's law which states that the limiting electron current grows as 3/2 power of the voltage, cannot be applied to ESD because the velocity of electrons in a vacuum is proportional to the potential difference, while that of charged ES products in the gas phase is proportional to the gradient of the potential (electric field). Though the effects of space charge in ES source were numerically analyzed [117], it is instructive to derive approximate analytical expressions which allow one to easily see the scale of these effects and their dependence on different parameters. We limit ourselves to the simplest case of a spherical ES emitter.

To find the limiting current for a spherical emitter one has to solve the Poisson's equation:

$$(1/r^2)(r^2V_t')_r' = -\rho/\varepsilon_0, \tag{8}$$

where the sign ($_r$') means differentiation by radius. The charge density, ρ(r), should change with the distance to the emitter in such a way as to keep the total current, I, constant:

$$\rho(r) = I/4\pi r^2 v. \tag{9}$$

Considering that the velocity of charged species, v, in air may be described by Stokes law, we have for the velocity of particles with a diameter, d and Z charges:

$$V_r' = V_I'(Ze/3\pi\eta d) \tag{10}$$

where η is air viscosity. Denoting $y = r^2 V_r'$ and substituting (9) and (10) into (8) we obtain a differential equation for y:

$$yr'\, y = -Br^2 \tag{11}$$

where

$$\mathrm{B} = 3\mathrm{I}\,\eta d/4\,\varepsilon_0\,Ze. \tag{12}$$

Solving (11) with the boundary condition in the emitting regime (charges leave a small electrode at a zero velocity and move to a larger electrode, we take $y_r' = 0$ at $r = r_o$) we obtain a solution for y:

$$y^2 = -(2B / 3)(r^3 - r_0^3) \tag{13}$$

and returning back to the potential we have another differential equation for V:

$$V_r' = -(2B/3)^{1/2} \ (r^3 - r_0^3)^{1/2} \ (1/r^2) \tag{14}$$

Direct integration of (14) gives the potential difference between r_o and Ro:

$$V = (2Br_0) / 3) \int_1^{(R_0/r_0)} (x^3 - 1)^{1/2} x^{-2} dx. \tag{15}$$

Noting that large values of x contribute mostly to the integral value we can approximate the solution as

$$\int_1^{(R_0/r_0)} (x^3 - 1)^{1/2} x^{-2} \mathrm{d}x \approx \int_1^{(R_0/r_0)} x^{-1/2} \mathrm{d}x \approx 2(R_0 / r_0)^{1/2}. \tag{16}$$

Then

$$V \approx 2(2BR_0 / 3)^{1/2}. \tag{17}$$

Substituting (13) into (17) we have for the maximum current emitted by a sphere:

$$I_{\max} \approx (V^2 \varepsilon_0 Ze / 2R_0 \eta d). \tag{18}$$

Thus, unlike the Child's law, the limiting current in ES follows a stronger quadratic dependence of the limiting current on voltage. A similar expression differing by a numerical coefficient was obtained by Sigmond for the limiting case of a space limited current in a point-to-plane corona discharge [118].

Considering the specific example of an ES emitter with a radius of $r_o << R_o = H = 10$ cm (where H is the distance to the substrate, collector) under a potential of $V = 10$ kV producing a cloud of charged macroions with radius d = 4 nm and Z = 10 charges, we estimate from (18) that space charge around a spherical emitter will limit total current of such macroions to $I_{max} = 200$ nA.

Considering another limiting case of droplets charged to the Rayleigh limit we have for the limiting current:

$$I_{\max}' \approx 4.44[V^2 (\varepsilon_0^3 X \gamma d)_{1/2} / R_0 \eta]. \tag{19}$$

For water droplets with $\gamma = 0.07$ N m^{-1}, radius of droplets, $d = 0.5$ μm, and air viscosity, $\eta = 1.8 \times 10^{-5}$ N s m^{-2}, we obtain $I'_{max} = 1.7$ μA

We present here simple estimates for a spherical ES emitter to demonstrate the possible effects of space charges. In a real point-to-plane geometry the maximal current will be lower by approximately a factor of $(S/4\pi R_o^2)$, where S is the surface area of the collector.

To conclude this section, in most practical cases of electrospraying, the space charge formation in the vicinity of the capillary tip will probably not substantially affect the ESD. The problem has been recently experimentally addressed by Gamero-Castanõ,

et al. [119] who concluded that ES of electrolytes under normal atmospheric pressure at currents lower than 100 nA is limited by flow rate rather than by space charge.

2.5 *Evolution of Charged Clouds on the Way to the Substrate*

When a charged cloud of ES products moves toward the substrate it simultaneously expands its cross-section due to repulsion of the peripheral products by space charge as illustrated schematically in Fig. 10a. The problem of charged cloud evolution in point-plane geometry has been analyzed in detail for corona discharge by Jones [120] who found an analytical solution for a self-expanding sphere of charged ions:

$$r(t) = r_0(1+\rho_0 \chi t / \varepsilon)^{1/3}, \tag{20}$$

where r_o, χ, and ρ_o are the initial cloud radius, ion mobility, and initial space charge density in the cloud, respectively. From a practical point of view it is important to note that the expansion of a cloud is a weak function of time. The analytical solution for the time of flight to the substrate obtained by Jones [120] is to too complex to present here and it does not account for the effect of electrical wind, which, according to our observations, substantially contributes to the dynamics of a charged cloud far from the capillary tip.

The combined action of space charge, electrostatic forces and electrical wind results in a nearly linear dependence of the deposition diameter as a function of capillary height at a constant current, as illustrated in Fig. 10b.

Another illustration of the role which space charge plays in ESD is presented in Fig. 11, which shows how the diameter of the deposited spot depends on the ES current at a constant capillary height. One can see that injection of larger number of charges into the cloud at larger currents results in a faster expansion during the flight

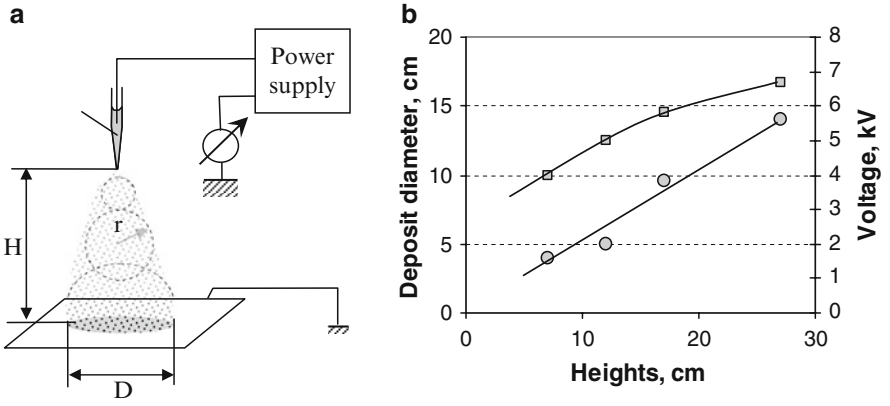

Fig. 10 Schematic of electrospray deposition (**a**) and diameter of the deposit, *D*, as a function of height, *H* (**b**). The diameter of a spot of ES generated glycerol microdroplets from a 10% solution of glycerol in EtOH is marked by *filled circles*. Deposition was performed at a constant current of 60 nA, which was kept constant by changing the voltage as shown by the *filled squares* in (**b**)

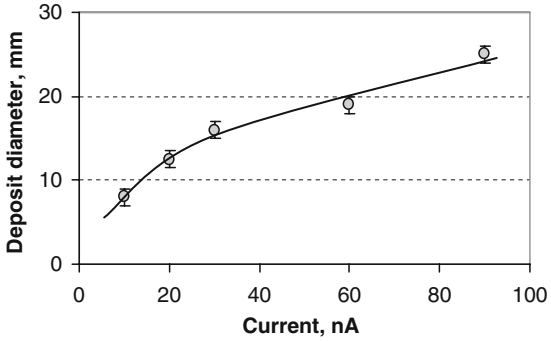

Fig. 11 Role of space charge in deposition. Rhodamin 6G solution (0.01 mg mL^{-1} in ethanol) was ES deposited at a positive mode from the height of 20 mm at different currents. The voltage was varied from 2.8 to 3.1 kV

time. We may attribute the entire fourfold increase in the deposit diameter to cloud expansion because the time of flight is expected to decrease by 10% at high current, following the 10% increase in the voltage. Thus, when a large area on a substrate needs to be coated in ESD, deposition should be performed at high current.

2.5.1 Deposition Density

Obviously, peripheral charged particles are subjected to the largest electric field generated by the space charge while those particles that happen to locate close to the cloud center are not affected by the space charge. That is why the density of particles on the perpendicular axis connecting the capillary tip with the substrate will be the highest, independent of the gap between the capillary tip and substrate. Due to the distribution of products inside the cloud, the deposition density on the substrate surface has a maximum in the center and decreases toward the periphery of the deposited spot. This nonuniform distribution of density was noted already in the first applications of the ESD for manufacturing thin-layer radioactive sources [13]. An early approach for the correction of this drawback of ESD included motion of the capillary over the substrate surface, a sort of "brushing" with the electrosprayer.

We suggested another simple means to prepare a uniform deposit after it was discovered that deposition inside a perforated cylinder made of a plastic mesh enabled a highly uniform distribution of the deposit inside the cylinder cross-section, provided that the capillary height was adjusted properly. As seen in Fig. 12a, at a low height where the charged cloud does not touch the cylinder wall, a normal bell-like distribution of the deposition density is observed. However, when the tip is raised to a height at which the deposit size without the screen would exceed the size of the screen – a perfectly uniform distribution was observed as seen in Fig. 12a. We explain this phenomenon by assuming that charging of the lower part of the cylinder by incoming ES products creates an electrostatic corral, which confines the cloud until it "fills" all the available cross-section of the screen before landing. It was observed that the phe-

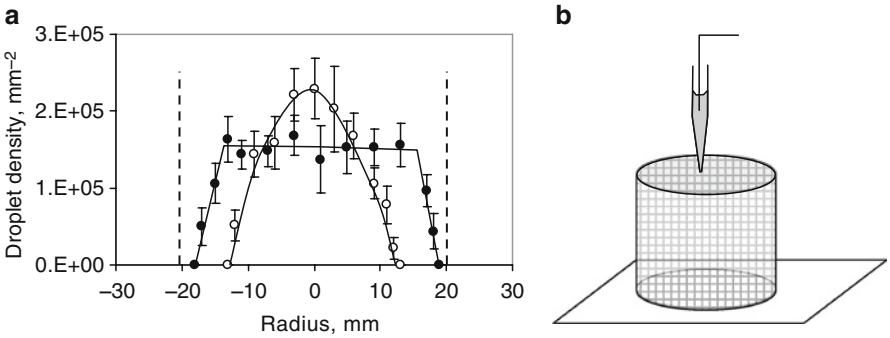

Fig. 12 **a** Radial distribution of the surface density of microdroplets generated by ES from a 10% water solution of glycerol deposited onto a polished metal surface inside a perforated cylindrical dielectric shield, 40 mm in diameter, from a capillary placed axially at heights of 30 mm (*open circles*) and of 43 mm (*filled circles*) over the substrate. **b** A typical arrangement of a cylinder screen and the capillary necessary for obtaining a uniform density distribution of the deposited material

nomenon requires a conductive surface larger than the diameter of the cylinder, as shown in Fig. 12b. Presumably, some leakage of charges from the cylinder to the substrate to prevent its overcharging is essential for the phenomena of distribution. The tip should be located on the axial line of the cylinder and its height over the substrate should be properly adjusted. The plastic screens can be of a conical or cylindrical body and made of a woven dielectric material permeable to air.

Filtration of air pushed through the screen by the electric wind could be considered as another potential function of the screen and as a mechanism of screen charging. We shall further consider this important factor for ESD below.

2.5.2 Role of Electrical Wind in Deposition

It is well known that any corona discharge is accompanied by electric wind which is created by motion of corona-generated ions which transfer part of their momentum to the neutral air molecules. This phenomenon is used in corona drying processes [121] and for cooling of computer processors [122–124]. Because charged ES products accelerated in vicinity of the Taylor cone also transfer their momentum to gas phase electric wind accompanies ESD process as well. We will estimate velocity of ES-generated electric wind using Loeb' formula for velocity of electric wind in corona discharge [81]:

$$v = (2\,P\,/\,\omega)^{1/2} = (2I\,r/\rho S\chi)^{1/2}, \tag{21}$$

where ω is air density, P is the pressure created by the corona discharge, χ is the ion mobility, r is the distance to the tip, I is the current and S is the effective cross-section area. The pressure drop created by the wind over the gap, H, between the ES tip and substrate is

$$P = I\,H/S\chi, \tag{22}$$

where the mobility, χ, of the charged products may be estimated assuming that they are charged to their Rayleigh limit as

$$\chi = Ze / 3\pi\eta d = 0.94(\varepsilon_0 \gamma d\}^{1/2} / \eta. \quad (23)$$

In a typical ESD experiment with $I = 100$ nA, $H = 10$ cm, $S = 20$ cm^2, and the air density, $\omega = 1.20$ kg m^{-3}, water nano-droplets with a diameter of 20 nm charged to the Rayleigh limit and having the mobility of $\chi = 5.8 \times 10^{-6}$m^2 V^{-1}s^{-1} will create a pressure of $P \sim 0.1$ mm H_2O, which will support a wind velocity of $v \sim 1.3$ m s^{-1}.

Though admittedly crude, this estimate definitely indicates that the transport of electrospray-generated products by electric wind should be taken into account. Direct measurements of electric wind in electrospray have not been made, however measurements of droplet velocity based on the Doppler effect revealed that ES generated droplets having a velocity of 40–100 m s^{-1} in the vicinity of the capillary tip reduce their velocity asymptotically to ~5 m s^{-1} at a distances larger than 2–5 cm [125, 126]. The latter velocity is close to our estimate and may be entirely supported by electric wind.

Now let us compare the estimated wind velocity with the velocity of the same droplets in the electric field. A point-to-plane electric field typical for ESD is characterized by a very strong field in the vicinity of the tip (which is necessary for electrospraying to happen, see (3)) which quickly decreases with the distance from the tip. For the axial field as a function of distance, r, to the tip the following analytical expression was obtained [127]:

$$E(r) = V[(1/r)+1/(2H-r)] \quad (24)$$

where H is the distance between the tip of the capillary and the substrate. Neglecting the space charge effects, for microdroplets and clusters charged to their Rayleigh limit we obtain a velocity in vicinity of the substrate of

$$v = 1.9(V/\eta H)(\varepsilon_0 \gamma d)^{1/2}. \quad (25)$$

For a droplet $a = 20$ nm in diameter, $V = 5$ kV and H = 10 cm we obtain $v = 60$ cm s^{-1}. In the absence of electric wind this would be the rate at which charged products approach the substrate. We see that far from the tip electric wind provides a larger driving force than the electric field itself.

An example illustrating the contribution of electric wind in ESD is presented in Fig. 13. Here, an array of glycerol microdroplets was deposited through a mesh placed either directly onto a conducting substrate, as shown in Fig. 13a, or with a gap between the mesh and the substrate, as illustrated in Fig 13b. Characteristic dunes similar to those made by wind on snow or sand are seen in Fig. 13b, which we attribute to the effect of the electric wind.

The relatively slow speed with which charged ES products approach the substrate make it essential to keep air still; i.e., the deposition should take place in a closed chamber. ESD in a chamber results in a deposit much less contaminated with dust particles present in the ambient air, while ESD in the open air acts as a small vacuum cleaner which electrifies and collects a lot of dust. Though the author

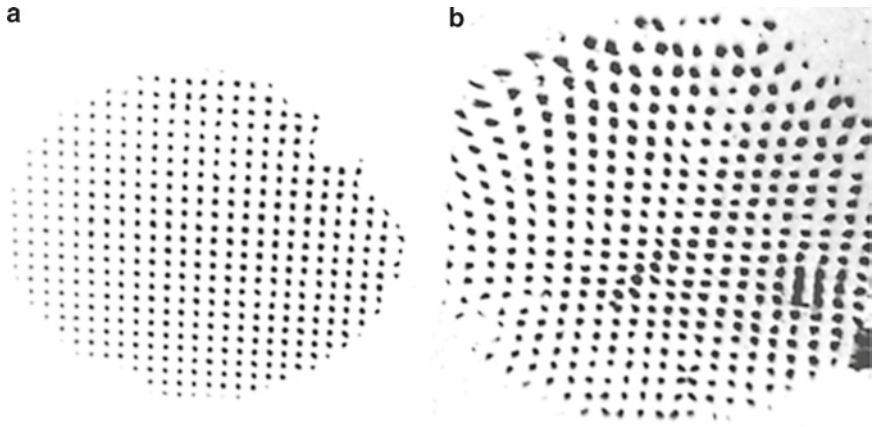

Fig. 13 Illustration of the effect of electric wind in deposition through a mesh used as a mask. A 10% glycerol solution in EtOH was deposited through a mesh with 0.4 × 0.4 mm^2 windows spaced by 0.8 mm. The mesh was placed directly on aluminated plastic (**a**) and with a gap of 12.6 mm (**b**)

used plastic chambers, it should be remembered that the walls of such a chamber may be charged by the ES products. To diminish the effects of stray charges on the chamber walls the deposition area should be placed far from the walls. Another danger of using a plastic chamber is its ability to be charged by induction. When touched by hand, the induced charge is removed from the outer side of the chamber, leaving uncompensated charges on the inner side of the wall. Those charges may survive for hours and affect deposition uniformity and efficiency.

2.6 Formation of Charged Electrospray Products

2.6.1 Mechanism of ESI and Formation of Charged Nano-Clusters

After long debates and arguments concerning the mechanisms by which ions are generated in ESI, the consensus which satisfies all the experimental data has been achieved [30]. It states that small ions are generated by the mechanism of field evaporation, when a fluctuation on the surface of a highly charged nano-droplet is further destabilized until an ion becomes torn off the droplet together with a cluster of bound solvent molecules [128]. This mechanism, first suggested by Thompson [129, 130], cannot, however, account for generation of macro-ions like charged protein molecules, which are generated by a completely different mechanism as dry residues upon complete evaporation of nano-droplets (the mechanism initially suggested by Dole et al. [25]), when most of the small ions escape from the droplet surface, leaving on the protein surface as many ions as this surface can hold. Thus, protein molecules and clusters are charged due to small ions which initially charged

the droplets [131]. There is no reason to believe that formation of charged nanoclusters containing hundreds of protein molecules proceeds via a mechanism different from that proposed by Dole et al. We also expect that the number of charges on the cluster will increase in proportion to the cluster surface as it does in a series of protein ions of different sizes [132].

The maximum number of charges which any particle or macro-ion can hold depends on a number of factors. Thus, the average charge of protein ions as well as poly-(propyleneimine) dendrimers substantially increases with the increase in the surface tension of the solvent used [133]. A higher surface tension keeps a larger density of ions on the droplet surface according to (7), which results in a higher population of charges left on the macro-ions. The presence of a low volatility solvent with high surface tension may change the density of charges substantially because their concentration will grow in the shrinking microdroplet [134]. The chemical nature of the polymer surface is another important factor determining the charge density since the presence of groups which strongly hold ions will promote charging (e.g., amino groups which bind protons promote formation of highly positively charged ions, while carboxyl and other acid groups favor negative charging).

Only at very low concentrations (10^{-3}–10^{-5} mg mL^{-1}) will separate protein molecules predominate in the ES products, as the AFM picture in the Fig 14 and graphs in Figs. 15a and 15b illustrate. The heights of the deposited molecules in Fig. 14 roughly correspond to the value expected for the size of native lysozyme molecules. This favors the idea that protein molecules survive both ESI and the

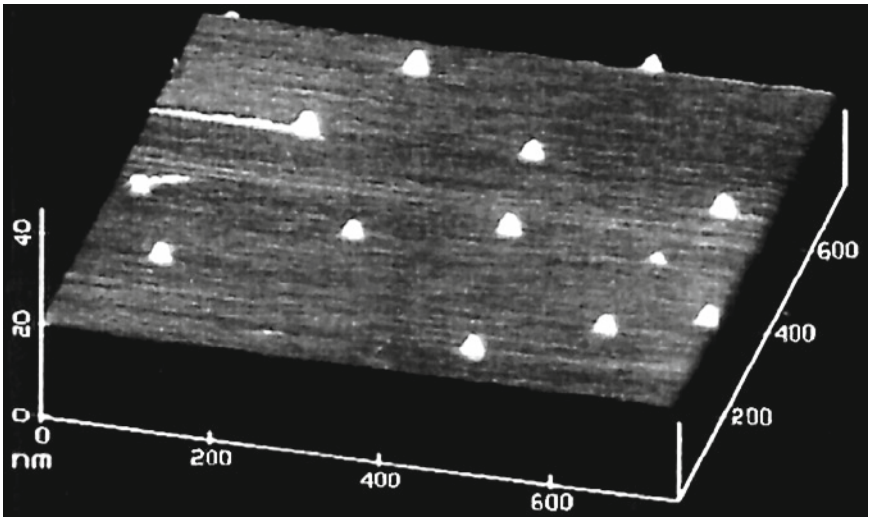

Fig. 14 Lysozyme molecules deposited onto a mica surface from a dilute water solution with corona neutralization. The average height is 3 ± 0.5 nm. Protein ions were deposited on freshly cleaved, slightly heated mica with neutralization of deposited ions by corona discharge as illustrated in Fig. 23

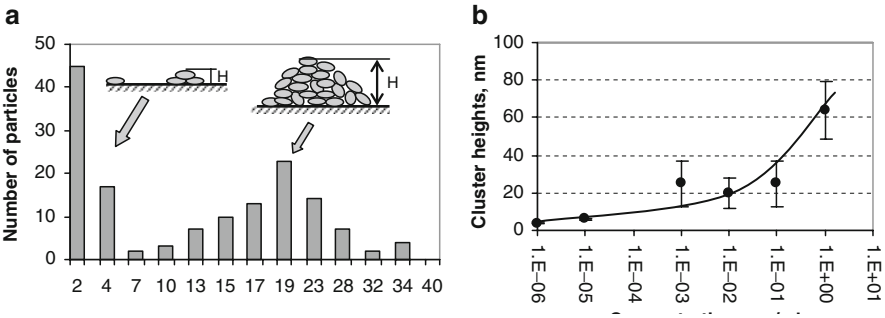

Fig. 15 **a** Distribution of cluster heights obtained upon deposition of a dialyzed solution of hen egg white lysozyme (0.1 mg mL^{-1}) onto a rotating mica surface with corona recharging as shown schematically should be HSA in Fig. 23. **b** Average heights of HSA clusters in AFM images after ESD from different HSA concentrations

landing process. It is worth noting that ESD from solutions in which protein molecules are destabilized or denatured results in quite a different picture. When HSA was dissolved at a concentration of 10 ng mL^{-1} in MeOH (50% MeOH and 3% acetic acid) the cluster height was only 0.5 ± 0.2 nm, presumably due to spreading of the denatured molecule over the surface. When deposited by ESD from a water solution under identical conditions, HSA molecules had average heights of 4 ± 1 nm. Similarly, direct deposition of a diluted HSA solution in 3% acetic acid resulted in particles which were only 0.3–0.5 nm high. Deposition of lysozyme and HSA were made with a plastic capillary and a Pt electrode because it was observed that even ultra-pure water electrosprayed from a glass capillary with Pt electrode resulted in formation of clusters 1– 3 nm high, presumably due to dissolution of the glass itself and formation of salt clusters on the mica surface.

In most practical cases of protein deposition described, deposition was performed in the form of dried nano-clusters. Fig. 15a illustrates a typical distribution of heights in an AFM image of ES products after deposition of lysozyme from a 0.01% solution in water. Although the numbers of small and large particles are approximately equal, the latter have ~1,000 times more protein in each particle. Therefore, we have to conclude from the data in Fig. 15a that 99.9% of all the deposited protein landed in the form of clusters. The size of these clusters increases with an increase in concentration, as illustrated in Fig. 15b.

2.7 What Kind of Substrates may be Used for ESD?

The substrates onto which charged particles are deposited should possess adequate conductivity to support the electric field necessary for ESD. Metals, metallized plastics (e.g., aluminated Mylar film used by Avseenko et al. [135, 136]), and conducting ITO-coated glass [106] are obvious choices of good substrates.

Semiconductors can also be readily used as substrates. To estimate the level of acceptable conductivity of a semiconductive material, we consider a practical example of deposition onto a layer of such material with thickness of h = 30 μm through a mask with 1,200 holes, 50 μm diameter each. With the total open area under the mask of S_h = 2.4 mm^2, and an acceptable potential drop over the film thickness of V_d = 1,000 V at a total ES current of I = 20 nA we have for the minimum conductivity required:

$$\kappa_S = hI / S_h V_d. \tag{26}$$

This gives for the above presented parameters a minimum conductivity of $\kappa_s = 2.5 \times 10^{-10}$ S m^{-1}. Thin films of hydrophilic polymers such as cellophane, which have substantial conductivity even at low moisture (cellophane's conductivity at a moisture of 10.7% was found to be 3×10^{-6} S m^{-1} [137]), can be used as substrates. This also applies to layers of hydrophilic polymers. We found that protein deposition can be effectively made on a layer of polyvinyl alcohol (PVA), polyvinylpyrrolidone (PVP), dextran, sodium alginate, polyethylene glycol (PEG) and other hydrophilic polymers. After deposition of a protein film on such a layer the protein molecules could be cross-linked in glutaraldehyde vapor and the cross-linked film could then be easily released into a water droplet after dissolution of the sacrificial polymer layer. This technique was used to manufacture free protein films for mechano-chemical sensors [106, 138, 139].

Recently a dialysis membrane was used in the author's laboratory as a substrate for arraying protein molecules by distal electrospray deposition [140–143]. The choice of this material was dictated by the necessity of applying an electric field perpendicular to the array surface in order to enable rapid and complete collection of charged analytes like protein antigens, antibodies and whole viruses onto the array surface. Methods of immobilization of protein molecules on such a substrate are described in refs. [123, 140, 142–145].

Using a conducting surface is another option for an ESD substrate. The author successfully employed freshly cleaved mica [39] and plasma-cleaned glass [55] as substrates for deposition of protein molecules and arrays. It cannot be excluded that surface conductivity contributes substantially to deposition onto any low-conducting substrate. In the example presented above, holes 50 μm in diameter were separated by 1.5 mm. Therefore, if the surface conductivity (e.g., due to a layer of adsorbed water) exceeds the bulk conductivity, then instead of considering the conductivity only under the open hole area, we should take the entire array area into account. This increases the effective surface area by a factor of ~1000 and identically decreases the minimum required bulk conductivity to $\kappa_s \sim 10^{-13}$ S m^{-1}. The latter conductivity is characteristic of a good insulator. This explains why a thin layer of a good dielectric can be used as a substrate in ESD. We were able to deposit an array onto a 3–15 μm thick layer of acrylic polymer which coats a metal layer on the surface of a standard CD disk.

We should emphasize that the conductivity of dielectric materials in ESD hardware might substantially deviate from the conductivity tabulated in monographs because of two major factors. The first factor is the very high electric field, at which

polymer conductivity deviates from Ohm's law (actually, current becomes proportional to a square of voltage applied [146]). The second factor is injection of external charges into the dielectric from the deposited charged clusters. Most polymer dielectrics have low conductivity, not because the mobility of charges is low, but because they lack mobile charges. Injection of such charges makes polymers conductive, as the remarkable increase by 8 orders of magnitude in the conductivity of a dry lysozyme film resulting from a change of copper to palladium electrodes illustrates [147]. The latter electrode is capable of injection protons into the film, making it highly conductive.

3 Two Basic Types of Electrospray Deposition

3.1 Proximal ESD

Depending on ESD conditions, deposition may be in the form of micro- and nanodroplets or in the form of dry nano-clusters and ions. We will further refer to the first mode as "wet deposition" and to the second as "dry deposition." We will also classify ESD techniques as "proximal" if deposition is performed from a capillary placed close to the surface and as "distal" if the distance between the capillary tip and substrate substantially exceeds the distance necessary for transformation of a cloud of charged droplets into a cloud of dry products. The latter distance was estimated in Sect. 2.3.1. Wet distal deposition may be achieved if the ESD chamber is filled with air saturated with vapor of the solvent used in ES. Microdroplets and smaller satellite droplets neither evaporate nor undergo a series of coulomb fissions described above, and land as droplets. Another way to achieve the wet deposition mode is to reduce the distance between the tip and the substrate so that droplets do not have enough time to turn into dry, charged products. This mode of proximal wet ESD has been developed by Moerman et al. [56, 86] and by other authors [148]. In this technique, schematized in Fig. 16, the capillary tip is placed about 130–350 μm above a conducting substrate so that ES generated droplets reach the substrate in a small area under the tip, forming a spot.

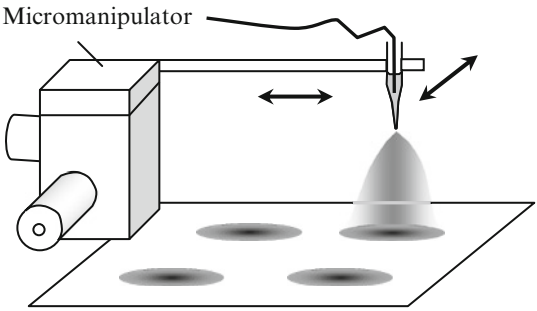

Fig. 16 Principle of proximal ESD

An extremely small volume (40–100 pL) of solution may be deposited by properly controlling the voltage pulse applied to the capillary. After depositing one spot the capillary is shifted with a micro-manipulator to a new position and the next spot is deposited. We shall further discuss the advantages and drawbacks of this technique later when comparing different ESD-based arraying approaches.

3.2 Dry Distal ESD Techniques

We will consider here separately two cases using distal ESD for fabrication of samples from biological materials. Formation of small micron-thick films of proteins for mechanical [138, 149–151] and optical tests [152] as well as formation of samples for scanning microscopy (STM and AFM [39]) does not require spreading the electrosprayed material over a large substrate area. On the contrary, a cloud of charged, dry ES products should be collected in a highly localized area on a conducting substrate to make a thick protein film or to economically use a valuable substrate like an atomically flat crystalline ultra-pure gold surface [39]. One cannot place the capillary tip as close to the substrate in this case as in proximal ESD, because formation of ions and dry clusters requires passage through a minimum distance. Therefore, ESD products should be collected in a small substrate area from a large charged cloud, which makes space charge effects very notable as we will see below. Opposite requirements are needed for application of ESD to the fabrication of microarrays: a large area should be evenly coated with spots. Since a hole (or an array of holes) in a plastic dielectric is used in both these cases let us, first, consider how it works.

3.3 How are Charges Kept on a Mask and How do they Move and Neutralize?

3.3.1 Dielectric Mask with a Hole as Collimator

That a hole in a dielectric mask is capable of concentrating incoming charged products was noted in early deposition experiments in the preparation of isotope sources [14, 15] when the electrosprayed material was found to be deposited as spots having a size smaller than the holes in the mask. This “lens effect” was reproduced in our experiments. Figure 17 shows how the diameter of a spot deposited through a single hole in a thin plastic mask depends on the gap between the mask and conducting substrate. One can see that Teflon provides a lens effect (measured as a ratio between the spot diameter and the diameter of a hole) less pronounced than polystyrene (PS). This difference is entirely due to the difference in the surface properties of these two materials, because after being soaked in a soup and dried the Teflon mask becomes a lens as powerful as that made of PS. We interpret this

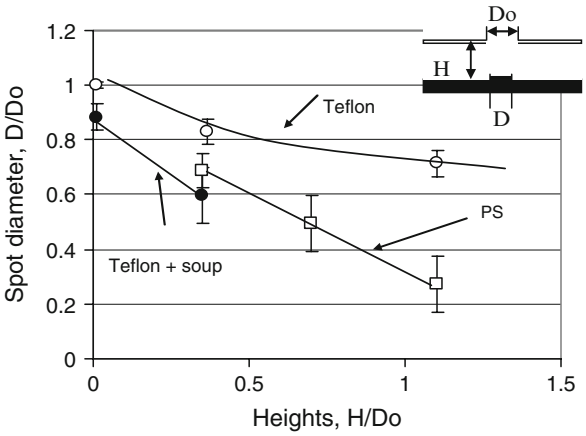

Fig. 17 Dependence of the spot average diameter on the height at which the mask is placed over a conductive substrate. A Teflon sheet, 0.1 mm thick, and a polystyrene plate, 2.8 mm thick, were used as a mask with a hole, *Do* = 7.9 mm in diameter

fact as an indication that trapping charges on a dielectric mask is of great importance for the lens effect. Since Teflon cannot effectively trap and hold free charges it is not as effective as PS in concentrating charged ES products.

The lens effect may be explained by adsorption of a fraction of charged products onto the mask surface, creating an electrostatic field that repels the incoming ES products and directs them into the hole(s) of the mask. This charging should be seen as a stationary process: while some trapped charges are lost due to bulk or surface conductivity, new charges are allowed to land on the mask to maintain its potential. It is noteworthy that the operation of such an electrostatic lens is different from that in electron microscopes because the inertial forces which determine the trajectories in a vacuum electrostatic lens are negligible in air under normal conditions where viscous forces dominate.

The electrostatic lens effect has two advantages: (1) great economy of electrosprayed material, which is not lost on the mask and (2) reducing the size of the deposit below the size the hole in the mask. The latter feature considerably reduces the technological problems in the fabrication of masks suitable for deposition of spots of micron and submicron size since the holes do not need to be as small as the spots themselves. We have demonstrated that protein spots with sizes of 5–7 μm could be deposited through a mask having 23–24 μm holes set 47 μm apart in a polypropylene mesh [55]. The image of mask used in these experiments is presented in Fig. 18b.

The electrostatic lens effect can also be used to produce samples with large height-to-lateral size aspects, as illustrated in Fig. 18a, where arrays of needle-like samples of pancreatic ribonuclease fabricated by ESD through the mask shown in Fig. 18b, is presented. Arrays of such rod-like samples were also fabricated from organic substances, such as light green dye.

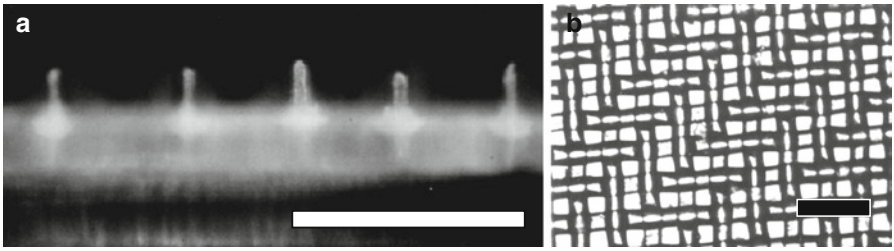

Fig. 18 "Nails" manufactured by ESD of an RNAse solution (0.55% protein, 0.16% sucrose and 0.05% glycerol) on an aluminated plastic as a substrate (**a**). Protein was deposited for 10 min through a polyester mesh (**b**) in a closed chamber with a relative humidity of 18%, at +4.0 kV applied to the capillary with an internal diameter of 10 μ and a current of 10 nA. *Bar* denotes 100 μm

3.3.2 Dry Distal ESD in Manufacturing Small Samples

The size of the hole cannot be reduced without paying a price. The small substrate area exposed through a hole in the mask creates a strong field only in the vicinity of the hole. The field decreases inversely proportional to the distance from the exposed substrate area in the absence of the charged cloud. The space charge of the cloud screens the field still further, making the substrate "invisible" for incoming charged products, which are then lost on the chamber walls following the motion of air and stray electric field. Thus, the efficiency of ESD drops dramatically with a decrease in the size of the hole.

This problem was noted in the first applications of ESD and a special collimating ring was introduced [14]. A similar problem is also well recognized in collection of ES generated ions in mass spectrometers. An electrostatic concentrator has been recently described by Kremer, who demonstrated that a series of insulated conducting rings with progressively decreasing internal diameter is capable of concentrating corona-generated ions ~100-fold [153]. The author reported an apparatus which included a plastic sheet with electrodes on both sides having a central ion canal [39]. A potential difference across the two electrodes was used to move the electrospray product through the canal onto an atomically flat crystalline gold substrate. All these designs are variants of a collimating ring which we consider in more detail below.

3.3.3 Collimating Ring

We found that the efficiency of deposition into a single small hole in the mask may be substantially increased by decreasing the size of the collimating ring and by placing it closely to the deposition area. As illustrated schematically in Fig. 19, charged ES products move in the field created by the ring and only in the vicinity of the ring do they start to follow a local electric field between the exposed substrate

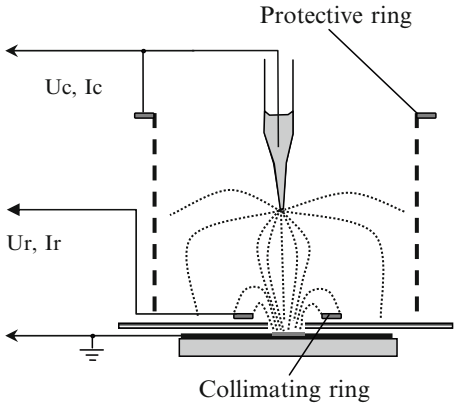

Fig. 19 Arrangement used to manufacture small size samples by distal ESD. Two conductive rings are introduced: a protective ring and a collimating ring. The potential on the collimating ring, U_r, was 20–50% of the potential on the capillary and the protective ring, U_c

and the ring which directs them to the substrate. It is important to emphasize that such "changing lines" is possible only if charged products are subjected to additional force. We speculate that electric wind may be considered as such force.

Experiments were performed to find the optimal ring size and ring potential by direct measurements of the amount of protein deposited from an aqueous solution. It was found that, under optimal conditions (typically, U_c = 4–5 kV, U_r = 1.3–2.3 kV, I_c = 20–30 nA, I_r = 7–15 nA), 10–20% of the electrosprayed protein was found in the protein spot with a size of 0.7 × 0.2 mm^2, while only 2–5% was deposited without the collimating ring. Deposition was performed from heights H = 20 mm with a ring having a 2 mm ID and 1 mm wide. The ring was coated with a conducting paint.

It was found that the current efficiency (fraction of total current, I_c, passed through the substrate) was always notably higher (30–80%) than the mass deposition efficiency. This discrepancy may be explained by stray conductivity through the mask, whose area was ~10^4 larger than the exposed substrate area. The mass deposition efficiency was further increased to ~30% by decreasing the height to 10 mm and by performing ESD at a low current (I_c < 10 nA), although some of the deposited material landed in the form of nano-droplets in this case.

An example of a protein film obtained by ESD through a hole in mica is presented in Fig. 20a. Protein films deposited from heights of 20 mm under humidity less than 70% were usually opaque. AFM imaging revealed a rough surface comprised of nano-clusters and their agglomerates, as illustrated in Fig. 20b. Brief exposure to a humid air turned most of the ESD-formed protein samples into a transparent films and made their surface quite smooth as illustrated in Fig. 20c for a hemoglobin film: the root-mean-square profile decreased from 620 ± 80 nm to 160 ± 20 nm. Further details of the structure of the ESD deposited protein films may be found in publication of Uematsua et al. [151]. Thick films (up to 50 μm) were manufactured by ESD from collagen [154] and from cellulose acetate [21].

When cross-linked in glutaraldehyde vapor over wet NaCl (to keep the film dry), the protein film retains its opaqueness after insertion into water. Such cross-linked

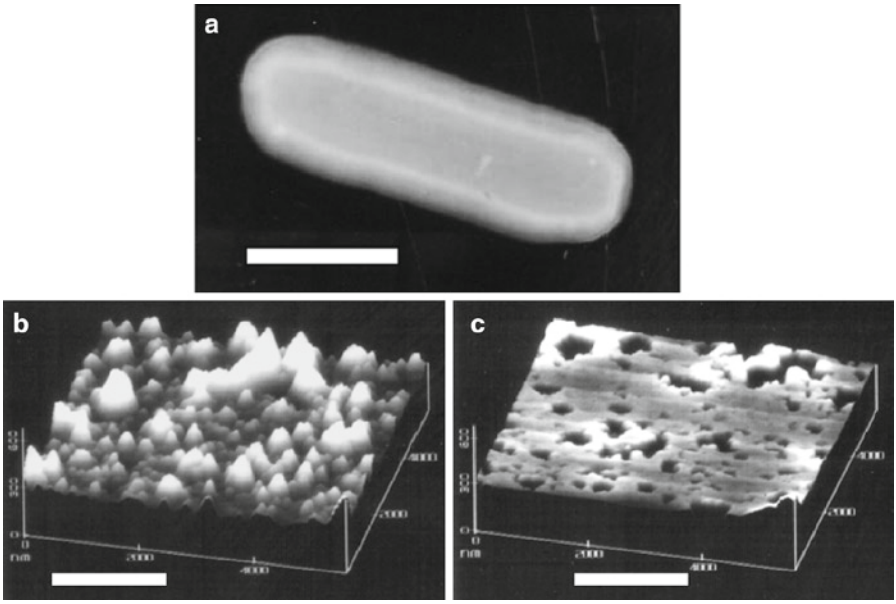

Fig. 20 BSA film manufactured by ESD of 1 μL of a solution containing 0.35% of protein, 0.1% sucrose and 0.03% of glycerol (**a**). Deposition was made through a hole in a mica screen. AFM images of the surface profile in ESD deposited protein film before (**b**) and after (**c**) a 15-min exposure to a humid air. The film was deposited at a humidity of 10% from human Hb solution in water, 0.6 mg mL^{-1}. *Bar* denote 200 μm in **a** and 2 μm in the **b** and **c**. *Vertical scale* in **b** and **c** is 600 nm

films of globular proteins (BSA, ribonuclease, lysozyme) showed a remarkable increase in the diffusion of dye molecules as compared to similar films prepared by drying the same protein solutions on a glass surface. The nano-channels within the ESD-fabricated films make them especially suitable for use in biosensors where other molecules should penetrate the films to react with immobilized protein molecules [54, 139, 149, 150, 155, 156]

3.3.4 Distal Deposition Through a Mask with an Array of Holes. Patterning Surfaces and Fabrication of Multi-Component Microarrays

Although ESD may be used in combination with a pre-patterned surface to ensure local immobilization of the deposited molecules (see the example of such deposition onto a patterned gel [87]), such deposition results in a highly inefficient use of the material. It is easier to protect certain substrate areas with a mask, as has been done in the first use of ESD for patterning the surface challenging a control of cells adhesion [157]. These authors used a conducting mask (a grid for electron microscopy), which has the same potential as the conducting substrate. Equality of the substrate and mask

potentials resulted in deposition on both the substrate and the mask proportionally to their surface area. Such a "shadow" mask caused large losses of the material.

As we emphasized above, a dielectric mask has serious advantages over the shadow masks in economy (most material goes into holes) and, hence, quick deposition. It is also important that the holes in the dielectric mask are capable of concentrating the material (lens effect) to allow deposition of spots with a diameter several times smaller than the diameter of holes. Polyester and nylon meshes were routinely used as masks to manufacture mono- and simple multi-component arrays in our experiments. An array 60 mm in diameter deposited through a mesh shown in Fig. 18b contains 1.1×10^6 spots with a diameter of 5–10 μm [55, 135]. Such an array is produced in 1–5 min depending on the solution conductivity.

The substrate or mask can be shifted after deposition, as schematically illustrated in Fig. 21. In this case, if the shift is larger than the spot size but smaller than the distance between the holes in the mask and if a new substance is deposited after each shift, a multi-component microarray is formed under each hole. With a mesh like that shown in Fig. 18b microarrays up to nine components may be manufactured due to the limited distance between the holes in the mesh. To produce more complex arrays a special mask with larger distance between holes must be used.

As previously mentioned, the conductivity of polymer materials used in high electric field, combined with injection of external charges, e.g., protons, may be substantially higher than usual. We found that polymer masks are contaminated more quickly than mica, especially around the hole. We explained this by the ability of the polymer mask to become conductive upon injection of charges [146], and worked further with mica masks. Other solid inorganic dielectrics, like fused

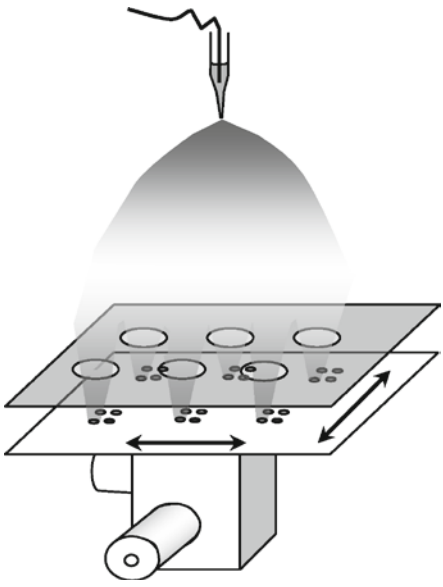

Fig. 21 Schematic of a distal ESD through a dielectric mask with an array of holes employed for parallel manufacturing of multi-component microarrays

quartz, glass, or Sitall may also be used; however, mica is the material of choice for masks designed in a laboratory since it is readily available in thin sheets and holes may be easily drilled either mechanically or by sand blasting [62, 152, 158]. Yet another advantage of mica in comparison to polymer materials is the lack of plastic deformations, which often ruin thin plastic masks as the latter are subjected to large stress upon detachment of the charged mask from the substrate.

To drill holes mechanically we glued mica to a polished stainless steel plate which was attached to a micromanipulator. A tungsten wire sharpened with a diamond file was used as a drill. The electric motor automatically stopped when the tungsten tip touched the stainless steel plate. A total of 1,200 conic holes were drilled into a mica sheet ~100 μm thick, with an input diameter of 250 μm and an output diameter of 50 μm arranged as a square lattice with a distance between neighboring holes of 1.5 mm. The mica mask was then glued to a glass frame. The latter was used to attach the mask in the ESD arrayer.

The design of the mask and ESD arrayer should account for a strong electrostatic attraction of mask and substrate. It is recommended to wait 20–30 s after switching out the voltage from the capillary to let the charges leak from the mask. To shift the mask into a new position we first pull the substrate down by 1–2 mm to break mica-substrate contact, shift the X–Y position, and then return substrate to its original height. All these motions of the substrate are made with an X–Y–Z-micromanipulator.

Distal dry ESD has the following advantages as applied to arraying [141]:

1. Parallel fabrication. Deposition of many identical spots proceeds simultaneously
2. Highly miniature spots can be manufactured
3. Large economy of proteins: 20–60% of the protein placed in capillary ends up in the spots
4. Proteins remain intact throughout array fabrication
5. The technique is compatible with a variety of technological procedures used in the manufacture of microelectronic chips
6. The deposited material is uniformly distributed over the spot area, making quantitative analysis with such arrays easier and more precise
7. The amount of the deposited material is not limited by spreading the droplet over the substrate surface as in the microspotting and ink jetting techniques
8. A highly porous protein deposit may be formed under dry conditions, which allows easy access of proteins to interaction with specific ligands [151, 152, 155]

The following limitations and disadvantages are inherent in this technique:

1. ESD can only be performed from low-salt solutions.
2. Strict requirements for flatness of the mask and substrate. Variations in the gap between them results in variations of deposition efficiency.
3. Arraying should be performed in a dust-free environment. The high electrostatic field sucks dust particles from the air.
4. A slow rate of solution electrospray (typically 1 μL min^{-1}). Air jet-assisted or ultra-sound-assisted ES [62] solve this problem but make the procedure more complex.

3.3.5 How Does Spatial Charge Affect Deposition Through a Mask?

Collection of charges onto a small collector is a more difficult task in terms of overcoming the effects of space charge as compared to emitting charges, which we considered in Sect. 2.4. A similar situation is observed with collection and emission of electrons in a vacuum [116]. To illustrate the effects of space charges upon collection of ES products, consider again a small spherical collector with radius, r_o, positioned in the center of larger emitter, with radius, R_o, where the density of charges is kept constant. Solving (12) with the boundary condition $y_r' = 0$ at $r = R_o$ we get

$$y^2 = (2B/3)(R_0^3 - r^3) \tag{27}$$

and

$$V_r' = (2B/3)^{1/2}(R_0^3 - r^3)^{1/2}(1/r^2). \tag{28}$$

Direct integration gives

$$V = (2BR_0/3)\int_1^{(r_0/R_0)} (1-x^3)^{1/2}x^{-2}dx. \tag{29}$$

Because small values of x give the greatest contribution to the integral this time we have

$$\int_1^{(r_0/R_0)} (1-x^3)^{1/2}x^{-2}dx \approx \int_1^{(r_0/R_0)} x^{-2}dx \approx (R_0/r_0)$$

and

$$V \approx (2BR_0^3/3r_0^2)^{1/2}. \tag{30}$$

The maximum current is then calculated as

$$I_{max} \approx (2V^2\varepsilon_0 Zer_0^2)/(R_0^3\eta d). \tag{31}$$

Similar to the difference in solution of the Langmuir–Blodgett equation for a spherical emitter [116], in a converging flow of charges the maximum current is by a factor of $4(r_o^2/R_o)^2$ smaller than the maximum current in diverging flow described in the previous case. A numerical example presented in the previous case for molecular ions, with $d = 4$ nm, $Z = 10$ gives for the converging current for an electrode with a diameter $r_o = 0.5$ mm and a potential $V = 5$ kV at a distance $R_o = H = 5$ cm a value of $I_{max} \sim 20$ pA.

Deposition of charged nanodroplets with a diameter, d, charged to the Rayleigh limit of electrostatic stability gives for the maximum current:

$$I_{max} \approx [5.6\pi V^2(\varepsilon_0^3\gamma d)^{1/2}r_0^2]/(R_0^3\eta). \tag{32}$$

For particles with a diameter, $d = 20$ nm, surface tension, $\gamma = 0.07$ J m^{-2}, and radius of collector, $r_o = 0.5$ mm, the maximum current is $I_{max} \approx 40$ pA We should remember

that in real deposition through a hole all charges approach the hole from one hemisphere, which should result in at least a twofold decrease in I_{max}. This numerical example clearly illustrates that space charge limits the deposition onto a small substrate area.

In ESD through a mask with an array of holes, a space charge is formed over each hole at a distance comparable to a distance between neighboring holes. It is difficult to estimate the maximal current for this case since the voltage drop in the vicinity of each hole is not determined.

3.3.6 Resolution. How Small Can ESD Spots be Made?

In the author's experiments, the minimal spot size achieved was ~2 μm [55, 87, 106]. Welle and Jacobs [159] demonstrated that electrosprayed gold nanoparticles, 100 nm in diameter, partly neutralized by passing over a Po^{210} alpha source, could be deposited into a 100-nm pattern of charges on a polymer surface. Is this a theoretical limit of resolution?

The physical limit for the size of the deposit as well as for the lateral precision with which the deposition may be made is determined by a number of factors. The discrete nature of the electrical charges is one such factor. Considering the highest possible charging limited by the electric strength of dielectric material, we have for the density of the surface charges:

$$\sigma_m = \varepsilon\varepsilon_0 E_m / e \tag{33}$$

where ε is the dielectric constant of the material, ε_o is the vacuum dielectric constant and E_m is the maximum electric field the dielectric can hold without destruction. Taking mica as an example, we have for the electrical breakdown strength E_m ~1,000 MV m^{-1} and for ε = 6 [160]. Substituting these values into (33) we have σ_m = 0.33 nm^{-2}, or approximately 1 charge per 3 nm^3, meaning that the average distance between neighboring charges is 1.7 nm. With the charges imprinted onto the substrate surface as in the Welle and Jacobs experiments [159] this is the physical limit of deposition resolution using mica as the substrate. In charging PS with corona, a charge density of ~7×10^{-4} C m^{-2} is achieved [161], which corresponded to an average distance between unitary charges of 15 nm. Practically, a resolution of ~150 nm was reported upon micro-stamp patterning of charges on a polymer surface [162].

Deposition through a hole in a dielectric mask is controlled by the electric field in the air. With the air breakdown strength of $E_m = 3 \times 10^6$ V m^{-1} [163] and ε = 1 the density of surface charges near the hole in the mica mask cannot exceed σ_m = 166 μm^{-2}, which gives a distance between the charges of 77 nm. With a corral of such charges spaced by ~100 nm, the deposition resolution cannot be better than ~ 100 nm, which should be considered as an ultimate resolution in ESD through a dielectric mask in air. The resolution could be improved if ESD is performed in vacuum, under high gas pressure, or in a dielectric liquid.

4 Physics of Landing. Estimates for Kinetic Energy of Collision with the Substrate Surface

Assuming that charges can accept or give electrons to a conducting substrate only upon direct contact of the charged ion or cluster with the surface, one may estimate the level of energy liberated upon landing as a result of its interaction with the induced (or "mirror") charge:

$$W_e = (Ze)^2 / 4\pi\varepsilon\varepsilon_0 d. \quad (34)$$

Use of this formula in air under normal conditions where the free path of atoms is 66 nm is verified by the fact that most of this energy is liberated and transformed into kinetic energy in the vicinity of the surface and thus cannot be lost in collisions with air atoms. For a typical protein molecule with radius, $d = 4$ nm, and an average number of charges on such protein ion, $Z \sim 10$ [30], we estimate that $W_e \sim 36$ eV or 3.5 MJ M^{-1}. Though this energy is high enough to break 10–12 covalent bonds [164, 165], it is highly improbable that the entire energy will be concentrated on a small fraction of ~1,000 bonds in a typical protein ion of such size.

Considering that the heat capacity of protein material is $C_p = 1{,}250$ J $kg^{-1}grad^{-1}$ [166] and the protein density is $\theta = 1{,}300$ kg m^{-3} [167], we estimate that, being transformed into heat, this energy is capable of increasing the molecule's temperature by

$$\Delta T = 6W_e / \pi d^3 \theta C_p, \quad (35)$$

which gives for a protein ion with $d = 4$ nm, $\Delta T \sim 110$ °C. Though the temperature increase is high, the protein ion still has a good chance to maintain its native structure because the heat will dissipate very quickly and because dry proteins are known to keep native structure even when the temperature is raised by 100–150 K above their denaturation temperature [168].

Finally, when turned into elastic deformation of the protein molecule, such energy will result in the molecule deformation by [169]:

$$(\Delta d / d) = 0.5(8\ W_e / Gd^3)^{2/5}, \quad (36)$$

where Δd is the sphere deformation and G is the Young's modulus of protein "material." Taking $E = 6$ GPa for the modulus of a dry protein molecule [168], we estimate from (36) that the relative deformation, $(\Delta d/d) \sim 21\%$. Considering that such deformation will persist for only a few picoseconds and that it requires several minutes for protein molecules subjected to ~30% deformation to become irreversibly unfolded [170], we may expect that a single multicharged dry protein ion will not be irreversibly damaged upon landing on a solid undeformable surface. It is not excluded that the protein ion may bounce against the substrate surface several times before losing its kinetic energy.

These rough estimates show that, although the energy released upon a soft landing is quite high, single protein ions are likely to retain their native structure. This

explains the successful application of ESD in preparation of samples for STM and AFM [39, 113]. Because hydrated protein molecules have an elastic modulus 10–20 times lower than in the dry state, their deformation may be much greater upon landing in the wet form so that the molecule may not be able to adapt its native conformation. This might explain why deposition at high humidity resulted in a loss of specific activity of alkaline phosphatase [54]. When considering the experimental results on retention of structure and function of protein molecules we must remember that in real deposition of a cluster of protein molecules onto a soft material (e.g., on a protein film) the impact energy will be distributed between many protein molecules in the cluster and in the substrate, thus substantially decreasing deformation and temperature changes in individual molecules and increasing their chances for survival.

5 How Charges are Neutralized on a Conductive Substrate

As schematically illustrated in Fig. 22a, upon contact of a charged particle with a metal surface (or semiconductor with *n*-type conductivity), protons and other ions (or more exactly hydrated protons and other solvated ions [112, 128]) migrate over the particle surface or through the particles, reach the conductive surface, and become neutralized with electrons. Some of the neutralized products, such as H_2 and NH_3, are volatile and easily leave the scene. Others may react with water, carbon dioxide and other components and impurities in the atmosphere to form salts and hydroxides. Thus, the metal substrate should be considered as another electrode in the electrochemical circuit.

Deposition in the negative mode will result in adducts of hydrated negative ions [171, 172] which migrate over the surface of the charged deposit until they discharge by giving an electron to the conductive substrate.

Deposition onto a substrate with an ionic type of conductivity will result in migration of charges from the ES product to the substrate, where they will continue to travel

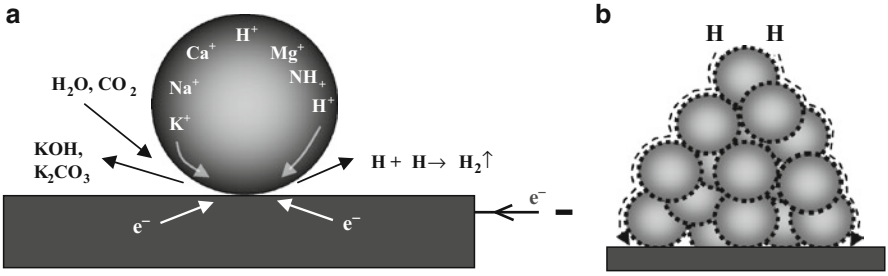

Fig. 22 **a** Schematic of charge neutralization upon contact with a metal conductor or a semiconductor surface with *n*-type conductivity. **b** Schematic of neutralization by ions traveling along the protein surface

until encountering an electrode where they will be discharged in an electrochemical reaction. A similar process is believed to occur during deposition on paper and on other semipermeable filters like PVDF [55] or dry dialysis membrane [140].

As a special case of deposition onto a thick, low-conductive surface we consider deposition of a thick layer of protein. How does neutralization proceed through a 20–30 μm thick protein layer as shown in Fig. 18a? As already mentioned above, injected charges can move in dielectric media [146, 173–175]. Protonic conductivity is highly dependent on the number of bound water molecules, as was reported for a lysozyme film [147] and for a monolayer of BSA molecules [176]. As illustrated in Fig. 22b, protons can be transferred in a layer of bound water or as a defect in an array of hydrogen bonds according to a mechanism suggested by Nagle and Morowitz [177]. It was also shown that protein films have some electronic conductivity, with water molecules acting as donors [178, 179]. In view of these data, formation of thick protein deposits like those illustrated in Fig. 18a, as well as deposition on other hydrophilic materials, does not look surprising.

6 Neutralization by Gas Phase Counter-Ions

6.1 Deposition with Neutralization by Periodic Exposure to Counter-Ions

In this type of neutralization a dielectric substrate is periodically exposed to the ES capillary and to a corona emitter which is generating counter-ions, as illustrated schematically in Fig. 23. The lower surface of the disk should be conductive in order to allow polarization of the dielectric disk. This type of neutralization has been used to prepare samples of electrosprayed synthetic polymers and DNA onto mica surfaces for subsequent analysis by AFM [113]. Although no defects of linear

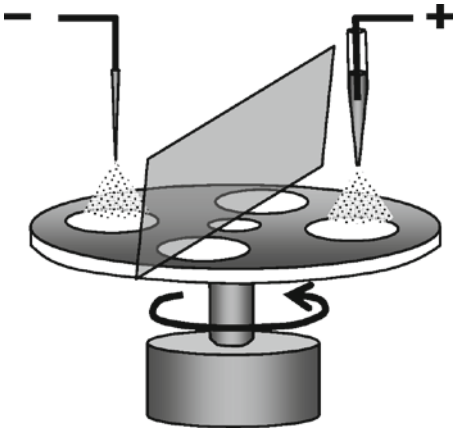

Fig. 23 Schematic of ESD on a dielectric surface with neutralization of the deposited charged products by counter ions generated in a corona discharge

polymers have been seen in AFM of dry samples, a brief exposure to humid atmosphere revealed breaks along the thinnest fibers comprised of small number of polymer chains, appearing as gaps. We speculate that these breaks resulted from chemical reactions with highly active products of the corona discharge: ozone, atomic oxygen, hot atoms and radicals [180]. To avoid this, the corona emitter may be replaced by another capillary filled with a volatile solvent such as alcohol. We applied this type of neutralization in electrospinning of polymer nanomats [181].

6.2 Gas-Phase Neutralization by Electrospray-Generated Counter-Ions

Reduction of charges in ESI-generated products by corona discharge and by ions generated by radioactive isotopes has been described in a number of publications [159, 182–184]. Camelot et al. [185] described a method of rapidly mixing two reagents by coalescence of oppositely charged micro-droplets generated by ES. Solid products precipitated in the coalesced droplets and were then turned into mono-disperse particles upon solvent evaporation.

In our recent studies we extended the neutralization principle to all other possible combinations of oppositely charged electrospray-generated products [181] from volatile and nonvolatile substances, such as small solvent ions, macromolecular ions, nano-clusters and nano-fibers, as well as for mother and daughter solvent droplets. The electrospray-generated nano-clusters partly neutralized by electrospray-generated counter-ions may be used in deposition onto a pattern of charges [159]. Gas-phase neutralization of polymer nano-fibers allows the manufacture of free nano-mats and the design of filters and other nano-structured materials.

7 How to Retain Structural and Functional Properties of ES Deposited Biomolecules?

This is the final problem in ESD which we address in this chapter. We already estimated that landing is potentially damaging for protein molecules. Where else in the ESD process might protein and other fragile molecules be damaged? This problem has been discussed in detail in a previous review on microarray fabrication methods [141]. Briefly, the following damaging factors in ESD should be considered if functional activity of the deposited protein molecules is low:

1. *Electrochemical reactions in the capillary.* Though protein molecules can theoretically be directly oxidized on metal electrodes in the positive ES mode, no data on this damage mechanism is available. Under ES conditions, a local drop in pH due to generation of protons may prevent protein molecules from contacting the electrode. When a negatively charged molecules moves toward a positively charged Pt wire which is surrounded by a cloud of protons it eventually

reaches a layer around the electrode where the pH equals the pI of the protein, and the molecule stops. Extreme pH values that are easily reached if the capillary end is clogged present a much more real danger. Addition of glycerol and/or sucrose eliminates the tip clogging that is often observed with pure protein solutions at concentrations of 0.1–1 mg mL^{-1}.

2. *Hydrodynamics in the Taylor cone.* It was demonstrated by optical observations and by simulations that ES is accompanied by an intense liquid rotation inside the Taylor cone. The linear flow rate may reach 60 m s^{-1}, which corresponds to a shear rate of ~500,000 s^{-1} [186]. It has been shown that DNA breaks at much lower shear rates [187].
3. *Formation of clusters, drying.* Evaporation of micro- and nano-droplets results in increased concentration of low-volatility molecules. Such molecules have little effect at low concentration, but may denature protein molecules at high concentrations. Protein dehydration may also result in aggregation of protein molecules [188], in large conformational changes, breakage of intramolecular disulfide bonds and in formation of new intermolecular bonds [189, 190]. Fortunately, the process of transformation of microdroplets into nano-clusters takes only a few milliseconds and many of these potentially disastrous processes that take place in wet protein samples simply do not have adequate time to proceed. Nevertheless, addition of carbohydrates (sucrose or trehalose at more than 50% of the protein weight) was shown to completely eliminate loss of enzyme activity [54]. Protein molecules may be even completely embedded into sucrose nano-clusters to protect them throughout ES [191] and ESD [135, 136].
4. *Landing impact*. We have already discussed the potential effects of landing for a single protein ion. Because ESD results mostly in the formation of charged clusters, the energy released upon landing of such clusters should be smaller on a per molecule basis. Although this does not rule out the possibility that a small number of molecules in the cluster might be damaged, the majority of molecules will survive.
5. *Neutralization process.* Accumulation of nonvolatile products of neutralization might have some effect on protein structure and function, especially if the substrate is made of a metal which is prone to corrosion.
6. *Changes after deposition*. Certain precautions should be taken to keep the deposited protein active during the entire ESD procedure, especially if it takes a long time (hours). One should remember that exposure of a dry protein film to moderate humidity (60–80%) for 1–2 h may result in a complete loss of protein solubility due to thiol–disulfide exchange [189]. It is also important to avoid periodic wetting of the deposit, e.g., by occasional macrodroplets landing on the deposit before evaporation. As we discussed above, ESD in air is always accompanied with a weak corona discharge which generates hot atoms and radicals. These might react with protein molecules in-flight and after deposition. Radical scavengers and antioxidants (such as DTT, 2-mercaptoethanol, and ascorbic acid) can be added as protective reagents. Finally, the voltage and current should be kept low (usually 100–200 nA per capillary) to keep corona effects at minimum.

8 Conclusions

ESD as a method to manufacture micro- and nano-structures from biological molecules is a new technique in the wide range of micro- and nano-technologies now under development. Its unique feature consists in using a gas-phase charged aerosol as a deposition entity. This allows conditions which are not attainable in any other deposition technique. Thus, water soluble substances may be deposited on a substrate cooled to a subzero temperature, under vacuum, or on a layer of water-soluble material. The lack of solvent makes the ESD technology compatible with planar electronic technologies, where protein and DNA molecules could be integrated into electronic chips to serve as recognition elements in biosensors. It is important that the density of the material deposited is not limited to a monolayer (as in many other techniques, like microstamps [192, 193]): spots, tens of microns thick, may be easily deposited with a unique porous internal structure which cannot be reproduced by any other deposition technique.

References

1. Bose GM (1745) Recherches Sur La Cause Et Sur La Veritable Theorie De L'Electricite, Wittembergae
2. Rayleigh L (1882) Phil Mag 14:184
3. Burton EF, Wiegand WB (1912) Phil Mag 23:150
4. Zeleny J (1914) Phys Rev 3:69
5. Zeleny J (1915) Proc Cambr Phil Soc 18:71
6. Zeleny J (1917) Phys Rev 10:1
7. Coley JF (1902) US Patent 692631
8. Morton WJ (1902) US Patent 705691
9. Pugh E (1932) US Patent 1855869
10. Michelson D (1990) Electrostatic atomization. IOP, New York
11. Chang JS, Kelly AJ, Crowley JM (1995) (eds) Handbook of electrostatic processes. Wiley, New York
12. Robinson PS (1995) Nucl Instrum Methods 40:136
13. Van der Eijk W, Oldenhof W, Zehner W (1973) Nucl Instr Methods 112:343
14. Bruninx E, Rudstam G (1961) Nucl Instrum Methods 13:131
15. Blumberg LN, Stein P, Gursky JC (1962) Los Alamos Sci Lab Report
16. McNeal CJ, Macfarlane RD, Thurston EL (1979) Anal Chem 51:2036
17. Hensel RR, King RC, Owens KG (1997) Rapid Commun Mass Spectrom 11:1785
18. Wang YX, Zhou Y, Balgley BM, Cooper JW, Lee CS, DeVoe DL (2005) Electrophoresis 26:3631
19. Rietveld IB, Kobayashi K, Yamada H, Matsushige K (2006) J Phys Chem 110B:23351
20. Kumbar SG, Bhattacharyya S, Sethuraman S, Laurencin CT (2007) J Biomed Mater Res 81B:91
21. Hoyer B, Sorensen G, Jensen N, Nielsen DB, Larsen B (1996) Anal Chem 68:3840
22. Balachandran W, Miao P, Xiao P (2001) J Electrostatics 50:249
23. Wilhelm O, Pratsinis SE, Perednis D, Gauckler LJ (2005) Thin Solid Films 479:121
24. Ishida Y, Sogabe K, Haklai K, Baba A, Asano T (2006) Jpn J Appl Phys Part 1 Reg Papers Brief Commun Rev Pap 45:6475

25. Dole M, Mack LL, Hines RL, Mobley RC, Ferguson LD, Alice MB (1968) J Chem Phys 49:2240
26. Yamashita M, Fenn JB (1984) J Phys Chem 88:4451
27. Whitehouse CM, Dryer RN, Yamashita M, Fenn JB (1985) Anal Chem 57:675
28. Alexandrov ML, Gall LN, Krasnov MV, Nikolaev VI, Pavelenko VA, Shkurov VA (1984) Dokl Akad Nauk SSSR 277:379
29. Alexandrov ML, Gall LN, Krasnov MV, Nikolaev VI, Shkurov VA (1985) J Anal Chem USSR 40:1227
30. Fernandez de la Mora J (2000) Anal Chim Acta 406:93
31. Kebarle P, Tang L (1993) Anal Chem 65:972A
32. Kebarle P (2000) J Mass Spectrom 35:804
33. Kebarle P, Peschke M (2000) Anal Chim Acta 406:11
34. Fenn J (2002) J Biomol Tech 13:101
35. Gaskell SJ, Bolgar MS, Riba I, Summerfeld SG (1997) NATO ASI Ser C 504:3
36. Veenstra TD (1999) Biophys Chem 79:63
37. Przybylski M, Glocker MO (1996) Angew Chem Int Edn 35:807
38. Thundat T, Warmack RJ, Allison DP, Ferrell TL (1992) Ultramicroscopy 42–44:1083
39. Morozov VN, Seeman NC, Kallenbach NR (1993) Scann Microsc 7:757
40. Cheng X, Camp DG, Wu Q, Bakhtiar R, Springer DL, Morris BJ, Bruce JE, Anderson GA, Edmonds CG, Smith RD (1996) Nucl Acids Res 24:2183
41. Quist AP, Ahlbom J, Reimann CT, Sundqvist BUR (1994) Nucl Instrum Meth 88B:164
42. Ledbetter MC, Beuler RJ, Friedman L (1987) Proc Natl Acad Sci U S A 84:85
43. Sullivan PA, Axelsson J, Altmann S, Quist AP, Sundqvist BUR, Reinmann CT (1996) J Am Soc Mass Spectrom 7:329
44. Reimann CT, Quist AP, Kopniczky J, Sundquist BUR, Erlandsson R, Tengvall P (1994) Nucl Instr Meth B88:29
45. Maleknia SD, Chance MR, Downard KM (1999) Rapid Commun Mass Spectrom 13:2352
46. Rauschenbach S, Stadler FL, Lunedei E, Malinowski M, Koltsov S, Costantini G, Kern K (2006) Small 2:540
47. Ouyang Z, Takats Z, Blake TA, Gologan B, Guymon AJ, Wiseman JM, Oliver JC, Davisson VJ, Cooks RG (2003) Science 301:1351
48. Volny′ M, Tureček F (2006) J Mass Spectrom 41:124
49. Volny′ M, Elam WT, Ratner BD, Turecˇek F (2005) Anal Chem 77:4846
50. Gologan B, Takats Z, Alvarez J, Wiseman JM, Talaty N, Ouyang Z, Cooks RG (2004) J Am Soc Mass Spectrom 15:1874
51. Blake TA, Zheng OY, Wiseman JM, Takats Z, Guymon AJ, Kothari S, Cooks RG (2004) Anal Chem 76:6293
52. Wang P, Hadjar O, Laskin J (2007) J Am Chem Soc 129:8682
53. Volny' M, Sengupta A, Wilson CB, Swanson BD, Davis EJ, Turecˇek F (2007) Anal Chem 79:4543
54. Morozov VN, Morozova TY (1999) Anal Chem 71:1415
55. Morozov VN, Morozova TY (1999) Anal Chem 71:3110
56. Moerman R, Frank J, Marijnissen JC, Schalkhammer TGM, van Dedem GWK (2001) Anal Chem 73:2183
57. Chowdhury SK, Chait BT (1991) Anal Chem 63:1660
58. Verdingh V, Lauer KF (1967) Nucl Instrum Methods 49:179
59. Wilm MS, Mann M (1994) Int J Mass Spectrom Ion Processes 136:167
60. Manisali I, Chen DDY, Schneider BB (2006) Trends Anal Chem 25:243
61. Aksyonov S, Williams P (2001) Rapid Commun Mass Spectrom 15:1890
62. Kim JW, Yamagata Y, Takasaki M, Lee BH, Ohmori H, Higuchia T (2005) Sens Actuators B107:535
63. Xue Q, Foret F, Dunayevskiy YM, Zavracky PM, McGruer NE, Karger BL (1997) Anal Chem 69:426
64. Duby MH, Deng W, Kim K, Gomez T, Gomez A (2006) Aerosol Sci 37:306
65. Deng W, Klemic JF, Lib X, Reed MA, Gomez A (2006) Aerosol Sci 37:696

66. Jaworek A, Lackowski M, Krupa A, Czech T (2006) Exper Fluids 40:568
67. Bocanegra R, Galán D, Márquez M, Loscertales IG, Barrero A (2005) Aerosol Sci 36:1387
68. Liu HH, Felten C, Xue QF, Zhang BL, Jedrzejewski P, Karger BL, Foret F (2000) Anal Chem 72:3303
69. Van Berkel GJ, Zhou F, Aronson JT (1997) Int J Mass Spectrom Ion Processes 162:55
70. Van Berkel GJ, Zhou F (1995) Anal Chem 67:3958
71. Van Berkel GJ, Zhou F (1995) Anal Chem 67:2916
72. Fernandez de la Mora JF, Van Berkel GJ, Enke CG, Cole RB, Martinez-Sanchez M, Fenn JB (2000) J Mass Spectrom 35:939
73. Pozniak BP, Cole RB (2007) Anal Chem 79:3383
74. Tang KQ, Gomez A (1995) J Colloid Interface Sci 175:326
75. Vonnegut B, Neubauer R (1952) J Colloid Sci 7:616
76. Ahire DV, Kamra AK (1984) Mausam (formerly Indian J Meteor Geophys) 35:27
77. Taylor GI (1964) Proc R Soc Lond 280:383
78. Higuera FJ (2003) J Fluid Mech 484:303
79. Fernandez de la Mora JF (2007) Ann Rev Fluid Mech 39:217
80. Altun Z, Abdel-Rheim M (2002) Rapid Commun Mass Spectrom 16:738
81. Loeb L (1965) Electrical coronas – their basic physical mechanisms. University of California Press, Berkley and Los Angeles
82. Shorey JD, Midelson D (1970) Nucl Instrum Methods 82:295
83. Li WJ, Shanti RM, Tuan RS (2006) Electrospinning technology for nanofibrous scaffolds in tissue engineering. Wiley, Weinheim
84. Greiner A, Wendorf JH (2007) Angew Chem Int Edn 46:5670
85. Li D, Xia YN (2004) Adv Materials 16:1151
86. Moerman R, Frank J, Marijnissen JC, van Dedem GWK (1999) J Aerosol Sci 30:551
87. Bhatnagar P (2007) Appl Phys Lett 91:014102
88. Stoilov YY (1998) Langmuir 14:5685
89. Gente G, La Mesa C (2000) J Sol Chem 29:1159
90. de Juan L, Fernandez de la Mora JF (1996) In: Chow GM, Gonsales KE (eds) Nanotechnology. Molecularly designed materials. ACS, Washington DC, p 20
91. Sauerbrey G (1959) Z Phys 155:206
92. Chowdhary SK, Katta W, Chait BT (1990) J Am Chem Soc 112:9012
93. Fernandez de la Mora J, Loscertales IG (1994) J Fluid Mech 260:155
94. Tang K, Gomez A (1994) J Aerosol Sci 25:1237
95. Higuera FJ, Barrero A (2005) Phys Fluids 17:018104
96. Grigoriev AI, Senkevich OA (1985) Lett JTP 11:182
97. English WN (1948) Phys Rev 74:179
98. Sugimoto T, Asano K, Higashiyama Y (2001) J Electrost 53:25
99. Higashiyama Y, Yanase S, Sugimoto T (2002) J Electrost 55:351
100. Robinson JA, Bergougnou MA, Cairns WL, Castle GS, Inculet II (1998) IEEE Trans Indust Appl 34:1218
101. Jaworek A, Czech T, Rajch E, Lackowski M (2005) J Electrost 63:635
102. Tang KQ, Smith RD (1997) Int J Mass Spectrom Ion Processes 162:69
103. Borra JP, Ehouarn P, Boulaud D (2004) Aerosol Sci 35:1313
104. Thomas MC, Mitchell TW, Blanksby SJ (2006) J Am Chem Soc 128:58
105. Morand K, Talbo G, Mann M (1993) Rapid Commun Mass Spectrom 7:738
106. Morozov VN, Morozova TY (2002) US Patent 6350609 B1
107. Koufen P, Stark G (2000) Biochim Biophys Acta Mol Basis Disease 1501:44
108. Stanton J, Taucherscholz G, Schneider M, Heilmann J, Kraft G (1993) Rad Environm Biophys 32:21
109. Cole RB (2000) J Mass Spectrom 35:763
110. Betelu SI, Fontelos MA, Kindelan U, Vantzos O (2006) Phys Fluids 18:051706
111. Woenckhaus J, Hudgins RR, Jarrold MF (1997) J Am Chem Soc 119:9586
112. Rodriguez-Cruz SE, Klassen JS, Williams ER (1999) J Am Soc Mass Spectrom 10:958

113. Morozov VN, Morozova TY, Kallenbach NR (1998) Int J Mass Spectrom Ion Processes 178:143
114. De Juan L, Fernandez de la Mora J (1997) J Colloid Interface Sci 186:280
115. Fuchs NA (1959) Evaporation and droplet growth in gaseous media. Pergamon, New York
116. Forrester AT (1988) Large ion beams. Fundamentals of generation and propagation. Wiley, New York
117. Busman M, Sunner J (1991) Int J Mass Spectrom Ion Processes 108:165
118. Sigmond RS (1982) J Appl Phys 53:891
119. Gamero-Castano M, Aguirre-de-Carcer L, de Juan L, Fernandez de la Mora J (1998) J Appl Phys 51:2428
120. Jones JE (1993) In: Lakhtakia A (ed) Essays on the formal aspects of electromagnetic theory. World Scientific, Singapore, p 228
121. Lai FC, Sharma RK (2005) J Electrost 63:223
122. Yang Y, Jewell-Larsen NE, Brown DL, Pendergrass K, Parker DA, Krichtafovitch IA, Mamishev AV (2003) In: Smit A (ed) Thirteenth International Symposium on High Voltage Engineering. Mill, Netherlands, Rotterdam, p 1
123. Rashkovan A, Sher E, Kalman H (2002) Appl Thermal Eng 22:1587
124. Magnier P, Hong D, Leroy-Chesneau A, Pouvesle JM, Hureau J (2007) J Electrost 65:655
125. Olumee Z, Callahan JH, Vertes A (1998) J Phys Chem 102:9154
126. Venter A, Sojka PE, Cooks RG (2006) Anal Chem 78:8549
127. Chot GS, Kim DE, Kangt SO (1990) J Phys Appl Phys 23D:85
128. Znamenskiy V, Marginean I, Vertes A (2003) J Phys Chem 107A:7406
129. Iribarne JV, Thomson BA (1976) J Chem Phys 64:2287
130. Thomson BA, Iribarne JV (1979) J Chem Phys 71:4451
131. Felitsyn N, Peschke M, Kebarle P (2002) Int J Mass Spectrom 219:39
132. Kaltashov IA, Mohimen A (2005) Anal Chem 77:5370
133. Iavarone AT, Williams ER (2003) J Am Chem Soc 125:2319
134. Wortmann A, Kistler-Momotova A, Zenobi R, Heine MC, Wilhelm O, Pratsinis SE (2007) J Am Soc Mass Spectrom 18:385
135. Avseenko NV, Morozova TY, Ataullakhanov FI, Morozov VN (2001) Anal Chem 73:6047
136. Avseenko NV, Morozova TY, Ataullakhanov FI, Morozov VN (2002) Anal Chem 74:927
137. Christie JH, Sylvander SR, Woodhead IM, Irie K (2003) Fifth International conference on Electromagnetic wave interaction with water and moist substances, Rotorua, Neuseeland, p 129
138. Bukatina AE, Morozov VN, Gusev NB, Sieck GC (2002) FEBS Lett 524:107
139. Morozov VN, Morozova TY (2000) US Patent 6033913
140. Morozov VN, Morozova TY (2003) Anal Chem 75:6813
141. Morozov VN (2004) In: Schena M (ed) Protein microarrays. Jones and Bartlett, Sudbury, MA, USA, p 71
142. Morozov VN, Morozova TY (2006) Anal Chim Acta 564:40
143. Morozov VN, Evanskey M, Tan YK, Shaffer D, Morozova TY, Bailey C (2006) Langmuir 22:1742
144. Martinez AJ, Manolache S, Gonzales V, Young RA, Denes F (2000) J Biomater Sci Polymer Edn 11:415
145. Denes F, Young RA (1998) In: Dumitriu S (ed) Polysaccharides: structural diversity and functional versatility. Marcel Dekker, New York, p 1087
146. Reiser A, Lock MWB, Knight J (1969) Trans Farad Soc 65:2168
147. Bone S (1991) Biochim Biophys Acta 1078:336
148. Kim HS, Lee DY, Park JH, Kim JH, Hwang JH, Jung HI (2007) Exp Tech:1
149. Morozov VN, Morozova TY (1992) Anal Biochem 201:68
150. Kim JW, Yamagata Y, Kim BJ, Takeuchi S, Higuchi T (2003) Seventh International Conference on Miniaturized Chemical and Biochemical Analysts Systems. Squaw Valley, California, USA
151. Uematsua I, Matsumotoa H, Morotaa K, Minagawaa M, Tanioka A, Yamagata Y, Inoue K (2004) J Colloid Interface Sci 269:336

152. Lee B, Kamiya N, Machida S, Yamagata Y, Horie K, Nagamune T (2003) Biomaterials 24:2045
153. Kremer EP, Evans GJ, Jervis RE (2006) J Phys Appl Phys 39D:5008
154. Jayasinghe SN, Edirisinhe MJ (2003) J Mater Sci Lett 22:1617
155. Morozov VN, Gavryushkin VA, Deev AA (2002) J Biochem Biophys Methods 51:57
156. Morozov VN, Morozova TY, Johnson KL, Naylor S (2003) Rapid Commun Mass Spectrom 17:2430
157. Buchko CJ, Kozloff KM, Sioshansi A, O'Shea KS, Martin DC (1996) In: Cotell CM, Meyer AE, Gorbatkin SM, Grobe GL (ed) Material Research Society Symposium Proceedings. Materials Research Society, Pittsburgh, PA, p 23
158. Lee B, Kim J, Ishimoto K, Yamagata Y, Tanioka A, Nagamune T (2003) J Chem Eng Jpn 36:1370
159. Welle AM, Jacobsa HO (2005) Appl Phys Lett 87:263119
160. Hepburn DM, Kemp IJ, Shields AJ (2000) IEEE Electr Insul Mag 16:19
161. Yovcheva TA, Avramova IA, Mekishev GA, Marinova TS (2007) J Electrost 65:667
162. Jacobs HO, Whitesides GM (2001) Science 291:1763
163. Rigden JS (1996) Macmillan encyclopedia of physics. Simon and Schuster, New York
164. Grandbois M, Beyer M, Rief M, Clausen-Schaumann H, Gaub HE (1999) Science 283:1727
165. Adamson AV (1979) A textbook of physical chemistry. Academic, New York
166. Sturtevant JM (1977) Proc Natl Acad Sci U S A 74:2236
167. Fischer H, Polikarpov I, Craievich AF (2004) Protein Sci 13:2825
168. Morozov VN, Morozova TY (1993) J Biomol Struct Dyn 11:459
169. Tanaka Y, Yamazaki Y, Okumura K (2003) Europhys Lett 63:146
170. Singh-Zocchi M, Hanne J, Zocchi G (2002) Biophys J 83:2211
171. Yamashita M, Fenn JB (1984) J Phys Chem 88:4611
172. Takashima K, Riveros JM (1998) Mass Spectrom Rev 17:409
173. Eberle G, Schmidt H, Eisenmenger W (1996) IEEE Trans Dielectr Electr Insul 3:624
174. Kallmann H, Pope M (1960) J Am Chem Soc 32:300
175. Sessler GM (1980) In: Sessler GM (ed) Electrets (Topics in Applied Physics). Springer, Berlin Heidelberg New York, p 13
176. Gabriel B, Teissie J (1996) Proc Natl Acad Sci U S A 93:14521
177. Nagle JF, Morowitz HJ (1978) Proc Natl Acad Sci U S A 75:298
178. Vincent P, Tomaselli VP, Morris H, Shamos MH (1974) Biopolymers 13:2423
179. Postow E, Rosenberg B (1970) J Bienerg Biomembr 1:467
180. Hudis M (1974) In: Hollahan JR (ed) Techniques and applications of plasma chemistry. Wiley, New York, p 113
181. Morozov VN, Vsevolodov NN, Bailey C (2007) US Patent Application 20070113530
182. Ebeling DD, Westphall MS, Scalf M, Smith LM (2000) Anal Chem 72:5158
183. Frey BL, Lin Y, Westphall MS, Smith LM (2005) J Am Soc Mass Spectrom 16:1876
184. Li Q, Koropchak JA (2004) Anal Chem 76:5539
185. Camelot D, Marijnissen JCM, Scarlett B (1999) Ind Eng Chem Res 38:631
186. Lastow O, Balachandran W (2006) J Electrost 64:850
187. Adam RE, Zimm BH (1977) Nucl Acids Res 4:1513
188. Kaddis CS, Lomeli SH, Yin S, Berhane B, Apostol MI, Kickhoefer VA, Rome LH, Loo JA (2007) J Am Soc Mass Spectrom 18:1206
189. Liu WR, Langer R, Klibanov AM (1991) Biotechnol Bioeng 37:177
190. Volkin DB, Klibanov AM (1990) In: Creighton TE (ed) Protein function – a practical approach. IRL, Oxford, New York, p 1
191. Kaufman SL (2000) Anal Chim Acta 406:3
192. Quist AP, Pavlovic EP, Oscarsson S (2005) Anal Bioanal Chem 381:591
193. Geissler M, Bernard A, Bietsch A, Schmid H, Michel B, Delamarche E (2000) J Am Chem Soc 122:6303

Part IV
Processing Technology

Adv Biochem Engin/Biotechnol (2010) 119: 165–177
DOI: 10.1007/10_2008_47
© Springer-Verlag Berlin Heidelberg 2009
Published online: 23 June 2009

Droplet Handling

Toru Torii

Abstract When quantitative analysis or quantitative chemical synthesis is performed using a micrototal analysis system (microTAS), the technologies for precise metering, transporting, and mixing of droplets are required. In this chapter, several technologies for the handling of droplets are described. For metering, dispensing and transporting of droplets, pneumatic and electrokinetic forces are used. Separation of cells and particles is also performed by electrical operation. Other handling technique, such as ultrasonic or centrifugal force applications, are also reviewed. Robotic synthesis devices or high throughput screening devices are promising applications for these technologies.

Keywords Centrifugal microfluidics, Electrokinetic force, microTAS, SAW, Separation

Contents

T. Torii
Kashiwanoha 5-1-5, Kashiwa-shi, Chiba, 277-8563, Japan
e-mail: torii@k.u-tokyo.ac.jp

Abbreviations

microTAS	Micrototal analysis system
PDMS	Polydimethylsiloxane
SAW	Surface acoustic wave

1 Introduction

AU1

The microTAS device has a great potential to reduce the amount of samples and reagents, and time for analysis and synthesis, though most of them were based on the continuous flows in microchannels. For quantitative analysis of samples, such as cells or biochemical materials, using a microTAS device for precise metering of droplets is essential. For the handling of microdroplets as well as cells and particles, electrostatic force, pneumatic pressure, and ultrasonic applications are the expected methods. In this chapter, the use of electrokinetic force and pneumatic pressure for the said purpose is mainly described and the references of the work done mainly in the last 10 years is quoted.

2 Electrokinetic Handling

2.1 Dielectrophoresis

When charged particles are put in an electric field, the particles with positive charge will move towards the cathode, and the negatively charged particles towards the anode. This is well known as "electrophoresis" (Fig.1a). In contrast, when conductive materials such as aqueous droplets, organic particles and cells are set in a non-uniform electric field, dielectrophoretic force is produced (Fig.1b). The dielectrophoresis was initially named by Pohl [1], and defined in his book as "Dielectrophoresis is the translational motion of neutral matter caused by polarization effect in a non-uniform electric field" [2].

Dielectric force (F_{DEF}) is expressed as follows [3]:

$$F_{DEF} = 2\pi\varepsilon_1 a^3 \mathrm{Re}[K(\omega)]\nabla E^2$$

$$K(\omega) = \frac{\varepsilon_2^* - \varepsilon_1^*}{\varepsilon_2^* - 2\varepsilon_1^*} \tag{1}$$

where ε_2^* is permittivity of particle (droplet) (complex), ε_1^* permittivity of medium (complex), a radius of particle, E electric field strength, and $K(\omega)$ Clausius-Mossotti function.

When $\mathrm{Re}[K(\omega)] > 0$, particles will move to the left (positive dielectrophoresis), and when $\mathrm{Re}[K(\omega)] < 0$, particles will move to the right (negative dielectrophoresis) (Fig.1b).

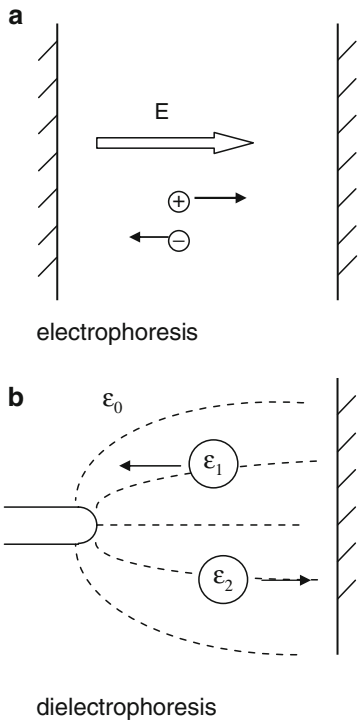

Fig. 1a,b Electrophoresis **(a)** and dielectrophoresis **(b)**. Conductive particles or cells move left ($\varepsilon_0 < \varepsilon_1$), and right ($\varepsilon_0 > \varepsilon_2$).

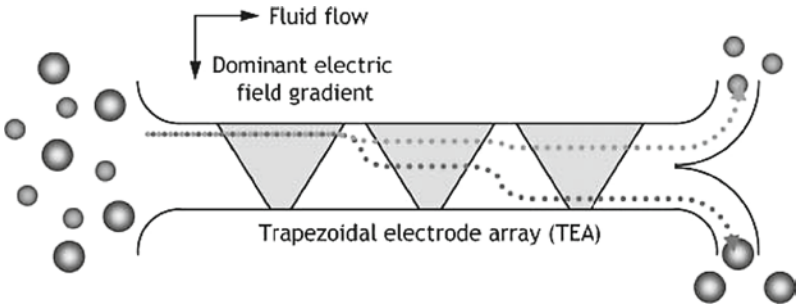

Fig. 2 Dielectrophoretic separation of beads using trapezoidal electrodes

Pohl first separated living cells from dead cells using the dielectrophoresis technique in 1966 by applying the difference in permittivity between two cells [4]. Pohl also described the various applications of dielectrophoresis in his book [2].

Dielectrophoresis has been widely used for particle or cell separation, and one of the recent examples is shown in Fig. 2. A trapezoidal electrode was used to produce dielectrophoretic force to separate 6 and 15 μm beads in a microchannel [5]. The dimensions of the trapezoidal electrodes were 120 μm longer base, 20 μm shorter base, and 60 μm height, and the gap between the electrodes had the inverse

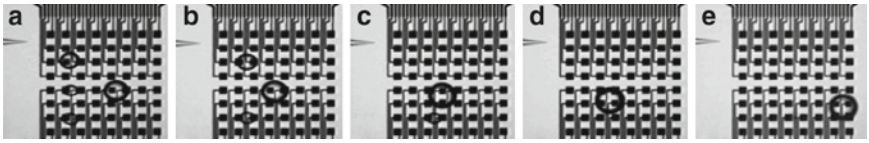

Fig. 3 Dielectrophoretic manipulation of droplets on PFP device. **a** Four droplets on electrode. **b–d** Small droplets merged large one. **e** Transportation

configuration of the trapezoidal electrode. The microfluidic channel was 30 μm in depth and 50 μm in width. Phosphate buffered saline with an electrical conductivity of 2.2 mS m^{-1} set by adjusting the conductivity with deionized water was prepared as a separation buffer. Values for Re($K(\omega)$ were −0.12 and −0.19 for polystyrene beads of 6 and 15 μm diameters at an applied field frequency of 50 kHz, 8 V_{p-p} in the buffer, respectively.

Advanced techniques of dielectrophoresis are electrorotation and traveling wave dielectrophoresis. Electrorotation was used especially for the measurement of certain properties of cells or materials, such as bacterial motor characteristics of living cells [6, 7]. It was also applied to droplet or particle rotation for mixing in microchannels [8]. Traveling wave dielectrophoresis was also applied to the separation of particles, cells and droplets. It can levitate the particles and transport them using dielectrophoretic forces, other particles sticking to the electrode at the same time. The separation is caused by differences in permittivity, which produces the positive and negative dielectrophoresis [9].

The Gascoyne group reported the programmable chip for droplet actuation using dielectrophoresis. Figure 3 shows multiple droplets movement, droplets motion and fusion on an 8 × 8 Programmable Fluidic Processor with a 30-μm electrode, increasing the applied voltage to $180V_{p-p}$, with the frequency between 5 and 500 kHz. Droplet dispensing of 3 pl has also been performed by applied voltage of 120 V_{p-p} and frequency 150 kHz [10]. Furthermore, there was an increase in size up to 32 × 32 embodiment based on a scaleable CMOS architecture [11].

2.2 Electrowetting

The term electrowetting was first introduced in 1981 to describe an effect proposed for designing a new type of display device [12]. It is attractive as a new type of a flat panel display [13]. Electrowetting is an effect which is caused by voltage being aplied to droplets, thereby changing wettability. Figure 4 illustrates the principle of electrowetting and relationships of surface tensions. It can transport, merge, separate, and dispense droplets [14] (Fig. 5).

From the Young–Laplace equation, the contact angle is obtained as follows [15]:

$$\gamma_{SL} = \gamma_{SG} + \gamma_{GL} \cos\theta \tag{2}$$

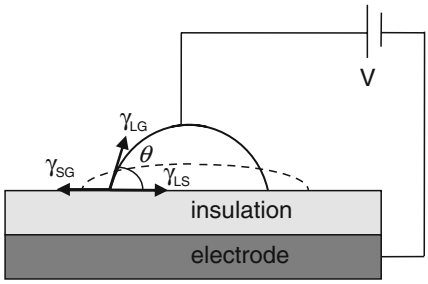

Fig. 4 Schematic view of the electrowetting electrode [14]

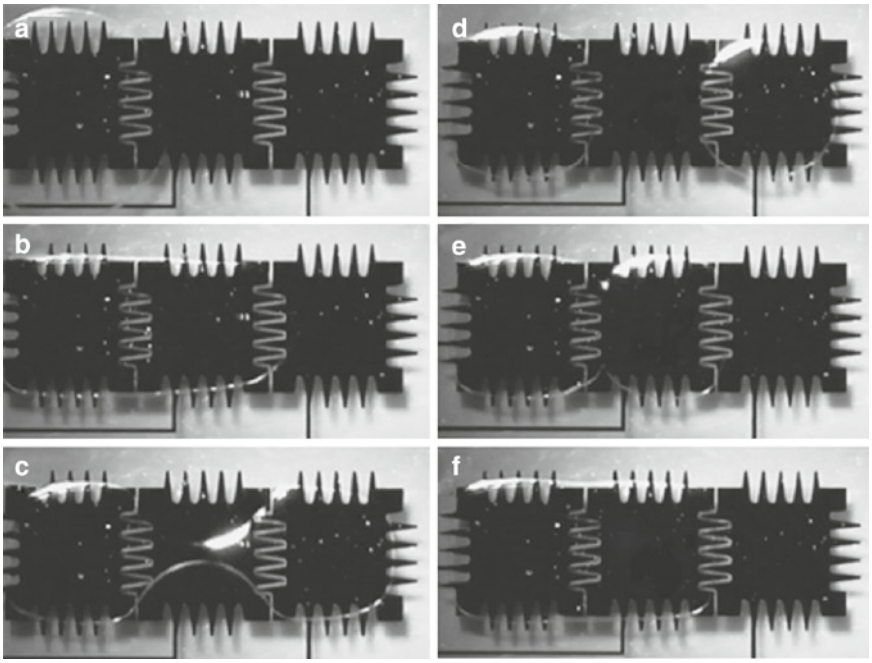

Fig. 5 Droplet separation and merging by electrowetting [14]

where γ_{SG} is the interfacial tension between solid and gas, γ_{GL} is the interfacial tension between gas and liquid, γ_{SL} is the interfacial tension between solid and liquid, and θ is the contact angle.

From Lippmann's equation [16],

$$\gamma_{SL} = \gamma_{SL}^{0} - \frac{1}{2}CV^2 \tag{3}$$

where $\gamma_{SL}{}^{0}$ denotes the contact angle without applied voltage, and C is capacitance. The contact angle after applying voltage is described as follows [16]:

$$\cos\theta \frac{\gamma_{SL}^{0} = \gamma_{SL} - \frac{1}{2}CV^{2}}{\gamma_{GL}}$$

$$\theta = \cos^{-1}\left(\frac{\gamma_{SG}^{0} - \gamma_{SG} - \frac{1}{2}CV^{2}}{\gamma_{GL}}\right) \tag{4}$$

Electrowetting devices were applied to various types of Lab-on-a-Chip devices, e.g., a glucose sensor using a colorimetric enzyme-kinetic method based on Trinder's reaction in which a photodiode sensor was used [17], a mixing device for samples and reagents of biological and chemical applications [18], a clinical application for diagnostic testing of human physiological fluids such as whole blood, serum, plasma, urine, saliva, sweat and tears, using integrated digital fluidics [19]. Other applications were sample preparation (protein and peptide) device for MALDI-MS, which would be a useful device for a high-throughput sample preparation device [20], and sample purification for MALDI-MS which was performed when droplets were moved on the dried spots [21].

2.3 Other Electrostatic Handling

The electrowetting device is composed of two electrodes installed at the top and bottom, where the droplets are inserted, and the vertical force to the top and bottom electrode are cancelled, so the applied voltage is not high. However, droplet manipulation on one side electrode as a simple arrangment was also executed, though the applied voltage was larger than that of electrowetting. Washizu [22] achieved droplet actuation by multiphase electrodes for chemical reactions on hydrophobic solid surfaces where basic unit operations, such as transport, sorting, and mixing of reagents, were performed. Teflon AF was used as a hydrophobic material, and 60 Hz a.c. voltage up to 400 V_{rms} was applied to 12-phase electrodes (100 μm width, 100 μm gap). Droplets of deionized water, ionic biological buffer solutions, and protein solutions with volumes 0.5–5 μL were manipulated. Tokkeli [23] analyzed droplet actuation on a planar surface precisely with modeling and experiment. An example of electrode size was 400 μm in width and 200 μm in space width with an applied voltage of 300 V, though he used various types of electrodes.

Taniguchi [24] applied a six-phase electrode to aqueous droplet handling in the immiscible medium, such as oils, and investigated chemical and biochemical reactions (Fig.6a). Two kinds of electrodes were used. One was a normal parallel electrode, which was made by a silkscreen printing process with silver paste and an insulating covering film. The electrode arrays had a multi-pitch length of 0.5–2.0 mm and width 0.2 mm. Another was an 18 × 18 dot matrix with a pitch of 0.8 mm and diameter of dot 0.55 mm (through a hole of 0.34 mm). Manipulation of droplets took place by applying sequential voltages to the six-phase electrode columns or

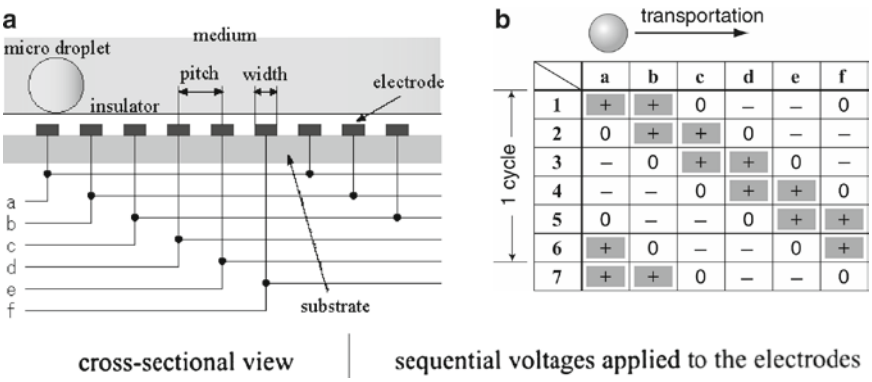

	a	b	c	d	e	f
1	+	+	0	–	–	0
2	0	+	+	0	–	–
3	–	0	+	+	0	–
4	–	–	0	+	+	0
5	0	–	–	0	+	+
6	+	0	–	–	0	+
7	+	+	0	–	–	0

Fig. 6 Principle of electrostatic manipulation of microdroplet [23]

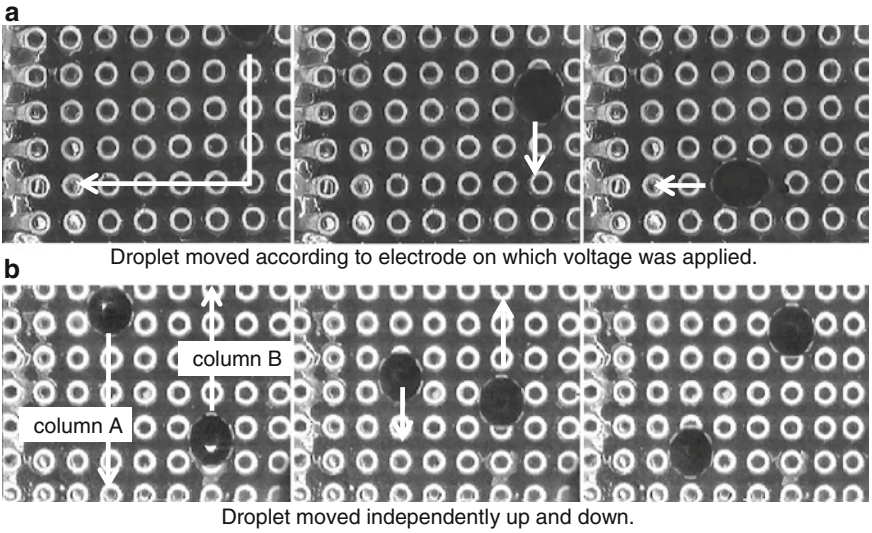

Fig. 7 Droplet manipulation on electrode dots. Microdroplet moved according to the applied voltage lines

six-phase electrode lines. The sequential voltages had a six-phase rectangular profile (Fig.6b). The sequence [+ + + − − −] was the most efficient for droplet transport. Using the electrode dot device, microdroplets were manipulated independently. The microdroplets consisting of 1 μL of water-based ink were put into the medium. Sequential voltages (450 $V_{0\text{–}p}$, 0.5 Hz, pattern; + + + − − −) were applied according to the line with arrows in Fig.7a. The microdroplet was moved according to the line downward, and then turned at right angle. Two microdroplets consisting of 1 μL of water-based ink were put into the medium (Fig.7b). The same sequential voltages were applied only to the electrode column A and column B and the microdroplet on column A moved upward; in contrast, the droplet on column B moved downward independently. It would also be possible to improve the programmable connections

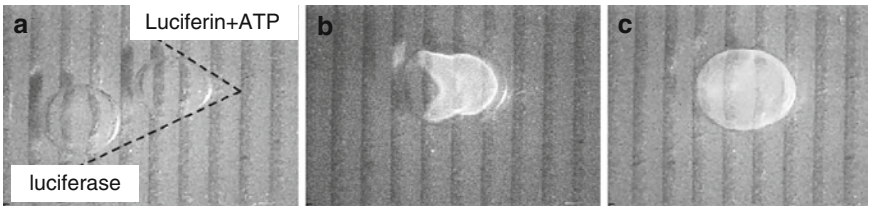

Fig. 8 Luciferin luminescence reaction caused by mixing of droplets [24]

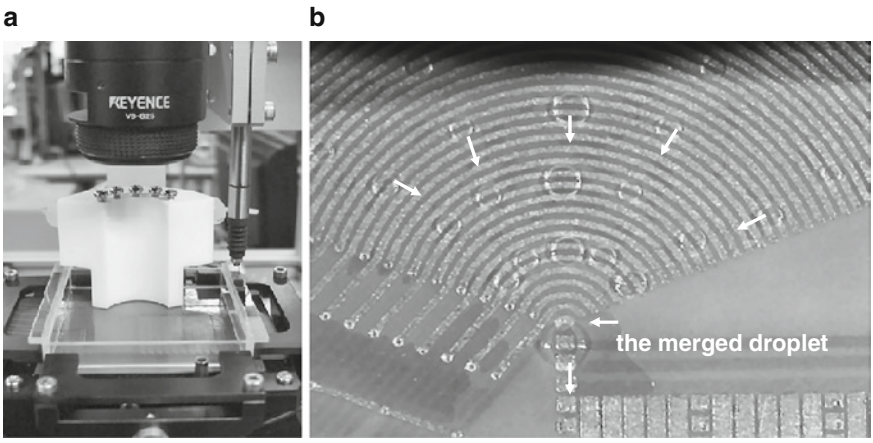

Fig. 9 A multiple droplet dispenser. Five droplets were dispensed in synchronization, and merged at the center of the arc then transported to downward

to each dot electrode. As a result of chemical reactions, a luciferin–luciferase enzyme reaction was achieved in a mixed droplet. Microdroplets of luciferin and ATP aqueous solution and of luciferase aqueous solution were placed into the medium, on the six-phase electrode arrays device with guidance films (Fig.8; both droplets had a volume of 1 μL and the voltage was 650 $V_{0\text{–p}}$ with 0.7 Hz at a pattern of (+ + + − − −)). When applying the sequential voltage to the electrodes, the droplet of luciferase solution was transported along the guidance film (from the left in the figure), merging of the two droplets caused a chemical reaction, and the luciferin fluoresced in the mixed droplet. Other applications were also presented such as DNA detection, and immunoassay [25, 26].

Droplet dispensing was also carried out. Direct droplet dispensing on the electrode reported using dielectrophoresis and electrowetting, though they had only one dispenser [10, 11, 14]. Choi [27] started their work from one dispenser and integrated to a multiple dispenser in the vicinity. A multiple-hole droplet dispenser was fabricated with a Teflon block and five holes with diameter of 130 μm by precision machining. The multiple droplet dispenser was setup on a card with a thin film put on the electrode (Fig.9a). The five droplets of pure water were dispensed from the

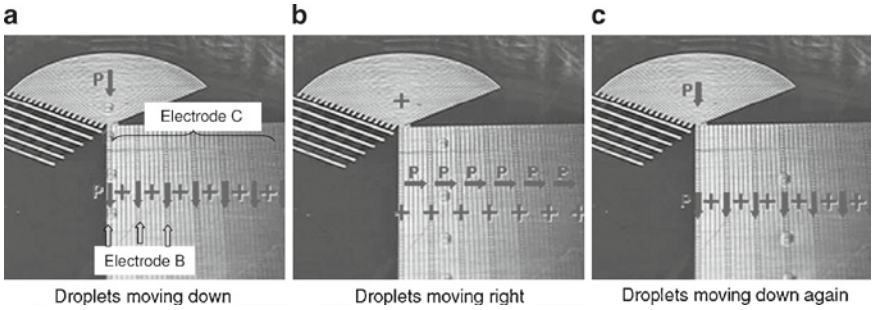

Fig. 10 Sequence of droplet handling in two dimensions

multiple-hole dispenser in synchronization on the arc-shaped electrode. The droplets moved toward the center of the arc, merging together, and moved downward (Fig.9b). The volume range of 15–140 nL could be changed.

Two-dimensional transportation of droplets was performed on a single electrode with 18-phase output power supply; sixphases for arc electrode, six for vertical, and six for horizontal [28]. Initially, droplets were dispensed on the arc electrode, and they moved to the center of the arc where droplets merged to become a large droplet. Figure 10 shows the sequence of the droplet transportation in two dimensions. The letter "P," associated with an arrow, indicates the traveling direction of the applied voltage pattern. The plus sign indicates a constant positive. The droplets were successfully transported in the two dimensions. In this experiment, a removable plastic films card put on the electrode was used to reduce the costs compared to a fixed electrode panel.

3 Handling Using Pneumatic Pressure

Two types of pneumatic pressure based manipulation of droplets has also been proposed; the air, directly and indirectly, in contact with droplets. For the direct manipulation method, hydrophobic valves were used.

Figure 11 shows the principle of the hydrophobic valve (Laplace valve). The critical pressure of the valve is described as follows, which is a famous Young–Laplace equation [15]:

$$P_c = \frac{2\gamma_{LG}\cos\theta}{R} = \frac{2\gamma_{LG}\cos\theta}{\left(\frac{1}{w}+\frac{1}{h}\right)}$$

where P_C is the critical pressure of the valve, θ is the contact angle of the liquid, γ_{LG} is the surface tension of the liquid, R is the radius of the liquid, and w and h are the width and height of the microchannel.

The critical pressure is determined by the contact angle which depends on the materials. If the material is hydrophobic, the critical pressure will be large. Hosokawa

Fig. 11 Schematic view of Laplace valve

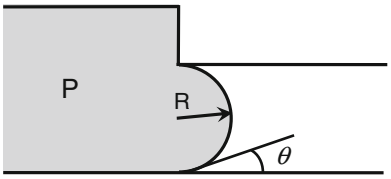

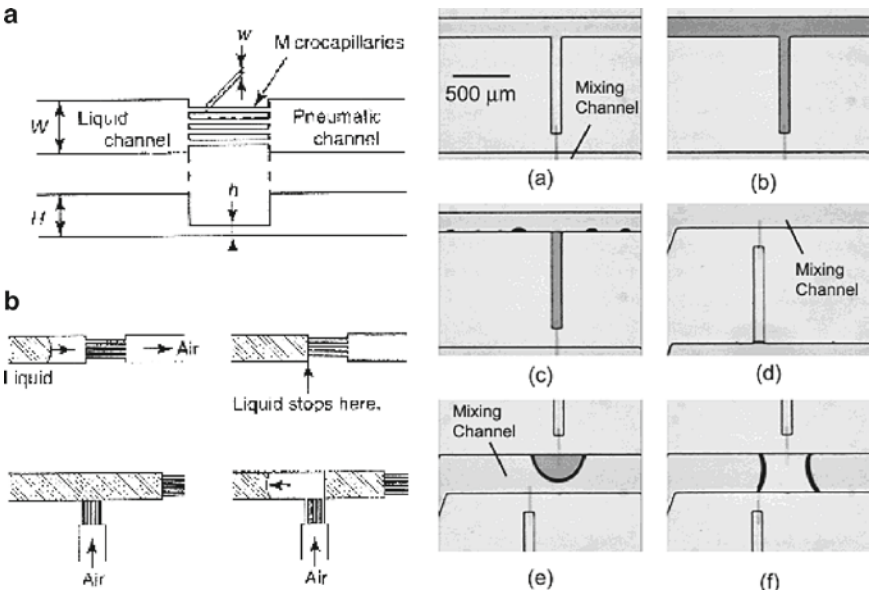

Fig. 12 Pneumatic handling of a droplet in a microchannel using Laplace valve. **(a)** mMicro-channnel size; $W \times xH$;100 μm × x25 μm, wx×h5 μm × x3 μm [29]. **(b)** mMetering of two reagent [30]

[29] initially used the Laplace valve in microchannels showing the transportation, metering, and mixing of picoliter-sized liquid samples with a main working area of 1 mm^2 (Fig.12a). The microchannel was made by PDMS with W×H of 100 μm × 25 μm, and w×h 5 μm × 3 μm. The barrier pressure was 30–35 KPa, while calculated value at 5 μm × 3 μm microchannel was 27 kPa, which was large enough for handling the droplets. Metering, transportation and mixing were performed only by pneumatic operations. They also showed the circulation in microdroplets which would be effective for mixing. Yamada [30] demonstrated the nanoliter sized liquid dispenser array using PDMS for microchannels and valves. Figure 12b shows the procedure of dispensing a dye and a reagent with each volume at 20 nL, merging, and mixing. The number of valves was integrated up to 50 in a 90-mm disk. The coefficient of variation of dispensed volume in 50 chambers was 1.2%, indicating the very high reproducibility of control and productivity. The critical pressure of the Laplace valve was due to the wettability of the microchannel. Takei [31] reported four different steps of wettability. Titania was first introduced to a

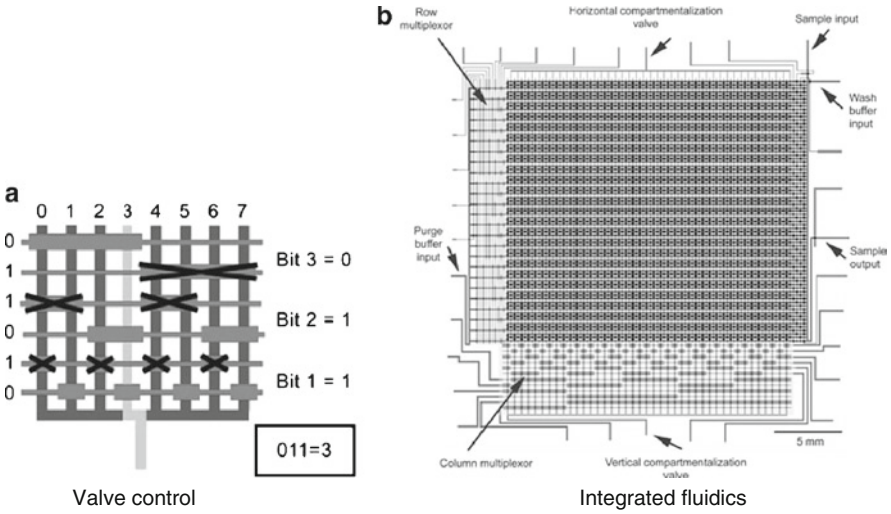

Fig. 13 Basic motion of pneumatic valve and its integration [33]

microchannel, and then octadecyltrichlorosilane (OTS) was coated on the titania. Light irradiation was applied to the surface, changing the irradiation time. The Laplace pressure of the valve was changed from 6.8 to 12.5 kPa.

For the indirect handling of droplets, pneumatic pressure was used to deform the microchannel as a valve. Hosokawa [32] presented a normal close valve for which negative pressure was used for the control of the valve. The Stephan Quake group performed a large scale integration of microfluidic devices using pneumatic valves [33–35]. The lines in Fig 13a were a pneumatic channel for the control of fluid, and channels in the column were fluid channels. Only six pneumatic inlets controlled eight fluidic channels, and then n fluid channel can be controlled by the $2 \log_2 n$ control lines. Figure 13b is one of the large scale integrated microchannel chips. This chip is especially used for protein crystallization, and Fluidigm Corp. put a special chip "TOPAZ" onto the market [36].

4 Other Handling Techniques

Some other droplet handling techniques were also performed. Droplet actuation using a surface acoustic wave (SAW) device was executed by some groups. The SAW is a wave which is generated on the surface of elastic materials, such as a Rayleigh wave, and produced using a piezoelectric material, such as $LiNbO_3$ (Fig.14). The amplitude is only a few nanometers. Wixforth group developed a droplet dispenser and applications using SAW devices [37–38], though flow streaming and atomization were previously performed [39]. Some SAW devices, using this technology, were put on the market [40]. Nanopump particle collection and its biomedical applications were reported [41–43].

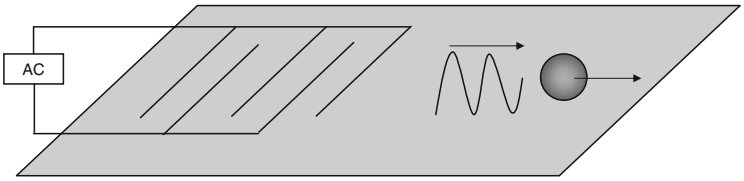

Fig. 14 Schematic view of droplet handling using SAW device

One of the main topics of microTAS 2000 was centrifugal microfluidics on CD devices [44]. This mechanism is the same as the Laplace valve, though centrifugal force is used instead of pneumatic force. It was mainly used for clinical analysis, such as multiple enzymatic assay [45], ELISA [46], and hybridization[47].

For handling a single droplet or cell, the optical tweezer has the potential for easy handling and some products have been commercialized [48].

5 Outlook

In these 10 years, various technologies for handling droplets have been developed, and some of these have already been put on the market. These techniques enable quantitative operations of reagents and samples, which would lead to microTAS from preprocessing to final analysis of samples. Robotic synthesis devices or high throughput screening devices such as protein crystallization devices are promising applications for these technologies, and further improvement, investigation, and commercialization of these technologies are also expected. A critical review for microfluidic platform was published lately, so it would be useful to read this article [49].

References

1. Pohl HA (1951) J Appl Phys 22:869
2. Pohl HA (1978) Dielectrophoresis. Cambridge University Press, Cambridge
3. Jones TB (1995) Electromechanics of particles. Cambridge University Press, Cambridge
4. Pohl HA, Hawk I (1966) Science 152:647
5. Choi S, Park JK (2005) Lab Chip 5:1161
6. Washizu M et al. (1993) IEEE Trans IA 29:286
7. Cristofanilli M et al. (2002). Clin Cancer Res 615:615
8. Wilson CF et al. (2002) Anal Chem 74:5099
9. Hughes MP (2002) Electrophoresis 23:2569
10. Schwartz JA, Vykoukal JV, Gascoyne PRC (2004) Lab Chip 4:11
11. Gascoyne PRC et al. (2004) Lab Chip 4:299
12. Beni G, Hackwood S (1981) Appl Phys Lett 38:207
13. Sun B, Zhou K, Lao Y, Heikenfeld J, Cheng W (2007) Appl Phys Lett 91:011106
14. Pollack MG, Shenderov AD, Fair RB (2002) Lab Chip 2:96

15. de Gennes PG, Wyart FB, Quere D (2004) Capillarity and wetting phenomena: drops, bubbles, pearls, waves. Springer, Berlin Heidelberg New York
16. Moon H, Cho SK, Garrel RL, Kim CJ (2002) J Appl Phys 92:4080
17. Srinivasan V, Pamula VK, Fair RB (2004) Anal Chim Acta 507:145
18. Paik P, Pamula VK, Fair RB (2003) Lab Chip 3:253
19. Srinivasan V, Pamula VK, Fair RB (2004) Lab Chip 4:310
20. Wheeler AR, Moon H, Kim CJ, Loo JA, Garrell RL (2004) Anal Chem 76:4833
21. Wheeler AR et al. (2005) Anal Chem 77:534
22. Masao WA (1998) IEEE Trans IA 34:732
23. Torkkeli A(2003)Droplet microfluidics on a planar surface. VTT Publications, Finland, VTT Publications 504, ISBN 951-386-2380
24. Taniguchi T, Torii T, Higuchi T (2002) Lab Chip 2:19
25 Goh LK et al. (2004) Micro TAS 2004. Malmo, Sweden, 442
26 Okada M et al. (2004) Micro TAS 2004. Malmo, Sweden, 243
27. Choi WK et al. (2007) Sens Actuators A 136:484
28. Lebrasseur WK et al. (2007) Sens Actuators A 136:358
29. Hosokawa K, Fujii T, Endo I (1999) Anal Chem 71:4781
30. Yamada M, Seki M (2004) Anal Chem 76:895
31. Takei G, Nonogi M, Hibara A, Kitamori T, Kim HB (2007) Lab Chip 7:596
32. Hosokawa K, Maeda R (2000) J Micromech Microeng 10:415
33. Thorsen T, Maerkl SJ, Quake SR (2002) Science 298:580
34. Hansen C et al. (2002) PNAS 99:16531
35. Quake SR (2007) Annu Rev Biophys Biomol Struct 36:213
36. http://www.fluidigm.com/index.html
37. Strobl C et al. (2004) IEEE Trans Ultrason Ferroelect Freq Contr 51:1432
38. Guttenberg Z, Muller H et al. (2005) Lab Chip 5:308
39. Kurosawa M, Watanabe T et al. (1995) Sens Actuators A 50:69
40. http://www.advalytix.com/
41. Renaudin A et al. (2006) Sens Actuators B 113:389
42. Tan MK, Friend JR, Yeo LY (2007) Lab Chip 7:618
43. Li H, Friend JR, Yeo LY (2007) Biomed Microdevices 9:647
44. van den Berg A, Olthuis W, Bergveld P (eds) (2000) Proceedings of MicroTAS. Kluwer, Dordrecht
45. Duffy DC, Gillis HL, Lin J et al. (1999) Anal Chem 71:4669
46. Lai S, Wang SN, Luo J et al. (2004) Anal Chem 76:1832
47. Bynum MA, Gordon GB (2004) Anal Chem 76:7039
48. http://www.palm-microlaser.com/
49. Haeberle S, Zengerle R (2007) Lab Chip 7:1094

Adv Biochem Engin/Biotechnol (2010) 119: 179–194
DOI: 10.1007/10_2010_68
© Springer-Verlag Berlin Heidelberg 2010
Published online: 9 June 2010

Integrated Microfluidic Systems

Shohei Kaneda and Teruo Fujii

Abstract Using unique physical phenomena at the microscale, such as laminar flow, mixing by diffusion, relative increase of the efficiency of heat exchange, surface tension and friction due to the increase of surface-to-volume ratio by downscaling, research in the field of microfluidic devices, aims at miniaturization of (bio)chemical apparatus for high-throughput analyses. Microchannel networks as core components of microfluidic devices are fabricated on various materials, such as silicon, glass, polymers, metals, etc., using microfabrication techniques adopted from the semiconductor industry and microelectromechanical systems (MEMS) technology, enabling integration of the components capable of performing various operations in microchannel networks. This chapter describes examples of diverse integrated microfluidic devices that incorporate functional components such as heaters for reaction temperature control, micropumps for liquid transportation, air vent structures for pneumatic manipulation of small volume droplets, optical fibers with aspherical lens structures for fluorescence detection, and electrochemical sensors for monitoring of glucose consumption during cell culture. The focus of this review is these integrated components and systems that realize useful functionalities for biochemical analyses.

Keywords Detection, Integration, Liquid handling, Temperature control

Contents

S. Kaneda and T. Fujii (✉)
LIMMS/CNRS-IIS, Institute of Industrial Science, University of Tokyo, Komaba 4-6-1, Meguro-ku, Tokyo153-8505, Japan
e-mail: tfujii@iis.u-tokyo.ac.jp

Abbreviations

μTAS	Micro total analysis systems
BFP	Blue fluorescent protein
CE	Capillary electrophoresis
CFTR	Cystic fibrosis transmembrane regulator
EOF	Electroosmotic flow
EWOD	Electrowetting on dielectric
GFP	Green fluorescent protein
GOx	Glucose oxidase enzyme
ITO	Indium tin oxide
MEMS	Microelectromechanical systems
PCR	Polymerase chain reaction
PDMS	Polydimethylsiloxane
PNA	Peptide nucleic acid
SBS	Single base substitution
ssDNA	Single-stranded DNA

1 Introduction

Over the past one and a half decades, microfluidic devices for high-throughput (bio) chemical analyses, so-called "micro total analysis systems (μTAS)" or "Lab-on-a-chip," have been attracting enormous attention and the research field is indeed growing rapidly [1, 2]. Microfluidic devices as miniaturized platforms for (bio) chemical analyses lead to many kinds of benefits, including reduced analysis time, reduced space and energy, reduced consumption of samples, reagents, reduced wastes and potentially harmful by-products, reduced cost in manufacturing for mass production, reduced labor by automation, higher separation resolution, and precision without expert operators. Since the devices can be disposable, and the systems can be portable and/or high-throughput, microfluidic systems can be used for a broad range of applications not only for analytical purposes but also for clinical diagnostics, chemical synthesis, environmental testing, and fundamental scientific research works.

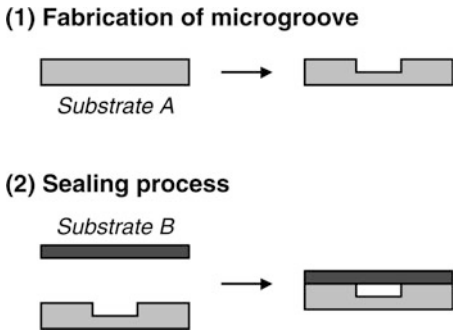

Fig. 1 Fabrication process of microfluidic device

The core component of a microfluidic device is microchannel structure having cross-sectional dimensions on the order of 10–1,000 μm. The microchannel structure is fabricated on various materials using microfabrication techniques based on photolithography. The advantageous feature of microfabrication is the higher flexibility in the design of microchannel structure, such as branches, intersections, changing cross-sectional shapes, etc. The fabrication process of microchannel structure is divided mainly into two parts: (1) fabrication of microgrooves on a substrate and (2) sealing the grooves by a flat substrate as shown in Fig. 1. In the early stage of this research field, the microchannel is mostly structured in glass and silicon. Polymers are recently used as inexpensive and low-cost material. While the fabrication techniques and related technology are not described in detail in this chapter, a number of excellent general reviews are available (e.g., fabrication process [3–5] and surface modification [6]).

The schematic of an integrated microfluidic device for biochemical analysis, including transportation of solutions and mixing for reaction with incubation, separation, and detection of the reaction products, is illustrated in Fig. 2. To achieve the complete processes on a single device, the integration technology of each of the functional components is required. Here, we review diverse integrated microfluidic devices that incorporate functional components for reaction temperature control, liquid handling, and detection. In order to show the realization of these functional integrations for specific purposes, integrated microfluidic devices for protein synthesis, on-chip capillary electrophoresis (CE) and cell culture are described, respectively.

2 Temperature Control Components

Heating or incubation of solutions is required for the reactions in biology-related analysis, such as polymerase chain reaction (PCR), DNA digestion by restriction enzymes and hybridization, etc. Since the efficiency of heat exchange is becoming higher, due to downscaling, than that in conventional test tubes, it is possible to

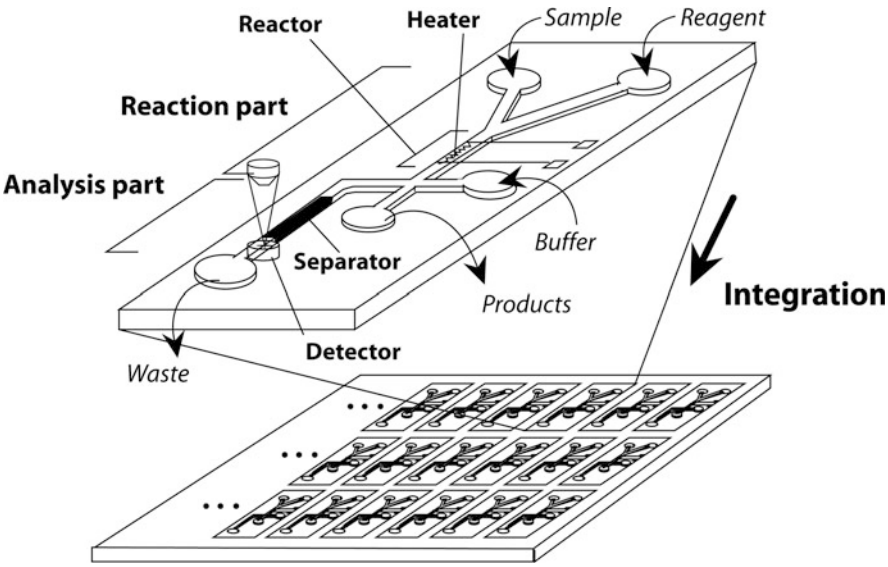

Fig. 2 Schematic illustration of integrated microfluidic device

reduce the time for reactions by using microchannel structures as reaction chambers. According to Fick's law [5], the time needed for heat transfer is proportional to the second power of the height of microchannels. This means that the time can be shortened exponentially by reducing the height. Rapid PCR operation in a microchamber, reported by the group of Northrup [7], is among the earliest works. A 500 μm high PCR chamber was formed on a silicon substrate equipped with a polysilicon thin film as a heating element. One thermal cycle for PCR can be done in 1 min leading to four times faster amplification than the conventional instruments. Continuous flow-based PCR (flow-through PCR) was demonstrated on a microfluidic device by the group of Manz [8]. The device made of glass has a folded microchannel (90 μm width, 40 μm height) for passing sample solution through three different temperature zones corresponding respectively to the denaturation, annealing and extension processes for PCR. In the device, 30 cycles of PCR for a 500-bp fragment could be conducted within 2.5 min. With simple calculation, the heating and cooling times are estimated, each less than 100 ms in their device [8].

The authors' group proposed an integrated microfluidic system incorporating temperature control components in the form of glass-polydimethylsiloxane (PDMS) hybrid structure [9]. Figure 3 shows the proposed microreactor array for high-throughput cell-free protein synthesis. The microreactor array is composed of a temperature control chip and a reaction chamber chip as shown in Fig. 3a. The temperature control chip is a glass-made device, on which heaters and temperature sensors are fabricated with an indium tin oxide (ITO) as shown in Fig. 3b. The reaction chamber chip made of PDMS is designed to have an array of reaction chambers. Thanks to the small thermal mass of the reaction chamber, short thermal

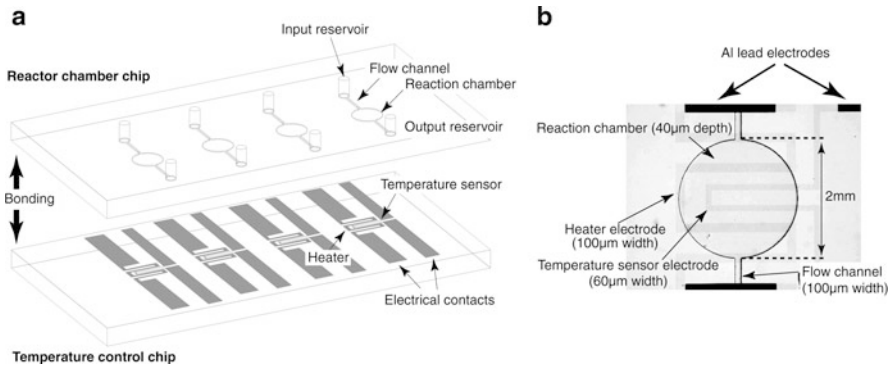

Fig. 3 Microreactor array for cell-free protein synthesis [9]. (**a**) Design of the microreactor array. (**b**) Magnified photograph of the reaction chamber

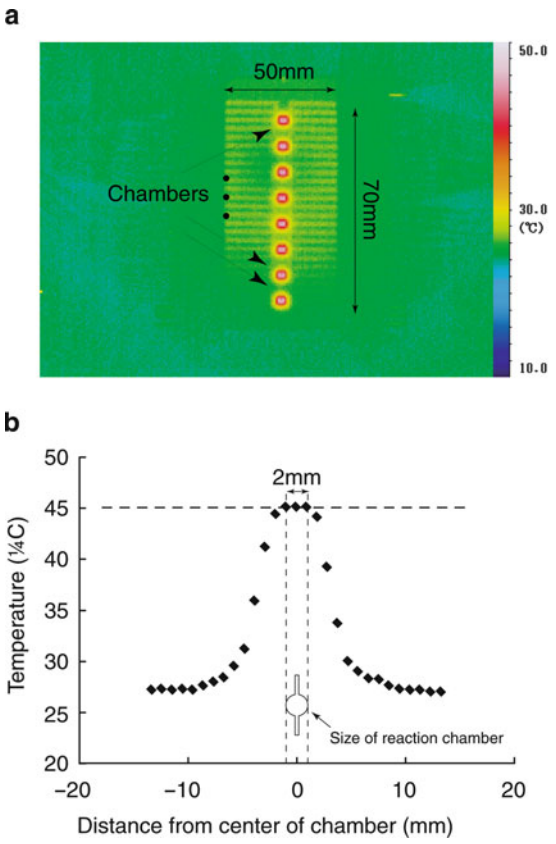

Fig. 4 Temperature profile of the microreactor array [9]. (**a**) Thermograph of the microreactor array. (**b**) Temperature profile across a reactor chamber

time constants of 170 ms for heating and 3 s for cooling could be achieved. And highly uniform temperature distribution could be realized on the microreactor array as shown in Fig. 4. The performance of the microreactor array was examined

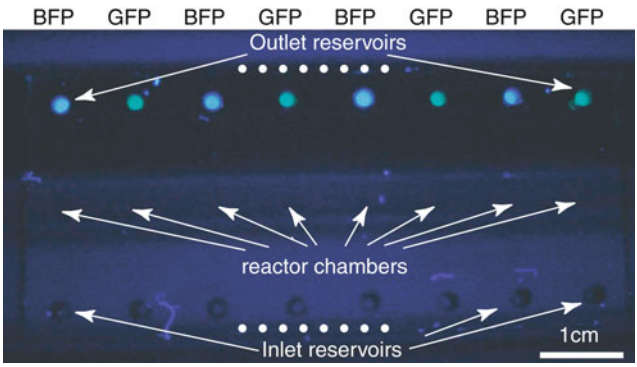

Fig. 5 GFP/BFP synthesis in the microreactor array [9]

through the experiments on cell-free protein synthesis and it was confirmed that green fluorescent protein (GFP) and blue fluorescent protein (BFP) were successfully synthesized using *Escherichia coli* extract as shown in Fig. 5. In the same way, Fukuba et al. developed a flow-through PCR microfluidic device integrated with ITO-based temperature control components [10].

3 Liquid Handling Components

Development of liquid handling techniques for small volume samples is indispensable for performing biochemical analyses using microfluidic devices. Since the typical volume of liquid handled in microfluidic devices is on the order of subnanoliter to microliter, it is quite difficult to handle such small volumes by manual operation using pipettes. Therefore, liquid handling operations including transportation, metering, mixing, etc., have been developed very actively in this field. Generally, liquid handling schemes are categorized into two cases: continuous flow and discrete flow as shown in Fig. 6. In the case of continuous flow, microchannel networks are filled with liquid samples (Fig. 6a). On the other hand, liquid samples are manipulated as small volume droplets (plugs) segmented by air or immiscible (inert) solution (e.g., oil) in the case of discrete flow (Fig. 6b). A continuous flow method has conventionally been used in this research field due to its simplicity. Tokeshi et al. [11] reported a microfluidic device to perform consecutive processes for Co(II) wet analysis, including a chelating reaction, solvent extraction, and purification by using combinations of laminar flow of both aqueous and organic solutions. The discrete flow method has emerged in the past decade and been growing rapidly. In this category, several ways for droplet manipulation have been proposed, such as electrowetting on dielectric (EWOD) [12], dielectric force [13], hydrodynamic force with multiphase flow [14], and pneumatic force [15].

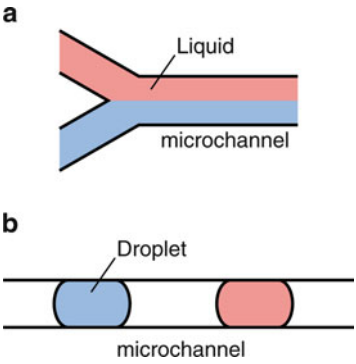

Fig. 6 Schematic illustrations of continuous flow and discrete flow methods

These principles are described in detail in the general reviews [16, 17]. Typically, the advantages of discrete flow methods are minimum dead volumes, flexibility in multistep reactions, or high-throughput sample handling (e.g., 1 kHz or higher [16]). A droplet-based microfluidic device for protein crystallization was proposed by Zheng et al. [14]. In the device, two-phase fluid flow (water/oil) was used to generate a train of droplets as a screening array of crystallization conditions with a gradual increase of concentration, which is commonly used in vapor diffusion techniques.

3.1 Micropumps

Regardless of the liquid handling technique, pressure sources to drive liquid samples in microchannels have to be considered. Some of the rather simpler liquid handling can be realized by so-called "autonomous pumping" by using capillary forces [18]. And by combining capillary breaks with centrifugal forces, multistep operations can be achieved in the CD format [19]. In most cases, however, integration of micropumps has been one of the most important issues from the viewpoint of miniaturization. Depending on the way to generate pressure, micropumps can generally be categorized into two groups: nonmechanical and mechanical systems.

Electroosmotic flow (EOF), originally studied in CE, can be one principle to generate pressure in a nonmechanical manner. Basically, by applying an electric field along a microchannel, flow with the desired direction and velocity could be obtained. Because of its simplicity and controllability, pumping by EOF has been widely used from the early days of this research field. However, applying voltage directly onto sample solution sometimes causes problems due to the changes in sample composition and bubble formation by electrode reaction. To overcome this problem, McKnight et al. [20] presented a hydraulic pumping system driven by

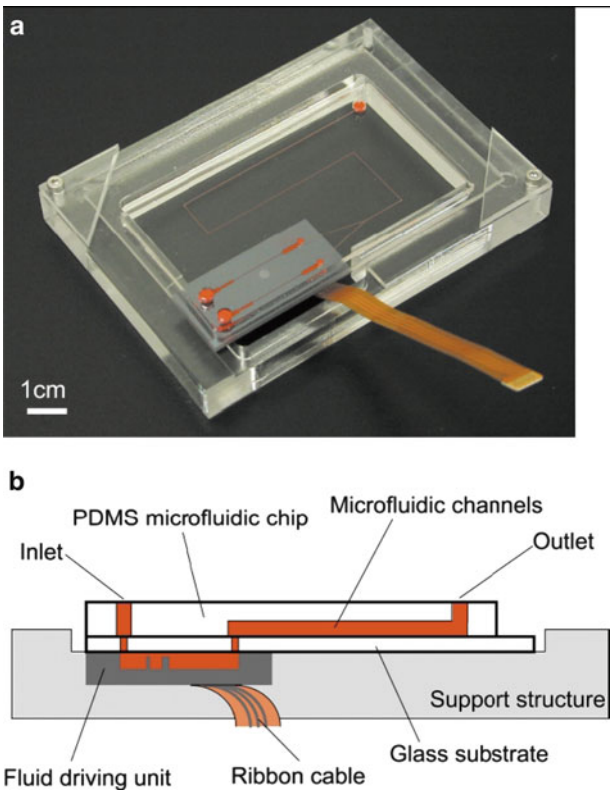

Fig. 7 Plug and play microfluidic device [21]. (**a**) Photo of the device. (**b**) Cross-sectional view of the device

EOF. In the system, EOF generated by interdigitated electrodes incorporated into a microchannel is used as a pressure source for hydraulic pumping to realize electric field-free pumping of sample solution.

In contrast to pumping by EOF, pumping by piezo-electric actuators is a typical example of mechanical systems. A silicon-based micropump driven by a piezo-electric device was presented by the author's group [21]. The microfluidic system is composed of a PDMS fluidic chip and a fluid driving unit as shown in Fig. 7. The one and only connection of the device to the external world is a set of electric control lines for the driving unit. Since it is easily to operate the device by just putting reagents and samples into the reservoirs, the device is named "plug and play microfluidic device." Thanks to the reversible feature of spontaneous bonding of PDMS, the fluidic chip could be a single use device to avoid chip-to-chip cross-contamination. The main component of the fluid driving unit is a silicon-based micropump bonded onto a glass substrate where the fluidic chip will be pasted on the other side as shown in Fig. 7. The performance of the device was confirmed by formation of two kinds of flow pattern, i.e., laminar flow and alternate pulsed flow.

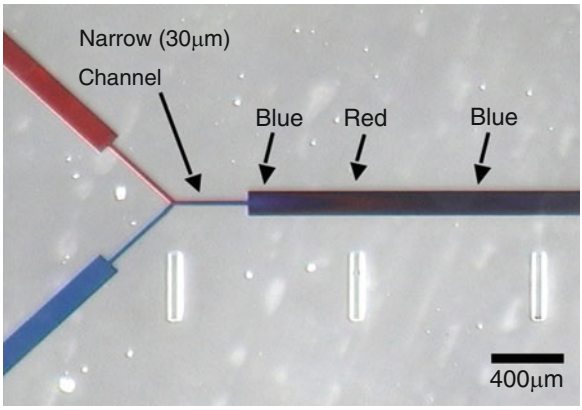

Fig. 8 Photo of the alternate pulsed flow generated by switching at 3 Hz [21]

Figure 8 shows formation of alternate pulsed flow by switching the pumps from one to the other quickly (typically at several Hz). To achieve highly efficient mixing, narrow channels (30 μm width and 150 μm height) are located at the Y-shaped junction. The thin skins of each solution formed by the alternate switching enhance the diffusion-based mixing along the axis parallel to the flow.

3.2 Droplet Handling for Reaction and Separation

While there are many works going on to deal with droplets in multiphase flow formats, i.e., water-in-oil in most cases, as described above, the author's group has continuously been pursuing the techniques for droplet handling using pneumatic forces, controlled through microcapillary air vent structure [15]. The pneumatic handling of droplets has advantageous features such as simplicity, minimal effect against (bio)chemical reactions, the compatibility with conventional separation (e.g., electrophoresis, etc.) schemes which had been developed well from the early stages of this research field [22–24], etc. We developed a microfluidic device combining droplet-based reactions with on-chip CE processes in order to realize the seamless coupling of analysis with reaction by fully automated operations [25]. As shown in Fig. 9, the developed device consists of a droplet handling fluidic chip made of PDMS, a glass substrate equipped with Au/Cr electrode for electrophoresis, and a glass substrate with patterned ITO heater and temperature sensor structures for temperature control both for reaction and electrophoretic separation (Fig. 9a). The microfluidic chip has access ports for sample liquid loading (denoted as L1–4) as well as pneumatic control (P1–4) and a long straight channel of 24.4 mm located in the center of the chip is used for electrophoretic separation as shown in Fig. 9b. All pneumatic channels are connected to liquid channels via

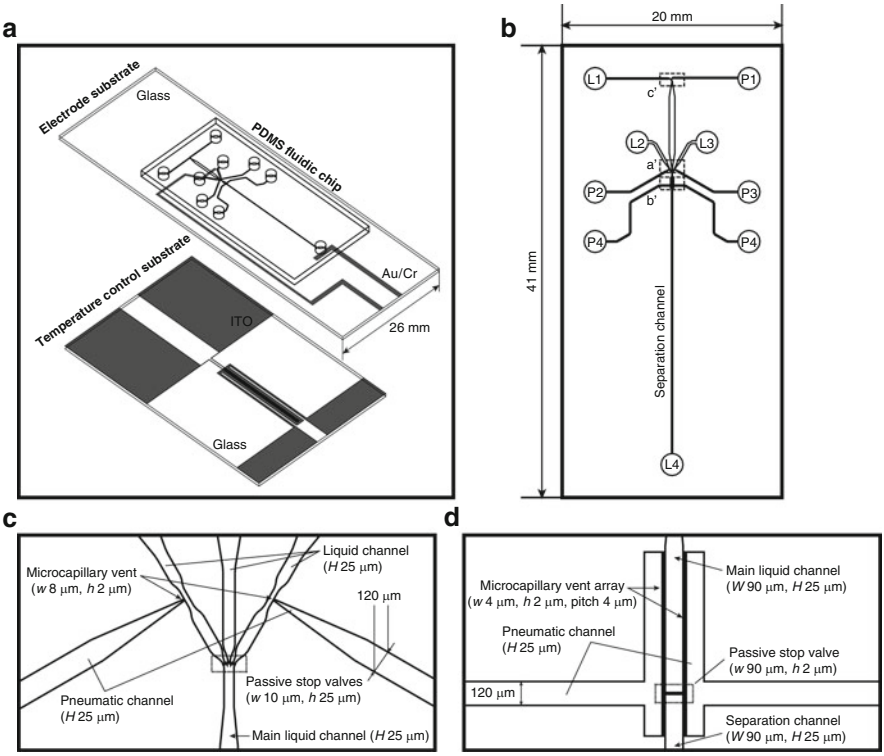

Fig. 9 Schematic of the droplet handling microfluidic device [25]. (**a**) Overview of the device. (**b**) The microchannel network in PDMS fluidic chip. The main working regions a' and b' shown in (**b**) are magnified in (**c**,**d**)

microcapillary vent structure (8 μm width, 2 μm height) or vent structure array (4 μm width, 2 μm height, 4 μm pitch) as shown in Fig. 9c,d. Since these vent structures resist to intrusion of aqueous liquid at a certain pressure due to the hydrophobicity of PDMS (fluidic chip material) and small cross section of the vent structures [15], the device can handle aqueous liquid samples inside the liquid channels by pneumatic manipulation through the vent structures. Passive stop valve structures (10 μm width, 25 μm height) for positioning of sample solutions are located in front of the main liquid channel (Fig. 9c). The main liquid channel is connected to the separation channel through a passive stop valve (90 μm width, 2 μm height) for positioning of generated droplet (Fig. 9d).

Droplet-based reaction of a single-stranded DNA (ssDNA) with a peptide nucleic acid (PNA) followed by electrophoretic separation of the reaction products is performed on the device as shown in Fig. 10. By conducting similar operations against two different ssDNA samples with a PNA molecule as a probe, rapid detection of single base substitution (SBS) of cystic fibrosis transmembrane regulator (CFTR) gene can be successfully carried out within 1.5 min with sample of 420 pL [25].

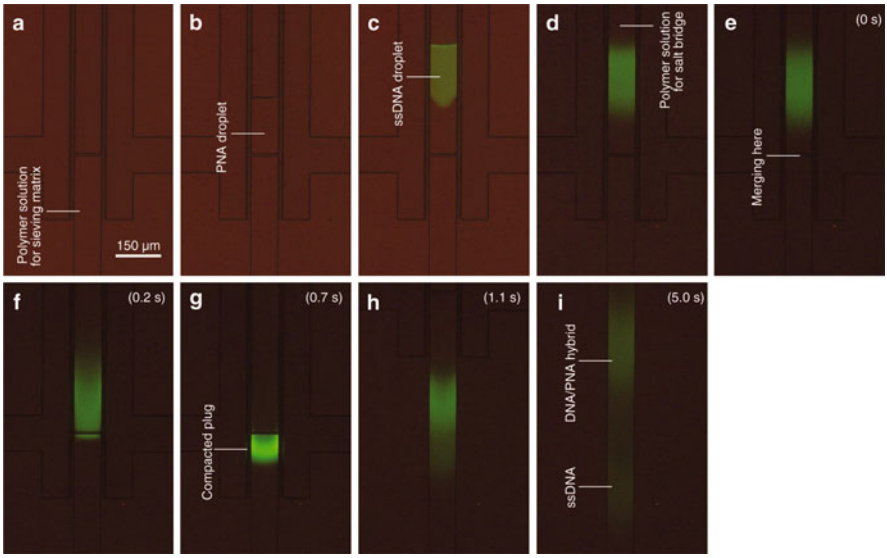

Fig. 10 A fluorescence images of droplet-based reaction and electrophoretic separation [25]. (**a**) A polymer solution for sieving matrix are introduced into the separation channel. (**b**) Droplet of a PNA is metered. (**c**) Droplet of a ssDNA is metered and merged with PNA droplet. (**d**) After 3 s incubation, a polymer solution for salt bridge are metered and merged with the mixed droplet. (**e**) Passive stop valve is broken for merging the droplet with the sieving matrix. (**f**) Electrophoresis is conducted by applying an electric field of 168.3 V cm^{-1}. (**g**) The sample plug is compacted at the interface of the sieving matrix. The ssDNA and DNA/PNA hybrid are separated shown in (**h**,**i**)

4 Detection Components

Integration of detection components into microfluidic devices is also one of the major issues in the development of miniaturized systems. Mainly two methods, i.e., optical and electrochemical detection, can be considered as detection schemes for integration.

4.1 Optical Detection

Fluorescence-based detection schemes, which can be highly sensitive and selective, require components for optical detection. In order to realize integrated microfluidic devices with fluorescence detection functions, miniaturization of such instruments as light sources, photodetectors, and optical interfaces has to be examined. Although there are some approaches to integrate photodetectors on a device [26], incorporating semiconductor devices on-chip is still not cost effective and not

compatible with the disposable use commonly required for bioanalytical or diagnostic purposes. It is, therefore, strongly desired to develop a practical miniaturized detection method, which is reliable, simple to use, and cost effective for disposable applications. As one of the possible approaches, it was proposed that optical fiber is simply embedded into microfluidic devices together with a photodetector [27] and with 2D optical lens to obtain higher sensitivity [28]. Ono et al. developed an on-chip CE device incorporated on-chip multi-aspherical lenses for optical fiber-based fluorescence detection as shown in Fig. 11 [29]. Besides the cross-shaped microchannel for on-chip CE, the device has two inlets ports and guide structures for introduction and positioning of both excitation and detection fibers. A multi-aspherical lens located in front of the excitation fiber is designed to achieve twice as much intensity as the light emitted from the optical fiber as shown in Fig. 12. The shapes of lenses are optimized using computer simulation and the light pass is visualized using PDMS fluidic chip containing a fluorescent dye. To evaluate the detection ability of the device, 100-bp DNA ladder was separated by on-chip CE and the fluorescent signal from the separated bands is successfully detected as

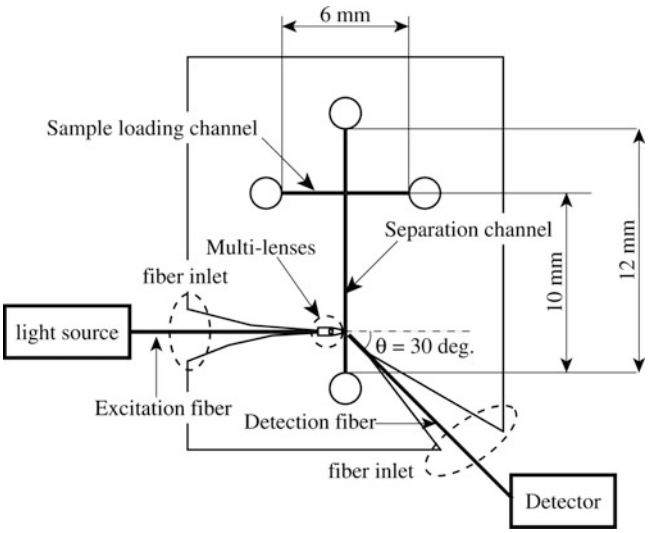

Fig. 11 Schematic design of the on-chip CE device with two inlets for optical fibers [29]

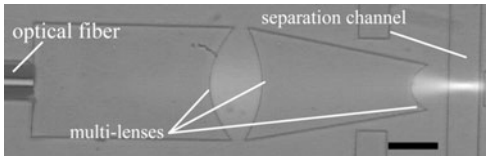

Fig. 12 Photo of the device with the 50 μm diameter core fiber illuminating the fluidic channel through lenses. Bright part is fluorescent dye mixed in PDMS [29]

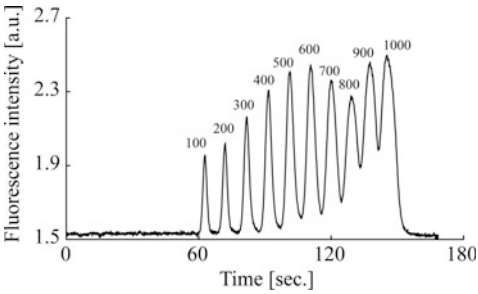

Fig. 13 Results of detection of 100 base-pairs DNA ladder separation [29]

shown in Fig. 13. The sensitivity and the resolution were comparable with those of the conventional detection scheme under a microscope. Moreover, the present optical setup does not require any elaborate alignment of each component and fluidic channels.

4.2 Electrochemical Detection

Electrochemical detection enables detection without labeling by just integrating electrodes onto the device by microfabrication. Because of its cost effectiveness and simplicity, it has been used in the past decade in this field. The sensitivity of the electrochemical detection is independent of optical path lengths and sample turbidity. To date, electrochemical detection components for on-chip CE have been well developed [30]. To apply electrochemical detection to cell cultures, Rodrigues et al. developed a microfluidic device with electrochemical detection components as sensors for monitoring dissolved glucose and oxygen in the cell culture medium [31]. The device is composed of specific glucose and oxygen amperometric sensors fabricated on a glass substrate and the cell-chamber chip made of PDMS as shown in Fig. 14. The two sets of sensors are located at the inlet and outlet of the PDMS cell-chamber to perform continuous real-time monitoring of the composition of the cell culture medium by comparing the measured values. The glucose sensor is fabricated by coating glucose oxidase enzyme (GOx) and a perfluorosulfonic acid-based layer onto the Au working electrode and the oxygen sensor is fabricated by coating the diluted perfluorosulfonic acid-based layer onto the Au working electrode. The long term simultaneous monitoring at the inlet and outlet in the case of transient and continuous injections of a certain concentration of glucose solution is successfully performed as shown in Fig. 15. This result shows that the fabricated sensors can be adapted to the monitoring of cellular glucose consumption as an indication of cellular activity during cell culture with dynamic flow conditions.

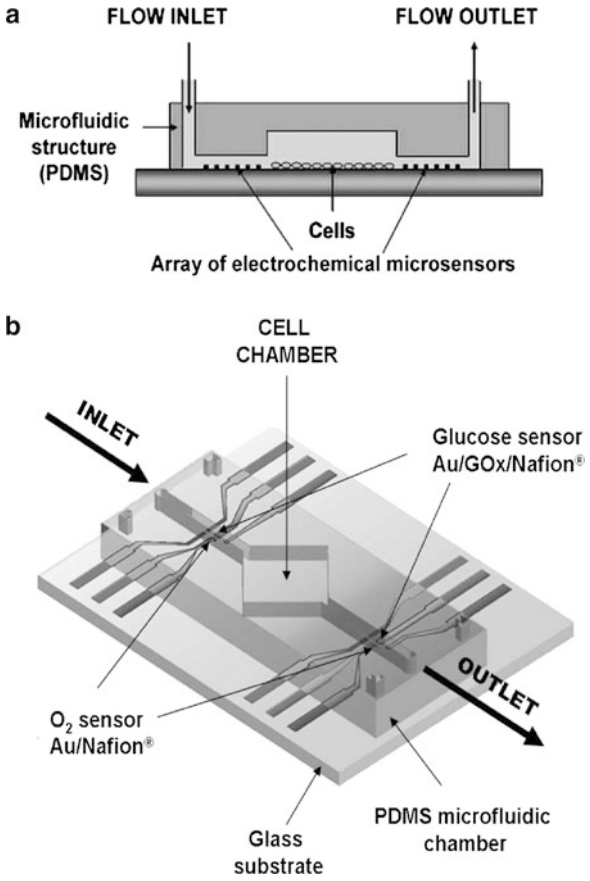

Fig. 14 Schematics of the electrochemical sensor integrated microfluidic device for cell culture monitoring [31]

5 Conclusion and Outlook

Microfluidic systems will play an important role in the development of miniaturized bioanalytical systems. In this chapter we have reviewed integrated microfluidic devices and related functional components. Since it seems that the density of the microchannel network has already become quite enough for practical use to date [32], the integration of functional components other than the network is becoming increasingly important. Although research works heading for integrated microfluidic devices are growing rapidly, there are still some hurdles to be cleared in developing bioanalytical systems capable of multistep operations in fully automated manners. The key step in the development is sample pretreatment to realize "sample-to-result" systems. Continuous efforts for integrating functional

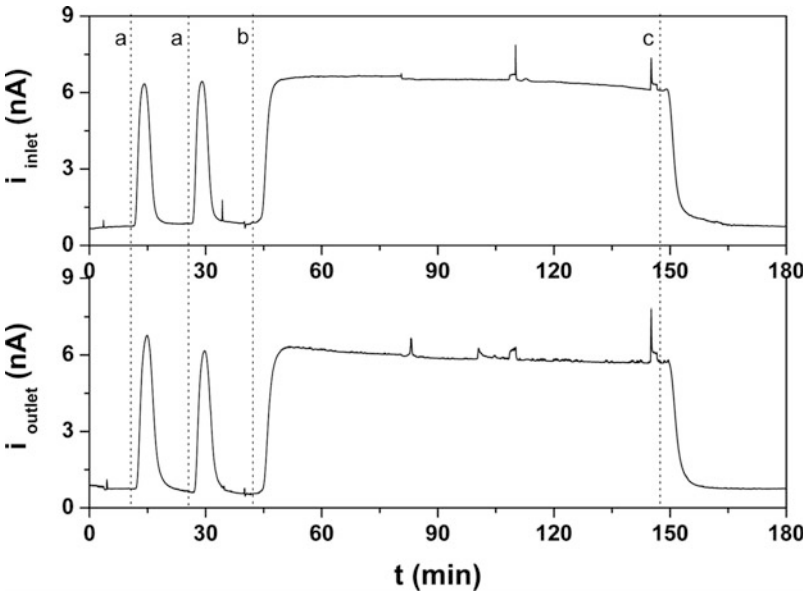

Fig. 15 Simultaneous response of inlet and outlet glucose sensor after consecutive additions of (**a**) glucose solution of 60 µl of 10 mmol L^{-1}, (**b**) only 10 mmol L^{-1} glucose solution, (**c**) only PBS. The *dashed lines* correspond to the injection times [31]

components into a single device lead to one-time use multifunction devices for future applications including clinical, diagnostic, and environmental purposes.

References

1. Reyes DR, Iossifidis D, Auroux PA, Manz A (2002) Micro total analysis systems. 1. Introduction, theory, and technology. Anal Chem 74:2623–2636
2. Auroux PA, Iossifidis D, Reyes DR, Manz A (2002) Micro total analysis systems. 2. Analytical standard operations and applications. Anal Chem 74:2637–2652
3. Verpoorte EB, Rooij NFD (2003) Microfluidics meets MEMS. Proc IEEE 91:930–953
4. McDonald JC, Duffy DC, Anderson JR, Chiu DT, Wu H, Schueller OJ, Whitesides GM (2000) Fabrication of microfluidic systems in poly(dimethylsiloxane). Electrophoresis 21:27–40
5. Becker H, Locascio LE (2002) Polymer microfluidic devices. Talanta 56:267–287
6. Belder D, Ludwig M (2003) Surface modification in microchip electrophoresis. Electrophoresis 24:3595–3606
7. Northrup MA, Ching MT, White RM, Watson RT (1993) DNA amplification with a microfabricated reaction chamber. In: Transducers'93 digest of technical papers, pp 924–926
8. Kopp MU, Mello AJ, Manz A (1998) Chemical amplification: continuous-flow PCR on a chip. Science 280:1046–1048
9. Yamamoto T, Fujii T, Nojima T (2002) PDMS-glass hybrid microreactor array with embedded temperature control device. Application to cell-free protein synthesis. Lab Chip 2:197–202

10. Fukuba T, Yamamoto T, Naganuma T, Fujii T (2004) Microfabricated flow-through device for DNA amplification – towards in situ gene analysis. Chem Eng J 101:151–156
11. Tokeshi M, Minagawa T, Uchiyama K, Hibara A, Sato K, Hisamoto H, Kitamori T (2002) Continuous-flow chemical processing on a microchip by combining microunit operations and a multiphase flow network. Anal Chem 74:1565–1571
12. Fair R (2007) Digital microfluidics: is a true lab-on-a-chip possible? Microfluid Nanofluidics 3:245–281
13. Jones TB, Gunji M, Washizu M, Feldman MJ (2001) Dielectrophoretic liquid actuation and nanodroplet formation. J Appl Phys 89:1441–1448
14. Zheng B, Tice JD, Ismagilov RF (2004) Formation of arrayed droplets by soft lithography and two-phase fluid flow, and application in protein crystallization. Adv Mater 16:1365–1368
15. Hosokawa K, Fujii T, Endo I (1999) Handling of picoliter liquid samples in a poly(dimethylsiloxane)-based microfluidic device. Anal Chem 71:4781–4785
16. Teh SY, Lin R, Hung LH, Lee AP (2008) Droplet microfluidics. Lab Chip 8:198–220
17. Huebner A, Sharma S, Srisa-Art M, Hollfelder F, Edel JB, Demello AJ (2008) Microdroplets: a sea of applications? Lab Chip 8:1244–1254
18. Juncker D, Schmid H, Drechsler U, Wolf H, Wolf M, Michel B, de Rooij N, Delamarche E (2002) Autonomous microfluidic capillary system. Anal Chem 74:6139–6144
19. Lai S, Wang S, Luo J, Lee LJ, Yang S-T, Madou MJ (2004) Design of a compact disk-like microfluidic platform for enzyme-linked immunosorbent assay. Anal Chem 76:1832–1837
20. McKnight TE, Culbertson CT, Jacobson SC, Ramsey JM (2001) Electroosmotically induced hydraulic pumping with integrated electrodes on microfluidic devices. Anal Chem 73:4045–4049
21. Fujii T, Sando Y, Higashino K, Fujii Y (2003) A plug and play microfluidic device. Lab Chip 3:193–197
22. Manz A, Harrison DJ, Verpoorte EMJ, Fettinger JC, Paulus A, Ludi H, Widmer HM (1992) Planar chips technology for miniaturization and integration of separation techniques into monitoring systems: capillary electrophoresis on a chip. J Chromatogr A 593:253–258
23. Harrison DJ, Manz A, Fan Z, Luedi H, Widmer HM (1992) Capillary electrophoresis and sample injection systems integrated on a planar glass chip. Anal Chem 64:1926–1932
24. Harrison DJ, Fluri K, Seiler K, Fan Z, Effenhauser CS, Manz A (1993) Micromachining a miniaturized capillary electrophoresis-based chemical analysis system on a chip. Science 261:895–897
25. Kaneda S, Nojima T, Yamamoto T, Fujii T (2008) A droplet on demand microfluidic device for detecting DNA single base substitution using PNA probe. In: Proceedings of the micro total analysis systems 2008, pp 176–178
26. Webster JR, Burns MA, Burke DT, Mastrangelo CH (2001) Monolithic capillary electrophoresis device with integrated fluorescence detector. Anal Chem 73:1622–1626
27. Chabinyc ML, Chiu DT, McDonald JC, Stroock AD, Christian JF, Karger AM, Whitesides GM (2001) An integrated fluorescence detection system in poly(dimethylsiloxane) for microfluidic applications. Anal Chem 73:4491–4498
28. Camou S, Fujita H, Fujii T (2003) PDMS 2D optical lens integrated with microfluidic channels: principle and characterization. Lab Chip 3:40–45
29. Ono K, Kaneda S, Camou S, Fujii T (2003) Integration of multi-aspherical lenses and optical fibers onto a PDMS microfluidic device for fluorescence-based detection. In: Proceedings of the micro total analysis systems 2003, pp 1307–1310
30. Joseph W (2005) Electrochemical detection for capillary electrophoresis microchips: a review. Electroanalysis 17:1133–1140
31. Pereira-Rodrigues N, Sakai Y, Fujii T (2008) Cell-based microfluidic biochip for the electrochemical real-time monitoring of glucose and oxygen. Sens Actuators B Chem 132:608–613
32. Thorsen T, Maerkl SJ, Quake SR (2002) Microfluidic large-scale integration. Science 298:580–584

Part V
Applications

Adv Biochem Engin/Biotechnol (2010) 119: 197–230
DOI: 10.1007/10_2008_40
© Springer-Verlag Berlin Heidelberg 2009
Published online: 28 March 2009

A Novel Nonviral Gene Delivery System: Multifunctional Envelope-Type Nano Device

Hiroto Hatakeyama, Hidetaka Akita, Kentaro Kogure, and Hideyoshi Harashima

Abstract In this review we introduce a new concept for developing a nonviral gene delivery system which we call "Programmed Packaging." Based on this concept, we succeeded in developing a multifunctional envelope-type nano device (MEND), which exerts high transfection activities equivalent to those of an adenovirus in a dividing cell. The use of MEND has been extended to in vivo applications. PEG/peptide/DOPE ternary conjugate (PPD)-MEND, a new in vivo gene delivery system for the targeting of tumor cells that dissociates surface-modified PEG in tumor tissue by matrix metalloproteinase (MMP) and exerts significant transfection activities, was developed. In parallel with the development of MEND, a quantitative gene delivery system, Confocal Image-assisted 3-dimensionally integrated quantification (CIDIQ), also was developed. This method identified the rate-limiting step of the nonviral gene delivery system by comparing it with adenoviral-mediated gene delivery. The results of this analysis provide a new direction for the development of rational nonviral gene delivery systems.

Keywords Gene delivery, Intracellular trafficking, MEND, Nano device, Nonviral

H. Hatakeyama, H. Akita, and H. Harashima (✉)
Faculty of Pharmaceutical Sciences, Hokkaido University, Kita 12 Nishi 6, Sapporo City, Hokkaido 060-0812, Japan
e-mail: harasima@pharm.hokudai.ac.jp

K. Kogure
Kyoto Pharmaceutical University, 5 Nakauchi-cho, Misasagi, Yamashina-ku, Kyoto, 607-8414, Japan

Contents

Abbreviations

Bmpr1a	Bone morphogenetic protein receptor type 1A
BSA	Bovine serum albumin
CAR	Coxsackie and adenovirus receptor
CDAN	*N*-Cholesteryloxycarbonyl-3,7-diazanonane-1,9-diamine
CHEMS	Cholesteryl hemisuccinate
Chol	Cholesterol
CIDIQ	Confocal image-assisted three-dimensionally integrated quantification
CLSM	Confocal laser scanning microscopy
DLinDMA	1,2-Dilinoleyloxy-*N*,*N*-dimethyl-3-aminopropane
DOPE	Dioleoylphosphatidylethanolamine
DOTAP	*N*-[1-(2,3-Dioleoyloxy)propyl]-*N*,*N*,*N*-trimethylammonium chloride
DOTMA	*N*-[1-(2,3-Dioleoyloxy)propyl]-*N*,*N*,*N*,-trimethylammonium chloride
ECM	Extracellular matrix
EPC	Egg phosphatidylcholine

EPR	Enhanced permeability and retention
GFP	Green fluorescent protein
HFs	Hair follicles
LA2000	Lipofectamine2000
LFN	Lipofectamine PLUS
LPD	Liposome–polycation–DNA lipoplex
MEND	Multifunctional envelope-type nano device
MMP	Matrix metalloproteinase
NLS	Nuclear localization signals
N/P	Nitrogen/phosphate
ODN	Oligodeoxynucleotides
ODN-MEND	R8-MEND-encapsulated ODN
pDNA	Plasmid DNA
PEG	Polyethyleneglycol
PEG-MEND	MEND modified with conventional PEG-lipid
PEI	Polyethyleneimine
PLL	Poly-l-lysine
PPD	PEG/peptide/DOPE ternary conjugate
PPD-MEND	MEND modified with PPD
PTN	Pleiotrophin
R8	Octaarginine
R8-MEND	MEND modified with high density R8 peptide
RES	Reticuloendothelial system
RISC	RNA-induced silencing complex
RNAi	RNA interference
SAINT-2	*N*-Methyl-4(dioleyl)methylpyridiniumchloride
siRNA	Short interfering RNA
SPLP	Stabilized plasmid-lipid particle
SUV*	Small, detergent-rich liposomes
Tf	Transferrin
Tf-L	Tf-modified liposomes

1 Introduction

Viruses are ideal gene delivery systems because they deliver their genome to target cells where the viral genome is replicated. However, it is very difficult to control the biodistribution and intracellular trafficking of viruses, thereby ensuring safe clinical application. Therefore, an artificial gene delivery system that can be tightly controlled and is safe and efficient in vivo is desirable. Gene delivery has been studied extensively; many compounds have been synthesized and their transfection activities examined. These studies address the many obstacles that must be overcome before the therapeutic gene can be delivered to the nucleus of the target cell for transcription of the DNA.

In this chapter, we propose a new concept for the development of efficient and safe nonviral gene delivery systems. The concept is explained using examples of applications of this concept. An optimized system requires quantitative feedback on intracellular trafficking of genes and carrier systems. We succeeded in developing such a quantitative evaluation system, CIDIQ, which identified the rate-limiting step in transfection by nonviral gene delivery systems.

2 A Novel Concept: "Programmed Packaging"

2.1 A Key Concept

Conventional nonviral gene vectors can be classified into two groups: polyplexes and lipoplexes. A polyplex is a complex of cationic high molecular weight compounds and nucleotides [1]. Typical polyplexes include complexes comprised of poly-L-lysine (PLL), polyethyleneimine (PEI), or plasmid DNA [1, 2]. PLL is a synthetic polymer, which has been in use for a long time. The ability of PEI to escape endosomes is excellent because of its proton-sponge activity [2]. Thus, these polyplexes are widely used. Biological polycations, such as spermine and protamine, also are used in the preparation of polyplexes [3–5]. The polyplex prepared with protamine, which is a cationic peptide derived from sperm nuclei, showed significantly higher transfection activity than a PLL/DNA polyplex [4]. Synthetic polycations, or biological cationic macromolecules, which have various functionalities, such as a cyclic RGD peptide-conjugated block copolymer [6], biocleavable polyrotaxane [7], galactose-modified 6-amino-6-deoxy chitosan [8] and cationic comb-type copolymers [9], are currently being developed. Thus, cationic polymers are the focus of research on the development of nonviral gene vectors in the field of material science. The other type of conventional nonviral gene vector is the lipoplex, which consists of nucleotides and liposomes containing cationic lipids. Since the transfection of plasmid DNA into cultured cells using the cationic lipid *N*-[1-(2,3-dioleyloxy)propyl]-*N*,*N*,*N*,-trimethylammonium chloride (DOTMA) was reported by the Felgner group [10], various synthetic cationic lipids have been developed, such as *N*-[1-(2,3-dioleoyloxy)propyl]-*N*,*N*,*N*-trimethyl ammonium chloride (DOTAP) [11], *N*-methyl-4(dioleyl)methylpyridiniumchloride (SAINT-2) [12] and *N*-cholesteryloxycarbonyl-3,7-diazanonane-1,9-diamine (CDAN) [13]. Lipoplexes are useful for the transfection of genes, as evidenced by the many commercially available transfection reagents containing various cationic lipids.

However, several biological barriers limit the efficiency of non-viral vector delivery of nucleic acids to eukaryotic cells (Fig. 1) [12, 14, 15]. The most significant intracellular barriers are lysosomal degradation, nucleolytic degradation in the cytosol, and inefficient delivery of the DNA to the nucleus [12, 15]; extracellular barriers include nucleolytic degradation in the serum, recognition by the reticuloendothelial system (RES), and nonspecific delivery [14]. A variety of approaches

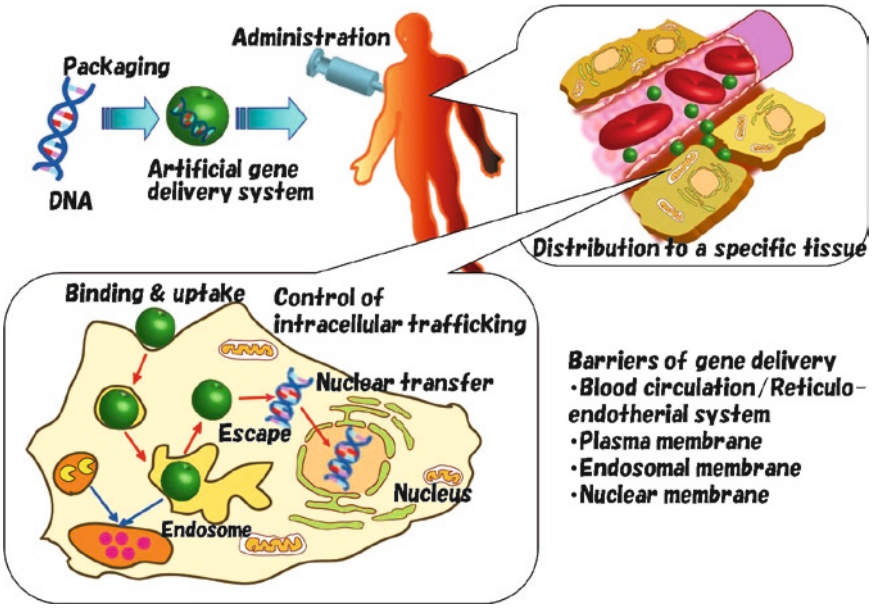

Fig. 1 Barriers to efficient gene delivery in artificial delivery systems

have been used to overcome these barriers, including ligand-mediated targeting of cell surface receptors, pH-sensitive fusogenic peptides that improve cytosolic delivery, and nuclear localization signals (NLS) to enhance nuclear uptake [14, 15]. Many of the currently available nonviral vectors have some functional devices that enhance their overall efficiency. For example, either the PEI-based polyplex is equipped with transferrin for the targeting of cancer cells and with polyethylenglycol (PEG) to enhance stability in systemic circulation [16], or the lipoplex contains a membrane fusion peptide derived from influenza virus hemagglutinin to enhance endosomal escape [17]. Nevertheless, nonviral gene vectors are still much less efficient than most viral vectors [18], which have evolved towards maximal efficiency through natural selection. Simple mixing of DNA with multiple devices does not guarantee that each device is functional and effective in reducing barriers to efficient gene delivery. In addition, mixing of DNA with multiple devices usually results in the formation of large aggregated complexes [19], which are not efficient vehicles for gene delivery in vivo. In contrast, smart nanotechnology-based devices offer a promising alternative for overcoming the barriers to effective gene delivery. Such devices can be applied according to a rational strategy, through which nanotechnology is used to assemble and integrate multifunctional devices into a single system [K-14].

Therefore, a novel packaging concept, “Programmed Packaging,” was proposed to assemble multiple devices into a single gene delivery system in which each device functions at the correct time and location according to a delivery strategy [20, 21].

This concept consisted of three components as follows: (1) a program to overcome all barriers; (2) design of functional devices and their three-dimensional assignment; and (3) use of nanotechnology to assemble all devices into a nano-sized structure. The program reflects a rational strategy for controlling the intracellular fate of nanoparticles using novel functional devices to overcome biological barriers to efficient gene delivery. The program also considers the topology of the functional devices to achieve maximal activity.

2.2 Importance of Topological Control

The topology of functional devices on nanoparticles must be controlled to exert each function correctly [20, 21]. For example, transferrin (Tf)-modified liposomes (Tf-L) were developed as a proto-type viral-like gene delivery system based on mechanisms of viral infection [22]. The model drug encapsulated in Tf-L was internalized by the human leukemia cell line, K562, via receptor-mediated endocytosis, but could not escape the endosome. Thus, Tf-L required a functional device for endosomal escape. A pH-sensitive fusogenic peptide, GALA (WEAALAEALAEALAE HLAEALAEALEALAA), which undergoes a conformational change from a hydrophilic random coil to a hydrophobic α-helix under acidic conditions, was investigated as a functional device to allow for endosomal escape via a membrane-fusion mechanism [23]. However, neither addition of free GALA to the Tf-L nor encapsulation of the GALA peptide in the Tf-L induced endosomal escape of the model drug encapsulated in the liposomes. In contrast, when GALA was anchored on the surface of the Tf-L via cholesterylization of the peptide, successful release of the encapsulated model drug into the cytosol was observed [22]. Therefore, the ability of GALA to function as a device for endosomal escape was possible because of the ability to control its topology. In addition, the mechanism of cellular uptake of nanoparticles modified with the cell-penetrating peptide, octaarginine (R8), was also dependent on the topology of R8 on the surface of the nanoparticles, as mentioned below [24]. Based on these observations, it was concluded that topological control of functional devices is very important for the development of efficient nonviral delivery systems based on Programmed Packaging.

3 A Novel Nonviral Gene Delivery System: MEND

A novel nonviral gene delivery system, multifunctional envelope-type nano device (MEND), was recently developed based on Programmed Packaging [20, 21, 25]. The ideal MEND, as shown in Fig. 2, consists of a condensed DNA core and a lipid envelope equipped with various functional devices. It is advantageous to condense the DNA into a compact core prior to its inclusion in the lipid envelope. DNA condensation protects DNA from DNase, limits the particle size, and improves the

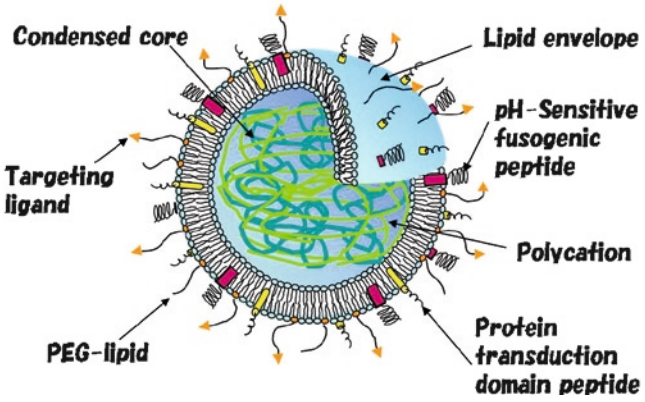

Fig. 2 Schematic representation of multifunctional envelope-type nano device (MEND). The MEND consists of condensed DNA molecules coated with a lipid envelope. The lipid envelope can be modified with functional devices as follows: PEG increases the half-life in systemic circulation; ligands target MEND to specific organs; protein-transduction domain peptides increase intracellular availability; and, fusogenic lipids enhance endosomal escape

packaging efficiency [21]. In the second step, complexes are incorporated into lipid envelopes such that the DNA core and lipid envelope exist as separate structures, rather than a disordered mixture, to control topology, by lipid coating of a core particle as mentioned below [21].

3.1 Packaging of pDNA into MEND

The MEND was constructed using the lipid film hydration method, which is a novel assembly method [25] based on packaging in three consecutive steps: (1) DNA condensation with polycations; (2) hydration of the lipid film for electrostatic binding of the condensed DNA; and (3) sonication to package the condensed DNA with lipids. This packaging mechanism is based on electrostatic interactions between DNA, polycations and lipids. Plasmid DNA is first condensed electrostatically with a polycation, such as PLL, by vortexing at room temperature. Kinetic control of this process is important for controlling the size and charge of the condensed DNA. In the case of PLL, small (approximately 100 nm) and positively charged (around 30 mV) PLL/DNA complexes are prepared at a nitrogen/phosphate (N/P) ratio of 2.4. A lipid film containing a negatively charged lipid, such as cholesteryl hemisuccinate (CHEMS), is hydrated with an aqueous solution containing PLL/DNA particles. Packaging of the PLL/DNA particles into a lipid bilayer is achieved by sonication in a bath-type sonicator. The diameter and zeta-potential of the MEND are approximately 300 nm and −40 mV, respectively. The encapsulation efficiency of the DNA is greater than 70% [25].

3.2 Optimization of MEND

The cell-penetrating peptide, R8, was investigated as a MEND functional device because R8 should enhance cellular association and induce efficient cellular uptake via nonclassical endocytosis, which can reduce lysosomal degradation as described later. MEND that had been modified with high density R8 peptide (R8-MEND) [20, 21], containing egg phosphatidylcholine (EPC)/cholesterol (Chol), showed higher transfection activities than PLL/DNA complexes. Increased transfection activity may result from enhanced cellular internalization due to the presence of R8. Substitution of EPC with the fusogenic lipid, dioleoylphosphatidylethanolamine (DOPE), increased the transfection activity by more than four orders of magnitude compared to negatively charged PLL/DNA particles [20, 21]. Furthermore, the transfection activity increased further by replacing Chol with the negatively charged fusogenic lipid, CHEMS. DOPE and CHEMS may enhance the efficiency of internalization into the cytoplasmic space due to their fusogenic properties, thus facilitating the nuclear delivery of DNA [21]. Thus, the transfection capability of R8-MEND was improved by approximately two orders of magnitude by optimization of the lipid envelope [20, 21].

Moreover, the ability of R8-MEND to deliver short interfering RNA (siRNA) expression plasmids was examined [26]. Plasmid DNA encoding antiluciferase siRNA was condensed by PLL and packaged into the R8-MEND. The silencing effect of R8-MEND(PLL) was significant – 96% inhibition of luciferase activity in a cotransfection study – without any detectable toxicity. The silencing effect was maintained at more than 60% even when the R8-MEND(PLL) were diluted 100-fold. In luciferase-transformed cells, however, the R8-MEND(PLL) have a significant silencing effect (10%), suggesting heterogeneous transfection using R8-MEND(PLL). To solve this problem, the DNA condensing agents were optimized by comparing PLL, STR-R8 and the spermatozoal peptide, protamine. While there was no difference in the silencing effect among these R8-MENDs in a cotransfection study, the R8-MEND showed a silencing effect of 70% in the transformed cells [26]. These results suggest that R8-MEND(protamine)-mediated transfection is less heterogeneous, while the heterogeneity of transfection resulting from R8-MEND(PLL) and R8-MEND(STR-R8) was large. Thus, the transfection ability of R8-MEND was further improved by optimization of the DNA-condensing agent.

3.3 Comparison with Adenoviruses

The transfection activity of the optimized R8-MEND was compared with that of an adenovirus, one of the strongest viral vectors, in human cervical cancer HeLa cells and in a human lung epithelial carcinoma cell line, A549 [20]. These cells display receptors for adenoviral serotype 5, such as the coxsackie and adenovirus receptor

(CAR) and integrin receptors. In both cell lines, the transfection activity of adenoviruses increased with increasing viral dosage up to 1×10^5 particles/cell, above which toxicity appeared and transfection activity decreased. Transfection activity of R8-MEND was as high as that of adenoviruses using 1×10^5 particles/cell [20]. As judged from the protein content in cell lysates after transfection, R8-MEND showed no significant cytotoxicity, while higher doses of adenoviruses produced significant cytotoxicity (~50% reduction in protein content). The optimized R8-MEND did not contain cationic lipids, and this may explain its low cytotoxicity.

4 Application of MEND to In Vivo

4.1 Topical Application

The ultimate goal of gene delivery research is to develop an efficient nonviral delivery system that can be used for in vivo gene therapy. For example, topical delivery of genes to hair follicles (HFs) is an attractive approach for in vivo gene therapy of skin and hair disorders. Li and Hoffman succeeded in delivery of the lacZ gene to the murine hair-forming hair matrix cells in hair follicle bulbs using a liposome-based nonviral delivery system [27]. Domachenko et al. also reported delivery of the lacZ gene to human and murine hair follicle progenitor cells using liposome-based nonviral systems [28]. Topical application of liposome-based nonviral systems requires that the skin be treated with depilatory cream and retinoic acid before DNA administration. In contrast, the topical application of R8-MEND to the skin of a 4-week-old ICR mouse resulted in gene delivery to the hair follicles without pretreatment of the skin [20]. Gene expression was observed in the hair shaft and follicle cells, which had been treated with R8-MEND encapsulating LacZ or green fluorescent protein (GFP) encoding plasmid DNA. The gene transfer efficiency of R8-MEND was significantly higher than that of lipoplexes comprising the commercially available reagent Lipofectamine and plasmid DNA. Although the reasons for the superior results obtained using MEND are not completely understood, the relatively small diameter of MEND particles and the resistance of MEND to lysosomal degradation are possible explanations. Next, R8-MEND containing DNA-encoding bone morphogenetic protein receptor type 1 A (Bmpr1a), which is related to the hair growth cycle, was applied to mouse skin. Topical application of R8-MEND encapsulating the Bmpr1a gene extended the period of hair growth.

4.2 Systemic Administration

Liposomes are composed of phospholipids, which also comprise cell membranes, and, therefore, are biocompatible and safe. Thus, liposomes are useful carriers in both drug and gene delivery systems. However, after entering the blood stream, liposomes are

readily opsonized by serum components and removed from the systemic circulation by the RES phagocytic cells of the liver and spleen [29].

In the early 1990s it was reported that liposomes coated with amphipathic PEG, which forms a hydrated layer over the liposome surface, exhibited a reduction in undesired interactions, lower RES recovery, and a long half-life in systemic circulation [30–32]. PEGylated liposomes are termed STEALTH® liposomes because they evade the RES, similar to stealth bombers, which avoid detection by enemy radar [33].

Long-circulating liposomes accumulate in tumors in large amounts due to the enhanced permeability and retention (EPR) effect, which was proposed by Matsumura et al. [34]. In addition, limiting the size of PEGylated liposomes to approximately 120 nm allows for efficient accumulation of the liposomes in tumor tissue [35]. The significant accumulation of PEGylated liposomes in tumor tissues results from the increased vascular permeability of neovasculature and the absence of drainage via the lymphatics in tumor tissue [36].

The accumulation of doxorubicin encapsulated in STEALTH® liposomes (Doxil®/Caelyx®) in tumor tissue is five- to tenfold higher than accumulation of free doxorubicin after i.v. administration [37–39]. Doxil®/Caelyx® treatment is indicated for patients with ovarian cancer and AIDS-related Kaposi's sarcoma [29]. Thus, liposomal formulations of anticancer drugs, such as doxorubicin, exhibit improved biodistribution of the drugs, which dramatically enhances their chemotherapeutic effect.

4.3 The PEG Dilemma

Despite the success of chemotherapeutic drug delivery systems using PEGylated liposomes, development of systemic gene carriers for cancer is still a major obstacle. As described above, PEG-shielding improves the stability of gene carriers in systemic circulation. In contrast, once the liposomes are taken up into the tumor tissue, PEG inhibits interactions between the gene carriers and the tumor cells. Subsequently, cellular uptake and endosomal escape of the liposomal carriers are reduced, resulting in a significant loss of transfection activity [40–42]. To overcome the dilemma related to the use of PEG, various cleavable and detached PEG systems have been constructed.

Szoka and colleagues have developed a cleavable PEG-lipid conjugate containing ortho-ester or diortho-ester linkages, which are highly sensitive to acidic conditions, but relatively stable at neutral pH [43–45]. The in vitro transfection study showed greater gene expression using pH-sensitive PEG-lipid lipoplexes compared with stable PEG-lipid lipoplexes. Another pH-controlled system that uses PEG-lipid with an acid-labile vinyl ether was developed by Thompson et al. [46]. PEG is cleaved in response to low intracellular pH in endosomes/lysosomes.

Zalipsky and colleagues synthesized a disulfide-linked PEG-lipid conjugate [47]. This PEG-lipid is thiolytically cleaved in response to a reducing intracellular environment. PEG-lipid conjugated to a short peptide, which is intracellularly

cleaved by enzymes like cathepsin B, has also been developed [48]. These strategies have the potential to enhance intracellular release of nucleic acids from liposomes.

MacLachlan and coworkers developed a strategy based on exchangeable PEG-lipids [49]. Liposomal pDNA formulated with the exchangeable PEG-lipid exhibited higher in vitro gene expression compared with liposomes comprised of conventional PEG-lipids.

4.4 New Strategy: PEG

Most of the current cleavable PEG devices were designed to be cleaved in response to the intracellular microenvironment. As described above, devices that are cleaved at low intracellular pH, by a specific enzyme in the endosome/lysosome, and by reducing conditions in the cytoplasm, have been developed. Therefore, a cleavable PEG-lipid triggered in a specific manner would be desired. To realize a tumor-specific cleavable PEG system, we focused on the enzyme, matrix metalloproteinase (MMP), which is involved in angiogenesis, invasion and metastasis of malignant tumors due to its ability to degrade the extracellular matrix (ECM) [50, 51]. In normal cells, MMP transcript levels are low; the MMP gene is induced in tumor cells, and MMP is secreted into the extracellular space.

The tumor-specific cleavable PEG-lipid is a ternary conjugate which is composed of the following: PEG/MMP-substrate peptide [52]/DOPE ternary conjugate (PPD), which is specifically cleaved by MMP in the extracellular space in tumor tissues [53]. The schematic diagram shown in Fig. 3 illustrates the strategy for overcoming the dilemma associated with the use of PEG. MEND modified with PPD (PPD-MEND) allows for gene transfer as follows. PEG prolongs the half-life of MEND in systemic circulation, allowing MEND to accumulate in tumor tissue as a result of the EPR effect. After extravasation of MEND from capillaries into the tumor tissue, PPD is cleaved by MMP secreted by the tumor, and PEG dissociates from the MEND. Finally, the PEG-free MEND can interact efficiently with the tumor cells, resulting in high transfection activity.

4.4.1 PPD Cleavage in Response to MMP on the Liposomes

We first investigated the cleavage of PPD on the surface of liposomes. It was previously shown that DOPE forms a hexagonal (H_{II}) phase and readily aggregates under physiological conditions [54]. However, when a PEG-conjugated lipid was added to the lipid component containing DOPE, stabilized liposomal structures formed in aqueous media. Similarly, stable liposomes with diameters of approximately 150 nm were prepared by hydrating a lipid film composed of DOPE and PPD. These liposomes were incubated with various concentrations of bovine serum albumin (BSA) or MMP-2 [53]. Treatment of the PPD-modified liposomes with 14 and 56 nM MMP-2

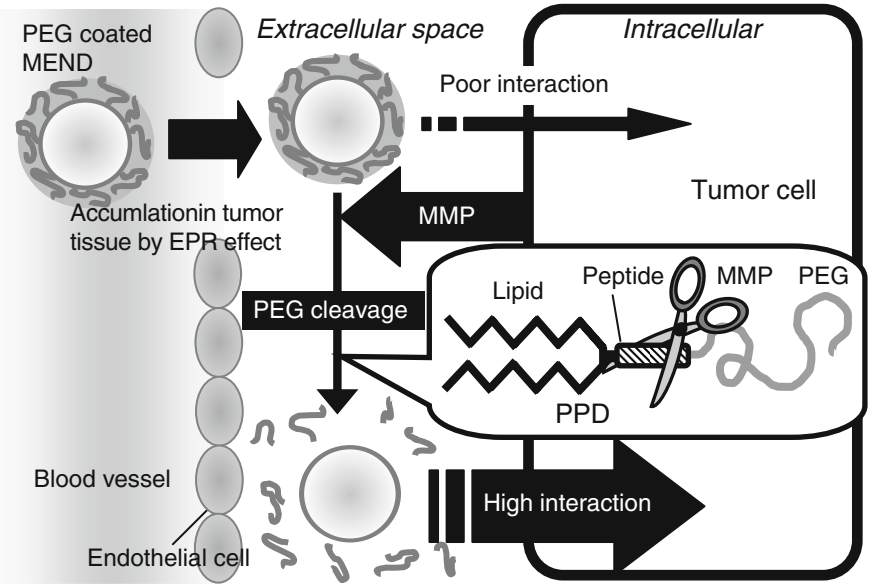

Fig. 3 Schematic diagram illustrating the strategy used to resolve the dilemma associated with the use of PEG. By modifying the gene carrier with PPD, the half-life in systemic circulation is prolonged and accumulation in the tumor is increased by the EPR effect. After extravasation from capillaries in the tumor tissue, PPD is cleaved by an extracellular MMP secreted from tumor cells. PEG dissociates from the gene carrier and the naked carrier can then associate efficiently with the tumor cell surface

for 24 h resulted in a significant increase in size (>2,000 nm). This result indicated that the PPD cleavage was dependent on MMP-2, resulting in an H_{II} transition. In contrast, MMP-2 treatment of the control liposomes, which were composed of DOPE and conventional PEG-lipid, increased the size of the liposomes.

4.4.2 In Vitro Transfection Study

The potential use of MMP-dependent PPD cleavage in a gene delivery system was then investigated. The transfection activity of MEND composed of DOTAP, DOPE and Chol with either conventional PEG-lipid or PPD using a total lipid concentration of 5% was evaluated. The MEND particle size was controlled to optimize the EPR effect (100–200 nm) by modification with PEG or PPD. In an in vitro study, HT1080 (fibrosarcoma cells) and HEK293 (human embryonic kidney cells) cells were used as model cells, in which MMP expression is high and low, respectively (Fig. 4a) [55, 56]. PEGylated MEND exhibited high transfection activity in both cell types (Fig. 4b). When the MEND were modified with conventional PEG-lipid (PEG-MEND), the transfection activity decreased to less than 1% in both cell types relative to the transfection activity of MEND. The transfection activity of PPD-MEND was enhanced 35-fold in comparison with that of PEG-MEND in

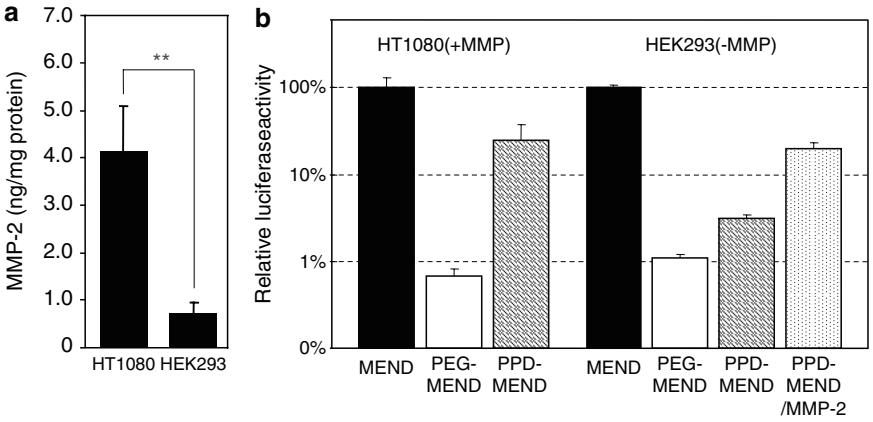

Fig. 4a.b In vitro transfection activities of MEND. **a** The expression level of MMP-2 in the supernatant of HT1080 and HEK293 cells was evaluated by an ELISA. **b** Luciferase activities of MEND, PEG-MEND and PPD-MEND in HT1080 cells and in HEK293 cells were evaluated at 48 h after transfection. Transgene expression in HEK293 cells was also evaluated after addition of MMP-2 protein in the culture medium at an equal concentration to HT1080, represented as PPD-MEND/MMP-2. Relative luciferase activities are expressed as % relative light units (RLU) per mg of protein compared to MEND. Each *bar* represents the mean ±SD, $n = 3$

HT1080 cells (Fig. 4b). In contrast, the transfection activity of PPD-MEND was less than 5% of that of MEND in HEK293 cells (Fig. 4b). Furthermore, the transfection activity of PPD-MEND was enhanced by coincubation with recombinant MMP-2 in HEK293 cells. These results suggest that activation of PPD-MEND is mediated by MMP-specific cleavage of PPD.

4.4.3 In Vivo Pharmacokinetics Study

The ability of PPD to improve stability in the systemic circulation, thereby augmenting accumulation of MEND in the tumor, was confirmed. The elimination profiles of MEND from systemic circulation were measured in mice via intravenous administration of [^{3}H]-labeled MEND [57] by tail vein injection. The half-lives of PPD-MEND in blood were slightly lower than those of PEG-MEND (Fig. 5a). However, compared with MEND, the half-lives of PPD-MEND were significantly increased. Therefore, PPD is an effective method of prolonging the half-life of MEND in systemic circulation. To investigate the tumor accumulation of MEND, [^{3}H]-labeled MEND were injected into tumor-bearing mice via the tail vein. Accumulation of PPD-MEND in the tumors was greater than that of MEND (Fig. 5b). These results show that PPD dramatically prolongs its half-life in systemic circulation, presumably by preventing entrapment by RES or other organs, thereby enhancing accumulation of MEND in the tumor.

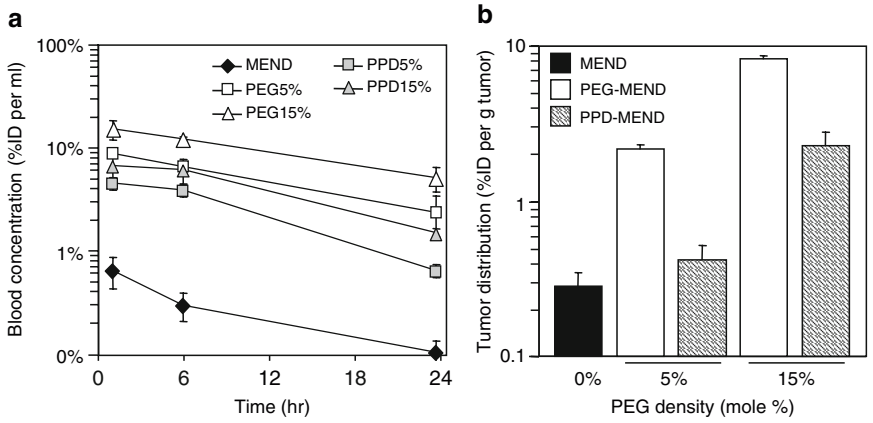

Fig. 5a,b Stability in systemic circulation and tumor distribution of MEND. **a** Blood concentrations of [^{3}H]CHE-labeled MEND were evaluated at 1, 6 and 24 h after i.v. injection. Data represent as the %ID per milliliter of blood. **b** Tumor distribution of MEND at 24 h in tumor-bearing mice, expressed as the %ID per gram tumor. Each *bar* represents the mean ± SD, $n = 3$

4.4.4 In Vivo Transfection Study in Tumor Tissue

The in vivo luciferase activity of the tumor was evaluated 48 h after i.v. administration of MEND at a dose of 25 μg pDNA/mouse. Transfection activity (Fig. 6a) was barely detectable using nonPEG-modified MEND. Although 15% PPD-MEND and 5% PEG-MEND exhibited comparable half-lives in systemic circulation and similar accumulation in the tumor, the transfection activity of 15% PPD-MEND was 55-fold higher than that of 5% PEG-MEND (Fig. 6a). In contrast, the transfection activities of 15% PEG-MEND and 15% PPD-MEND were comparable. However, it is noteworthy that the tumor accumulation of 15% PEG-MEND was approximately fourfold higher than that of 15% PPD-MEND (Fig. 5b). Therefore, the specific transfection activity of the particles, which is the in vivo transfection activity normalized to the number of particles delivered to the tumor (RLU/%ID), was threefold higher using the 15% PPD-MEND than the 15% PEG-MEND (Fig. 6b). These results show that PPD stabilizes MEND, even in systemic circulation, and offers superior in vivo transfection because it is cleaved by MMP in tumor tissue.

4.4.5 The Combination of PEG and PPD Enhances In Vivo Transfection Activity in Tumor Tissue

PPD modification of MEND improves stability in systemic circulation and enhanced accumulation of MEND in the tumor, whereas the ability of PPD to enhance systemic stability was slightly inferior to that of the conventional PEG-lipid. Therefore, to overcome the poor stability of PPD-MEND in systemic circulation, PPD-MEND

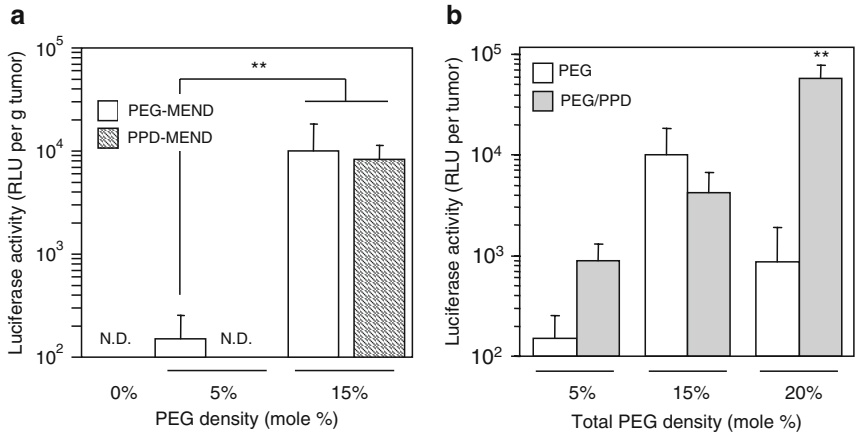

Fig. 6a,b In vivo tumor transfection activities of MEND. **a** Luciferase activity of MEND at 48 h, expressed as RLU per gram tumor. **b** The MEND was modified with PEG and PPD (1:1 mole ratio) at 5, 15 and 20% total PEG densities. A value of 10^6 RLU represents the luciferase activity of 5 ng luciferase protein. Each *bar* represents the mean ±SD, $n = 3$. $^{**}P < 0.01$

were modified with conventional PEG. A one to one mixture of PEG and PPD was attached to MEND (PEG/PPD-MEND) in varying amounts, such that the total content of PEG and PPD was 5, 15, and 20. For PEG-MEND, 15% PEG was sufficient to achieve maximum tumor accumulation [53]. However, in the case of PEG/PPD-MEND, tumor accumulation monotonically increased, depending on the total PEG/PPD content. As a result, at 20% PEG density, PEG/PPD-MEND achieved comparable tumor accumulation to PEG-MEND. In this situation, the transfection activity of PEG/PPD-MEND was more than 65-fold higher than that of PEG-MEND (Fig. 6b). This result indicates that combining PEG and PPD-MEND effectively improves both the pharmacokinetics and the in vivo transfection activity of MEND.

5 New Packaging Methods

5.1 A Novel Packaging Method: SUV Fusion Method*

Vector size is a critical factor in gene delivery via receptor-mediated cellular uptake, because the diameter of endosomes produced by receptor-mediated endocytosis is typically less than 200 nm. Moreover, intravenous administration in vivo requires small-sized vectors to achieve efficient delivery by avoiding clearance by the RES and allowing for direct translocation across the capillaries to the target tissue [58]. However, MEND prepared using the lipid hydration method are >300 nm and heterogeneous in size.

Cullis and coworkers [59, 60] previously developed a detergent dialysis method for the assembly of a stabilized plasmid–lipid particle (SPLP) nonviral gene delivery system using a mixture of DNA and lipid/detergent micelles. The SPLPs were less than 100 nm in size and were modified with PEG for in vivo application. Thus, the detergent dialysis method was used to prepare MEND from a mixture of PLL/DNA complex and lipid/detergent micelles. However, this method, which was developed for the preparation of SPLP, failed to produce MEND. Thus, it appears that lipid/detergent micelles are not a suitable lipid coating for DNA nanoparticles.

To overcome this obstacle, a novel method was developed using detergent-rich liposomes as follows. In the first step, DNA is condensed by electrostatic interactions between negatively charged DNA and a positively charged polycation, forming a DNA/polycation complex (DPC). Electron microscopy revealed that the condensed DNA formed a sphere [25] with a diameter of approximately 90 nm. In the second step, the DPC interact electrostatically with SUV*, which are small, detergent-rich liposomes containing the negatively charged lipid, dicetylphosphate, and PEgylated DOPE. In the final step, DPC are coated with lipid via fusion of SUV* and by addition of porous hydrophobic beads, resulting in rapid removal of the detergent. Previously, Ueno et al. found that SUV* particles fuse with each other to produce large unilamellar vesicles by complete removal of detergent [61]. The DNA encapsulation efficiency of the MEND was approximately 30% of the total DNA input. The diameter and zeta potential of the purified MEND were 196.7 nm and −37.9 mV, respectively. Moreover, modification of MEND with Tf at the tip of PEG resulted in MEND internalization via Tf receptor-mediated endocytosis [62].

5.2 Delivery of Antisense Oligodeoxynucleotides

In the field of gene-silencing research, antisense oligodeoxynucleotides (ODN) provide several advantages, including targeting of introns and improved selectivity and efficacy [63]. Moreover, various functional ODN, which enhance efficiency and specificity, have been synthesized. For example, Sasaki et al. developed a novel synthetic ODN, which induces intracellular sequence-selective alkylation between mRNA and ODN, thereby enhancing the antisense effect [64, 65]. Thus, attempts have been made to use ODN-based approaches in the treatment of diseases, such as cancer and hypertension [66–68]. However, there are some problems associated with this approach, such as degradation by nucleases and difficulties associated with targeting and intracellular delivery. Thus, an efficient ODN packaging method is needed to solve these problems.

Several ODN packaging methods have already been reported. Gokhale et al. encapsulated ODN in a lipid membrane by rehydrating a dried-lipid film in the presence of ODN [69]. Shi et al. reported the encapsulation of ODN in a cationic lipid using a freeze–thaw method [70]. In addition, Semple et al. constructed stabilized antisense-lipid particles by packaging ODN with a pH-sensitive cationic lipid

using an ethanol-injection method [71]. Recently, Yamauchi et al. described the encapsulation of antisense ODN in liposomes using an ethanol-dilution method [72]. These methods are based on electrostatic interactions between the anionic ODN and the cationic lipids, as described above for the preparation of MEND. Because R8-MEND effectively deliver plasmid DNA, R8-modified MEND may also be useful for the delivery of antisense ODN. Thus, R8-MEND-encapsulated ODN (ODN-MEND) were constructed by coencapsulation of luciferase-encoding pDNA and antiluciferase ODN [73, 74]. Three types of R8-MENDs were synthesized by condensation of the antiluciferase ODN with three different polycations – STR-R8, PLL and protamine. The antisense effects of the ODN-MEND were analyzed in a cultured cell line [74]. ODN-MEND packaged using protamine to condense the ODN showed a 90% antisense effect 8 h after transfection, and a persistent antisense effect of >75% for up to 48 h. ODN-MEND were much more effective antisense agents than LipofectAmine2000 (LA2000). In contrast, ODN-MEND prepared using PLL and STR-R8 to condense the ODN did not significantly inhibit luciferase activity. Although there was no specific relation between the physicochemical characteristics of the ODN-MEND and their antisense effect, the pattern of the ODN-MEND antisense effect was similar to the pattern of the silencing effect of R8-MEND encapsulating plasmid DNA encoding siRNA, i.e., only MEND prepared using protamine showed significant inhibition of the gene expression [26]. These results suggest that R8-MENDs are able to deliver encapsulated DNA to the cytosol, as well as to the nucleus, and that protamine is an efficient condenser in both the nucleus and cytosol.

5.3 siRNA Delivery

Synthetic siRNA can silence specific genes by RNA interference (RNAi), which is considered a more powerful gene-silencing tool than antisense ODN technology [75–78]. Delivery of sufficient siRNA into the cell is required for an efficient RNAi effect, although siRNA can be recycled by the RNA-induced silencing complex (RISC) [79, 80]. In general, cells are transfected with synthetic siRNA in vitro using various commercially available cationic liposomal reagents to form cationic liposome/siRNA complexes [13, 81–86]. However, cytotoxicity of the cationic lipids is widely recognized as a serious problem, especially in the case of vulnerable cell types, such as neurons. Moreover, control of the intracellular fate of cationic liposome/siRNA complexes needs to be improved because endocytosis, which is the predominant route by which LipofectAMINE PLUS/plasmid DNA (pDNA) complexes are taken up into cells, often directs complexes into the lysosomes [81, 87]. Thus, efficient introduction of siRNA into cells requires reduced toxicity and the ability to control intracellular trafficking.

Currently, many research groups are working to develop various carrier systems for siRNA delivery equipped with functional devices to overcome these limitations, including polyplex- and lipoplex-type systems [88–90]. Several polyplex-type vectors

have been reported. Grzelinski et al. used a well-known cationic polymer, polyethylenimine, to deliver siRNA for the silencing of the secreted growth factor, pleiotrophin (PTN), which is overexpressed in glioblastomal cells. The polyethylenimine/siRNA polyplex had a significant silencing effect on PTN gene expression in vitro and inhibited tumor growth in vivo [89]. Leng et al. synthesized highly branched HK peptides, H^3K8b, which should efficiently escape the endosome due to buffering with histidine residues. The H^3K8b/siRNA complex exhibited a significant RNAi effect on β-gal expression [88]. Furthermore, other vectors also have been developed. Hanai et al. used atelocollagen as a siRNA carrier; the atelocollagen/siRNA complexes delivered siRNA to metastatic bone tumors and inhibited tumor growth [91]. Matsui et al. synthesized a macrocyclic octaamine with a covalently liked lipid-bundle structure, and the siRNA complex silenced both the exogenous luciferase gene and the endogenous DsRed2 gene [92]. Veldhoen et al. used the cell-penetrating peptide, MPGα, which spontaneously forms complexes with nucleic acids, as a siRNA carrier [93]. In addition, several groups have used various liposomal formulations as siRNA delivery systems [94–100]. In general, stable nucleic acid–lipid particles are prepared via spontaneous vesicle formation using an ethanol-dilution method [94–98], in which siRNA is packaged into liposomes through electrostatic interactions with cationic lipids, such as 1,2-dilinoleyloxy-*N*,*N*-dimethyl-3-aminopropane (DLinDMA). As a result, siRNA is entrapped only on the inner surface of the liposomes and not in the aqueous phase of the vesicles. Recently, Heyes et al. improved the ethanol dilution method for the packaging of siRNA by using preformed siRNA polyplexes [100]. Alternatively, Li and Huang developed a tumor-targeted liposome–polycation–DNA lipoplex (LPD) siRNA delivery system modified with polyethyleneglycol and anisamide, which efficiently induced apoptosis [90]. Yet another packaging method utilized electrostatic interactions of siRNA with the cationic lipid, DOTAP [99]. In this system, siRNA was entrapped in the hydrophobic lipid bilayer that formed from the inverted hexagonal mixed micelles of the cationic lipid.

The R8-MEND also are expected to be an efficient and safe delivery system of siRNA because efficient inhibition of specific target genes was achieved using either R8-MEND-encapsulated siRNA-expressing pDNA [26] or R8-MEND-encapsulated antisense ODN [73, 74] as described above. However, it was not clear if siRNA could be packaged into MEND because the structure and physicochemical characteristics of double-stranded RNA (siRNA) differ from those of plasmid DNA and ODN. Thus, polycations were screened for their ability to condense siRNA to the size of a nanoparticle by measuring the size and zeta potential of complexes formed between siRNA and the polycations, PLL, STR-R8 and protamine [101]. Only STR-R8 compacted siRNA to form nano-size particles (<100 nm) [102], whereas all three polycations were able to condense pDNA or ODN [26, 74]. One possible explanation for this difference is that double-stranded siRNA assumes only an A-type conformation because of steric hindrance from the 2′-hydroxyl group [103]. Double-stranded DNA can form various secondary structures, such as A-, B- and Z-type conformations, and such conformational flexibility may be important for the compaction of nucleic acids with polycations [104]. Moreover, the

hydrophobic stearyl moiety, which is absent from PLL and protamine, may be critical in the compaction of siRNA into small particles; the short length of the R8 polycation also may be important. The silencing effect of R8-MEND-encapsulated siRNA (siRNA-MEND) was compared with that of LA2000. In HeLa cells stably expressing luciferase, siRNA-MEND inhibited luciferase activity by more than 80% for an extended period of time [101]. In addition, the R8-MEND-encapsulated siRNA were not cytotoxic. Furthermore, confocal microscopy was used to visualize cellular internalization of siRNA after transfection with siRNA-MEND containing Alexa546-labeled siRNA and NBD-labeled lipid. Most of the siRNA was internalized as siRNA-MEND and siRNA was effectively released from the lipid into cytoplasm near the nucleus [101]. Therefore, siRNA-MEND delivery of compacted siRNA nanoparticles into cells via siRNA-MEND results in an efficient and persistent silencing effect with minimum cytotoxicity.

6 Rate-Limiting Step in Nonviral Gene Delivery Systems

As described in Sect. 1, RNA and DNA viruses evolved sophisticated mechanisms for the efficient delivery of viral genes to the host nucleus, including the ability to control intracellular trafficking, over many years. Since the first report of gene delivery using a cationic liposome in the 1980s [105], many improvements to nonviral gene vectors have resulted from 20 years of research. However, the evolution of nonviral vectors is short compared with that of viruses, and then viral vectors remain superior to nonviral vectors regarding transgene expression efficiency. Therefore, much can be gained by understanding how viruses control intracellular trafficking in response to the intracellular environment. Furthermore, identification of the rate-limiting steps in intracellular trafficking using nonviral vectors can be ascertained from quantitative information on intracellular trafficking of viral vectors. In this section, strategies to control endosomal escape and nuclear delivery will be reviewed, followed by a discussion of intracellular rate-limiting processes.

6.1 Endosomal Escape

Nearly all vectors are taken up into cells via the vesicular transport system; therefore, most vectors have to escape the endosomal compartment prior to lysosomal degradation or to extracellular release and recycling. The importance of endosomal escape is evident in the significant enhancement in transfection efficiency resulting from use of lysosomotropic reagents, such as chloroquine, which accumulate in acidic lysosomes and destabilize the membrane by swelling.

Three categories of devices have been developed for the improvement of endosomal escape: (1) pH-sensitive fusogenic lipids; (2) polycations that have a proton sponge nature; and (3) pH-sensitive membrane fusogenic peptides. pH-sensitive

fusogenic lipids increase endosomal escape as a result of lipid-mixing between the endosomal membrane and cationic liposome, which leads to membrane fusion and release of the DNA into the cytosol. This mechanism is supported by enhanced transgene expression using DOPE-containing cationic liposomes [106, 107]. DPOE forms a stable lipid bilayer at physiological pH (~7.0) and a hexagonal-II structure at acidic pH (~5–6). This pH-dependent conformational change is a key event, which triggers fusion of the liposomal membrane with the endosomal membrane [108, 109]. Furthermore, cationic lipids release encapsulated macromolecules and complexed DNA into the cytosol [110, 111]. In addition to pH, the lipid composition of the target membrane also can be used to enhance membrane fusion. Bailey et al. demonstrated that fusion of the cationic liposomes containing DOPE was enhanced by increasing the negative charge of the surface of the target liposomes [112]. Because the negatively charged lipid (i.e., phosphatidylserine) content of the endosomal membrane is greater than that of the plasma membrane [113], it is likely that lipid composition of the endosomal membrane also affects membrane fusion.

The mechanisms of polycation-mediated endosomal release are partially understood. One of the well-accepted hypotheses is the "proton sponge mechanism," which is based upon proton-accepting structures, such as secondary amines in polyethyleneimine (PEI). Uptake of proton-accepting polymers into the endosome buffers endosomal protons, and subsequently drawing in additional protons, as well as chloride ions and water molecules [114]. The influx of ions and water causes swelling and osmotic lysis of the endosome. This hypothesis is supported by inhibition of PEI-mediated transgene expression by ionophores, which reduce the pH gradient between the endosome and cytosol [115].

The third device used to increase endosomal escape, pH sensitive membrane fusogenic peptide, was developed based on the endosomal escape mechanism of the influenza virus, which is an envelope-type RNA virus. In this virus, the hemagglutinin (HA) protein on the envelope membrane allows endosomal escape. A conformational change in the HA2 domain of the α-helix structure in the acidic compartment is the key event [116, 117]. Based on this mechanism, Wagner and coworkers used synthetic peptides derived from the N-terminus of HA to enhance transgene expression using DNA/PLL complexes [118–121]. Similarly, artificial amphipathic peptides (e.g., GALA [122] and JTS1 [123]), which also undergo structural changes to the α-helix under acidic conditions, have been synthesized and applied to various gene vectors. These peptides consist of an amphipathic helix motif partitioned by acidic residues, such as glutamic acid and aspartic acid. At neutral pH, the negative charge destabilizes the α-helix and, as a result, the peptide forms a random coil structure. However, in acidic environments, the negative charge on the carboxylic group is neutralized, and subsequently an α-helix forms.

Recently, endosomal lysis has been identified as a promising strategy for the enhancement of endosomal escape. In adenoviruses, protein VI, a 22-kDa cement protein located beneath the peripentonal hexons, plays an important role in endosomal lysis. Adenoviral capsids disassemble in response to low endosomal pH, triggering the release of protein VI from the adenoviral particle [124]. Ogris et al. demonstrated that endosomal escape was increased by the conjugation of melittin, a cationic membrane

lytic peptide derived from bee sting venom, resulting in a drastic improvement in transfection activity [125]. To avoid cytotoxicity resulting from nonspecific damage to the plasma membrane, a modified melittin was developed, which exhibits membrane lytic activity only at low endosomal pH (pH ~5.0) [126].

Another unique approach to control the cytoplasmic distribution of drugs or macromolecules is direct fusion of the liposome and plasma membrane assisted by the fusogenic protein, HA, and the F-fusion envelope proteins from the hemagglutinating virus of Japan (HVJ; Sendai virus) [127]. HVJ-liposomes were constructed by combining macromolecule-loaded liposomes and the fusogenic envelope proteins derived from HVJ. This endocytosis-independent delivery avoided lysosomal degradation [128]. Efficient transgene expression with DNA-encapsulated HVJ-liposomes was demonstrated both in vivo and in vitro [129, 130].

6.2 Cytoplasmic Stability and Trafficking of DNA

Once released into the cytosol, DNA must traverse the cytosol towards the nucleus. The current evidence and opinions regarding where in the cell pDNA should be released from the vector is controversial. Some data support pDNA release from the vector in cytosol for efficient transgene expression. This is consistent with results showing that direct cytoplasmic injection of the lipoplex exhibited much lower transgene expression compared with injection of naked DNA [131, 132]. In addition, Itaka et al. have demonstrated that, in various types of PEI-mediated transfection, the level of transgene expression correlates with the extent of DNA decondensation in the cytoplasm. [133]. Cytoplasmic translocation of pDNA may be driven by sequences encoded in the plasmid DNA, which are recognized by karyophilic proteins, such as the SV40 enhancer region [134, 135]. This region includes consensus sequences for various transcription factors (i.e., AP-1, AP-2 and NFκB). Therefore, transcription factor binding to pDNA may be a driving force for nuclear delivery. This strategy was also successful when other kinds of sequences were used (i.e., smooth muscle gamma actin (SMGA) promoter [136], NFκB-binding sequence [137, 138] and the oriP sequence derived from the Epstein–Barr virus [139]). Very recently, Dean and coworkers demonstrated that naked pDNA introduced into the cytoplasm can accumulate in the nucleus [140]. Since this accumulation was inhibited by disruption of microtubules and by the coinjection of antidynein antibodies, it is plausible that pDNA accumulates in the nucleus via dynein-mediated transport.

In contrast, data from several studies suggest that cytoplasmic decondensation of DNA is disadvantageous for transgene expression. Naked DNA is easily degraded by nuclease digestion in the cytoplasm with a half-life of dozens of minutes [131, 141]. Furthermore, diffusion of naked DNA in the cytoplasm is severely limited because the cytoplasm is highly viscous; the diffusion coefficient of naked DNA >2,000 bp in the cytoplasm is less than 1% of that in water [142]. In fact, pDNA released into the cytosol cannot enter the nucleus and, therefore, has no

appreciable transfection activity [143]. Very recently, real-time multiple particle tracking of PEI/DNA complexes in viable cells showed that the particles seem to be transported through the cytoplasm towards the perinuclear region on motor proteins running on the microtubule-network [144, 145], which is similar to the cytoplasmic translocation of adenoviruses [146–148] and HSV [149–151]. It is unknown whether this movement is due to vesicular transport or to direct interaction of the vector with motor proteins; however, condensation of pDNA with certain vectors is desirable for efficient cytoplasmic transport.

At this moment, the optimal intracellular site for pDNA release to effect efficient cytoplasmic transport and high transfection activity is yet to be identified. The intracellular site and timing of DNA decondensation must be tightly controlled.

6.3 Nuclear Transfer of DNA

The next barrier encountered is the nuclear membrane. Commonly used plasmid DNA is too large to pass through the nuclear pore complexes [135, 152–155] and, thus, pDNA primarily enters the nucleus when the nuclear membrane structure is diminished during the M-phase [156–158]. In fact, less than 1% of cytoplasm-microinjected plasmid DNA reaches the nucleus [131]. Wolff and coworkers investigated the effect of pDNA size on nuclear transport activity using digitonin-permeabilized cells [153, 154]. Short DNA (<200 bp) fragments were effectively imported into the nucleus, whereas nuclear import decreased when the size of the pDNA increased and was negligible at >1,500 bp. Typically, pDNA used in transfection is >3,000 bp. The efficient nuclear transfer of therapeutic DNA requires an elegant strategy.

One approach is the conjugation of NLS to the plasmid DNA itself using chemical linkages [155]. However, in this strategy, >100 NLS peptides/1 kbp are required to induce nuclear delivery of pDNA, severely inhibiting transcription. Although, Zanta et al. demonstrated that one NLS is enough to deliver linearized DNA to the nucleus based on the transfection assay [159], current microinjection studies [160, 161] cannot evaluate the utility of this strategy. Since it uses highly cationic NLS derived from the SV40 T-antigen, the negatively charged pDNA interferes with importin recognition of NLS.

A second approach is the conjugation of NLS to counter polycations. Condensation of pDNA with the PLL conjugated to SV40 NLS only slightly enhanced transgene expression compared with PLL, presumably because of the positively charged NLS peptide sequence [162, 163]. To avoid electric interactions between NLS and DNA, a novel NLS, derived from heterogeneous nuclear ribonucleoprotein-A1, with fewer cationic residues (M9) was created by modifying the cationic peptide (scattered SV40 NLS). Complexes of DNA and the M9-modified polycations exhibited enhanced transfection activity when introduced into cells using lipofection [164]. Currently, various NLS, such as tetramers of SV40 NLS [123], TAT oligomers [165], Mu peptide derived from the adenoviral core [166,

167], and protamine [168–170] are being investigated. DNA condensation with these peptides drastically enhances transgene expression.

However, it is difficult to control the NLS density on the particle surface because cationic residues in NLS_{SV40} interact with pDNA via strong electrostatic interactions. Recently, we proposed a third strategy for nuclear delivery, which mimics the nuclear gene delivery system of adenoviruses. In adenoviruses, NLS are spontaneously displayed on the adenovirus particle via a well-ordered assembly of capsid proteins around the DNA core. To control the topology of NLS on the particle surface, a lipid derivative of a nuclear-targeting device was synthesized with the lipid moiety incorporated into the envelope and the NLS spontaneously oriented outward towards the MEND surface. This strategy resulted in effective transfection of nondividing cells (i.e., primary dendritic cell cultures) [171].

Moreover, our group has also focused on sugars as nuclear-targeting devices. In recent decades it was reported that BSA modified with certain sugars accumulated in the nucleus [172, 173]. Surface modification of R8-MEND with sugars increased transfection activity 10- to 100-fold [174]. Investigation of the mechanism of enhanced transfection and optimization of sugar-modified MENDs are ongoing.

6.4 Quantitative Analysis of Intracellular Trafficking: CIDIQ

As described above, strategies to control intracellular trafficking of plasmid DNA, ODN, siRNA and proteins were developed based on the concept of Programmed Packaging. Additional rational strategies, based on feedback information regarding intracellular trafficking, are needed for development of the next generation of gene-delivery vectors. Feedback on intracellular trafficking would enable us to identify clearly which barriers need to be overcome to improve transfection activity.

The intracellular fate of DNA is determined by the interaction of many processes, including cellular uptake, endosomal release, nuclear binding, nuclear translocation, dissociation and protein synthesis. Thus, a computer-assisted intracellular kinetic model (Fig. 7) integrating these processes with kinetic parameters (i.e., first-order rate constant: $time^{-1}$) quantified experimentally is useful for the analysis, simulation and optimization of transgene expression [175–178]. Varga et al. integrated the processes of cellular uptake, endosomal release, nuclear binding, nuclear translocation, dissociation and protein synthesis in a first-order mass action kinetic model and demonstrated that the model was useful in the optimization of transgene expression [177].

In spite of the great advantages of kinetic modeling, the majority of studies evaluated only transfection activity while intracellular events remain in a black box. This is primarily because of a lack of adequate assay systems for quantifying pDNA organelle distribution. Recently, we and other researchers have established a method that quantifies plasmid DNA in the nucleus using nuclear fractionation followed by the polymerase chain reaction (PCR) [164, 178–182]. PCR is a very convenient technique for quantification of pDNA. Using these methods, we can

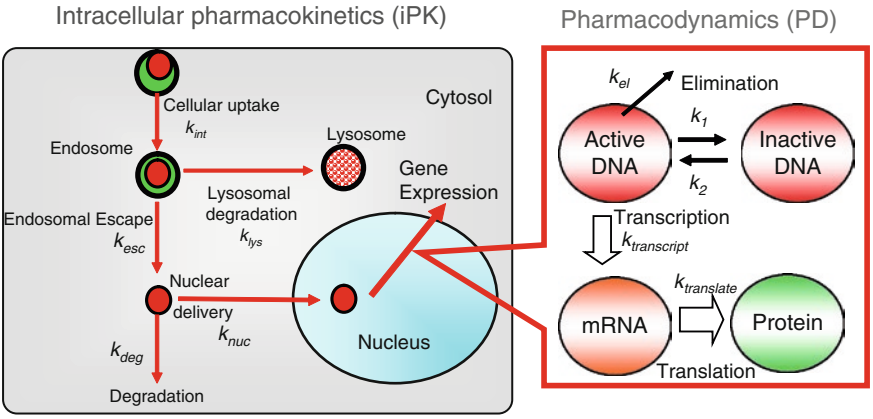

Fig. 7 Schematic diagram illustrating the intracellular pharmacokinetics and nuclear dynamics of DNA. Intracellular barriers to the development of gene-delivery systems are shown. DNA carriers bind to the plasma membrane electrostatically and are internalized via endocytosis (k_{int}). Endosomal pDNA fused with lysosomes is degraded (k_{lys}). A certain fraction of the endosomal DNA is released into the cytosol (k_{esc}) the DNA is degraded by nucleases (k_{deg}) or translocated to the nuclear membrane (k_{nuc}). In the nucleus, active pDNA (e.g., decondensed form of DNA) is subjected to transcription ($k_{transcript}$), followed by translation ($k_{translate}$)

investigate the relationships between applied doses of plasmid DNA and amounts of nuclear DNA and transgene expression. The kinetic data indicated that nuclear plasmid DNA increased linearly with the pDNA dose; however, remarkable saturation of transgene expression was observed [181]. These results indicate that it is necessary to enhance not only nuclear delivery of plasmid DNA, but also nuclear transcription efficiency. In contrast to the pDNA content in the nucleus, very few reports are available concerning the amount of plasmid DNA in the endosome/lysosome compartment, and, therefore, it is very hard to evaluate the efficiency of endosomal release. Although subcellular fractionation of the endosome/lysosome compartment may resolve this issue, many technical difficulties, such as the multistep protocol, the uncertainty of recovery of the endosomal fraction and mutual contamination, may prevent implementation of this strategy.

Recently, we proposed a novel strategy to simply and reliably quantify the distribution of pDNA in the cytosol, endosome/lysosome and nucleus simultaneously. We termed this method, which is based on sequential Z-series images captured by confocal laser scanning microscopy (CLSM), "confocal image-assisted three-dimensionally integrated quantification" (CIDIQ) [183]. A schematic diagram illustrating the method and relevant numerical formulas are summarized in Fig. 8. After transfection with rhodamine-labeled pDNA, the acidic intracellular compartments (endosome/lysosome) and nucleus were stained with Lysosensor DND-189 (green) and Hoechst 33342 (blue), respectively, to visualize the subcellular localization of the pDNA.

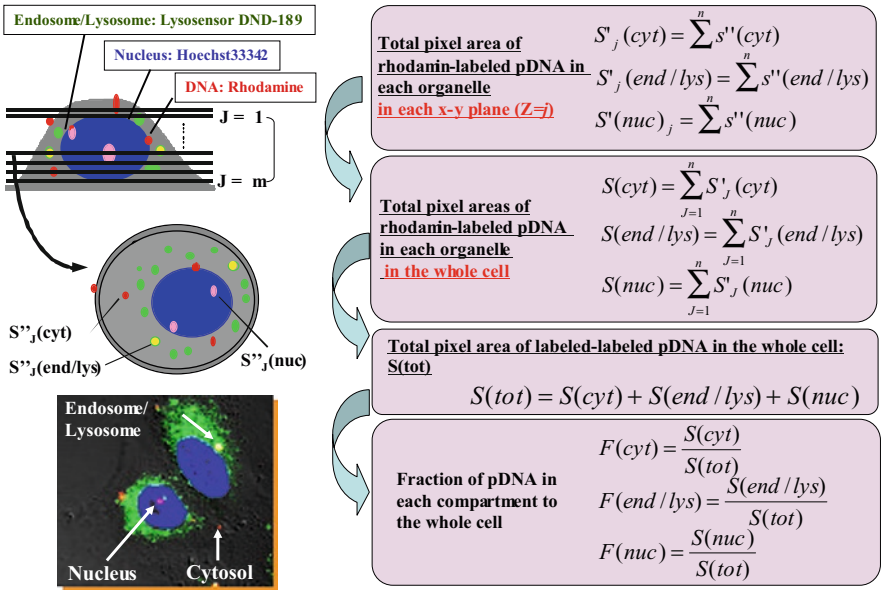

Fig. 8 Schematic diagram illustrating the strategy for the quantification of plasmid DNA with CLSM. NIH3T3 cells were transfected with rhodamine-labeled plasmid DNA using LipofectAMINE PLUS. Then 3 h after transfection, the endosome/lysosome compartment and nucleus were stained with Lysosensor DND-189 and Hoechst 33342, respectively. The pixel areas of the plasmid DNA in each *X*–*Y* plane were summed for each compartment and are denoted as *S'j*(*i*), where *i* represents each compartment (e.g., membrane-bound, endosome/lysosome, cytosol, perinucleus and nucleus). *S'j*(*i*) represents the total pixel area (which corresponds to the amount of plasmid DNA) in each *X*–*Y* plane for each compartment (*i*). *S'j*(*i*) was summed up in Z-series to obtain *S*(*i*), which represents the total pixel area in one cell for each compartment (*i*). All the *S*(*i*) values were combined to calculate *S*(tot), which reflects the total pixel area in one cell. *F*(*i*), representing the fraction of the plasmid DNA in each compartment in one cell, was calculated by dividing *S*(*i*) by *S*(tot)

Soon after transfection, plasmid DNA was detected as clusters. Plasmid DNA localized in the endosome/lysosome, cytosol and nucleus appeared as yellow, red and pink clusters, respectively. To quantify the pDNA in each subcellular location, the pixel areas of clusters were used as an index of the amount of pDNA. First, total pixel area of the plasmid DNA clusters in each subcellular compartment was determined in each *XY*-plane. Then these values were further integrated and denoted as *S*(cyt), *S*(endosome/lysosome) and *S*(nucleus). These values represent the amount of plasmid DNA in each organelle in one cell. *S*(tot), which represents the total cellular uptake of the plasmid DNA in one cell, was determined by integrating these value. Finally, the fractions of plasmid DNA in each compartment, relative to the total pDNA per cell, were calculated. As shown above, transgene expression of STR-R8 was significantly greater than that of R8, but was much less than that of the commercially available Lipoplex (Lipofectamine PLUS: LFN). This approach was used to identify the intracellular process that is the rate-limiting step in transfection.

Intracellular trafficking of pDNA, transfected by LFN, stearylated octaarginine (STR-R8) and R8 was analyzed. Transfection of pDNA using R8 resulted in most of the pDNA trapped in the endosome/lysosome compartment. STR-R8 exhibited endosomal escape followed by nuclear translocation in a time-dependent manner. These data suggest that the stearyl moiety enhances endosomal escape. Furthermore, LipofectAMINE PLUS was the most effective in rapidly delivering DNA to the nucleus as well as to the cytosol. Surprisingly, nuclear localization was observed within 1 h after transfection, which is similar to the time-course observed for adenoviruses. This phenomenon is consistent with the observation that transgene expression was detected within 3 h after transfection. Collectively, the differences in the transgene expression were adequately explained by the CIDIQ assessment of intracellular trafficking. In addition, results of inhibition studies of the internalizing process combined with the CIDIQ assessment provide a complete evaluation of the contribution of endocytosis to total cellular LFN-uptake. This method is applicable to intracellular pharmacokinetic analysis of various gene vectors and will be useful in the development of new gene delivery systems.

6.5 Quantitative Comparison of Intracellular Trafficking Between Viral and Nonviral Vectors

It is generally accepted that the most significant obstacle to the clinical use of nonviral vectors is low transfection activity. Viruses have evolved sophisticated mechanisms to overcome these barriers, such that delivery of the viral genome to the host nucleus for viral replication occurs. As a result, transfection efficiency of viral vectors is superior to nonviral vectors. Therefore, it is essential to clarify why and to what extent current nonviral vectors are inferior to viral vectors from the point of view of intracellular trafficking [183]. This information would enable us to identify which intracellular barriers must be overcome to improve transfection activity, and to what extent transfection activity might be improved if the barriers were overcome. Recently, our group compared intracellular trafficking between adenoviruses and LFN, as models of a viral and nonviral vector, respectively [179]. First, transfection activities were compared. When used according to the manufacture's protocol, the time course of pDNA expression with LFN was comparable to that with adenoviruses. However, based on the dose–response curves, comparable transgene expression between the two vectors was achieved only when the number of gene copies was 3–4 orders of magnitude higher using the LFN vector compared with the adenoviral vector. Therefore, it is important to identify which intracellular process is responsible for such a large difference in transfection activity.

First, the cellular uptake of pDNA transfected using LFN and adenoviruses were quantified. Then, 1 h after transfection, cells were collected and cellular uptake was evaluated using real-time PCR. Cellular uptake of DNA using LFN was approximately 15,000-fold greater than that using adenoviruses. Normalizing cellular uptake to the applied dose, more than 40% of the pDNA was taken up by the cell with LFN,

whereas, only 10% was taken up with adenovirus. Next, the intracellular distribution of pDNA and adenoviruses was quantified with TaqMan PCR and CIDIQ. Then, 1 h after transfection, nuclear delivery of DNA was more efficient with adenoviruses than with LFN. However, the nuclear transport efficiency of adenoviruses was only twofold greater than that of LFN. Thus, the large difference in transfection efficiency could not be explained by intracellular trafficking. Finally, comparison of the nuclear delivery of DNA revealed that LFN required three to four orders of magnitude more gene copies than did adenoviruses to obtain comparable transfection activities. Transcription efficiency was calculated as expression divided by the number of gene copies in the nucleus. Adenoviruses were 8,100-fold more efficient at nuclear transcription than LFN [179]. This result indicates that the difference in transfection efficiency between LFN and adenoviruses is due to a postnuclear-delivery process.

6.6 Mechanism for the Difference in Postnuclear Delivery Events Between Adenoviruses and LFN

To apply this quantitative information to the development of artificial vectors, we must understand why the transcription activity of adenoviral vectors is so high. To examine the influence of genome structure and sequence on transfection activity, adenoviral DNA and pDNA encoding GFP were microinjected into the nucleus and GFP expression efficiency was evaluated. GFP expression efficiency was comparable between adenoviral DNA and pDNA. Therefore, differences in DNA sequence and structure cannot explain the difference in transcription efficiency between adenoviruses and LFN [179]. Collectively, these data suggest that efficient transgene expression of DNA delivered to the nucleus in adenoviruses cannot be explained by adenoviral-derived factors.

Differences in intranuclear distribution of DNA were examined by visualizing decondensed DNA using in situ hybridization. It was confirmed that the ODN probe can access a specific sequence in naked DNA, but not in complexed DNA, due to steric hindrance. The pDNA signal was less prominent compared with the adenoviral genome, even though the total amount of nuclear DNA was higher with LFN transfection than with adenoviral transfection. Furthermore, it was determined that adenoviral DNA was localized on the euchromatin region where transcription activity is relatively high. In contrast, the plasmid DNA was randomly distributed. These results suggest that poor decondensation and poor targeting of DNA to the euchromatin region are responsible for the lower nuclear transcription efficiency of LFN compared with that of adenoviruses.

It is important to remember that transgene expression of DNA delivered to the nucleus is limited by transcription and translation. Therefore, the contributions of these two processes to the overall differences in efficiency of postnuclear processes were quantified by measuring cellular mRNA. Transcription efficiency was calculated as mRNA expression divided by nuclear DNA [179]. Similarly, translation

efficiency was calculated as transgene expression divided by mRNA expression. Translation efficiency with adenoviral transfection was approximately 16-fold higher than that with LFN. Furthermore, the translation efficiency of adenoviruses was 460-fold higher than that of LFN. Therefore, the difference in the postnuclear-delivery process between LFN and adenoviruses, which was three orders of magnitude, was due to a one order of magnitude difference in transcription efficiency and a two orders of magnitude difference in translation efficiency.

The mechanisms underlying the prominent differences in translation were examined. Because RNA is a negatively charged molecule, LFN may interact with mRNA via electrostatic interactions. If this assumption is correct, two hypotheses can explain the difference in translation efficiency. The first is that LFN may entrap mRNA in the nucleus, thereby interfering with its nuclear export. The second is that the recognition of cytoplasmic mRNA by ribosomal RNA or another translation-related protein is inhibited. To examine these hypotheses, the nuclear distribution of mRNA was compared after adenoviral- and LFN-mediated transfection. Then, 3 h after transfection, cellular and intranuclear mRNA were quantified using real-time RT-PCR. Therefore, electrostatic interactions between LFN and mRNA did not inhibit nuclear export of mRNA. To compare the effect of LFN and adenoviral vectors on cytoplasmic translation, mRNA encoding luciferase was subjected to in vitro translation with or without adenoviruses or LFN. When adenoviruses were applied, protein synthesis was inhibited 20% compared with no treatment. In contrast, when LFN was added, protein synthesis was drastically inhibited – by more than 90% [179]. These data indicate that the inhibition of translation due to electrostatic interactions between LFN and mRNA is a significant contributor to the difference in translation efficiency between LFN and adenoviruses.

6.7 Mechanisms for Heterogeneity in Nonviral Vectors

Another disadvantage of the current nonviral gene vectors is heterogeneous transgene expression. In an attempt to investigate the mechanism underlying this heterogeneity, the relationship between the efficiency of pDNA nuclear delivery and transgene expression was examined in individual cells transfected with LFN [185].

To visualize simultaneously nuclear delivery of pDNA and transgene expression in individual cells, lipoplexes were formed using a 1:1 mixture of β-galactosidase (LacZ)-encoding pDNA and rhodamine-labeled pDNA. The lipoplexes were used transfected to HeLa cells and, 3 h posttransfection, the nucleus was stained with Hoechst 33342 to distinguish nucleus-delivered pDNA from cytosolic pDNA. Transgene expression of LacZ was fluorescently visualized using an in vivo *lacZ* β-galactosidase detection kit. A Z-series of 20 images was captured by CLSM and each 8-bit image was transferred to Image-Pro Plus ver 4.0 software for quantitative analysis. Since pDNA was detected in clusters, the pixel area of each cluster was used as an index of the amount of pDNA.

Out of 204 randomly selected cells, 46 cells (22.5%) possessed nuclear pDNA. As expected, LacZ activity was below the detection limit in almost all of the nuclear pDNA-negative cells. However, simultaneous detection of nuclear pDNA and transgene expression showed that LacZ activity was detected in only 15 out of 46 nuclear pDNA-positive cells (32.6%), suggesting that nuclear delivery was not sufficient for transgene expression. The relationship between nuclear pDNA delivery and transgene expression was further investigated using synchronized HeLa cells. Cellular uptake and subsequent nuclear delivery were diminished. In contrast, nuclear delivery of pDNA was observed in M-phases and even in G_o/G_1 phases. This result was inconsistent with the generally accepted hypothesis that pDNA enters the nucleus mainly during the late S phase and M-phase when the nuclear membrane structure is diminished. In addition, the percentage of LacZ-positive cells relative to the percentage of nuclear pDNA-positive cells increased drastically when the synchronized cell population passed through the M-phase. These data suggest that mechanisms other than improved nuclear delivery of pDNA may enhance transgene expression during the M-phase. In cell lines stably transfected with luciferase, luciferase expression was independent of the cell-cycle phase, suggesting that the transcription machinery itself is active in each phase of the cell cycle. A possible explanation for the increase in pDNA expression in the M-phase is that pDNA may be inactivated by the tight condensation with LFN and may be reactivated by remodeling. These findings clearly indicated that optimization of postnuclear events is essential for the achievement of transgene expression that is comparable to that of viral vectors and for resolution of heterogeneity.

In summary, cellular uptake and nuclear delivery demonstrated that the large difference in transfection efficiency is primarily due to a postnuclear delivery process. Simultaneous visualization of markers for gene expression and nuclear transfer indicated that a postnuclear delivery process is also a key factor responsible for heterogeneity. Furthermore, by measuring mRNA expression, this difference can be partitioned into transcription- and translation-related events. During transcription, adenoviruses are efficient due to efficient decondensation and adequate intranuclear trafficking. During translation, the electrostatic interactions between LFN and mRNA may prevent efficient translation. Improvement of these processes is important for the development of efficient gene carriers. However, the importance of the regulation of intracellular pharmacokinetics cannot be excluded. Intracellular pharmacokinetics and postnuclear delivery processes (i.e., transcription and translation) function in tandem. Therefore, if intracellular pharmacokinetics are minimally regulated, transfection activity will be poor. Nuclear delivery remains a significant barrier for nonviral vectors, especially in nondividing cells. Therefore, it is important to emphasize that both intracellular pharmacokinetics and pharmacodynamics must be regulated to produce a nonviral vector with transfection activity comparable to that of adenoviruses.

Acknowledgments This study was performed through Special Coordination Funds for Promoting Science and Technology of the Ministry of Education, Culture, Sports, Science and Technology, the Japanese Government. The authors also wish to thank Dr. James L. McDonald for his helpful advice in writing the English manuscript.

References

1. Dinçer S, Türk M, Pi.kin E (2005) Gene Ther 12:139
2. Boussif O, Lezoualc'h F, Zanta MA, Mergny MD, Scherman D, Demeneix B, Behr JP (1995) Proc Natl Acad Sci USA 92:7297
3. Sorgi FL, Bhattacharya S, Huang L (1997) Gene Ther 4:961
4. Masuda T, Akita H, Harashima H (2005) FEBS Lett 579:2143
5. Eliyahu H, Siani S, Azzam T, Domb AJ, Barenholz Y (2006) Biomaterials 27:1646
6. Oba M, Fukushima S, Kanayama N, Aoyagi K, Nishiyama N, Koyama H, Kataoka K (2007) Bioconjug Chem 18:1415
7. Yamashita A, Yui N, Ooya T, Kano A, Maruyama A, Akita H, Kogure K, Harashima H (2006) Nat Protoc 1:2861
8. Satoh T, Kakimoto S, Kano H, Nakatani M, Shinkai S, Nagasaki T (2007) Carbohydr Res 342:1427
9. Sato A, Choi SW, Hirai M, Yamayoshi A, Moriyama R, Yamano T, Takagi M, Kano A, Shimamoto A, Maruyama A (2007) J Control Release 122:209
10. Felgner PL, Gadek TR, Holm M, Roman R, Chan HW, Wenz M, Northrop JP, Ringold GM, Danielsen M (1987) Proc Natl Acad Sci USA 84:7413
11. Simberg D, Weisman S, Talmon Y, Barenholz Y (2004) Crit Rev Ther Drug Carrier Syst 21:257
12. Zuhorn IS, Engberts JB, Hoekstra D (2007) Eur Biophys J 36:349
13. Zhang S, Zhao B, Jiang H, Wang B, Ma B (2007) J Control Release 23:1–10
14. Kamiya H, Akita H, Harashima H (2003) Drug Discov Today 8:990
15. Khalil IA, Kogure K, Akita H, Harashima H (2006) Pharmacol Rev 58:32
16. Knorr V, Allmendinger L, Walker GF, Paintner FF, Wagner E (2007) Bioconjug Chem 18:1218
17. Schoen P, Chonn A, Cullis PR, Wilschut J, Scherrer P (1999) Gene Ther 6:823
18. Hama S, Akita H, Ito R, Mizuguchi H, Hayakawa T, Harashima H (2006) Mol Ther 13:786
19. Bally MB, Harvie P, Wong FM, Kong S, Wasan EK, Reimer DL (1999) Adv Drug Deliv Rev 38:291
20. Khalil IA, Kogure K, Futaki S, Hama S, Akita H, Ueno M, Kishida H, Kudoh M, Mishina Y, Kataoka K, Yamada M, Harashima H (2007) Gene Ther 14:682
21. Kogure K, Akita H, Harashima H (2007) J Control Release 122:246
22. Kakudo T, Chaki S, Futaki S, Nakase I, Akaji K, Kawakami T, Maruyama K, Kamiya H, Harashima H (2004) Biochemistry 43:5618
23. Li W, Nicol F, Szoka FC Jr (2004) Adv Drug Deliv Rev 56:967
24. Khalil IA, Kogure K, Futaki S, Harashima H (2006) J Biol Chem 281:3544
25. Kogure K, Moriguchi R, Sasaki K, Ueno M, Futaki S, Harashima H (2004) J Control Release 98:317
26. Moriguchi R, Kogure K, Akita H, Futaki S, Miyagishi M, Taira K, Harashima H (2005) Int J Pharm 301:277
27. Li L, Hoffman RM (1995) Nat Med 1:705
28. Domashenko A, Gupta S, Cotsarelis G (2000) Nat Biotechnol 18:420
29. Torchilin VP (2005) Nat Rev Drug Discov 4:145
30. Klibanov AL, Maruyama K, Torchilin VP, Huang L (1990) FEBS Lett 268:235
31. Blume G, Cevc G (1990) Biochim Biophys Acta 1029:91
32. Allen TM, Hansen CB (1991) Biochim Biophys Acta 1068:133
33. eh B, Winterhalter M, Freddrik PM, Vallner JJ, Lasic DD (1997) Adv Drug Deliv Rev 24:165
34. Matsumura Y, Maeda H (1986) Cancer Res 46:6387
35. Ishida O, Maruyama K, Sasaki K, Iwatsuru M (1999) Int J Pharm 190:49
36. Maeda H, Sawa T, Konno T (2001) J Control Release 122:246
37. Symon Z, Peyser A, Tzemach D, Lyass O, Sucher E, Shezen E, Gabizon A (1999) Cancer 86:72
38. O'Shaughnessy JA (2003) Clin Breast Cancer 4:318

39. Gabizon AA (2001) Cancer Invest 19:424
40. Song LY, Ahkong QF, Rong Q, Wang Z, Ansell S, Hope MJ, Mui B (2002) Biochim Biophys Acta 1558:256
41. Mishra S, Webster P, Davis ME (2004) Eur J Cell Biol 83:97
42. Remaut K, Lucas B, Braeckmans K, Demeester J, De Smedt SC (2007) J Control Release 117:256
43. Guo X, Szoka FC (2001) Bioconjug Chem 12:291
44. Guo X, MacKay JA, Szoka FC (2003) Biophys J 84:1784
45. Choi JS, MacKay JA, Szoka FC (2003) Bioconjug Chem 14:420
46. Shin J, Shum P, Thompson DH (2003) J Control Release 91:187
47. Kirpotin D, Hong K, Mullah N, Papahadjopoulos D, Zalipsky S (1996) FEBS Lett 388:115
48. Ishida T, Kirchmeier MJ, Moase EH, Zalipsky S, Allen TM (2001) Biochim Biophys Acta 1515:144
49. Ambegia E, Ansell S, Cullis P, Heyes J, Palmer L, MacLachlan I (2005) Biochim Biophys Acta 1669:155
50. Mott JD, Werb Z (2004) Curr Opin Cell Biol 16:558
51. Coussens LM, Fingleton B, Matrisian LM (2002) Science 295:2387
52. Turk BE, Huang LL, Piro PB, Cantley LC (2001) Nat Biotechnol 19:661
53. Hatakeyama H, Akita H, Kogure K, Oishi M, Nagasaki Y, Kihira Y, Ueno M, Kobayashi H, Kikuchi H, Harashima H (2007) Gene Ther 14:68
54. Holland JW, Cullis PR, Madden TD (1996) Biochemistry 35:2610
55. Sato H, Kida Y, Mai M, Endo Y, Sasaki T, Tanaka J, Seiki M (1992) Oncogene 7:77
56. Miyamori H, Takino T, Kobayashi Y, Tokai H, Itoh Y, Seiki M, Sato H (2001) J Biol Chem 276:28204
57. Stein Y, Halperin G, Stein O (1980) FEBS Lett 111:104
58. Templeton NS, Lasic DD, Frederik PM, Stery HH, Roberts DD, Pavlakis GN (1997) Nat Biotechnol 15:647
59. Wheeler JJ, Palmer L, Ossanlou M, MacLachlan I, Graham RW, Zhang YP, Hope MJ, Scherrer P, Cullis PR (1999) Gene Ther 6:271
60. Fenske DB, Cullis PR (2005) Methods Enzymol 391:7
61. Ueno M, Kashiwagi H, Hirota N (1997) Chem Lett 1997:217
62. Sasaki K, Kogure K, Chaki S, Kihira Y, Ueno M, Harashima H (2005) Int J Pharm 296:142
63. Scherer LJ, Rossi JJ (2003) Nat Biotechnol 21:1457
64. Ali MM, Oishi M, Nagatsugi F, Mori K, Nagasaki Y, Kataoka K, Sasaki S (2006) Angew Chem Int Ed Engl 45:3136
65. Sasaki S, Nagatsugi F (2006) Curr Opin Chem Biol 10:615
66. Tamm I (2006) Clin Sci (Lond) 110:427
67. Van..ková I, Kopkan L, Husková Z, Vaňourková Z, Schejbalová S, Červenka L, Kramer HJ (2007) Vascul Pharmacol 47:63
68. Liang Y, Lin S, Zhou Y, Wang J, Yu X (2007) J Biomed Sci 14:155
69. Gokhale PC, Soldatenkov V, Wang FH, Rahman A, Dritschilo A, Kasid U (1997) Gene Ther 4:1289
70. Shi F, Hoekstra D (2004) J Control Release 97:189
71. Semple SC, Klimuk SK, Harasym TO, Dos Santos N, Ansell SM, Wong KF, Maurer N, Stark H, Cullis PR, Hope MJ, Scherrer P (2001) Biochim Biophys Acta 1510:152
72. Yamauchi M, Kusano H, Saito E, Iwata T, Nakakura M, Kato Y, Uochi T, Akinaga S, Aoki N (2006) J Control Release 114:268
73. Yamada Y, Kogure K, Nakamura Y, Inoue K, Akita H, Nagatsugi F, Sasaki S, Suhara T, Harashima H (2005) Biol Pharm Bull 28:1939
74. Nakamura Y, Kogure K, Yamada Y, Futaki S, Harashima H (2006) J Pharm Pharmacol 58:431
75. Bertrand JR, Pottier M, Vekris A, Opolon P, Maksimenko A, Malvy C (2002) Biochem Biophys Res Commun 296:1000
76. Vickers TA, Koo S, Bennett CF, Crooke ST, Dean NM, Baker BF (2003) J Biol Chem 278:7108

77. Chen X, Dudgeon N, Shen L, Wang JH (2005) Drug Discov Today 10:587
78. Hiroi N, Funahashi A, Kitano H (2006) Cancer Gene Ther 13:7
79. Scherer L, Rossi JJ (2003) Nat Biotechnol 21:1457
80. Scherer L, Rossi JJ (2005) Biotechniques 36:557
81. Colin M, Maurice M, Trugnan G, Kornprobst M, Harbottle RP, Knight A, Cooper RG, Miller AD, Capeau J, Coutelle C, Brahimi-Horn MC (2000) Gene Ther 7:139
82. Verma UN, Surabhi RM, Schmaltieg A, Becerra C, Gaynor RB (2003) Clin Cancer Res 9:1291
83. Dalby B, Cates S, Harris A, Ohki EC, Tilkins ML, Price PJ, Ciccarone VC (2004) Methods 33:95
84. Bollerot K, Sugiyama D, Escriou V, Gautier R, Tozer S, Scherman D, Jaffredo T (2006) Dev Dyn 235:105
85. Dykxhoorn DM, Palliser D, Lieberman J (2006) Gene Ther 13:541
86. Khoury M, Louis-Plence P, Escriou V, Noel D, Largeau C, Cantos C, Scherman D, Jorgensen C, Apparailly F (2006) Arthritis Rheum 54:1867
87. Akita H, Ito R, Khalil IA, Futaki S, Harashima H (2004) Mol Ther 9:443
88. Leng Q, Scaria P, Zhu J, Ambulos N, Campbell P, Mixson AJ (2005) J Gene Med 7:977
89. Grzelinski M, Urban-Klein B, Martens T, Lamszus K, Bakowsky U, Höbel S, Czubayko F, Aigner A (2006) Hum Gene Ther 17:751
90. Li SD, Huang L (2006) Mol Pharm 3:579
91. Hanai K, Takeshita F, Honma K, Nagahara S, Maeda M, Minakuchi Y, Sano A, Ochiya T (2006) Ann NY Acad Sci 1082:9
92. Matsui K, Horiuchi S, Sando S, Sera T, Aoyama Y (2006) Bioconjug Chem 17:132
93. Veldhoen S, Laufer SD, Trampe A, Restle T (2006) Nucleic Acids Res 34:6561
94. Heyes J, Palmer L, Bremner K, MacLachlan I (2005) J Control Release 107:276
95. Morrissey DV, Lockridge JA, Shaw L, Blanchard K, Jensen K, Breen W, Hartsough K, Machemer L, Radka S, Jadhav V, Vaish N, Zinnen S, Vargeese C, Bowman K, Shaffer CS, Jeffs LB, Judge A, MacLachlan I, Polisky B (2005) Nat Biotechnol 23:1002
96. Zimmermann TS, Lee AC, Akinc A, Bramlage B, Bumcrot D, Fedoruk MN, Harborth J, Heyes JA, Jeffs LB, John M, Judge AD, Lam K, McClintock K, Nechev LV, Palmer LR, Racie T, Röhl I, Seiffert S, Shanmugam S, Sood V, Soutschek J, Toudjarska I, Wheat AJ, Yaworski E, Zedalis W, Koteliansky V, Manoharan M, Vornlocher HP, MacLachlan I (2006) Nature 441:111
97. Geisbert TW, Hensley LE, Kagan E, Yu EZ, Geisbert JB, Daddario-DiCaprio K, Fritz EA, Jahrling PB, McClintock K, Phelps JR, Lee AC, Judge A, Jeffs LB, MacLachlan I (2007) J Infect Dis 193:1650
98. Judge AD, Bola G, Lee AC, MacLachlan I (2006) Mol Ther 13:494
99. Zhang C, Tang N, Liu X, Liang W, Xu W, Torchilin VP (2006) J Control Release 112:229
100. Heyes J, Palmer L, Chan K, Giesbrecht C, Jeffs L, MacLachlan I (2007) Mol Ther 15:713
101. Nakamura Y, Kogure K, Futaki S, Harashima H (2007) J Control Release 119:360
102. Khalil IA, Futaki S, Niwa M, Baba Y, Kaji N, Kamiya H, Harashima H (2004) Gene Ther 11:636
103. Happ CS, Happ E, Nilges M, Gronenborn AM, Clore GM (1988) Biochemistry 27:1735
104. Blackburn GM (1989) In: Blackburn GM, Gait MJ (eds) Nucleic acids in chemistry and biology. IRL Press, Oxford, p 17
105. Felgner PL, Gadek TR, Holm M, Roman R, Chan HW, Wenz M, Northrop JP, Ringold GM, Danielsen M (1987) Proc Natl Acad Sci USA 84:7413
106. Farhood H, Serbina N, Huang L (1995) Biochim Biophys Acta 1235:289
107. Hui SW, Langner M, Zhao YL, Ross P, Hurley E, Chan K (1996) Biophys J 71:590
108. Harashima H, Shinohara Y, Kiwada H (2001) Eur J Pharm Sci 13:85
109. Xu Y, Szoka FC Jr (1996) Biochemistry35:5616
110. Hafez IM, Maurer N, Cullis PR (2001) Gene Ther 8:1188
111. Tachibana R, Harashima H, Shono M, Azumano M, Niwa M, Futaki S, Kiwada H (1998) Biochem Biophys Res Commun 251:538

112. Bailey AL, Cullis PR (1997) Biochemistry 36:1628
113. Urade R, Hayashi Y, Kito M (1988) Biochim Biophys Acta 946:151
114. Boussif O, Lezoualc'h F, Zanta MA, Mergny MD, Scherman D, Demeneix B, Behr JP (1995) Proc Natl Acad Sci USA 92:7297
115. Kichler A, Leborgne C, Coeytaux E, Danos O (2001) J Gene Med 3:135
116. Bentz J, Mittal A (2000) Cell Biol Int 24:819
117. Jardetzky TS, Lamb RA (2004) Nature 427:307
118. Plank C, Oberhauser B, Mechtler K, Koch C, Wagner E (1994) J Biol Chem 269:12918
119. Skehel JJ, Cross K, Steinhauer D, Wiley DC (2001) Biochem Soc Trans 29:623
120. Wagner E (1998) J Control Release 53:155
121. Wagner E, Plank C, Zatloukal K, Cotton M, Birnstiel ML (1992) Proc Natl Acad Sci USA 89:7934
122. Parente RA, Nir S, Szoka FC Jr (1990) Biochemistry 29:8720
123. Ritter W, Plank C, Lausier J, Rudolph C, Zink D, Reinhardt D, Rosenecker J (2003) J Mol Med 81:708
124. Wiethoff CM, Wodrich H, Gerace L, Nemerow GR (2005) J Virol 79: 1992
125. Ogris M, Carlisle RC, Bettinger T, Seymour LW (2001) J Biol Chem 276:47550
126. Boeckle S, Fahrmeir J, Roedl W, Ogris M, Wagner E (2006) J Control Release 112:240
127. Nakamura N, Hart DA, Frank CB, Marchuk LL, Shrive NG, Ota N, Taira K, Yoshikawa H, Kaneda Y (2001) J Biochem 129:755
128. Kaneda Y (2003) Curr Drug Targets 4:599
129. Jiang C, Koyabu N, Yonemitsu Y, Shimazoe T, Watanabe S, Naito M, Tsuruo T, Ohtani H, Sawada Y (2003) Human Gene Ther 14:1181
130. Jiang C, Matsuo H, Koyabu N, Ohtani H, Fujimoto H, Yonemitsu Y, Kaneda Y, Narro M, Tsuruo T, Sawada Y (2002) J Drug Target 10:345
131. Pollard H, Remy JS, Loussouarn G, Demolombe S, Behr JP, Escande D (1998) J Biol Chem 273:7507
132. Zabner J, Fasbender AJ, Moninger T, Poellinger KA, Welsh MJ (1995) J Biol Chem 270:18997
133. Itaka K, Harada A, Yamasaki Y, Nakamura K, Kawaguchi H, Kataoka K (2004) J Gene Med 6:76
134. Dean DA (1997) Exp Cell Res 230:293
135. Wilson GL, Dean BS, Wang G, Dean DA (1999) J Biol Chem 274:22025
136. Vacik J, Dean BS, Zimmer WE, Dean DA (1999) Gene Ther 6:1006
137. Mesika A, Grigoreva I, Zohar M, Reich Z (2001) Mol Ther 3:653
138. Mesika A, Kiss V, Brumfeld V, Ghosh G, Reich Z (2005) Human Gene Ther 16:200
139. Langle-Rouault F, Patzel V, Benavente A, Taillez M, Silvestre N, Bompard A, Sczakiel G, Jacobs E, Rittner K (1998) J Virol 72:6181
140. Vaughan EE, DeGiulio JV, Dean DA (2006) Curr Gene Ther 6:671
141. Lechardeur D, Sohn KJ, Haardt M, Joshi PB, Monck M, Graham RW, Beatty B, Squire J, O'Brodovich H, Lukacs GL (1999) Gene Ther 6:482
142. Lukacs GL, Haggie P, Seksek O, Lechardeur D, Freedman N, Verkman AS (2000) J Biol Chem 275:1625
143. Cornelis S, Vandenbranden M, Ruysschaert JM, Elouahabi A (2002) DNA Cell Biol 21:91
144. Suh J, Wirtz D, Hanes J (2003) Proc Natl Acad Sci USA 100:3878
145. Suh J, Wirtz D, Hanes J (2004) Biotechnol Progr 20:598
146. Leopold PL, Kreitzer G, Miyazawa N, Rempel S, Pfister KK, Rodriguez-Boulan E, Crystal RG (2000) Human Gene Ther 11:151
147. Seisenberger G, Ried MU, Endress T, Buning H, Hallek M, Brauchle C (2001) Science 294:1929
148. Suomalainen M, Nakano MY, Keller S, Boucke K, Stidwill RP, Greber UF (1999) J Cell Biol 144:657
149. Lycke E, Hamark B, Johansson M, Krotochwil A, Lycke J, Svennerholm B (1988) Arch Virol 101:87

150. Sodeik B, Ebersold MW, Helenius A (1997) J Cell Biol 136:1007
151. Ye GJ, Vaughan KT, Vallee RB, Roizman B (2000) J Virol 74:1355
152. Branden LJ, Mohamed AJ, Smith CI (1999) Nat Biotechnol 17:784
153. Hagstrom JE, Ludtke JJ, Bassik MC, Sebestyen MG, Adam SA, Wolff JA (1997) J Cell Sci 110:2323
154. Ludtke JJ, Zhang G, Sebestyen MG, Wolff JA (1999) J Cell Sci 112:2033
155. Sebestyen MG, Ludtke JJ, Bassik MC, Zhang G, Budker V, Lukhtanov EA, Hagstrom JE, Wolff JA (1998) Nat Biotechnol 16:80
156. Mortimer I, Tam P, MacLachlan I, Graham RW, Saravolac EG, Joshi PB (1999) Gene Ther 6:403
157. Tseng WC, Haselton FR, Giorgio TD (1999) Biochim Biophys Acta 1445:53
158. Wilke M, Fortunati E, Van den Broek M, Hoogeveen AT, Scholte BJ (1996) Gene Ther 3:1133
159. Zanta MA, Belguise-Valladier P, Behr JP (1999) Proc Natl Acad Sci USA 96:91
160. Nagasaki T, Myohoji T, Tachibana T, Futaki S, Tamagaki S (2003) Bioconjug Chem 14:282
161. Tanimoto M, Kamiya H, Minakawa N, Matsuda A, Harashima H (2003) Bioconjug Chem 14:1197
162. Chan CK, Jans DA (1999) Human Gene Ther 10:1695
163. Chan CK, Senden T, Jans DA (2000) Gene Ther 7:1690
164. Subramanian A, Ranganathan P, Diamond SL (1999) Nat Biotechnol 17:873
165. Rudolph C, Plank C, Lausier J, Schillinger U, Muller RH, Rosenecker J (2003) J Biol Chem 278:11411
166. Keller M, Harbottle RP, Perouzel E, Colin M, Shah I, Rahim A, Vaysse L, Bergau A, Moritz S, Brahimi-Horn C, Coutelle C, Miller AD (2003) Chembiochem 4:286
167. Muller K, Nahde T, Fahr A, Muller R, Brusselbach S (2001) Cancer Gene Ther 8:107
168. Li S, Huang L (1997) Gene Ther 4:891
169. Li S, Rizzo MA, Bhattacharya S, Huang L (1998) Gene Ther 5:930
170. Masuda T, Akita H, Harashima H (2005) FEBS Lett 579:2143
171. Nakamura T, Moriguchi R, Kogure K, Minoura A, Masuda T, Akita H, Kato K, Hamada H, Ueno M, Futaki S, Harashima H (2006) Biol Pharm Bull 29:1290
172. Duverger E, Carpentier V, Roche AC, Monsigny M (1993) Exp Cell Res 207:197
173. Duverger E, Pellerin-Mendes C, Mayer R, Roche AC, Monsigny M (1995) J Cell Sci 108:1325
174. Masuda, Akita H, Nishio T, Niikura K, Ijiro K, Harashima H (2008) Biomaterials 9:2623
175. Banks GA, Roselli RJ, Chen R, Giorgio TD (2003) Gene Ther 10:1766
176. Ledley TS, Ledley FD (1994) Human Gene Ther 5:679
177. Varga CM, Hong K, Lauffenburger DA (2001) Mol Ther 4:438
178. Varga CM, Tedford NC, Thomas M, Klibanov AM, Griffith LG, Lauffenburger DA (2005) Gene Ther 12:1023
179. Hama S, Akita H, Iida S, Mizuguchi H, Harashima H (2007) Nucleic Acids Res 35:1533
180. Hama S, Akita H, Ito R, Mizuguchi H, Hayakawa T, Harashima H (2006) Mol Ther 13:786
181. Tachibana R, Harashima H, Ide N, Ukitsu S, Ohta Y, Suzuki N, Kikuchi H, Shinohara Y, Kiwada H (2002) Pharm Res 19:377
182. Tachibana R, Harashima H, Shinohara Y, Kiwada H (2001) Adv Drug Deliv Rev 52:219
183. Akita H, Ito R, Khalil IA, Futaki S, Harashima H (2004) Mol Ther 9:443
184. Kamiya H, Akita H, Harashima H (2003) Drug Discov Today 8:990
185. Akita H, Ito R, Kamiya H, Kogure K, Harashima H (2007) J Gene Med 9:197

Adv Biochem Engin/Biotechnol (2010) 119: 231–250
DOI: 10.1007/10_2009_13
© Springer-Verlag Berlin Heidelberg 2009
Published online: 14 October 2009

Sensors

Masato Saito, Ha Minh Hiep, Naoki Nagatani, and Eiichi Tamiya

Abstract With recent advances in nanotechnology, development of nanomaterial bioconjugates is growing exponentially towards eventual translation into biomolecular recognition layers on surfaces. Label-free monitoring of biorecognition events is also key-technology and provides a promising platform, which is simple, cost-effective, and requires no external modification to biomolecules. In this review, we describe the application of nanomaterials, mainly metal nanoparticles, and specific applications of carbon nanotubes (CNTs) based label-free approaches.

Keywords Carbon nanotubes • DNA sensors • Electrochemical immunosensor • Enzymatic biosensor • Field-effect transistors • Gold nanoparticle • Microchamber array • Molecular interface • Plasmonic sensors • Single cell • Single molecule DNA

Contents

M. Saito, H. Hiep, and E. Tamiya (✉)
Department of Applied Physics, Graduate School of Engineering Osaka University, 2-1 Yamadaoka, Suita, Osaka, 565-0871, Japan
e-mails: saitomasato@ap.eng.osaka-u.ac.jp; hiep@ap.eng.osaka-u.ac.jp; tamiya@ap.eng.osaka-u.ac.jp

N. Nagatani
Dpartment of Applied chemistry and Biotechnology, Faculty of Engineering, Okayama University of Science, 1-1 Ridai-cho, Kita-ku, Okayama, 700-0005, Japan
e-mail: nagatani@dac.ous.ac.jp

Abbreviations

μTAS	Micro total analysis system
Aβ	Amyloid-beta
AFB1	Aflatoxin B1
AFM	Atomic force microscope
CNTFETs	Carbon nanotube field-effect transistors
CNTs	Carbon nanotubes
DMPC	Dimyristoylphosphatidylcholine
DPV	Differential pulse voltammetry
FET	Field-effect transistor
GOx	GOD Glucose oxidase
HBM	Hybrid bilayer membrane
hCG	Human chorionic gonadotropin hormone
HRP	Horseradish peroxidase
IgE	Immunoglobulin E
LOD	Limit of detection
MWCNTs	Multi-walled CNTs
OP	Organophosphorus
OPH	Organophosphorus hydrolase
PDMS	Poly(dimethylsiloxane)
PNA	Peptide nucleic acid
QCM	Quartz crystal microbalance
SAM	Self assembled monolayer
SEM	Scanning electron microscopy
SNP	Single-nucleotide polymorphism
SSB	Single-stranded DNA binding protein
SWCNTs	Single-walled CNTs
TNF-α	Tumor necrosis factor-α gene
T-PSA	Prostate-specific antigen

1 Label-Free Plasmonic Sensors Based on Gold-Capped Nanoparticles Substrate

1.1 Introduction

The recent revolutionary developments of nanoscience and nanotechnology have made great contributions to optical sensors and nanodevices fields [1, 2]. Because of larger shapes compared to individual atoms and, smaller, to the bulk solid, nanostructures display the intermediate behavior between macroscopic solid and atomic or molecular system [3]. Their unique properties are high surface to volume ratio [4–6], quantum size effect [7], and electrodynamics interactions. The noble metal nanostructures, namely, gold, silver, and copper, possess unique optical property for sensing with refractive index of surrounding medium that have received considerable attention from researchers [8, 9].

A common plasmonic sensor based on the immobilization of gold nanoparticles on a glass slide has been discussed lately [10–12]. However, several drawbacks of this plasmonic sensor have been pointed out. One of them is the complicated chemistry required to form a self assembled monolayer (SAM) of gold nanoparticles; the slightest defect in the uniformity of SAMs might cause significant problems in the reproducibility and reliability of results. Moreover, integrating this plasmonic substrate into other technologies as well as their miniaturizations in the compact system is limited because of the necessity of Kretschmann configuration in its total internal reflection mode.

To overcome the above limitations, a flexible, stable nanostructure substrate, gold-capped nanoparticles structure, which can excite plasmonic signals in a simple collinear optical system, is proposed. This is shown in Fig. 1a [13–15]. In that construction, the silica nanoparticles are used as the “core” and thin gold films as the “cap” coated at the top of the “core.” The atomic force microscope (AFM) image evidently indicates that the nanoparticles formed a monolayer on the glass substrate (Fig. 1b). Therefore, we can control the excitation mode of absorption spectra of gold-capped nanoparticle structure by changing the size of silica nanoparticle and the thickness of gold layer. The results shown in Fig. 1c clearly indicate that when the gold thickness is increased, keeping the core size constant, the peak wavelength of the absorbance spectra is shifted to the shorter wavelength and the maximum of peak intensity is achieved at a particular gold thickness. On the basis of gold-capped nanoparticles substrate, two types of plasmonic sensors, protein and membrane sensors are presented with high sensitivity and selectivity, opening possibilities for massively parallel detection in a miniaturized package as well as incorporation with other methods such as electrochemical, quartz crystal microbalance (QCM), etc.

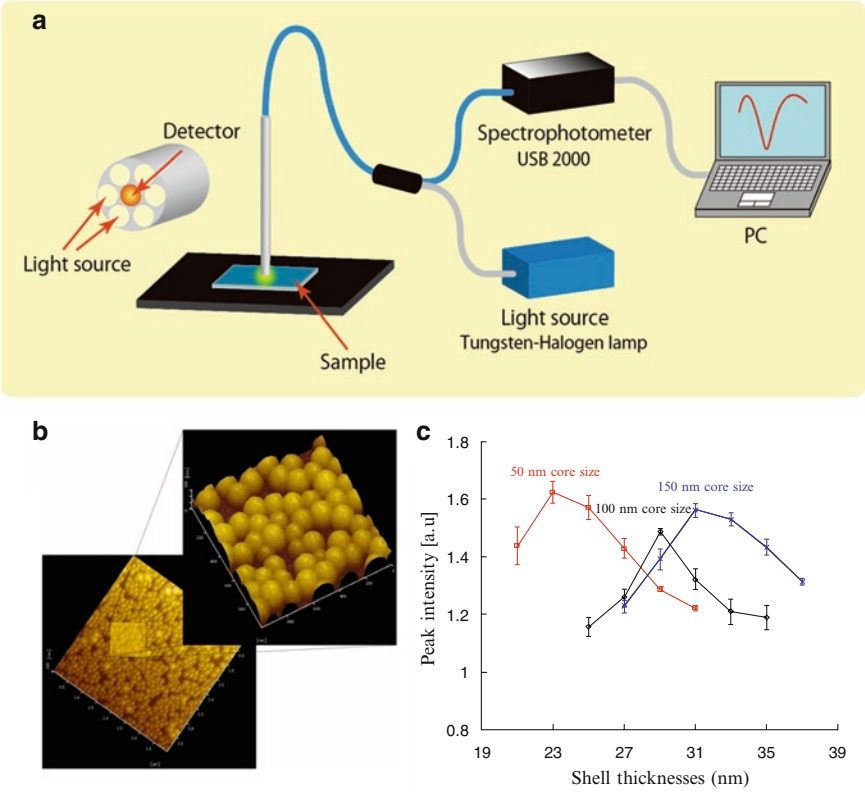

Fig. 1 **a** Experimental setup for optical measurement of the gold-capped nanoparticle substrate. **b** AFM image of substrate surface. **c** The peak intensity characterizations of the absorbance spectra for three core sizes of 50, 100, and 150 nm in diameter

1.2 A Protein Sensor for Label-Free Monitoring of Antigen–Antibody Interactions

Development of optical protein sensors based noble nanostructure currently receives great attention because of their potential for highly efficient, simultaneous analysis of a number of important biomolecules from proteomics to genetics. In this study, we utilize the absorbance spectra of gold-capped nanoparticle substrates for label-free detections of antigen–antibody reactions using protein A which it is hoped will make the "upright" orientation of the antibody so that it interacts better with the specific antigen (Fig. 2a). In this case, after attaching anti-casein antibodies onto the gold surface, we produce a casein sensor and use it to detect casein in a milk sample [16].

Adding casein onto the antibodies modified substrate surface, we find a peak absorbance increment caused by the specific antigen–antibody reactions (Fig. 2b). Analytical range and sensitivity of the casein sensor with different concentrations

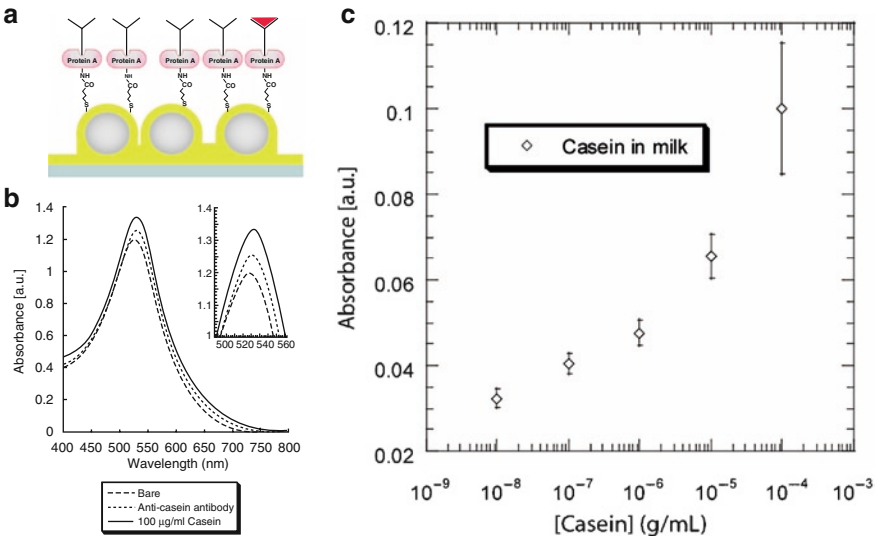

Fig. 2 **a** Scheme of protein sensor using protein A linker. **b** Absorbance spectra responses monitored using (*dashed line*) bare gold-capped nanoparticle substrate, (*dotted line*) anti-casein antibody immobilized substrate, (*solid line*) after the antigen–antibody reactions with 100 µg mL^{-1} casein. **c** Calibration plot using the milk samples spiked with casein at various concentrations

of casein, between 0 and 100 µg mL^{-1}, are also investigated. Hence, the dependences of absorbance intensity increments on the casein concentrations in milk are established as shown in Fig. 2c.

With high precision, the casein sensor based on gold-capped nanoparticle substrates can be further used as a promising candidate for low-cost and highly sensitive quantification of analytes in a simple and rapid format.

Another interested point regarding protein sensors is the development of a label-free system that allows studying biomolecular interactions in real-time. For this reason, Tamiya et al. propose a microfluidic chips fabricated by soft lithography technique using poly(dimethylsiloxane) (PDMS) material (Fig. 3a) [17]. This microfluidic based protein sensor enables us to interrogate specific insulin and anti-insulin antibody reaction in real-time with a limit of detection (LOD) of 100 ng mL^{-1} target insulin (Fig. 3b). Moreover, the kinetic constants for the process of interaction of insulin and anti-insulin antibody immobilized on a surface can be determined by linear transformation of sensograms with an overall affinity constant K (k_a/k_d) of $2.39 \times 10^7\,M^{-1}$. This microfluidic chip holds several advantages such as real-time detection at low experimental cost with less reagent consumption, kinetic constant determination of antigen–antibody interaction, and reduction of the total analysis time. It actually opens a crucial potential for micro total analysis system (µTAS) integration.

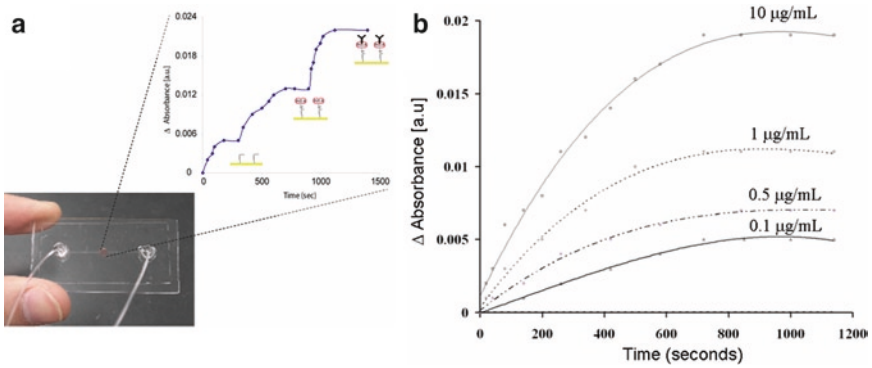

Fig. 3 **a** The PDMS based microfluidic chip for real-time monitoring of biomolecular interactions. **b** Real-time monitoring of insulin to anti-insulin antibody immobilized on chip surface

1.3 A Label-Free Membrane Sensor for the Detection of Peptide Binding Using Electrochemical–Optical Methods

Plasmonics and electrochemistry measurements connecting to gold-capped nanoparticles structure are successfully exploited in a simultaneous detectable scheme. A membrane-based sensor to detect optically the binding of peptide toxin melittin to hybrid bilayer membrane (HBM) and electrochemically assess its membrane-disturbing properties as a function of concentration has been presented in [18].

Optical behaviors of gold-capped nanoparticle substrate are investigated corresponding to the HBM deposition steps in Fig. 4a. Compared to the bare substrates, the absorbance spectra of alkanethiol-modified ones change due to the self-assembly formation of 1-decanethiol on the gold surface (Fig. 4b). Both the peak shift and the increase in absorbance of the gold-capped structure nanoparticle substrates can be used as the optical signatures to examine biomolecular interactions. Because of its slightly higher sensitivity, monitoring the peak intensity changes of the absorbance spectra is focused in this study. Dispersing with lipid vesicle solution, the alkanethiol-modified hydrophobic surface makes contact with acyl chains of polar lipids, orienting its polar headgroups towards the solution. Consequently, the formation of HBM causes an intensive increase in the absorbance spectrum by about 0.039 (a.u.) in comparison to the decanethiol modified surface.

On the other hand, the presence of 1-decanethiol and successive dimyristoylphosphatidylcholine (DMPC) layers on the bare substrate surface strongly suppresses the electrochemical reaction of redox probes. As demonstrated in Fig. 4c, decreases in the magnitude and insignificant changes in the peak separation achieved from 1-decanethiol modified substrate surface and HBM-covered substrate suggest that a simple membrane-based sensor is successfully created from gold-capped nanoparticle substrate. However, when a melittin solution of 100 ng mL^{-1} is introduced onto the HBM modified surface, the amperometric respond of $[Fe(CN)_6]^{3-/4-}$ considerably

increases. This enhancement implies that the melittin can interact with the mimic biomembrane, causing the leakage of this layer.

The binding of melittin to HBM mediated by its functionality is carried out in the same substrate using electrochemical-optical methods with the LOD of 10 ng mL^{-1} melittin (Fig. 4d). Up to now, there have been only a few studies on the interaction between melittin and biomembrane using electrochemical methods and plasmonic approaches. The reasons for the small amount of research on the above problem are widely considered in many aspects, especially the complex nature of interaction system and the lack of a suitable integrated chip. This work opens up an effective and trouble-free way to develop other membrane-based sensors for the detection of a huge number of functional protein toxins that does not require taking Kretschmann configuration for surface plasmon excitation into account. Current work is underway to integrate this sensor into microfluidic and expand it into multi-array format to make an impact contribution to μTAS progress.

1.4 Conclusions

The implementations of gold-capped nanoparticles substrates reported here provide the experimentally simple and convenient plasmonic sensors that can be easily used in most biochemistry laboratories. With user-friendly operations the gold-capped nanostructure is promising for creating a flexible detection capability in a highly miniaturized package.

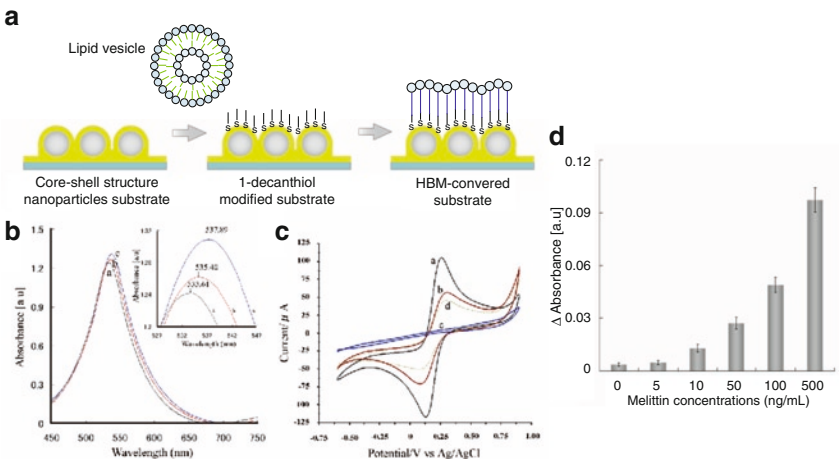

Fig. 4 **a** Fabrication of membrane-based sensor. **b** The peak absorbance intensity changes of the gold-capped structure nanoparticle substrate. **c** Cyclic voltammogram of the gold-capped structure nanoparticle substrate (a), of the thiol-modified substrate (b), of the HBM-covered substrate (c), and after incubation with 100 ng mL^{-1} melittin (d) in 2 mM $[Fe(CN)_6]$. **d** The calibration curves for the melittin on the membrane-based sensor using optical measurement

2 Biosensors Using Carbon Nanotubes

2.1 Introduction

Carbon nanotubes (CNTs) have been produced and observed under a variety of conditions prior to 1991 [19]. They are cylindrical graphite sheets with properties that make them potentially useful in a wide variety of applications in fields of materials science. They exhibit extraordinary strength and unique electrical properties and are used in electrochemical biosensors for promoting electron transfer reactions with electroactive species. There are two groups of CNTs: single-walled CNTs (SWCNTs) and multi-walled CNTs (MWCNTs) [20]. SWCNTs are comprised of a cylindrical graphite sheet of nanoscale diameter (~1 nm) capped by hemispherical ends. MWCNTs comprise several to tens of concentric cylinders of these graphite shells with a layer spacing of 3–4 Å. They have a diameter between 2 and 100 nm [21]. Since their first application to the study of dopamine [22], CNTs increasingly show potential in bioelectrochemistry.

2.2 CNTs Based Biosensor for Enzyme Reaction

Electrochemical biosensors using CNTs, particularly enzyme electrodes, have greatly benefited from properties of CNTs based devices to promote the electron transfer reactions of enzyme reactions. Besteman et al. [23] reported that glucose oxidase (GOx) was attached to the sidewalls of a semiconductive SWCNT by using a bifunctional reagent. The conductance of the enzyme-functionalized SWCNT was increased by the biocatalytic process, which started with the addition of glucose [23]. Wang et al. [24] reported a mediator free glucose sensor based Nafion-coated CNTs-modified glassy carbon electrode. The electrodes exhibit a strong and stable electrocatalytic response toward hydrogen peroxide. The marked acceleration of the hydrogen peroxide redox process is very attractive for the operation of oxidase-based amperometric biosensors for the highly selective low-potential (−0.05 V vs Ag/AgCl) biosensing of glucose. Rubianes and Rivas [25] also reported a highly selective and sensitive glucose biosensor without using any metal, redox mediator or antiinterference membrane. No interference was observed at −0.100 V even for large excesses of ascorbic acid, uric acid and acetaminophen. A linear response up to 30 mM (5.40 $g L^{-1}$) glucose with a detection limit of 0.6 mM (0.11 $g L^{-1}$) were obtained with CNTs paste electrodes modified with 10 wt% GOx. Musameh et al. [26] described CNTs-modified glassy carbon electrodes exhibiting strong and stable electrocatalytic response toward NADH. A substantial (490 mV) decrease in the overvoltage of the NADH oxidation reaction (compared to ordinary carbon electrodes) is observed using single-wall and multi-wall CNTs coatings, with oxidation starting at ca. −0.05 V (vs Ag/AgCl; pH 7.4). Furthermore, the NADH amperometric response of the coated electrodes is extremely stable, with 96% and 90% of the initial activity remaining after 60 min stirring of 2×10^{-4} and 5×10^{-3} M NADH solutions, respectively (com-

pared to 20% and 14% at the bare surface). Wang and Musameh [27] also reported on an MWCNTs-based alcohol biosensor, based on the incorporation of alcohol-dehydrogenase/NAD^+ within a three-dimensional MWCNTs/Teflon matrix. Deo et al. [28] described an amperometric biosensor for organophosphorus (OP) pesticides based on a CNT-modified transducer and an organophosphorus hydrolase (OPH) biocatalyst. The sensor performance was optimized with respect to the surface modification and operating conditions. Under optimal conditions the biosensor was used to measure as low as 0.15 μM paraoxon and 0.8 μM methyl parathion with sensitivities of 25 and 6 nA μM^{-1}, respectively. Tujita et al. [29] fabricated CNT amperometric chips with pneumatic micropumps by the combination of amperometric biosensors based on CNT-arrayed electrodes and microchannels with pneumatic micropumps made of PDMS (Fig. 5). CNTs-based transducers have been shown to be useful for their resistance to surface fouling of transducers and for enhancing the performance of enzyme electrodes.

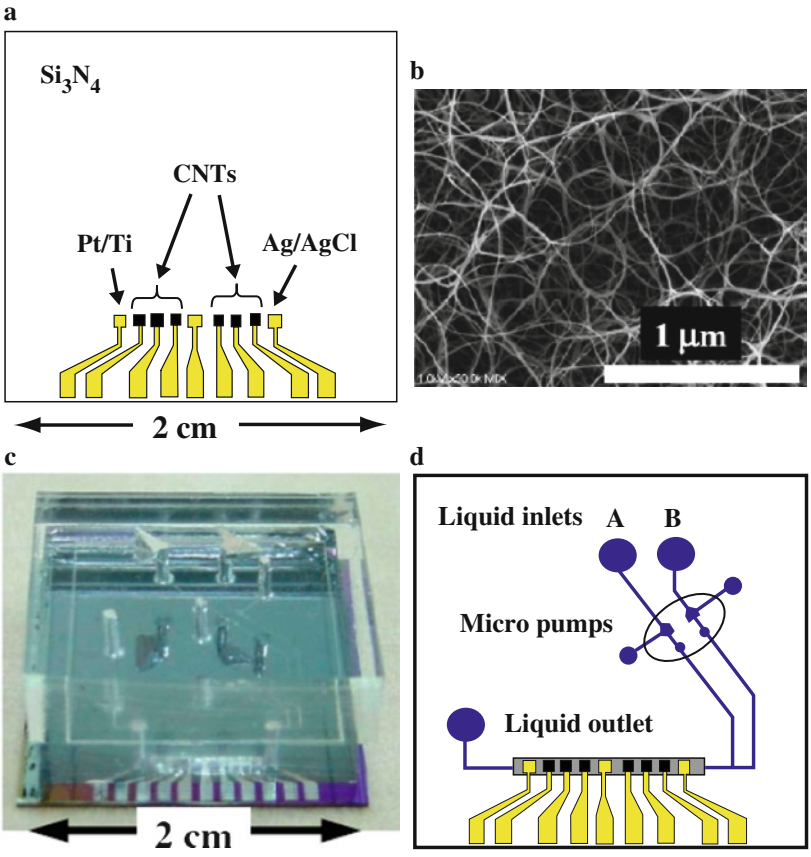

Fig. 5 Schematic plan-view image of CNT amperometric biosensor (**a**), scanning electron microscopy (SEM) image of CNT electrode (**b**), optical (**c**) and schematic plan-view (**d**) images of microfluidic chips with CNT-arrayed electrodes with pneumatic micropumps

2.3 CNTs Based Biosensor for Biomolecules (Proteins)

Electrochemical detection for biomolecules is of great interest owing to its high sensitivity and compatibility for miniaturization and mass-fabrication. Normally specific biomolecules can be measured by the methods involving antibody reaction. CNTs based biosensors for biomolecules combined antibodies have been reported. Okuno et al. [30] fabricated a label-free electrochemical immunosensor using microelectrode arrays modified with SWCNTs (Fig. 6). They measured total prostate-specific antigen (T-PSA) using differential pulse voltammetry (DPV). The label-free detection of T-PSA was carried out by measuring current signals, derived from the oxidation of tyrosine (Tyr), and tryptophan (Trp) residues, increased by the interaction between T-PSA on T-PSA-mAb covalently immobilized on SWCNTs. The detection limit for T-PSA was determined to be 0.25 ng mL^{-1} [31]. CNTs based biosensors for biomolecules using aptamers instead of antibodies was reported. Aptamers are synthetic oligonucleotides that can be generated to bind selectively to low molecular weight organic and inorganic substrates and to macromolecules such as proteins and drugs, with high affinity. Maehashi et al. [32] reported that a sensor based on aptamer-modified CNT-FET was developed for label-free detection of immunoglobulin E (IgE). Briefly, 5′-amino-modified aptamers were immobilized on CNT channels and the electrical properties monitored in

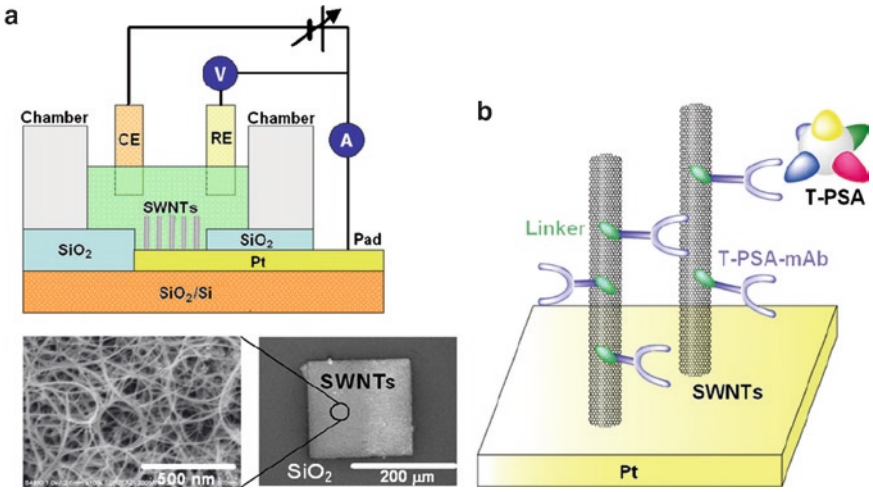

Fig. 6 **a** Illustration for the experimental setup with single-walled carbon nanotube (SWNT)-modified Pt microelectrode as the working electrode, Pt wire as the counter electrode, and the miniaturized reference electrode (RE, Ag/AgCl) with SEM images of a SWNT-modified microelectrode. **b** Illustration for the label-free electrochemical immunosensor design. Monoclonal antibodies against total prostate-specific antigen (T-PSA-mAb) were covalently anchored onto the SWNTs using 1-pyrenebutanoic acid succinimidyl ester (Linker). The peak current for the intrinsic oxidation of proteins, deriving from their electroactive amino acids, increases as the antigen–antibody complex is formed

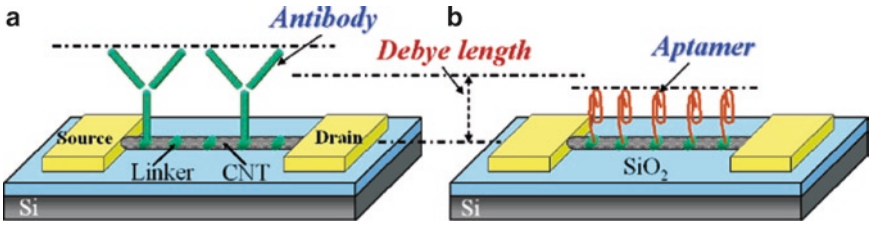

Fig. 7 Schematic representation of label-free protein biosensors based on CNT field-effect transistors (CNTFETs): **a** antibody-modified CNT-FET; **b** aptamer-modified CNT-FET

real-time. Upon introduction of IgE, a sharp decrease in the source-drain current was observed. After optimization, the LOD was determined at 250 pM IgE. They also compared the performance of this aptasensor and the IgE immunosensor described earlier in the same article [31]; under similar conditions the aptasensor provided better sensitivity (Fig. 7). So et al. [32] also utilized the real-time detection of protein using SWCNT-field-effect transistor (FET) based aptasensors. Antithrombin aptamers, highly specific to serine protein thrombin, were immobilized on the sidewall of an SWCNT-FET using carbodiimidazole-activated Tween 20 as the linking molecules. The binding of thrombin aptamers to SWCNT-FETs caused a rightward shift of the threshold gate voltages, presumably due to the negatively charged backbone of the DNA aptamers.

2.4 CNTs Based Biosensor for Nucleic Acids

Optical detection methods have commonly been used for detections of DNA hybridization, which are highly sensitive and specific methods [33, 34]. However, they need professional knowledge and techniques, and are very difficult to miniaturize. Recently, a number of CNTs based electrochemical biosensors for sensing DNA have appeared. Williams et al. [35] monitored the attachment of a 12-mer peptide nucleic acid (PNA) probe to a CNT by using atomic force microscopy. An MWCNT nanoelectrode array was used for the electrochemical detection of DNA hybridization in connection with a ruthenium complex [36]. The open ends of MWCNT exposed at the dielectric surface acted as nanoelectrodes on a planarized SiO_2 matrix [36]. Kerman et al. [37] developed a nanosensor array composed of CNT field-effect transistors (CNTFETs) on SiO_2/Si substrates. A SAM of PNA probes associated with the tumor necrosis factor-α gene (TNF-α) was attached onto the gold electrode on the reverse side of the CNT-FET device (Fig. 8). A time dependent conductance increase was monitored upon sequential introduction of wild-type DNA samples through a microfluidic channel of the PDMS chip. High selectivity of PNA probes only toward the full-complementary wild-type DNA samples enabled rapid and simple discrimination against single-nucleotide polymorphism

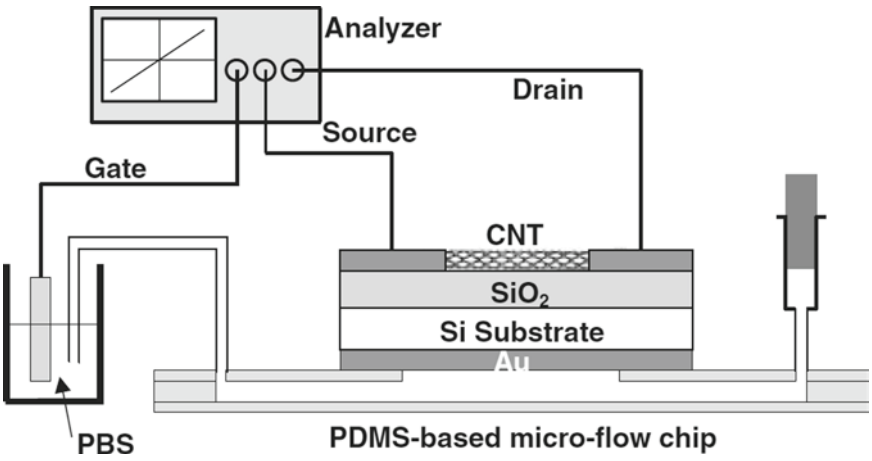

Fig. 8 Schematic diagram for the integration of the microflow chip and the electrical detection system for real-time monitoring of DNA hybridization by CNTFETs

(SNP) or noncomplementary DNA. Concentration dependent measurements indicated an LOD of 6.8 fM wild-type DNA [37].

2.5 Conclusions

Exploiting the electrical properties of CNTs with nanotechnology, CNTs continue to attract enormous interest as component in biosensors. Biosensors using CNTs are increasingly becoming one of the most promising candidates for measuring enzyme reactions, biomolecules and nucleic acids. We suggest that CNTs based electrochemical detections are promising methods for applications in numerous biosensor schemes.

3 Biosensors Using Gold Nanoparticles

3.1 Introduction

Nowadays there is great interest in using metal nanoparticles in electrochemical biosensors. In this part we will discuss their sensor applications by focusing on several unique physicochemical properties of metal nanoparticles, especially of gold nanoparticles. Gold nanoparticles have been used in many areas of bioanalytical methods through the unique properties, such as extremely high extinction coefficients and straightforwardness in introducing surface functionality.

3.2 Gold Nanoparticles Based Electrochemical Biosensor for Proteins

The pioneering works about the use of gold nanoparticles as electrochemical labels for the voltammetric detection of proteins were performed by González-García et al. [38] and Dequaire et al. [39]. The high affinity between streptavidin and biotin was detected using the adsorptive stripping voltammetric signal of gold nanoparticles down to the 2.5 nM streptavidin level [38]. The heterogeneous sandwich immunoassay based on the stripping voltammetric detection of gold nanoparticles involved the binding of the Au-labeled secondary antibody, followed by acid dissolution and anodic stripping electrochemical measurement of the solubilized gold tracer on a bare screen-printed carbon strip [39]. Since their first application, an immunosensor for the detection of antigen–antibody reactions, a variety of electrochemical biosensing schemes involving enzymes [40–42], and colloidal metal nanoparticles [43–45] as labels have been reported. In particular, metal nanoparticles have excellent conductivity and catalytic properties. Metal nanoparticle can act as "electronic wires" and promote the communication between the redox centers in proteins and electrode surfaces [46]. Liu et al. [47] has developed an immunosensor for the detection of aflatoxin B1 (AFB1) based on a bioelectrocatalytic reaction involving Au nanoparticles using microcomb electrodes. The microcomb electrode was fabricated by means of self-assembling horseradish peroxidase (HRP) and AFB1 antibody molecules onto gold nanoparticles functionalized biorecognition surfaces. The presence of nanogold provided a congenial microenvironment for the immobilized biomolecules and decreased the electron transfer impedance, leading to a direct electrochemical behavior of the immobilized HRP. Liang and Mu [48] modified screen-printed electrodes with Au nanoparticles and performed a flow injection immunobioassay for the detection of interleukin-6 in humans. Their immunosensor was prepared by entrapping HRP-labeled IL-6 antibody into gold nanoparticles-modified composite membrane at a screen-printed graphite electrode. Idegami et al. [49] developed a sensitive immunosensor for the detection of pregnancy marker, human chorionic gonadotropin hormone (hCG) using the direct electrical detection of gold nanoparticles. They utilized disposable screen-printed carbon strips for the development of our immunosensor, which provided cost-effective tests with the required antigen sample volume as small as 2 mL. After the recognition reaction between the surface-immobilized primary antibody and hCG, the captured antigen was sandwiched with a secondary antibody that was labeled with Au nanoparticles. Au nanoparticles were exposed to a preoxidation process at 1.2 V for 40 s, which was subsequently followed with a reduction scan on the same surface using DPV (Fig. 9). Additionally, they observed that the number of gold nanoparticles on the immunosensor was determined using scanning electron microscopy images, and showed a linear relationship with the current intensity obtained from the DPV measurements with a detection limit of 36 pg mL^{-1} hCG (612 fM, 3.6×10^{-4}IU mL^{-1}). Recently, an electrochemical biosensor combining gold nanoparticles with saccharides for detection of Alzheimer's amyloid-beta (Aβ) was developed. Chikae et al. [50] reported the

electrochemical sensing of saccharide–protein interactions using a couple of sialic acid derivatives and Aβ. The densely-packed saccharide area for recognition of protein was fabricated onto a carbon electrode by three steps – electrochemical deposition of gold nanoparticles on a screen-printed strip, SAM formation of the acetylenyl group on gold nanoparticles, and the cycloaddition reaction of an azide-terminated sialic acid to the acetylenyl group (Fig. 10). The intrinsic oxidation signal of the captured Aβ (1-40) and (1-42) peptides, containing a single Tyr residue, was monitored at a peak potential of 0.6 V (vs Ag/AgCl within this sensor) in connection with DPV. The peak current intensities were concentration dependent.

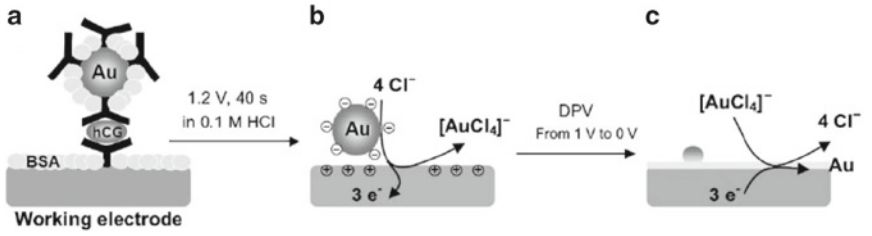

Fig. 9 Schematic illustration of the disposable immunosensor system. The primary antibody was immobilized directly on the screen-printed carbon strip surface, and a series of sandwich-type immunoreactions were performed on a single strip (**a**). A high potential, at 1.2 V, was applied in 0.1 M HCl for the oxidation of Au nanoparticles, called as the preoxidation (**b**), and then, the voltammetric measurement was performed (**c**)

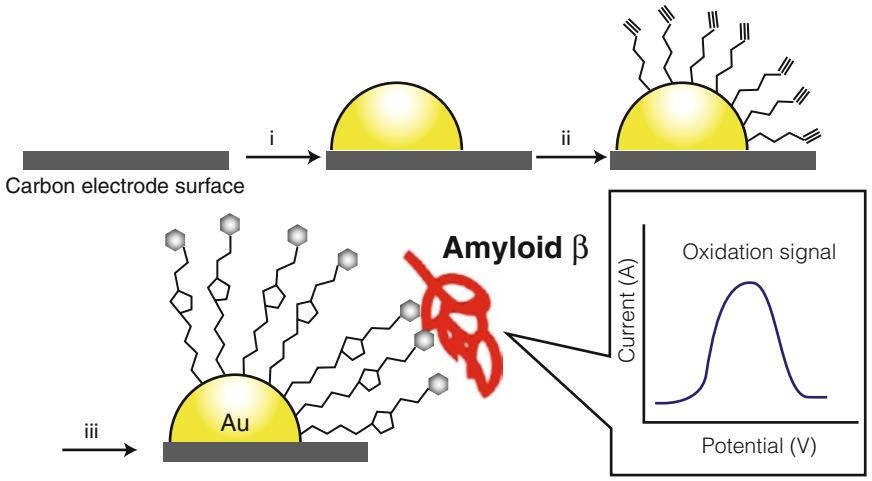

Fig. 10 Schematic illustration of the nanobioelectronic detection system for Alzheimer's Aβ peptides. The sugar immobilized substrate was prepared through i–iii steps (i) deposition of gold nanoparticle on carbon electrode, (ii) formation of acetylenyl-terminated self assembled monolayer, and (iii) saccharide immobilization for Aβ detection. The attachment of Aβ peptide to the sugar layer and the electrochemical detection were realized on a single electrode. The peak oxidation current response of Tyr residue of Aβ was utilized as the analytical signal

3.3 Gold Nanoparticles Based Electrochemical Biosensor for Enzyme Reaction

Gold nanoparticles have been extensively used for promoting the direct electron transfer for electrochemical biosensors such as a glucose sensor. Liu and Ju [51] report a high sensitivity with GOx immobilized on colloidal gold modified carbon paste electrode. They showed this could be used for glucose detection with a high sensitivity (8.4 μA mM^{-1}), a linear range from 0.04 to 0.28 mM, and a detection limit of 0.01 mM at a signal-to-noise ratio of 3σ. Since the pioneering works on the use of gold nanoparticles as electrochemical labels for the voltammetric detection of proteins, a number of glucose sensors have been reported. Zhang et al. [52] developed a feasible method to fabricate glucose biosensor by covalent attachment of GOx to a gold nanoparticle monolayer modified gold electrode. The sensor provided a linear response to glucose over the concentration range of 2.0×10^{-5} to 5.7×10^{-3} M with a sensitivity of 8.8 μA $mM^{-1}\,cm^{-2}$ and a detection limit of 8.2 μM. Zao et al. [53] reported that the direct electron transfer of GOD was achieved based on the immobilization of GOD/colloidal gold nanoparticles on a glassy carbon electrode by a Nafion film. Enzyme reactions other than those involving glucose can also be measured by electrochemistry using gold nanoparticles. Kerman et al. [54] demonstrate the application of gold nanoparticles in the electrochemical detection of protein phosphorylation. Their method is based on the labeling of a specific phosphorylation event with gold nanoparticles, followed by electrochemical detection. The phosphorylation reaction is coupled with the biotinylation of the kinase substrate using a biotin-modified adenosinetriphosphatase as the cosubstrate. When the phosphorylated and biotinylated kinase substrate is exposed to streptavidin-coated gold nanoparticles, the high affinity between the streptavidin and biotin resulted in the attachment of gold nanoparticles on the kinase substrate. The electrochemical response obtained from gold nanoparticles enables monitoring of the activity of the kinase and its substrate, as well as the inhibition of small molecule inhibitors on protein phosphorylation (Fig. 11). Du et al. [55] developed a novel electrochemical method for investigation of pesticide sensitivity using acetylcholinesterase biosensor based on colloidal gold nanoparticle modified sol–gel interface screen-printed electrode.

3.4 Gold Nanoparticles Based Electrochemical Biosensor for Nucleic Acids

Recently, an impressive number of interested designs for gold nanoparticles based electrochemical sensing for DNA have appeared. A novel gold nanoparticle–streptavidin conjugate covered with a large number of ferrocenylalkanethiol molecules was synthesized, and applied to amplified sandwich hybridization assays of oligonucleotides and real samples related to hepatitis B virus [56]. Electrochemical

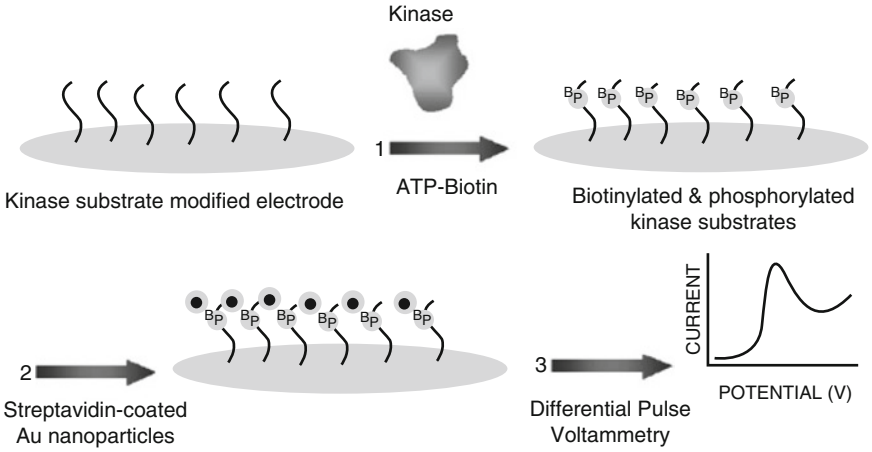

Fig. 11 Schematic representation of the principal for gold nanoparticle-based detection of protein phosphorylation. The phosphorylation and biotinylation of the immobilized peptide on a screen-printed carbon electrode (1) is followed by the attachment of streptavidin-coated gold nanoparticles (2). The reduction signal of gold nanoparticles was monitored using differential pulse voltammetry (3)

detection of DNA immobilized on gold nanoparticles by a SAM modified electrode with silver nanoparticle label has recently been reported by Wang et al. [57]. The electrochemical oxidation signal of gold nanoparticles anchored on a probe enabled the detection of factor V Leiden mutation in PCR samples [58]. Kerman et al. [59] reported that the unique binding event between *Escherichia coli* single-stranded DNA binding protein (SSB) and single-stranded oligonucleotides conjugated to gold nanoparticles was utilized for the electrochemical detection of DNA hybridization. SSB was attached to SAM of single-stranded oligonucleotide modified gold nanoparticle, and the resulting gold tagged SSB was used as the hybridization label. Changes in the gold oxidation signal were monitored upon binding of gold tagged SSB to probe and hybrid on the electrode surface. The amplified oxidation signal of gold nanoparticles provided a detection limit of 2.17 pM target DNA, which can be applied to genetic diagnosis applications (Fig. 12). Tsai et al. [60] developed an electrical DNA detection method that detected target DNA at concentrations as low as 1 fM by using self-assembly multi-layer gold nanoparticle structure between nano-gap electrodes.

3.5 Conclusions

Gold nanoparticle can promote the communication between the redox centers in proteins and electrode surfaces. The catalytic activity of gold nanoparticles to amplify the electrochemical reactions gives them a significant priority in the design

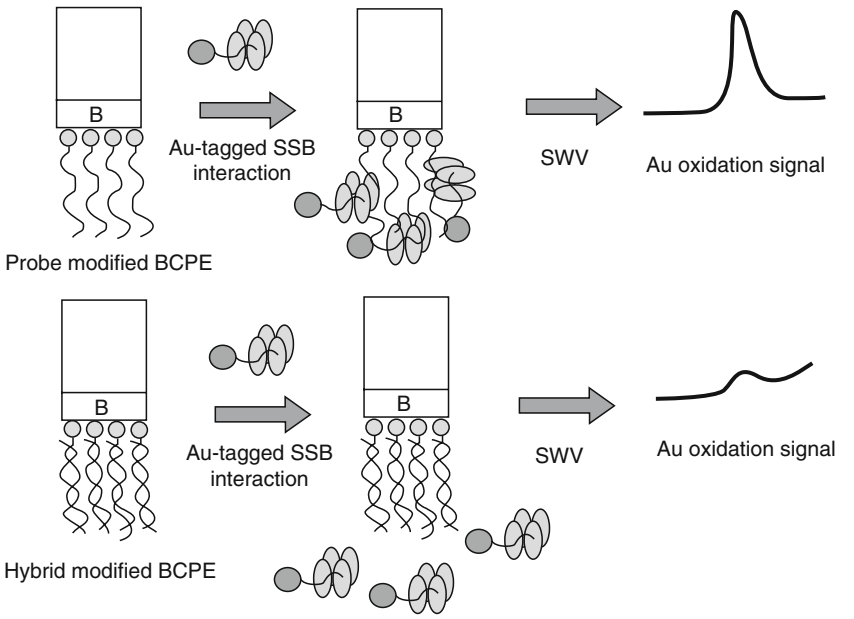

Fig. 12 Schematic illustration of the hybridization detection protocol. Au-tagged SSB can bind to the single-stranded probe, thus amplify the Au oxidation signal. However, only a low Au signal can be obtained from the double-stranded hybrid after interaction with SSB

of electrochemical biosensors. The combination of electrochemical detection methods and gold nanoparticles provides a promising platform for the development of highly sensitive and convenient biosensors.

References

1. Hutter E, Fendler J (2004) Exploitation of localized surface plasmon resonance. Adv Mater 16:1685–1706
2. Ghosh SK, Pal T (2007) Interparticle coupling effect on the surface plasmon resonance of gold nanoparticles: from theory to applications. Chem Rev 107:4797–4862
3. Kreibig U, Vollmer M (1995) Optical properties of metal clusters. Springer, Berlin
4. Ghosh SK, Kundu S, Mandal M, Pal T (2002) Silver and gold nanocluster catalyzed reduction of methylene blue by arsine in a micellar medium. Langmuir 18:8756–8760
5. Ghosh SK, Pal T, Kundu S, Nath S, Pal T (2004) Fluorescence quenching of 1-methylaminopyrene near gold nanoparticles: size regime dependence of the small metallic particles. Chem Phys Lett 395:366–372
6. Ghosh SK, Pal A, Kundu S, Nath S, Panigrahi S, Pal T (2005) Dimerization of eosin on nanostructured gold surfaces: size regime dependence of the small metallic particles. Chem Phys Lett 412:5–11
7. Kubo R (1962) Electronic properties of metallic fine particles I. J Physical Soc Japan 17:975–986

8. Mulvaney P (1996) Surface plasmon spectroscopy of nanosized metal particles. Langmuir 12:788
9. Yonzon CR, Jeoung E, Zou S, Schatz GC, Mrksich M, Van Duyne RP (2004) A comparative analysis of localized and propagating surface plasmon resonance sensors: the binding of concanavalin A to a monosaccharide functionalized self-assembled monolayer. J Am Chem Soc 126:12669
10. Nath N, Chilkoti A (2002) A colorimetric gold nanoparticle sensor to interrogate biomolecular interactions in real time on a surface. Anal Chem 74:504–509
11. Nath N, Chilkoti A (2004) Label-free biosensing by surface plasmon resonance of nanoparticles on glass: optimization of nanoparticle size. Anal Chem 76:5370–5378
12. Fujiwara K, Watarai H, Itoh H, Nakahama E, Ogawa N (2006) Measurement of antibody binding to protein immobilized on gold nanoparticles by localized surface plasmon spectroscopy. Anal Bioanal Chem 386:639–644
13. Ha MH, Endo T, Kim DK, Tamiya E (2007) Nanostructure and molecular interface for biosensing devices. Proc SPIE 6768:67680I1–67680I11
14. Vestergaard M, Kerman K, Kim DK, Ha MH, Tamiya E (2008) Detection of Alzheimer's tau protein using localised surface plasmon resonance-based immunochip. Talanta 74:1038–1042
15. Endo T, Kerman K, Nagatani N, Ha MH, Kim DK, Yonezawa Y, Nakano K, Tamiya E (2006) Anal Chem 78:6465–6475
16. Ha MH, Endo T, Kerman K, Chikae M, Kim DK, Yamamura S, Takamura Y, Tamiya E (2007) Sci Tech Adv Mater 8:331–338
17. Ha MH, Nakayama T, Saito M, Yamamura S, Takamura Y, Tamiya E (2008) A microfluidic chip based on localized surface plasmon resonance for real-time monitoring of antigen-antibody reaction. Jpn J Appl Phys 47:1337–1341
18. Ha MH, Endo MS, Chikae M, Kim DK, Yamamura S, Takamura Y, Tamiya E (2008) Label-free detection of melittin binding to a membrane using electrochemical-localized surface plasmon resonance. Anal Chem 80:1859–1864
19. Iijima S (1991) Helical microtubules of graphitic carbon. Nature 354:56–58
20. Zhao Q, Gan Z, Zhuang Q (2002) Electrochemical sensors based on carbon nanotubes. Electroanalysis 14:1609–1613
21. Merkoci A, Alegret S (2005) Towards nanoanalytical chemistry: case of nanomaterial integration into [bio]sensing systems. Contrib Sci 3:57–66
22. Britto PJ, Santhanam KSV, Ajayan PM (1996) Carbon nanotube electrode for oxidation of dopamine. Bioelectrochem Bioenerg 41:121–125
23. Besteman K, Lee J, Wiertz FGM, Heering HA, Dekker C (2003) Enzyme-coated carbon nanotubes as single-molecule biosensors. Nano Lett 3:727–730
24. Wang J, Musameh M, Lin Y (2003) Solubilization of carbon nanotubes by nafion toward the preparation of amperometric biosensors. J Am Chem Soc 125:2408–2409
25. Rubianes MD, Rivas GA (2003) Carbon nanotubes paste electrode. Electrochem Commun 5:689–694
26. Musameh M, Wang J, Merkoci A, Lin Y (2002) Low-potential stable NADH detection at carbon-nanotube-modified glassy carbon electrodes. Electrochem Commun 4:743–746
27. Wang J, Musameh M (2003) Reagentless amperometric alcohol biosensor based on carbon-nanotube/teflon composite electrodes. Anal Lett 36:2041–2048
28. Deo RP, Wang J, Block I, Mulchandani A, Joshi KA, Trojanowicz M, Scholz F, Chen W, Lin Y (2005) Determination of organophosphate pesticides at a carbon nanotube/organophosphorus hydrolase electrochemical biosensor. Anal Chim Acta 530:185–189
29. Tsujita Y, Maehashi K, Matsumoto K, Chikae M, Torai S, Takamura Y, Tamiya E (2008) Carbon nanotube amperometric chips with pneumatic micropumps. Jpn J Appl Phys 47:2064–2067
30. Okuno J, Maehashi K, Kerman K, Takamura Y, Matsumoto K, Tamiya E (2007) Label-free immunosensor for prostate-specific antigen based on single-walled carbon nanotube array-modified microelectrodes. Biosens Bioelectron 22:2377–2381
31. Maehashi K, Katsura T, Kerman K, Takamura Y, Matsumoto K, Tamiya E (2007) Label-free protein biosensor based on aptamer-modified carbon nanotube field-effect transistors. Anal Chem 79:782–787

32. So HM, Won K, Hwan Kim YH, Kim BK, Ryu BH, Na PS, Kim H, Lee JO (2005) Single-walled carbon nanotube biosensors using aptamers as molecular recognition elements. J Am Chem Soc 127:11906–11907
33. Palecek E (2004) Surface-attached molecular beacons light the way for DNA sequencing. Trends Biotechnol 22:55–58
34. Watterson JH, Piunno PAE, Krull UJ (2002) Towards the optimization of an optical DNA sensor: control of selectivity coefficients and relative surface affinities. Anal Chim Acta 457:29–38
35. Williams KA, Veenhuizen PTM, de la Torre BG, Eritja R, Dekker C (2002) Nanotechnology: carbon nanotubes with DNA recognition. Nature 420:761
36. Li J, Ng HT, Cassell A, Fan W, Chen H, Ye Q, Koehne J, Han J, Meyyappan M (2003) Carbon nanotube nanoelectrode array for ultrasensitive DNA detection. Nano Lett 3:597–602
37. Kerman K, Morita Y, Takamura Y, Tamiya E, Maehashi K, Matsumoto K (2005) Peptide nucleic acid-modified carbon nanotube field-effect transistor for ultra-sensitive real-time detection of DNA hybridization. NanoBiotechnology 1:65–70
38. González-García MB, Fernández-Sánchez C, Costa-García A (2000) Colloidal gold as an electrochemical label of streptavidin–biotin interaction. Biosens Bioelectron 15:315–321
39. Dequaire M, Degrand C, Limoges B (2000) An electrochemical metalloimmunoassay based on a colloidal gold label. Anal Chem 72:5521–5528
40. Díaz-GonzáLez M, Hernaández-Santos D, González-Garcí MB, Costa-García A (2005) Development of an immunosensor for the determination of rabbit IgG using streptavidin modified screen-printed carbon electrodes. Talanta 65:565–573
41. Tonning E, Sapelnikova S, Christensen J, Carlsson C, Winther-Nielsen M, Dock E, Solná R, Skládal P, Norgaard L, Ruzgas T, Emnéus J (2005) Chemometric exploration of an amperometric biosensor array for fast determination of wastewater quality. Biosens Bioelectron 21:608–617
42. Preechaworapun A, Dai Z, Xiang Y, Chailapakul O, Wang J (2008) Investigation of the enzyme hydrolysis products of the substrates of alkaline phosphatase in electrochemical immunosensing. Talanta 76:424–431
43. Zhang S, Huang F, Liu B, Ding J, Xu X, Kong J (2007) A sensitive impedance immunosensor based on functionalized gold nanoparticle–protein composite films for probing apolipoprotein A-I. Talanta 71:874–881
44. Liang WB, Yuan R, Chai YQ, Li Y, Zhuo Y (2008) A novel label-free voltammetric immunosensor for the detection of α-fetoprotein using functional titanium dioxide nanoparticles. Electrochim Acta 53:2302–2308
45. Liang KZ, Qi JS, Mu WJ, Chen ZG (2008) Biomolecules/gold nanowires-doped sol–gel film for label-free electrochemical immunoassay of testosterone. J Biochem Biophys Methods 70:1156–1162
46. Luo X, Morrin A, Killard AJ, Smyth MR (2006) Application of nanoparticles in electrochemical sensors and biosensors. Electroanalysis 18:319–326
47. Liu Y, Qin Z, Wu X, Jiang H (2006) Immune-biosensor for aflatoxin B_1 based bio-electrocatalytic reaction on micro-comb electrode. Biochem Eng J 32:211–217
48. Liang KZ, Mu WJ (2006) Flow-injection immuno-bioassay for interleukin-6 in humans based on gold nanoparticles modified screen-printed graphite electrodes. Anal Chim Acta 580:128–135
49. Idegami K, Chikae M, Kerman K, Nagatani N, Yuhi T, Endo T, Tamiya E (2008) Gold nanoparticle-based redox signal enhancement for sensitive detection of human chorionic gonadotropin hormone. Electroanalysis 1:14–21
50. Chikae M, Fukuda T, Kerman K, Idegami K, Miura Y, Tamiya E (2008) Amyloid-β detection with saccharide immobilized gold nanoparticle on carbon electrode. Bioelectrochemistry 74:118–123
51. Liu S, Ju H (2003) Reagentless glucose biosensor based on direct electron transfer of glucose oxidase immobilized on colloidal gold modified carbon paste electrode. Biosens Bioelectron 19:177–183

52. Zhang S, Wang N, Yu H, Niu Y, Sun C (2005) Covalent attachment of glucose oxidase to an Au electrode modified with gold nanoparticles for use as glucose biosensor. Bioelectrochemistry 67:15–22
53. Zhao S, Zhang K, Bai Y, Yang W, Sun C (2006) Glucose oxidase/colloidal gold nanoparticles immobilized in Nafion film on glassy carbon electrode: direct electron transfer and electrocatalysis. Bioelectrochemistry 69:158–163
54. Kerman K, Chikae M, Yamamura S, Tamiya E (2007) Gold nanoparticle-based electrochemical detection of protein phosphorylation. Anal Chim Acta 588:26–33
55. Du D, Chen S, Cai J, Zhang A (2007) Electrochemical pesticide sensitivity test using acetylcholinesterase biosensor based on colloidal gold nanoparticle modified sol–gel interface. Talanta 74:766–772
56. Wang J, Li J, Baca AJ, Hu J, Zhou F, Pan W, Pang D-W (2003) Amplified voltammetric detection of DNA hybridization via oxidation of ferrocene caps on gold nanoparticle/streptavidin conjugates. Anal Chem 75:3941–3945
57. Wang M, Sun C, Wang L, Ji X, Bai Y, Li T, Li J (2003) Electrochemical detection of DNA immobilized on gold colloid particles modified self-assembled monolayer electrode with silver nanoparticle label. J Pharm Biomed Anal 33:1117–1125
58. Ozsoz M, Erdem A, Kerman K, Ozkan D, Tugrul B, Topcuoglu N, Ekren H, Taylan M (2003) Electrochemical genosensor based on colloidal gold nanoparticles for the detection of Factor V Leiden mutation using disposable pencil graphite electrodes. Anal Chem 75:2181–2187
59. Kerman K, Morita Y, Takamura Y, Ozsoz M, Tamiya E (2004) Modification of *Escherichia coli* single-stranded DNA binding protein with gold nanoparticles for electrochemical detection of DNA hybridization. Anal Chim Acta 510:169–174
60. Tsai CY, Chang TL, Chen CC, Ko FH, Chen PH (2005) An ultra sensitive DNA detection by using gold nanoparticle multilayer in nano-gap electrodes. Microelectron Eng 78–79:546–555

Adv Biochem Engin/Biotechnol (2010) 119: 251–265
DOI: 10.1007/10_2008_43
© Springer-Verlag Berlin Heidelberg 2009
Published online: 27 March 2009

Development of Fundamental Technologies for Micro Bioreactors

Kiichi Sato and Takehiko Kitamori

Abstract This chapter reviews the development of fundamental technologies required for microchip-based bioreactors utilizing living mammalian cells and pressure driven flow. The most important factor in the bioreactor is the cell culture. For proper cell culturing, continuous medium supply from a microfluidic channel and appropriate modification of the channel surface to accommodate cell attachment is required. Moreover, the medium flow rate should be chosen carefully, because shear stress affects cell activity. The techniques presented here could be applied to the development of micro bioreactors such as microlivers, pigment production by plant cells, and artificial insemination.

Keywords Artificial insemination, Cell culture, Microchip, Shear stress, Surface modification

K. Sato
Department of Applied Biological Chemistry, The University of Tokyo, Yayoi, Bunkyo-ku, Tokyo 113-8657, Japan;
Center for NanoBio Integration, The University of Tokyo, Hongo, Bunkyo-ku, Tokyo 113-8656, Japan; and
PRESTO, Japan Science and Technology Agency (JST), Sambancho, Chiyoda-ku, Tokyo 102-0075, Japan
e-mail: analchem@mail.ecc.u-tokyo.ac.jp

T. Kitamori (✉)
Department of Applied Chemistry, The University of Tokyo, Hongo, Bunkyo-ku, Tokyo 113-8656, Japan;
Center for NanoBio Integration, The University of Tokyo, Hongo, Bunkyo-ku, Tokyo 113-8656, Japan; and
Micro Chemistry Group, Kanagawa Academy of Science and Technology, Sakado, Takatsu-ku, Kawasaki, Kanagawa 213-0012, Japan
e-mail: kitamori@icl.t.u-tokyo.ac.jp

Contents

1 Introduction

1.1 Microchips for Chemical Reactors

Microchips or microfluidic devices for chemical and biochemical processes have been extensively developed owing to the progress of microfabrication techniques. Microchemical systems using these devices have attracted much attention from scientists and engineers. This new field of chemistry is known by the name of micro total analysis systems (μ-TAS) or lab-on-a-chip. As indicated by the name, the concept of these microchip-based systems proposes the integration of various chemical operations involved in conventional chemical processes done in a laboratory, such as mixing, reaction and separation, into a miniaturized flow system.

Most studies on microchip-based chemical systems have concerned DNA analysis by microchip electrophoresis with laser-induced fluorescence detection. These microchip-based electrophoretic systems have shown great advantages in some applications, especially in clinical diagnosis and molecular biology fields. However chemical operations which include several chemical processing steps are required for various applications such as on-chip synthesis, extraction, etc. For these complicated systems, where the chemical properties and potentials of molecules differ vastly, microfluidic systems using pressure-driven flow are more suitable. Recently, the importance of synthetic methods for small-scale synthesis of various chemicals is becoming evident. For example, in drug discovery, high-throughput and small-scale synthesis of a great variety of candidate chemicals is inevitable. Characteristics of microspaces, such as short diffusion length, large specific interfacial area (surface to volume ratio: S/V) and small heat capacity, are effective not only for analyses

but also for chemical syntheses, and microchips are expected to be used for such high-throughput synthesis. However, not all reactions are improved by microchips. What is most important is to choose properly an appropriate chemical reaction, for which the characteristics of microspaces are really beneficial. The large specific interfacial area and short molecular diffusion distance play important roles not only for determining effectiveness of the main reaction, but also for avoiding undesirable side reactions. On the basis of this idea, chemical reactors using microchips have been reported, for example, 2 × 2 combinatorial synthesis has been successfully carried out [1, 2], and a phase transfer diazocoupling reaction with fast and high yield conversion was implemented into a microchip system [3]. In the later case, to increase the production amount, a higher number of microchips were utilized instead of scaling up the process. Using this approach, a ten-layered pile-up reactor could produce a few grams per hour [4].

1.2 Bioreactors

A bioreactor is a kind of chemical reactor in which biochemical processes are carried out with biological cells or biochemically active substances (in most cases enzymes) derived from different organisms. Bioreactors are useful for the production of complicated compounds, optically active substances, and biologically active agents like medicines. Because the biocatalysts, i.e., cells or enzymes, are usually fixed on the surface or carrier particles in the bioreactor, a large specific interfacial area is required for efficient reaction. Also the required production amount of these compounds is in some cases low. These requirements make microchips suitable as bioreactors.

Whereas enzyme bioreactors may be realized by small modification of the chemical reactors using catalysts, realization of bioreactors using living cells require further technical development. In this chapter we review the development of fundamental technologies required for the realization of a microchip-based biochemical reactors using living cells with pressure-driven flow for continuous and sequential biochemical processes. In particular, we focus on mammalian cells as biocatalysts, although plant cells, yeasts, molds, and bacteria could also be useful for these purposes.

2 Fundamentals of Microchips

2.1 Characteristics of the Microchip Chemistry

A liquid microspace has several characteristic features different from the bulk scale, i.e., short diffusion distances, large specific interfacial area and small heat capacity. These characteristics are important to consider in the construction of chemical unit operations, such as mixing, reaction, extraction and separation, and constructing

integrated chemical systems. In particular, the scale of the microchannel dictates the molecular transportation time and the specific interface area. The transport time is proportional to the square of the scale. Therefore, the transport time are from several hours to 1 day when the diffusion distance is 1 cm, since the diffusion coefficient of typical molecular ions is on the order of 10^{-5} cm^2 s^{-1}. In contrast, it only takes some tens of seconds when the diffusion distance is 100 μm. The specific interface area of the 100-μm-scale microspace is equivalent to that provided by using a separatory funnel with rather vigorous mechanical shaking. Generally, these characteristics of the microspace described above become obvious below a scale of 250 μm.

2.2 Fabrication of Microchips

In general, a microchip is made from a glass plate, a silicon wafer, polydimethylsiloxane (PDMS), polymethylmethacrylate (PMMA), other polymers, or combinations thereof. Because of the chemical and physical stability, biocompatibility, and optical transparency for detection, glass microchips are suitable for various applications.

Glass microchips are typically fabricated using a photolithographic wet etching technique. Mechanically polished 0.7-mm-thick Pyrex glass plates are used for top and bottom plates. Inlet and outlet holes are drilled with a diamond-coated drill on the top plate. Then 20-nm-thick Cr and 100-nm-thick Au layers are vapor deposited on the bottom glass plate (substrate) under vacuum for good contact between the glass substrate and the photoresist and to provide protection of the glass substrate during the later glass etching. A 2-μm-thick positive photoresist layer is spin-coated onto the Au metal layer and baked at 90 °C for 30 min. A mask containing the microchannel is placed on top of the glass substrate and aligned with precision using a mask aligner. Subsequent UV light exposure degrades the photoresist polymer and transfers the microchannel pattern to the glass substrate. The photoresist is developed and a pattern with down to 10-μm-wide lines can quite easily be obtained. The Au and Cr layers are etched with I_2/NH_4I and $Ce(NH_4)_2(NO_3)_6$ solutions. The bare glass surface with the microchannel pattern is then etched with a 50% HF solution at an etching rate of 13 μm min^{-1}. After glass etching, the remaining photoresist is removed in acetone and metals are removed in I_2/NH_4I and $Ce(NH_4)_2(NO_3)_6$ solutions. The etched bottom plate and the top plate with the inlet and outlet holes are thermally bonded without any adhesives in an oven at ~650 °C.

PDMS or PDMS-glass hybrid microchips are also popular for biological applications because fabrication processes are simple. PDMS microchips can be fabricated using soft-lithographic techniques. First, a negative thick photoresist (SU-8) is microfabricated on a glass plate by photolithography to be a master template. Next, the PDMS prepolymer is cast on this template. After heating (at 70 °C for 1 h) and peeling from the template, the PDMS plate is bonded with a flat-bottom PDMS or glass plate using oxygen plasma to form a channel structure.

3 Cell Culture in a Microchip

Cell culturing is the most important factor of the cell-based micro bioreactor. Quite recently, cell culturing in microchips have received much attention for use in biochemical studies and bioassay systems [5]. In most of the studies, however, long-time culture has not been accomplished because long-time culture is not strongly required for cell analysis purposes. For cell based micro bioreactors, however, it is important to develop a life support system inside the microchip for long-time culturing. Surface modification for cell retention and activity is required as well as a continuous supply of oxygen and nutrients where microfluidic channels provide an efficient route for highly controlled delivery. Since integration is a convenient merit of microchips, a microchip-based culture chamber can be combined with chemical processors in which, in principle, all procedures required for biochemical experiments concerning the cultured cells, i.e., cell culture, cell analysis, biological reaction and measurement, can be performed.

In this section, a typical system using hepatocytes (liver cells) is used as an example of cell culturing. Hepatocyte cultures are well known as an assay tool for drug metabolism studies, biochemical syntheses, and bioreactors.

3.1 Basic Operations for Microchip Cell Cultures

Figure 1 shows a glass microchip for culturing cells. The chip has a micro cell culture chamber which is 100 μm deep, 1 mm wide, and 1 cm long and a connecting microchannel (100 μm deep and 250 μm wide). Prior to cell introduction, the

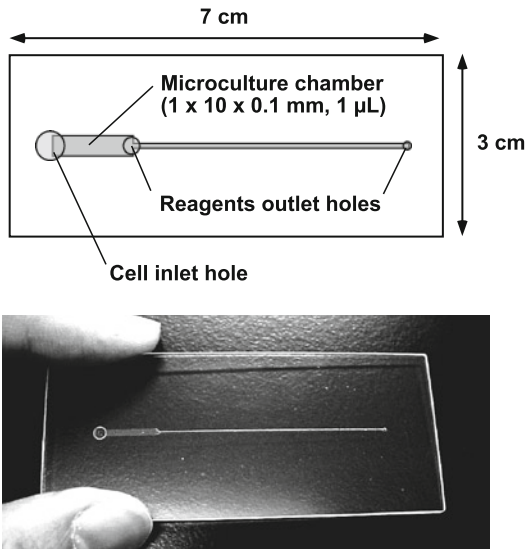

Fig. 1 Example of the glass microchip for cell culture

microchip is washed with 0.1% NaOH and rinsed with pure water, followed by autoclaving at 120 °C for 15 min. The inside walls of the microchamber are coated with 0.1% collagen type I solution for 15 min and then rinsed with PBS. Next, a medium supplemented with 10% FBS is introduced into the treated microchip and washed away after 10 min incubation; this gives a fibronectin coating on the microchamber and channels. After that, cells suspended with a small amount of the fresh medium are applied to the cell introduction hole on the chip. Cells move into the microchamber by capillary action. The chip is transferred to a 10-cm dish filled with fresh medium, and incubated in a CO_2 incubator at 37 °C with 5% CO_2.

3.2 Medium Supply

Growth rate and biological activity of the cultured cells are strongly dependent on the culture conditions. In the case of conventional static cultures, cells are usually attached to the surface of a commercially available polystyrene dish or flask for cell culture, and there is a relatively large amount of medium (2–3 mm in depth) with open air above. Supply of nutrients and oxygen is usually sufficient, and thus only medium composition is an important factor. In the microchip culture, however, the micro culture chamber is closed and thickness of the medium is ~0.1 mm. Shortage of both nutrients and oxygen and accumulation of the waste products may cause serious damage to the cell.

Since the metabolic rate and oxygen consumption of the hepatocytes are very high, a shortage of nutrients and/or oxygen may occur in the center of the microculture chamber [6]. In Fig. 2a the static hepatocyte culture grew well only near the inlet holes. Cultured cells in the center of the microchamber, i.e., far from the inlet holes, exhibited a significant decrease in viability. These suboptimal growth conditions were overcome when the chip was connected with a microsyringe pump via a Teflon capillary, and the medium was introduced continuously by injection or withdrawal. Different flow rates were investigated ranging from 0.1 to 1 μL min^{-1} in the injection or withdrawal mode. With higher flow rates than 1 μL min^{-1}, cells were washed away. On the other hand, with low flow rates, cells lost their viability as a result of a shortage of nutrients and/or oxygen. For these experimental conditions, the optimum flow rate was concluded to be 0.5 μL min^{-1} and good cell growth was obtained throughout the whole microchamber for at least 4 days (Fig. 2b). However, it should be noted that the optimum conditions are dependent on the dimensions of the chamber, cell density, and cell strain.

For some experiments like chemical stimulation, medium delivery through injection is suitable. If the conditioned medium is to be used for further experiments after the cultivation, the withdrawal mode for medium delivery is suitable to collect the medium. In the injection mode, however, air bubble interference in the microchamber has been found in some cases. Since air bubbles cause serious damage to the cells, they should be avoided, and therefore, in most cases, the withdrawal mode

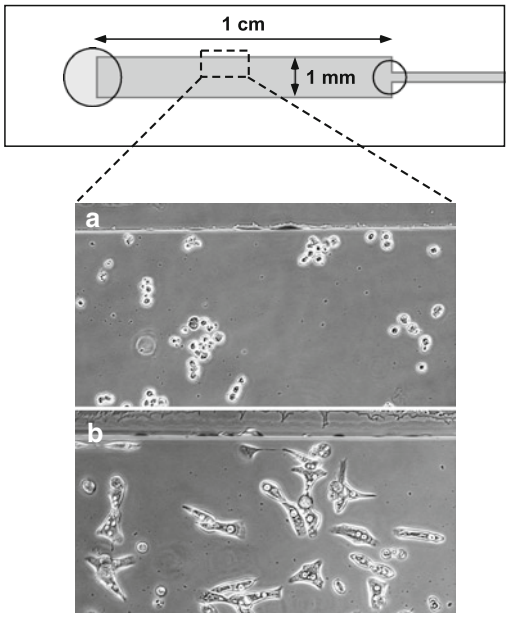

Fig. 2 Phase contrast images of hepatocytes cultured in the center of the microchamber (**a**) without or (**b**) with medium flow

may be preferable. Also, in withdrawal mode, the dead-volume can be decreased by using a short capillary and the medium temperature be easily kept at 37 °C by placing the medium container in the incubator with the microchip.

One of the primary goals of the cell culture is to sustain the cell-specific functions of the cultured cells. Thus, albumin productivity was examined as an indicator of liver specific function. To evaluate the performance of the hepatocytes, albumin synthesis was monitored for 4 days in a microchip with a continuous supply of fresh medium. The ability of hepatocytes to synthesize albumin increased during the first 3 days of the culture, meaning that the hepatocytes were active in albumin biosynthesis. Albumin secretion rates obtained in this experiment was comparable to those obtained from hepatocytes in a primary culture in a cell culture dish. Moreover, the hepatocytes in the microchip exhibited maintained urea secretion comparable to that obtained from hepatocytes in a primary culture in a cell-culture dish with the same medium.

3.3 Shear Stress

Since the medium is flowing in a continuous microchip culture, the cells are subjected to varying degrees of shear stress. To avoid damage to the cells, the flow rate must be tuned to deliver sufficient amount of medium while causing minimal damage to the

cell. The effect of shear stress on endothelial cells cultured in a microchip has been previously reported [7]. Below is another example of the effects of shear stress on human hepatoblastoma cell line Hep G2 cells cultured in a microchip [8].

Cells were cultured on a flat glass surface of a microchannel. The shear stress is regulated by the flow rate and the viscosity of the medium, which can be adjusted by the addition of dextran (MW = 200,000).

It is known that vascular endothelial cells can sense shear stress and regulate their morphology. The responsiveness of hepatocytes to shear stress was observed with a phase-contrast microscope in for changes in morphology. Figure 3 shows the images of the cells under various shear stress conditions after 24 h. To our knowledge, the shear stress in normal hepatic sinusoids is as high as 0.5 Pa. The images suggested that the morphology of the cells under 0.5 Pa remained in the same shape as in a static culture. From 0.6 to 1.2 Pa, the morphology of the cells was stretched in the direction of the flow. Over 2 Pa, cells were relatively round in shape and loose as seen after trypsin treatment. Under this shear flow condition, cells were washed away after 1 day.

Shear stress is claimed not only to affect endothelial cell morphology but also their biological activity in the vascular system. As a reporter of hepatocyte function, the albumin synthesis rate was measured for hepatocyte cultures in microchips under various conditions (Fig. 4). At the shear stress of 6.0 Pa, the albumin synthesis rates progressively decreased throughout the 3 days of experiment. Under lower shear stress conditions, the albumin synthesis rates remained unchanged after 1 day of culture. When higher shear stress was applied, there was significant decrease in the albumin synthesis rate from day 0 to day 1, whereas the cells under lower shear stress conditions showed the higher albumin synthesis rates. The results indicate that high shear stresses may be harmful to hepatocytes. Thus, although increasing medium flow rate supplies more nutrients and oxygen to the cells, it also damages them.

3.4 Attachment of Cells to Surfaces

Adherent cells must attach to the surface to survive, and chemical properties of the attachment surface are very important, because the biological activity of the cell, i.e., growth rate and cell differentiation, is dependent on the cell attachment. While the commercially available cell culture dishes have specially treated polystyrene surface for cell attachment, untreated flat glass and PDMS are not suitable for cell attachment. Therefore appropriate surface treatment is required on the microchannel surface to accommodate cell attachment, and if highly functionalized surfaces are constructed, special characters of the cells may be revealed.

The simplest way to modify the surface is physical adsorption of proteins that posses cell adhesive properties, i.e., extracellular matrix proteins. Collagens, fibronectin and Matrigel are popular, and polylysine is also used for some kinds of cells. for this kind of modification, a protein solution is introduced into the microchip,

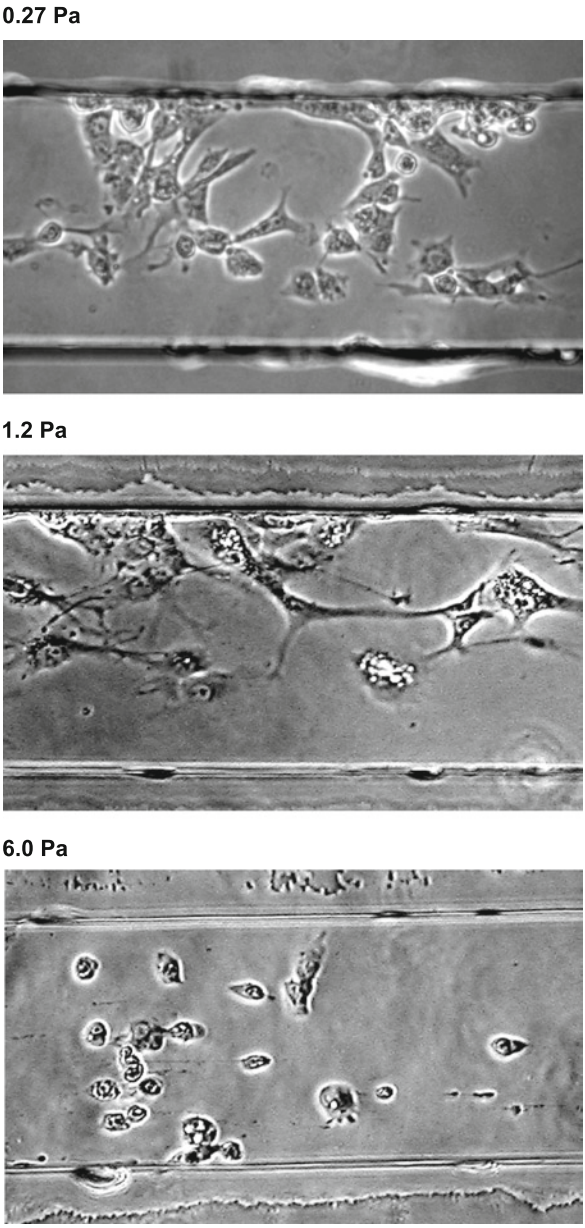

Fig. 3 Phase contrast images of Hep G2 cells cultured in the microchip under various shear stress conditions

which has been cleaned with an alkaline solution followed by sterile water in advance. After a 1-h incubation, the solution is removed and the channel is washed with medium. The washing process is important because excess unbound protein

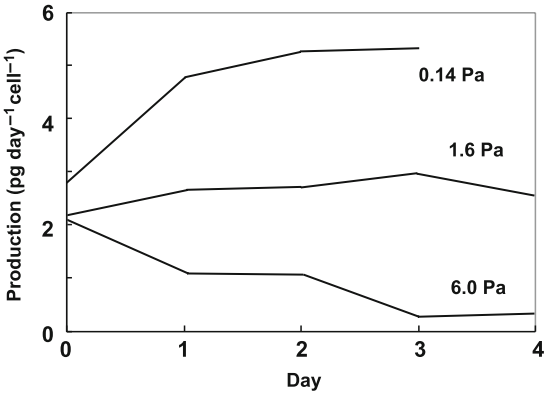

Fig. 4 Albumin production by Hep G2 cells cultured in the microchip under various shear stress conditions

may cause damage to the cells. The effect of the protein to the cell, i.e., cell attachment rate, growth rate, differentiation and so on, is dependent on the protein. For example, Hep-G2 cells on the fibronectin-coated surface are firmly attached, but albumin production rate was relatively poor. Thus, selection of the protein which will be used for the attachment of the cells is important. Alternatively, permanent modification of the channel with a silanization agent may also be an effective route for channel modification.

Moreover, micro/nano fabrication techniques can produce unique surfaces for cell attachment. To investigate and control interactions between cells and the surface in conventional bulk scale experiments, several kinds of nanofabricated structures were developed by colloidal lithography [9], polymer mixing [10], copolymer formation [11], and electron-beam lithography.

In addition, a nanostructure with a selective chemical modification has been fabricated in a microchannel [12]. Here, an electron-beam resist layer and a conductive polymer layer were coated on the substrate with a spin-coater (Fig. 5). Micro or nano patterns were drawn on the polymer layer by electron-beam lithography. After development, titanium and gold layers were deposited by sputtering. The substrates were immersed in solvent to remove metals on the resist layer. The metal pattern size was as small as 300 nm in width and about 150 nm in height. Next, the substrate was immersed in 1 mM 1-octadecanethiol in dehydrated ethanol for 24 h to attach the octadecane group onto the gold surface. After the immersion, the substrate was rinsed with ethanol and washed with 0.01 M NaOH and water, successively. Before cell culture, the substrate was treated with a fibronectin solution (10 μg mL^{-1} in PBS) at 37 °C for 1.5 h. By this treatment, fibronectin was adsorbed onto the nano-striped gold thin film, and Hep-G2 cells cultured on the nanostriped gold aligned with the stripes (Fig. 6). Hopefully, these new technologies may become useful new tools for cell culturing.

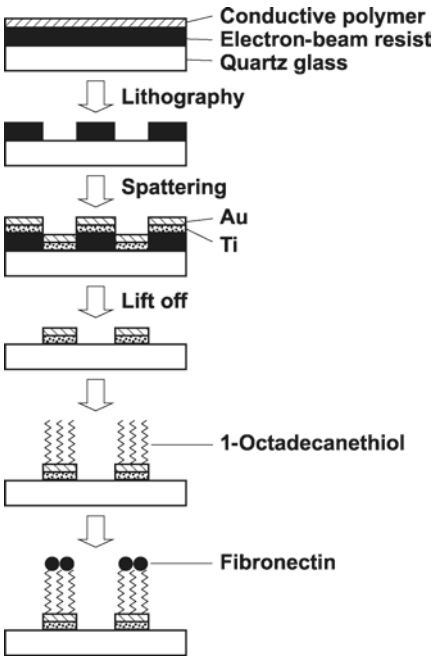

Fig. 5 Procedure for fabrication of cell culture surface with nanometer-scaled modification

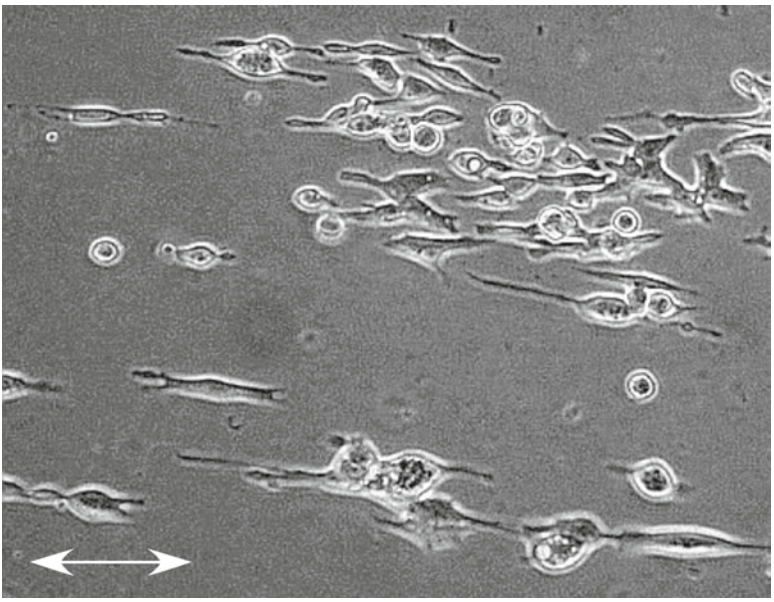

Fig. 6 Phase contrast images of Hep G2 cells cultured on a PDMS sheet with a stripe structure 550 nm in width and 960 nm intervals. The *arrow* shows the direction of the nanostripe

4 Applications

4.1 Microliver

The liver is the main chemical reactor in an animal body, and liver cells, hepatocytes, are the central machinery responsible for various biochemical reactions. Therefore, integration of liver functions into a microchip could create a versatile micro bioreactor [13, 14]. As described above, maintaining the liver functions was successful by controlling the attachment surface, medium supply, and shear stress. These techniques will be useful for the production of proteins like albumin, mammalian metabolism models and so on.

4.2 Pigment Production by Plant Cells

Plant cells are also useful for production of various compounds. Synthesis and accumulation of anthocyanin by strawberry cells cultured in a microchip has been reported [15]. Here, a PDMS microchip was fabricated with microchambers 400 μm wide, 500 μm long and 100 μm deep (20 nL). A suspension of strawberry cells (*Fragaria ananassa*) was introduced into the microchamber. The cells were cultured with a continuous medium flow of 5 μL min^{-1} at a point just outside of the chamber. Production parameters such as culture medium, initial cell density, and medium flow rate was optimized and after 9 days of culturing, anthocyanin accumulated in the vacuoles. Using this technique, it is expected that various useful compounds can be produced.

4.3 Micro Artificial Insemination

Micro bioreactors can produce not only chemical compounds and proteins, but also living matter itself. While an animal is much larger than a microchip, an embryo is as small as a microchannel. Moreover, oviduct and uterus contain small and closed spaces that resemble microchannels. Therefore, the microchip could be a useful tool for embryos handling. One example is shown below.

The concept of the system is illustrated in Fig. 7. The system has three steps, i.e., in vitro maturation of oocytes, in vitro fertilization (IVF), and in vitro culture (IVC) of embryos to the blastocyst stage. Glass microchips were fabricated by photolithography and wet etching, and had culture chambers 500–1,000 μm in diameter and connecting microchannels that were 50 μm deep and 100 μm wide. The matured porcine oocytes were transferred to the chamber, freeze-thawed, and preincubated boar epididymal spermatozoa were put into the other chamber (10^5 spermatozoa/chamber). Then fertilization medium, which was equilibrated with a gas consisting

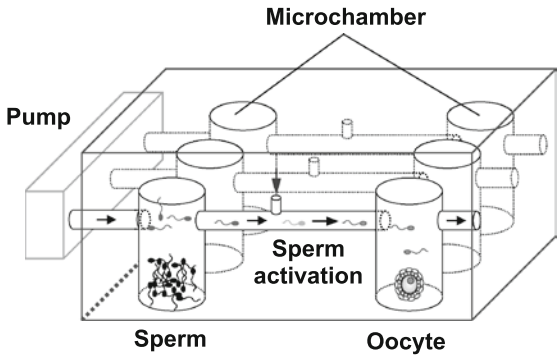

Fig. 7 Illustration of the microchip system for artificial insemination

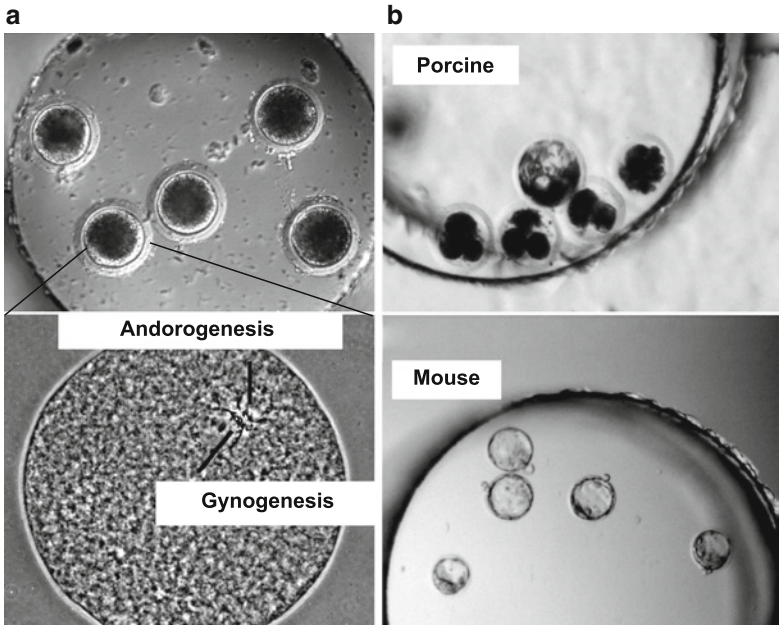

Fig. 8 **a** Photographs of the gametes during in vitro fertilization in a microchip. **b** Photographs of the embryos after in vitro culture for 4 days in microchip

of 5% CO_2 and 5% O_2 in advance, flowed continuously (10 μL h^{-1}) for 3 h at 38.5 °C to give the opportunity of the gametes to encounter each other. This was followed by the flowing of IVC medium for 7 h. Figure 8a shows the gametes during IVF in a microchip. Monospermic fertilization rate was calculated as 20%, which was comparable with that in the conventional method.

Porcine embryos and in vivo produced mouse embryos were cultured in the microchip. The mouse embryos at the mono-cell stage and porcine embryos at

the two- to four-cell stages were transferred into microchips and cultured at 37 or 38.5 °C, respectively, under continuous IVC medium flow (6 μL h^{-1}) conditions. Figure 8b shows photographs of the embryos after IVC for 4 days in microchip with a 700-μm microchamber. All mouse embryos and 28% of porcine embryos developed to the blastocyst stage. The rate was almost the same as that of the conventional method.

This [16] and related techniques [17, 18] are useful for in vitro production of embryos of domestic animals, which is very important in livestock farming for lower cost. Moreover, they may prove useful for artificial insemination of humans.

4.4 Bioreactors for Analytical Purposes

Most cells cause a specific reaction in response to stimulation. Determination of the stimulant can be performed by detection of the reaction products. Because a microchip is a very small device, a very small amount of the products can be detected without severe medium dilution. Moreover, a series of chemical reactions necessary for specific and sensitive detection of the products can easily be integrated into a microchip, and the microchip is suitable for microscopic optical detection. Therefore microchips with cultured cells are useful for various bioassays including assays of anticancer and antiallergic agents [19–21]. A typical example is described below.

Macrophages release nitric oxide (NO) upon stimulation, and thus macrophage activating agents or immune activating agents can be assayed by measuring the NO levels. The whole process of the assaying NO could successfully be integrated into a microchip [22]. A microchamber for cell culture and microchannels for reactions and detection were fabricated on a Pyrex glass substrate by photolithography and wet etching techniques. Cell culture, chemical and enzymatic reactions, and detection were integrated into the microchip. NO produced and released from macrophage-like cells stimulated by lipopolysaccharide was successfully monitored with the microchip, a temperature control device, and a thermal lens microscope. The total assay time was reduced from 24 h to 4 h, and detection limit of NO was improved from 1×10^{-6} M to 7×10^{-8} M compared with conventional methods. Moreover, the system could monitor a time course of the release, which is difficult to measure by conventional batch methods.

5 Conclusions

In this chapter we reviewed the most fundamental techniques for micro bioreactors utilizing mammalian cells. Proper cultivation of the cells in a microchip is the most important and essential factor of the micro bioreactor. Microchips provide a high level of control of culturing parameters and adjustment of the production scale can easily

be done by increasing the number of chips utilized. Hopefully, these kinds of systems will be used for the production of various proteins, drugs, and other expensive biochemical compounds in the near future.

Acknowledgements We thank Drs. Björn Renberg and Kae Sato for critical reading of the manuscript.

References

1. Kikutani Y, Kitamori T (2004) *Macromol Rapid Commun* 25:158
2. Kikutani Y, Horiuchi T, Uchiyama K, Hisamoto H, Tokeshi M, Kitamori T (2002) *Lab Chip* 2:188
3. Hisamoto H, Saito T, Tokeshi M, Hibara A, Kitamori T (2001) Chem Commun 2662
4. Kikutani Y, Hibara A, Uchiyama K, Hisamoto H, Tokeshi M, Kitamori T (2002) *Lab Chip* 2:193
5. Andersson H, van den Berg A (2004) *Lab Chip* 4:98
6. Tanaka Y, Sato K, Yamato M, Okano T, Kitamori T (2006) *J Chromatogr A* 1111:233
7. Song JW, Gu W, Futai N, Warner KA, Nor JE, Takayama S (2005) *Anal Chem* 77:3993
8. Tanaka Y, Yamato M, Okano T, Kitamori T, Sato K (2006) *Meas Sci Technol* 17:3167
9. Dalby MJ, Berry CC, Riehle MO, Sutherland DS, Agheli H, Curtis ASG (2004) *Exp Cell Res* 295:387
10. Dalby MJ, Riehle MO, Johnstone HJH, Affrossman S, Curtis ASG (2003) *J Biomed Mater Res A* 67A:1025
11. Long SF, Clarke S, Davies MC, Lewis AL, Hanlon GW, Lloyd AW (2003) *Biomaterials* 24:4115
12. Goto M, Tsukahara T, Sato K, Konno T, Ishihara K, Sato K, Kitamori T (2007) *Anal Sci* 23:245
13. Ostrovidov S, Jiang JL, Sakai Y, Fujii T (2004) *Biomed Microdev* 6:279
14. Leclerc E, Sakai Y, Fujii T (2004) *Biotechnol Prog* 20:750
15. Miyanaga K, Morita A, Unno H, Yamada M, Seki M (2004) *Proc APCChE* 2004 3P-01-094
16. Sato K, Sato K, Ozawa M, Kikuchi K, Nagai T, Kitamori T (2005) *Proc MicroTAS 2005* 2:883
17. Suh RS, Zhu XY, Phadke N, Ohl DA, Takayama S, Smith GD (2006) *Hum Reprod* 21:477
18. Clark SG, Haubert K, Beebe DJ, Ferguson CE, Wheeler MB (2005) *Lab Chip* 5:1229
19. Tanaka Y, Sato K, Yamato M, Okano T, Kitamori T (2004) *Anal Sci* 20:411
20. Tokuyama T, Fujii S, Sato K, Abo M, Okubo A (2005) *Anal Chem* 77:3309
21. Fujii S, Uematsu M, Yabuki S, Abo M, Yoshimura E, Sato K (2006) *Anal Sci* 22:87
22. Goto M, Sato K, Murakami A, Tokeshi M, Kitamori T (2005) *Anal Chem* 77:2125

Index